

# Time-Resolved Terahertz Spectroscopy of Semiconductor Nanomaterials

by

Charles E. Jensen

A thesis submitted in partial fulfillment of the requirements for the degree of  
Doctor of Philosophy

Department of Physics  
University of Alberta

©Charles E. Jensen, 2024

# Abstract

We investigate the microscopic nature of charge-carrier conduction in nanoscale ( $\sim 10^{-9}$  m) semiconducting materials using time-resolved terahertz spectroscopy (TRTS). TRTS uses picosecond ( $10^{-12}$  s) pulses of terahertz radiation (0.5-2.5 THz) to explore photoexcited charge-carrier lifetimes and dynamics with picosecond resolution. Owing to the small length scales probed by THz radiation ( $\sim 10$  nm), TRTS provides a valuable, non-contact approach to characterize charge-carrier transport in the novel nanomaterials studied herein for the first time.

Photoexcited charge-carriers are known to catalyze chemical reactions in CdS nanowires, however, the underlying ultrafast photoconductivity dynamics remain relatively unexplored. Here, we combine TRTS and time-resolved photoluminescence (TRPL) to form a new, self-consistent understanding of ultrafast transport in CdS nanowires wrapped in  $C_3N_5$  nanosheets. We find that charge carriers exhibit Drude-Smith conductivity spectrum, with bulk-like mobilities ( $\sim 400$   $cm^2/Vs$ ) on short length scales ( $< 25$  nm). We construct a theoretical model of band-edge photoconductivity and photoluminescence lifetimes in CdS nanowires that encompasses charge-carriers undergo subpicosecond hot-carrier cooling, bimolecular recombination, and surface recombination for the first time. By simultaneously

fitting photoconductivity and photoluminescence lifetimes we reveal that charge-separation ( $\sim 150$  ps) plays a significant role in the relaxation dynamics of CdS nanowires.

Atomically thin materials are a rapidly growing field of study, and there is a growing number of studies conducted in the THz frequency band. Here, we explore the temperature- and fluence-dependent charge carrier dynamics in a WSe<sub>2</sub> monolayer. We find that ultrafast exciton dissociation yields localized charge-carriers that dominate the photoconductivity in the THz frequency range. Furthermore, we find that the charge carrier mobility does not significantly change with fluence (50 - 500  $\mu\text{J}/\text{cm}^2$ ) or temperature (80 - 295 K).

High mobility semiconductors are desirable in battery applications, but the price is prohibitive in large-scale manufacturing. Inverse-opal nanostructures can simultaneously reduce costs and enhance device performance, however, it is unknown how this affects charge-carrier participation in battery chemistry. Here, we use TRTS to investigate charge-carrier dynamics in Si<sub>x</sub>Ge<sub>17-x</sub> inverse opal films. Our Drude-Smith fits indicate long-range ( $> 30$  nm) mobilities of  $\sim 3 - 19$   $\text{cm}^2/\text{Vs}$ . The photoconductivity lifetimes indicate significant charge-carrier trapping in inverse-opal films, with activation energies of  $\sim 40 - 140$  meV.

Silicene is a candidate for next-generation optoelectronics and photovoltaics because it may be easier to integrate into existing technologies than graphene, however, silicene quickly oxidizes when exposed to air. Encapsulation techniques prevent oxygen from reaching the nanosheet, but it is unknown how C<sub>12</sub>H<sub>25</sub> (dodecene) encapsulation impacts the photoconductivity of a silicon nanosheet (SiNS). Here, we use TRTS to explore ultrafast photoconductivity in SiNSs for the first time. Dodecene encapsulation results in a short-lived ( $\sim 1$  ps) photoconductivity, which is an improvement over the nonexistent photoconductivity we observe in hydrogen terminated SiNSs. Our Drude-Smith fits indicate strong localization in

the dodecene-encapsulated SiNSs ( $c = 0.99 \pm 0.06$ ) that nearly halts long range ( $> 30$  nm) transport.

Gallium nitride nanowalls permit control over the facets exposed to erosion during photocatalysis, which can enhance the lifetime of the nanowalls. How this morphology impacts the ultrafast photoconductivity is unknown. Here, we use TRTS to study charge-carrier dynamics in GaN nanowalls for the first time. We find that the photoconductivity lifetimes are described by a bi-exponential model, with recombination lifetimes of  $5.45 \pm 0.08$  ps and  $67 \pm 3$  ps. We also find a long-lived recombination mechanism that lasts longer than 125 ps.

# Preface

The research conducted in this thesis was performed from September 2017 to March 2024. Unless explicitly stated, this thesis is a work of my own. Some of the work in this thesis was performed as part of the ATUMS (University of Alberta - Technical University of Munich) International Graduate School for Functional Hybrid Materials, which, herein, will be referred to as the ATUMS collaboration.

Chapter 5 contains time-resolved terahertz spectroscopy of CdS nanowires. This work resulted in one publication, one draft of a subsequent publication, two conference abstracts, one conference poster, and three conference presentations. Kazi Alam wrote the article published in ACS Advanced Materials, and I wrote the time-resolved terahertz spectroscopy section with help from David Purschke. These results can be found in Section 5.3.1. The CdS nanowires studied in the ACS Advanced Materials paper were made by Kazi Alam under the supervision of Karthik Shankar in the Department of Electrical and Computer Engineering at the University of Alberta. I designed the time-resolved terahertz spectroscopy experiments after preliminary measurements conducted by Naaman Amer. Some of the time-resolved terahertz spectroscopy was performed with Anders Palmgren as part of his undergraduate thesis under the supervision of Prof. Frank Hegmann. Some of the SEM images in Section 5.2.1 were provided courtesy of Kazi Alam and Karthik Shankar.

In the later sections of Chapter 5, a deeper study of the charge-carrier dynamics in CdS nanowires was performed. The CdS nanowires were made by Kazi Alam under the supervision of Prof. Karthik Shankar. I designed the time-resolved terahertz spectroscopy experiments and performed measurements with Anders Palmgren as part of his undergraduate thesis under the supervision of Prof. Frank Hegmann. I performed the analysis contained in this thesis. Prof. Alkiviathes Meldrum provided initial time-resolved photoluminescence

measurements that stimulated further research. Howe Simpson, Aran McDowell, and myself performed the time-resolved photoluminescence spectroscopy contained in Chapter 5. Christian Weindl, Navneet Kumar, and I performed the scanning electron microscopy. Christina Strilets helped perform time-resolved terahertz spectroscopy, and Julieta Hernandez measured the film thicknesses.

Chapter 6 contains time-resolved terahertz spectroscopy of atomically thin  $\text{WSe}_2$ . The measurements were performed by myself and Sydney Dufresne as part of her undergraduate thesis supervised by Prof. Frank Hegmann. Leonie Gommell and Naaman Amer assisted with analysis and data acquisition. The  $\text{WSe}_2$  sample was purchased from 2D Semiconductors, and BeiPei Shi provided technical assistance. The interpretation and analysis in this thesis is my own.

Chapter 7 contains time-resolved terahertz spectroscopy of inverse-opal germanium nanostructures. The results of this work were presented in my poster that won first place in the student poster competition. Michael Giebel made the inverse opal nanostructures under the supervision of Prof. Thomas Fässler at the Technical University of Munich as part of the ATUMS collaboration. I trained Michael on the ultrafast laser system. Michael and I designed/executed the subsequent time-resolved terahertz spectroscopy experiments under the supervision of Prof. Frank Hegmann at the University of Alberta. Michael and I analyzed the results with help from Naaman Amer. The analysis and interpretation in this thesis are my own.

In Chapter 8 we explore ultrafast carrier dynamics in silicon nanosheets. The results of this work were presented in my poster that won first place in the student poster competition. Josef Mock and Marc Kloberg made the silicon nanosheets at the University of Alberta under the supervision of Prof. Jonathan Veinot as part of the ATUMS collaboration. I trained Josef on the ultrafast laser system with help from Naaman Amer. Josef and I conceived/executed the time-resolved terahertz spectroscopy measurements at the University of Alberta under the supervision of Prof. Frank Hegmann with help from Naaman Amer, Sydney Dufresne, and Leonie Gommel.

In Chapter 9 we study charge carrier dynamics in GaN nanowalls. The GaN nanowalls were grown by Andreas Ziedler and Theresa Hoffman under the supervision of Martin Stutz-

mann at the Technical University of Munich. Andreas Zeidler, David Purschke and I conceived the experiment, and I trained Andreas on the ultrafast laser system. Preliminary analysis was performed by Andreas, Theresa Hoffman, David Purschke and myself. The analysis and interpretation in this thesis is my own.

Appendix E contains time-resolved terahertz spectroscopy of a  $\text{Hg}_{0.8}\text{Cd}_{0.2}\text{Te}$  film. The terahertz spectroscopy performed on this sample has resulted in three conference abstracts and one submitted paper. Appendix E contains an initial attempt to describe the physical origin of a negative real photoconductivity. Nils Refvik organized and executed the experiment, with help from myself, and Howe Simpson. The data that is fit in Appendix E was provided by Nils Refvik, and the analysis is my own.

## Peer-Reviewed Articles

K. M. Alam, **C. E. Jensen**, P. Kumar, R. W. Hooper, G. M. Bernard, A. Patidar, A. Manuel, N. Amer, A. Palmgren, D. N. Purschke, N. Chaulagain, J. Garcia, P. S. Kirwin, L. C. T. Schoute, K. Cui, S. Gusarov, A. E. Kobryn, V. K. Michaelis, F. A. Hegmann and K. Shankar, “Photocatalytic mechanism control and study of carrier dynamics in  $\text{CdS}@\text{C}_3\text{N}_5$  core-shell nanowires,” *ACS Applied Materials & Interfaces*, **2021**.

The CdS nanowires studied here were made by Kazi Alam under the supervision of Prof. Karthik Shankar in the Department of Electrical and Computer Engineering at the University of Alberta. I designed the time-resolved terahertz spectroscopy experiments after preliminary measurements conducted by Naaman Amer. The measurements were performed with Anders Palmgren as part of his undergraduate thesis under the supervision of Prof. Frank Hegmann. I wrote the time-resolved terahertz spectroscopy section of this paper with help from David Purschke.

D. N. Purschke, M. R. P. Pielmeier, E. Üzer, C. Ott, **C. E. Jensen**, A. Degg, A. Vogel, N. Amer, T. Nilges, and F. A. Hegmann, “Ultrafast Photoconductivity and Terahertz Vibrational Dynamics in Double-Helix SnIP Nanowires”, *Advanced Materials*, **2021**.

I contributed to the interpretation of results and editing drafts in a paper on SnIP nanowires.

## Peer-Reviewed Abstracts

**C. E. Jensen**, K. M. Alam, A. Palmgren, D. N. Purschke, N. Amer, K. Shankar, and F. A. Hegmann, “Ultrafast Carrier Dynamics of CdS Nanowires Wrapped in  $C_3N_5$  nanosheets”, 45th International Conference on Infrared, Millimeter, and Terahertz Waves (IRMMW-THz), **2020**.

In 2020 I presented my work on CdS nanowires at the International Conference on Infrared, Millimeter, and Terahertz Waves (IRMMW-THz). The CdS nanowires in this study were made by Kazi Alam under the supervision of Prof. Karthik Shankar in the Department of Electrical and Computer Engineering at the University of Alberta. I designed the time-resolved terahertz spectroscopy experiments after preliminary measurements conducted by Naaman Amer. The measurements were performed with Anders Palmgren as part of his undergraduate thesis under the supervision of Prof. Frank Hegmann. I wrote the time-resolved terahertz spectroscopy section of this paper with help from David Purschke.

K. M. Alam, P. Kumar, D. Laishram, **C. E. Jensen**, A. Degg, N. Chaulagain, F. A. Hegmann, T. Nilges, R. Sharma, and K. Shankar, “ $C_3N_4$  and  $C_3N_5$  Nanosheets As Passivation Layers and Carrier Extractors for Inorganic Semiconductor Nanowires and Quantum Dots”, ECS Meeting Abstracts, **2022**.

I contributed to this abstract by editing the draft. I also conducted the the time-resolved terahertz spectroscopy study of CdS nanowires with Anders Palmren as part of his undergraduate thesis under the supervision of Prof. Frank Hegmann.

N. B. Refvik, D. N. Purschke, W. Pan, **C. E. Jensen**, H. R. J. Simpson, W. Lei, R. Gu, J. Antoszewski, G. A. Umana-Membreno, L. Faraone, and F. A. Hegmann, “Ultra-High Mobility and Temperature-Dependent Carrier Dynamics in Narrow-Gap  $Hg_{1-x}Cd_xTe$  Films”, 47th International Conference on Infrared, Millimeter and Terahertz Waves (IRMMW-THz), **2022**.

In this conference abstract, I participated in planning, execution, and interpretation of the time-resolved terahertz spectroscopy.

N. B. Refvik, D. N. Purschke, W. Pan, **C. E. Jensen**, H. R. J. Simpson, W. Lei, R. Gu, J. Antoszewski, G. A. Umana-Membreno, L. Faraone, and F. A. Hegmann, “Non-Contact Characterization of Carrier Mobility and

Ultrafast Dynamics in Long-Wave Infrared HgCdTe Films using Time-Resolved Terahertz Spectroscopy”, 41st annual US workshop on the physics and chemistry of II-VI materials, **2022**.

In this conference abstract, I participated in planning, execution, and interpretation of the time-resolved terahertz spectroscopy.

N. B. Refvik, L. K. Reb, C. Lindenmeir, **C. E. Jensen**, H. R. J. Simpson, D. Vrushabendrakumar, K. Shankar, P. Muller-Buschbaum, and F. A. Hegmann, “Characterization of morphology-dependent transport in lead-halide perovskite printed films using time-resolved terahertz spectroscopy”, 48th International Conference on Infrared, Millimeter and Terahertz Waves (IRMMW-THz), **2023**.

In this conference abstract, I planned and conducted the photoluminescence measurements that were presented at the conference with help from Lennart Reb.

## Conference Presentations

**C. E. Jensen**, F. A. Hegmann, “Time-resolved Terahertz Spectroscopy of nanomaterials”, Canadian Photonics Online Meetup (CanPOM), **2020**.

I gave a talk on how time-resolved terahertz spectroscopy is used to explore the ultrafast transport properties of nanomaterials.

**C. E. Jensen**, K. M. Alam, A. Palmgren, K. Shankar, F. A. Hegmann, “Time-resolved Terahertz Spectroscopy of nanomaterials”, ATUMS Annual General Meeting (online), **2020**.

I gave talk about how time-resolved THz spectroscopy is used to explore the ultrafast transport properties of nanomaterials in our laboratory, with preliminary results from measurements on CdS nanowires. I planned and performed the acquisition, analysis and interpretation of these results. Anders Palmgren aided in the acquisition and interpretation of these results during his undergraduate thesis under the supervision of Prof. Frank Hegmann. Kazi Alam made the samples under the supervision of Prof. Karthik Shankar.

**C. E. Jensen**, K. M. Alam, A. Palmgren, K. Shankar, F. A. Hegmann, “Time-resolved Terahertz Spectroscopy of Nanomaterials”, ATUMS Annual General Meeting, **2023**.

I gave talk about how time-resolved THz spectroscopy is used to explore the ultrafast trans-

port properties of nanomaterials, using CdS nanowires as an example. I planned and performed the acquisition, analysis and interpretation of these results. Anders Palmgren aided in the acquisition and interpretation of these results during his undergraduate thesis under the supervision of Prof. Frank Hegmann. Kazi Alam made the samples under the supervision of Prof. Karthik Shankar.

## Conference Posters

**C. E. Jensen**, M. A. Giebel, J. Mock, M. Narreto, A. Lyuleeva, M. Kloberg, S. Y. Dufresne, N. Amer, T. Helbich, J. G. C. Veinot, B. Reiger, P. Lugli, T. F. Fässler, and F. A. Hegmann. “THz Spectroscopy of Functionalized Nanomaterials”, ATUMS General Meeting, **2018**, 1<sup>st</sup> place poster prize.

In 2018 my work on silicon nanosheets and inverse opal germanium nanostructures was presented in a poster at the ATUMS annual general meeting where I won first prize for student posters. The terahertz spectroscopy was an extension of the photoluminescence measurements made by Mary Narreto during her PhD. Alina Lyuleeva, Marc Kloberg, and Tobias Helbich synthesized the silicon nanosheets under the supervision of Prof. Jonathan Veinot, Prof. Bernhard Reiger, Paolo Lugli. Josef Mock and Marc Kloberg organized the synthesis of the silicon nanosheets at the University of Alberta, and participated in time-resolved terahertz spectroscopy. Michael Giebel synthesized the inverse opal germanium nanostructures at the Technical University of Munich under the supervision of Prof. Thomas Fässler. Michael Giebel participated in the planning and execution of the time-resolved terahertz spectroscopy.

**C. E. Jensen**, K. M. Alam, A. Palmgren, D. N. Purschke, N. Amer, K. Shankar, and F. A. Hegmann, “Ultrafast Carrier Dynamics of CdS Nanowires Wrapped in  $C_3N_5$  nanosheets”, 45th International Conference on Infrared, Millimeter, and Terahertz Waves (IRMMW-THz), **2020**.

In 2020 I presented a poster of my work on CdS nanowires at the International Conference on Infrared, Millimeter, and Terahertz Waves (IRMMW-THz). I analyzed the data and wrote the abstract under the supervision of Prof. Frank Hegmann with help from David Purschke. Kazi Alam made the CdS nanowires in this study under the supervision of Prof. Karthik Shankar. The data presented at this conference included results from Anders Palmgren’s

undergraduate thesis project, but the interpretation was my own.

## Submitted Articles

N. B. Refvik, **C. E. Jensen**, D. N. Purschke, W. Pan, H. R. J. Simpson, W. Lei, R. Gu, J. Antoszewski, G. A. Umana-Membreno, L. Faraone, and F. A. Hegmann, “Non-contact characterization of carrier mobility in long-wave infrared HgCdTe films with terahertz time-domain spectroscopy”, *IEEE Transactions on Terahertz Science and Technology*, **Jan 2024**.

I contributed to the interpretation of results and editing drafts in a paper on terahertz time-domain spectroscopy of  $\text{Hg}_{1-x}\text{Cd}_x\text{Te}$  films.

## Research Articles In Preparation

**C. E. Jensen**, K. M. Alam, A. Palmgren, D. N. Purschke, H. R. J. Simpson, N. B. Refvik, C. L. Weindl, N. Kumar, A. J. N. McDowell, C. Strilets, J. Hernandez, N. Amer, A. Meldrum, K. Shankar, and F. A. Hegmann, “Time-resolved Terahertz Spectroscopy of CdS nanowires wrapped in  $\text{C}_3\text{N}_5$  nanosheets”, in preparation.

The CdS nanowires studied here were made by Kazi M. Alam and Navneet Kumar under the supervision of Prof. Karthik Shankar in the Department of Electrical and Computer Engineering at the University of Alberta. I designed the time-resolved terahertz spectroscopy experiments and performed measurements with Anders Palmgren as part of his undergraduate thesis. Prof. Alkiviathes Meldrum performed initial photoluminescence spectroscopy that prompted further research. I performed the analysis contained in this thesis. Howe Simpson, Aran McDowell and I measured the time-resolved photoluminescence presented in this thesis. Christian Weindl, Navneet Kumar, Kazi Alam, and I performed the scanning electron microscopy. Christina Strilets helped perform time-resolved terahertz spectroscopy, and Julieta Hernandez measured the film thicknesses.

# Acknowledgements

I am extremely grateful to my supervisor Dr. Frank A. Hegmann. I learned much from Frank in the classroom, more in the lab, and even more at Karaoke night. Thank you for teaching me how to think like an experimental physicist and allowing me the freedom to make mistakes and learn from them.

I want to thank the Hegmann group, past and present. Dr. Naaman Amer, I am glad we finally resolved the  $\sqrt{2}$  debate once and for all. Naaman is an excellent researcher, with an intuition paralleled only by his love for his family and soccer. Thanks to the undergrads who worked in our lab. Anders, Julieta, Christina, Chenxi, Sanjina, and Cole, it has been a pleasure introducing you to THz research. I hope you enjoyed your time in the lab as much as I did. David Purschke, Cameron Hough, Vedran Jelic, Mary Narreto, Yang Luo, Aaran McDowell and Alex Marin, it is insane how quickly the entire group changed. I already miss working with you in the lab. To the new members of the Hegmann group, Howe Simpson, Nils Refvik, Max Stratmann Meouchi, Niloufar Sadeghi, Sam Ruttiman, and Makoto Schreiber, I look forward to passing on the things I learned throughout my Ph.D. as we dive into future projects.

Thank you to all the amazing friends I've made since moving to Edmonton. Jimmy, Kameron, Bernal, and Haille, thanks for finding ways to pry me away from my desk. To my friends who moved away, Ajay Manuel, Ketty Na, Alex Hamilton, Sydney Dufresne, Alyona Sharunova, Sebastian Sanchez Herrera, Kai-Lynn Gan, Mason Protter, and Will Giang, I deeply miss you and wish you all the best. To all my friends still in Edmonton, Catherine Bina, Sourav Sarkar, Leon Olifer, Rachel To, and Athena Tillie, thanks for being there for me. I couldn't have done this without you. Danika and Gabe, Anna, Kenwick, Andrew and Annie, Pen, and all of the friends I made at ECCC, I will never forget your kindness during

the hardest times of my Ph.D. Some day, when we're able, we'll finally break bread and celebrate.

Thanks to my friends in the ATUMS collaboration. Josef Mock, Michael Giebel, Nuri Hohn, Andreas Ziedler, and Theresa Hoffman, you were there for me when times were tough. Thank you for working so hard in your short time here; it gave me the time I needed to be with my family. Max Spechbacher, Alex Bourgund, Marc Kloberg, and Alina Lyuleeva, I am so glad to call you my friends. Thanks to Leah Veinot and Sergey Vagin for organizing everything. I had a great time at the collaboration meetings.

Thanks to the fantastic Technical staff Greg Popowich, James Chaulk, Beipei Shi, and Manvir Gil. Thanks to Lorne Roth and Taylor Rogers at Undergraduate Labs for the amazing help with virtually anything lab related. Thank you to the administrative staff Sarah McKinnon, Holly Johnson, and Kailey Robertson.

I want to extend a special thanks to Alec Wilkes. The lunches we spent looking at universities on your micro laptop changed the path of my life in ways I could have never imagined. This one's for you buddy.

To my friends in Yellowknife, Helen, Jon, Bernie, Kyle, Gerald, Arvin, and Alex, thanks for the many hours of distraction and honest conversation. Rest in peace Kyle, you were a good friend and we miss you dearly. I hope to see you all again soon.

Finally, I'd like to thank my parents, George and Loretta Jensen. Writing this thesis I could practically hear my father's sayings echoing through my mind. "There's no such thing as can't, only won't" helped me recognize when I was choosing to ignore a problem. "Nothing worth doing in life ever comes easy" gave me the perspective I needed for the long-term gain that arises from a persistent effort. "If wishes were horses, beggars would ride" helped me see that everyone is already doing the easy things. To stand out, you must be brave enough to face what others are actively ignoring. My mother taught me how to be compassionate and patient with those around me, which has enabled me to be an effective mentor for the undergraduate and graduate students under my supervision. Without your example this thesis would not exist. Thanks for being such great parents.

# Table of Contents

<b>Abstract</b>	<b>ii</b>
<b>Preface</b>	<b>v</b>
<b>Acknowledgements</b>	<b>xii</b>
<b>1 Introduction</b>	<b>1</b>
<b>2 Ultrafast Carrier Dynamics in Semiconductors</b>	<b>15</b>
2.1 Introduction . . . . .	15
2.1.1 Band Structure . . . . .	15
2.1.2 Semiclassical Absorption . . . . .	16
2.1.3 Carrier Dynamics . . . . .	20
2.1.4 Photoluminescence . . . . .	21
2.1.5 Models of Charge-Carrier Recombination . . . . .	23
Monomolecular, Bimolecular, and Auger Recombination . . . . .	24
Multilevel Systems . . . . .	24
Surface Recombination . . . . .	25
2.2 Transient Conductivity . . . . .	26
2.2.1 Conductivity Spectrum . . . . .	26
2.2.2 Conductivity Models . . . . .	28
Drude Model . . . . .	28
Lorentz Oscillator Model . . . . .	30
Drude-Smith Model . . . . .	31

Modified Drude-Smith Model . . . . .	33
Plasmon Model . . . . .	35
Bruggeman Effective Medium Theory . . . . .	37
Disordered Metals . . . . .	38
2.2.3 Diffusion . . . . .	38
2.3 Summary . . . . .	41
<b>3 Terahertz Spectroscopy</b>	<b>42</b>
3.1 Terahertz Pulses . . . . .	42
3.1.1 Generation via Optical Rectification . . . . .	42
3.1.2 Detection via Electro-Optic Sampling . . . . .	48
3.2 Terahertz Time-Domain Spectroscopy . . . . .	53
3.3 Time-Resolved Terahertz Spectroscopy . . . . .	55
Photoconductivity Dynamics . . . . .	61
Photoconductivity Spectroscopy . . . . .	62
Bulk germanium . . . . .	62
3.4 Summary . . . . .	64
<b>4 Experimental Details</b>	<b>65</b>
4.1 Introduction . . . . .	65
4.2 Time-Resolved Terahertz Spectroscopy . . . . .	65
4.3 Time-Resolved Photoluminescence . . . . .	70
4.3.1 Time-Integrated Photoluminescence . . . . .	70
4.3.2 Time-Resolved Photoluminescence . . . . .	72
<b>5 CdS Nanowires wrapped in C<sub>3</sub>N<sub>5</sub> Nanosheets</b>	<b>76</b>
5.1 Introduction . . . . .	76
5.2 Experimental Details . . . . .	77
5.2.1 Wrapping CdS Nanowires in C <sub>3</sub> N <sub>5</sub> nanosheets . . . . .	77
5.2.2 Sample Thickness . . . . .	79
5.2.3 Terahertz Time-Domain Spectroscopy . . . . .	80

5.2.4	Time-Resolved Terahertz Spectroscopy . . . . .	80
5.2.5	Time-Resolved Photoluminescence . . . . .	83
5.3	Results . . . . .	84
5.3.1	Photoconductivity for Photocatalytic Applications . . . . .	84
5.3.2	Terahertz Time-Domain Spectroscopy . . . . .	89
	Background Conductivity of Bulk CdS Crystal . . . . .	89
	Background Conductivity of CdS Nanowires . . . . .	92
5.3.3	Time-Resolved Terahertz Spectroscopy . . . . .	93
	Ultrafast Photoconductivity Dynamics of CdS Crystal . . . . .	93
	Ultrafast Photoconductivity Dynamics of CdS Nanowires . . . . .	96
	Ultrafast Photoconductivity Spectra of CdS Crystal . . . . .	98
	Ultrafast Photoconductivity Spectra of CdS Nanowires . . . . .	103
5.3.4	Time-Resolved Photoluminescence . . . . .	104
5.3.5	Summary of Results . . . . .	106
5.4	Discussion . . . . .	107
5.4.1	Ultrafast Photoconductivity Spectra . . . . .	107
	Terahertz Photoconductivity in CdS Nanomaterials . . . . .	107
	Modelling Photoconductivity in CdS Nanowires . . . . .	109
	Localized Carrier Dynamics in CdS Nanowires . . . . .	112
5.4.2	Modelling Charge-Carrier Lifetimes . . . . .	119
	Charge-Carrier Lifetimes in CdS and CdS Nanomaterials . . . . .	119
	Example Fit . . . . .	124
	Fitting Lifetimes . . . . .	126
5.5	Summary . . . . .	133
<b>6</b>	<b>Atomically Thin WSe<sub>2</sub></b> . . . . .	<b>136</b>
6.1	Introduction . . . . .	136
6.2	Sample Properties . . . . .	139
6.2.1	Monolayer Thickness . . . . .	139
6.2.2	Optical Absorption . . . . .	139

6.3	Terahertz Time-Domain Spectroscopy . . . . .	143
6.4	Time-Resolved Terahertz Spectroscopy . . . . .	147
6.4.1	Experimental Details . . . . .	147
6.4.2	Photoconductivity Map . . . . .	147
6.4.3	Charge-Carrier Lifetimes . . . . .	151
	Room Temperature . . . . .	151
	Low Temperature . . . . .	152
6.4.4	Terahertz Electrodynamics . . . . .	156
	Room Temperature . . . . .	156
	Low Temperature . . . . .	161
6.5	Summary . . . . .	163
<b>7</b>	<b>Inverse-Opal <math>\text{Si}_x\text{Ge}_{17-x}</math> Nanostructures</b>	<b>166</b>
7.1	Introduction . . . . .	166
7.2	Terahertz Spectroscopy Considerations . . . . .	168
7.2.1	Spectroscopy . . . . .	168
7.2.2	Lifetimes . . . . .	170
7.2.3	Effective Mass . . . . .	171
7.3	Sample Preparation . . . . .	171
7.4	Results . . . . .	172
7.4.1	$\text{Si}_{17}$ (0% Ge) . . . . .	172
	Lifetimes . . . . .	172
	Spectroscopy . . . . .	173
7.4.2	$\text{Si}_{12}\text{Ge}_5$ (30% Ge) . . . . .	174
	Lifetimes . . . . .	174
	Spectroscopy . . . . .	175
7.4.3	$\text{Si}_5\text{Ge}_{12}$ (70% Ge) . . . . .	175
	Lifetimes . . . . .	175
	Spectroscopy . . . . .	176
7.5	Discussion . . . . .	177

7.5.1	Ultrafast Transient Photoconductivity . . . . .	177
7.5.2	THz Electrodynamics . . . . .	180
7.6	Summary . . . . .	182
<b>8</b>	<b>Functionalized Silicon Nanosheets</b>	<b>183</b>
8.1	Introduction . . . . .	183
8.2	Sample Preparation . . . . .	184
8.3	Results and Discussion . . . . .	185
8.4	Summary . . . . .	188
<b>9</b>	<b>GaN Nanowalls</b>	<b>189</b>
9.1	Introduction . . . . .	189
9.2	Sample Properties . . . . .	190
9.3	Results and Discussion . . . . .	190
9.4	Summary . . . . .	196
<b>10</b>	<b>Conclusions</b>	<b>197</b>
	<b>References</b>	<b>202</b>
<b>A</b>	<b>Numerically Solving the Diffusion Equation</b>	<b>245</b>
A.1	Introduction . . . . .	245
A.2	Discretization . . . . .	246
A.2.1	Boundary Conditions . . . . .	247
A.3	Neumann Boundary Condition . . . . .	247
A.4	Surface Recombination Boundary Condition . . . . .	250
<b>B</b>	<b>Lock-In Detection and the 2-Chop Technique</b>	<b>252</b>
B.1	Introduction . . . . .	252
B.2	Lock-In amplifier theory . . . . .	253
B.2.1	Simple Example . . . . .	253
B.2.2	General Input Signal . . . . .	255
B.2.3	Measuring $V_1 + V_2$ . . . . .	257

B.2.4	Measuring $V_1 - V_2$ . . . . .	259
B.2.5	Using Values from Two Different Lock-In Amplifiers . . . . .	261
<b>C</b>	<b>Generalized Drude Model</b>	<b>263</b>
<b>D</b>	<b>A New Approach to Time-Resolved Spectroscopy</b>	<b>264</b>
D.1	Introduction . . . . .	264
D.2	Time-Frequency Analysis Fundamentals . . . . .	265
D.3	Optical Constants . . . . .	267
D.4	Simulating $\mathcal{E}_{pump}$ with Time-Frequency Analysis . . . . .	267
D.5	Discussion . . . . .	272
D.6	Summary . . . . .	272
<b>E</b>	<b>Negative <math>\sigma_1</math> Impulse Response</b>	<b>274</b>
E.1	Introduction . . . . .	274
E.2	Application to $\text{Hg}_{0.8}\text{Cd}_{0.2}\text{Te}$ Thin Film . . . . .	276

# List of Tables

3.1	THz generation parameters. . . . .	45
3.2	Electro-optic sampling variables. . . . .	53
3.3	Drude fit parameters from THz-TDS of intrinsic silicon crystal. . . . .	56
3.4	Table of transmission symbols. . . . .	61
5.1	Table of CdS nanowire film thicknesses. . . . .	80
5.2	Table of biexponential fit parameters from Alam, Jensen et al.. . . . .	87
5.3	Table of Drude-Smith fit parameters from Alam, Jensen et al.. . . . .	89
5.4	Parameters used in modelling the transmission function. . . . .	91
5.5	Table of biexponential fit parameters for CdS nanowire lifetimes. . . . .	100
6.1	Exciton Binding energies in common semiconductors. . . . .	138
6.2	Best-fit electron-phonon coupling parameters from the fits in Fig. 6.4. . . . .	143
7.1	Table of power law best-fit values for the Si <sub>17</sub> inverse opal film. . . . .	172
7.2	Table of Drude-Smith best-fit values for the Si <sub>17</sub> inverse opal film. . . . .	173
7.3	Table of power law best-fit values for the Si <sub>12</sub> Ge <sub>5</sub> inverse opal film. . . . .	174
7.4	Table of Drude-Smith best-fit values for Si <sub>12</sub> Ge <sub>5</sub> inverse opal film. . . . .	175
7.5	Table of power law best-fit values for the Si <sub>5</sub> Ge <sub>12</sub> inverse opal film. . . . .	176
7.6	Table of Drude-Smith best-fit values for Si <sub>5</sub> Ge <sub>12</sub> inverse opal nanostructutes. . . . .	177
7.7	Table of power-law best-fit values for inverse opal nanostructutes. . . . .	180
8.1	Table of exponential best-fit values for SiNS-dodecene fluence dependence. . . . .	187
8.2	Table of Drude-Smith best-fit values for SiNS. . . . .	188

9.1	Table of biexponential best-fit values for GaN Nanowall lifetime. . . . .	191
9.2	Best-fit photoconductivity parameters for the GaN nanowalls. . . . .	194

# List of Figures

1.1	THz bandwidth. . . . .	2
1.2	Charge-carrier localization modifies the conductivity. . . . .	6
1.3	THz pulse and bandwidth. . . . .	7
1.4	Pump-probe terahertz spectroscopy configuration. . . . .	9
1.5	CdS nanowires on a substrate. . . . .	10
1.6	WSe <sub>2</sub> monolayer on a substrate. . . . .	11
1.7	Inverse opal Ge on a substrate. . . . .	12
1.8	Silicon nanosheets on a substrate. . . . .	13
1.9	Gallium nitride nanowalls on a substrate. . . . .	14
2.1	Relaxation timeline. . . . .	22
2.2	Drude model for GaAs. . . . .	30
2.3	Simulated Lorentz oscillator model for GaAs nanowires. . . . .	32
2.4	Drude-Smith model on gold thin films. . . . .	33
2.5	Diffusion simulation for GaAs. . . . .	41
3.1	THz generation simulation. . . . .	46
3.2	Optical and THz indexes in ZnTe. . . . .	48
3.3	ZnTe crystal properties. . . . .	49
3.4	Schematic of electro-optic sampling. . . . .	52
3.5	Time-domain spectroscopy geometry. . . . .	54
3.6	Example THz-TDS on intrinsic silicon. . . . .	56
3.7	Schematic of TRTS experiment. . . . .	57
3.8	Schematic of reference transmission in TRTS experiment. . . . .	58

3.9	Schematic of pump-induced transmission in TRTS experiment. . . . .	60
3.10	Example of TRTS on Ge crystal. . . . .	63
4.1	Overview of Ultrafast Spectroscopy Laboratory. . . . .	66
4.2	TRTS experiment chamber. . . . .	68
4.3	Schematic of photoluminescence system. . . . .	71
4.4	Time-correlated Single Photon Counting. . . . .	75
5.1	FESEM images of CdS nanowires. . . . .	79
5.2	Imaging nanowire film morphology with a Witek confocal microscope. . . . .	81
5.3	Experimental details for TRTS of CdS nanowires. . . . .	82
5.4	Preliminary photoconductivity lifetimes of CdS nanowires. . . . .	86
5.5	Preliminary photoconductivity spectra of CdS nanowires. . . . .	88
5.6	THz-TDS of Wurtzite CdS Crystal. . . . .	90
5.7	THz-TDS of CdS nanowires. . . . .	94
5.8	THz-TDS of wrapped CdS nanowires. . . . .	95
5.9	Photoconductivity lifetimes of bulk CdS crystal. . . . .	97
5.10	Photoconductivity lifetimes of CdS-NW films. . . . .	98
5.11	Maximum differential transmission of the CdS-NW films. . . . .	99
5.12	TRTS of bulk CdS crystal. . . . .	101
5.13	Results of fitting bulk CdS photoconductivity to a Drude model. . . . .	102
5.14	Photoconductivity spectra of CdS-NW films. . . . .	104
5.15	Time-Resolved Photoluminescence of CdS nanowires. . . . .	105
5.16	Time-Resolved Terahertz Spectroscopy of CdS nanowires. . . . .	110
5.17	Fitting CdS-NW photoconductivity to the Bruggeman model. . . . .	112
5.18	Drude-Smith fit parameters for the CdS-NWs. . . . .	114
5.19	Drude-Smith fits of the ES-WNWs and the IS-WNWs. . . . .	115
5.20	Best-fit parameters of the Drude-Smith fits on the wrapped CdS nanowires. . . . .	116
5.21	Ambipolar diffusivity of CdS nanowires. . . . .	118
5.22	Comparing photoconductivity and photoluminescence lifetimes. . . . .	120
5.23	Schematic of carrier relaxation in CdS nanowires. . . . .	123

5.24	Spatial evolution for charge carriers in CdS NWs. . . . .	125
5.25	Simultaneous fit of the photoconductivity and photoluminescence lifetimes of CdS NWs excited at 400 $\mu\text{J}/\text{cm}^2$ . . . . .	127
5.26	Fluence dependent fits of the bare CdS-NWs lifetimes. . . . .	128
5.27	Fluence dependent fits of the ES-WNW lifetimes. . . . .	128
5.28	Fluence dependent fits of the IS-WNW lifetimes. . . . .	129
5.29	Fluence dependent surface recombination velocity, bimolecular recombination coefficient, separation lifetime, and cooling timescales in all three CdS nanowire samples. . . . .	130
5.30	Schematic of charge-carrier lifetime in CdS nanowires. . . . .	133
6.1	Schematic crystal structure of WSe <sub>2</sub> monolayer. . . . .	137
6.2	AFM of WSe <sub>2</sub> monolayer. . . . .	140
6.3	UV-Vis absorption in WSe <sub>2</sub> monolayer. . . . .	142
6.4	Simultaneous fit of the electron-phonon coupling model in monolayer WSe <sub>2</sub> . . . . .	144
6.5	$E'$ phonon mode in monolayer WSe <sub>2</sub> . . . . .	145
6.6	$E''$ phonon mode in monolayer WSe <sub>2</sub> . . . . .	146
6.7	THz-TDS of monolayer WSe <sub>2</sub> . . . . .	148
6.8	Schematic of WSe <sub>2</sub> raster scan. . . . .	149
6.9	Photoconductivity map of monolayer WSe <sub>2</sub> . . . . .	150
6.10	Example WSe <sub>2</sub> charge carrier lifetime model. . . . .	153
6.11	Fluence dependent lifetimes in WSe <sub>2</sub> at 295 K. . . . .	154
6.12	WSe <sub>2</sub> 295 K lifetime best fit parameters. . . . .	155
6.13	Low temperature lifetime fits of WSe <sub>2</sub> monolayer. . . . .	157
6.14	Low temperature lifetime fit parameters of WSe <sub>2</sub> monolayer. . . . .	158
6.15	WSe <sub>2</sub> 295 K Drude-Smith fits. . . . .	159
6.16	WSe <sub>2</sub> 295 K Drude-Smith fit parameters. . . . .	160
6.17	WSe <sub>2</sub> 295 K Drude-Smith DC sheet conductivity and lifetimes for all fluences. . . . .	161
6.18	Low temperature TRTS of WSe <sub>2</sub> monolayer. . . . .	162
6.19	Low temperature Drude-Smith best-fit results for WSe <sub>2</sub> monolayer. . . . .	163

6.20	Temperature dependence of $-\Delta\mathcal{E}/\mathcal{E}_{ref}$ and $\sigma_{DC}$ . . . . .	164
7.1	$K_4Ge_9$ Zintl phase unit cell and inverse opal structure. . . . .	168
7.2	Photoconductivity lifetimes for the $Si_{17}$ inverse opal film. . . . .	173
7.3	Photoconductivity spectra for the $Si_{17}$ inverse opal film. . . . .	174
7.4	Photoconductivity lifetimes for the $Si_{12}Ge_5$ inverse opal film. . . . .	175
7.5	Photoconductivity spectra for the $Si_{12}Ge_5$ inverse opal film. . . . .	176
7.6	Photoconductivity lifetimes for the $Si_5Ge_{12}$ inverse opal film. . . . .	177
7.7	Photoconductivity spectra for the $Si_5Ge_{12}$ inverse opal film. . . . .	178
7.8	Lifetime analysis inverse opal thin films. . . . .	180
8.1	Lifetimes of $SiNS-C_{12}H_{25}$ and $SiNS-H$ at 295 K and 100 K. . . . .	185
8.2	Lifetimes of $SiNS-C_{12}H_{25}$ at 214, 274, and 321 $\mu J/cm^2$ . . . . .	186
8.3	$SiNS$ lifetime and photoconductivity. . . . .	187
9.1	Dimensions of GaN nanowalls. . . . .	190
9.2	Time-resolved terahertz spectroscopy of GaN nanowalls. . . . .	192
9.3	Photoconductivity models for GaN nanowalls. . . . .	193
A.1	Discretization schematic. . . . .	247
B.1	The reference and Dirac Comb input given by Eq.(B.17) are shown. . . . .	256
B.2	Dirac comb input in $V_1 - V_2$ mode. . . . .	259
D.1	Bank of reeds analogy. . . . .	266
D.2	$\mathcal{E}_{ref}-n(\tau)$ relationship. . . . .	269
D.3	Photoconductivity surface in time-frequency space. . . . .	269
D.4	Transmission function. . . . .	270
D.5	Time-frequency $\mathcal{E}_{ref}$ . . . . .	270
D.6	Time-frequency $\mathcal{E}_{pump}$ . . . . .	271
D.7	$\mathcal{E}_{pump}$ simulated with time-frequency analysis. . . . .	271
D.8	$\Delta\mathcal{E}$ contour plot. . . . .	273
E.1	Impulse-response function with negative real conductivity. . . . .	275

E.2	Fitting the $\text{Hg}_{0.8}\text{Cd}_{0.2}\text{Te}$ TRTS with the custom impulse response. . . . .	277
E.3	Temperature dependent fit parameters of $\text{Hg}_{0.8}\text{Cd}_{0.2}\text{Te}$ thin film. . . . .	278

# List of Symbols and Acronyms

## Physical Constants

Symbol	Value	Description
$\epsilon_0$	$8.854 \times 10^{-12} \text{ Fm}^{-1}$	Permittivity of free space
$\hbar$	$1.054 \times 10^{-34} \text{ Js}$	Reduced Planck constant
$c$	$2.9989 \times 10^8 \text{ m/s}$	Speed of light in vacuum
$k_B$	$1.380 \times 10^{-23} \text{ J/K}$	Boltzmann constant
$Z_0$	$3.767 \times 10^2 \Omega$	Impedance of free space

## Materials

Acronym	Defintion
GaAs	Gallium Arsenide
WSe <sub>2</sub>	Tungsten diselenide
MHP	C <sub>3</sub> N <sub>5</sub> nanosheets (Polymerized melem hydrazine)
Ti:Al <sub>2</sub> O <sub>3</sub>	Titanium doped sapphire
C <sub>12</sub> H <sub>25</sub>	Dodecene
CdS	Cadmium sulfide
GaN	Gallium Nitride
Ge	Germanium
Si	Silicon
PMMA	Poly(methyl methacrylate)
SiNS	Silicon nanosheet
NW	Nanowire
ES-WNW	Ex-situ wrapped nanowire
IS-WNW	In-situ wrapped nanowire

## Physical Properties

Symbol	Defintion	Units
Electromagnetic waves		
$\lambda$	Wavelength	m
$k$	Wavevector	$\text{m}^{-1}$
$\omega$	Angular Frequency	$2\pi$ Hz
$\mathcal{E}$	Electric field	V/m
$I$	Intensity	$\text{W}/\text{m}^2$
$V$	Voltage	V (J/C)
$\phi(\omega)$	Complex phase	Unitless
$\tilde{T}$	Complex transmission function	Unitless
Electrons/Holes		
$P$	Polarization	Cm
$T$	Temperature	K
$W$	Transition rate	Hz
$m^*$	Effective mass	kg
$n$	Carrier density	$\text{cm}^{-3}$
$R$	Recombination rate	$\text{cm}^{-3}\text{s}^{-1}$
$G$	Generation rate	$\text{cm}^{-3}\text{s}^{-1}$
$S_0$	Surface recombination velocity	cm/s
$E$	Energy	eV
$\psi$	Wavefunction	Unitless
$f(E)$	Occupancy distribution function	Unitless
$g(E)$	Joint density of states	$\text{eV}^{-1}\text{cm}^{-3}$
$J_{drift}$	Drift current density	$\text{Cs}^{-1}\text{m}^{-2}$
$J_{diff}$	Diffusion current density	$\text{Cs}^{-1}\text{m}^{-2}$
$L_{ave}$	Distribution thickness	m
$D^*$	Ambipolar diffusion constant	$\text{cm}^2/\text{s}$
$\ell_D$	Diffusion length	m
$\mu$	Mobility	$\text{cm}^2\text{V}^{-1}\text{s}^{-1}$
$\omega_p$	Plasma frequency	Hz
$\tau$	Time constant	s
Crystal		
$E_g$	Band gap energy	eV
$\alpha$	Absorption coefficient	$\text{cm}^{-1}$
$r_{41}$	Electro-optic coefficient	$\text{pmV}^{-1}$
$\tilde{n}$	Index of refraction ( $n + i\kappa$ )	Unitless
$\tilde{\sigma}$	Conductivity ( $\sigma_1 + i\sigma_2$ )	$\Omega^{-1}\text{cm}^{-1}$
$\tilde{\epsilon}$	Dielectric function ( $\epsilon_1 + i\epsilon_2$ )	Unitless
$a$	Lattice constant	Å

## Common Units

Symbol	
$\mu\text{J}/\text{cm}^2$	Fluence
$\text{cm}^2/\text{Vs}$	Mobility
nm	Nanometer
ps	Picosecond ( $10^{-12}$ s)
THz	Terahertz ( $10^{12}$ Hz)
W	Watt

## Acronyms

Acronym	Defintion
AFM	Atomic force microscope
EOS	Electro-optic sampling
FESEM	Field-emission scanning electron microscope
HR-TEM	High-resolution transmission electron microscope
UV-Vis	Ultraviolet-visible
PL	Photoluminescence
TRPL	Time-resolved photoluminescence
THz-TDS	Terahertz time-domain spectroscopy
TRTS	Time-resolved terahertz spectroscopy
FET	Field-effect transistor

## Time-resolved terahertz spectroscopy symbols

Symbol	Defintion
$\tilde{n}_s$	Substrate refractive index
$\tilde{n}_f$	Photoexcited film refractive index
$\Phi_{s,0}$	Substrate induced phase shift
$\Phi_{f,s}$	Film-Substrate induced phase shift
$\Phi_{0,f}$	Film induced phase shift
FP $_{f,s}$	Fabry-Perot reflection term
$\tilde{t}_{0,f}$	Fresnel transmission from vacuum into film
$\tilde{t}_{f,s}$	Fresnel transmission from film into substrate
$\tilde{t}_{s,0}$	Fresnel transmission from substrate into vacuum
$\tilde{t}_{0,s}$	Fresnel transmission from vacuum into substrate

# Listings

A.1 Diffusion equation with Neumann boundary conditions. . . . .	249
A.2 Diffusion simulation with surface recombination boundary conditions. . . . .	251

# Chapter 1

## Introduction

As the demand for high-speed computation and communication increases, it becomes necessary to consider how materials operating at gigahertz frequencies ( $1 \text{ GHz} = 10^9 \text{ Hz}$ ) might behave differently at terahertz frequencies ( $1 \text{ THz} = 10^{12} \text{ Hz}$ ) [1–3]. Fig. 1.1 shows the THz band of the spectrum lying between the microwave and infrared regions. For many years it was difficult to manufacture sources of radiation at these frequencies [4]. Indeed, this can be seen in the designation of far-infrared radiation ( $10 \text{ cm}^{-1}$  to  $200 \text{ cm}^{-1}$ ), which arose from technical limitations of infrared spectroscopy at the time [4, 5]. The only way to obtain suitably bright far-infrared radiation was to use high temperature black bodies (such as a mercury lamp  $\sim 1300 \text{ K}$ ) combined with strong filtering of the higher frequencies [4, 6]. Detection also proved to be exceptionally difficult. Often, the monochromators had gratings which were manufactured in-house, and the entire detector had to be designed around operation in vacuum conditions [4].

Nonetheless, scientists still constructed spectrometers to specifically explore the far-infrared regime. Early interest focused on molecular rotation modes that occur at far-infrared frequencies because they give rise to sharply defined absorption lines [7, 8]. Perhaps the most unwelcome example is water vapor, which has rotational transitions near  $74 \text{ cm}^{-1}$  that can obscure the behavior of materials under study [4, 7–11]. Intramolecular bond-stretching ( $\lesssim 200 \text{ cm}^{-1}$ ) [4] and bending ( $\sim 20 \text{ cm}^{-1}$ ) also showed strong resonances in the far-infrared [4, 11, 12]. Of particular interest to this thesis, semiconductors exhibit strong absorption in the far-infrared that arises from three main sources: phonon modes, free charge carriers, and

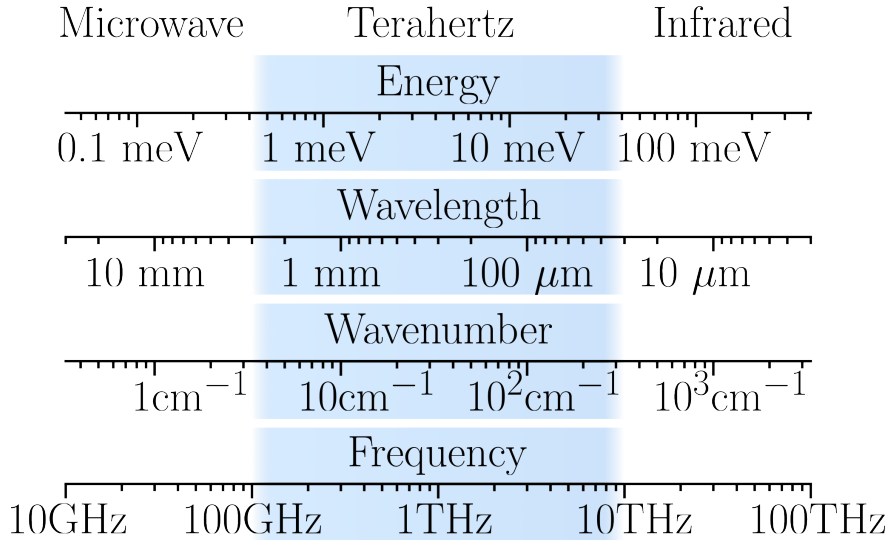


Figure 1.1: THz band of the spectrum (highlighted in blue).

transitions at localized impurities or lattice defects [13].

A crystal can be considered the sum of a Bravais lattice and a basis [14]. The lattice describes the periodic nature of the crystal, while the basis affixes atoms to the lattice coordinates. One can construct a crystal by repeating the lattice with the basis atoms attached. Vibrations can occur along the bonds of basis atoms, forming what are collectively known as phonons. In polar crystals, the infrared absorption of optical phonon modes is strong because polarization is directly associated with the displacement of ions. Electromagnetic waves can inelastically scatter on optical (acoustic) phonons, giving rise to the Stokes and anti-Stokes shifts used in Raman (Brillouin) scattering experiments [15–21]. Inelastic neutron scattering measurements rely on neutrons to interact with the nucleus of the basis atoms through spin-spin interactions [22]. The phonon dispersion can be measured by recording the energy lost to (or gained by) the crystal as a function of neutron momentum [23–30]. Far infrared photons can create transverse optical phonons which generally give rise to sharp peaks in the far-infrared absorption spectrum. Since phonons arise from damped oscillations, their absorption spectrum is well described by a Lorentzian function that is centered at a singular resonance frequency [31–38]. Combining photon scattering, neutron scattering, and infrared spectroscopy experiments provides powerful evidence of the structural features that impact vibrational modes of nanomaterials [39–44].

Due to the periodicity of the atoms that make up semiconductors, the Bloch condition gives rise to bands of energy that electrons can occupy up to the Fermi energy. The highest occupied band is called the valence band. The next unoccupied energy band is called the conduction band and is separated from the valence band by an energy gap. Through thermal excitation, some electrons are in the conduction band (conduction electrons), and some vacancies (holes) are in the valence band. The conductivity of a semiconductor is thus determined only by the conduction electrons and holes, generally called free charge carriers [13]. Measuring the response of free carriers to external stimuli such as an electric or magnetic field can inform us of the mechanisms that limit charge-carrier transport in nanomaterials. Despite the difficulty of manufacturing clean electrical contacts, great success has been found in measuring the resistivity of nanomaterials such as atomically thin semiconductors, nanowires, nanowalls, and nanoporous structures [45–52]. Far infrared spectroscopy provides a non-contact alternative that allows us to infer the microscopic dynamics of free charge carriers. Free carriers absorb far-infrared photons due to the availability of nearby states. Free carrier absorption is described by the Drude model, where free carriers scatter isotropically with an average scattering time  $\tau$ . Signatures of free carrier absorption include strong absorption at low THz frequencies and a  $1/\omega^2$  roll off in the conductivity at higher far-infrared frequencies [53–61].

Imperfection in the crystalline order gives rise to energy states within the band gap. Since these energy levels exist within the band gap, they are susceptible to excitation with energies below the band gap energy. Hence, if the state is close enough to the conduction or valence band, it may be excited by far-infrared radiation. These energy levels are often referred to as localized states or traps because carriers that occupy these states do not contribute to the long-range conductivity of the semiconductor. Imaging techniques like field emission scanning electron microscopy (FESEM) and optical microscopy allow for direct observation of dislocations such as grain boundaries, twin boundaries, point defects, and stacking faults [62–65]. Luminescence lifetimes measured with time-resolved photoluminescence (TRPL) and conductivity lifetimes measured with time-resolved terahertz spectroscopy (TRTS) are sensitive to a nanomaterial’s ultrafast trapping timescale. Combining knowledge of the defect distribution with indirect observations of carrier trapping thus provides a powerful statement

of the microscopic subpicosecond recombination pathways that are (are not) limiting carrier transport in nanomaterials [66–73].

This thesis will discuss phonons, free carriers, and localized states extensively as we explore the THz dynamics of free carriers in nanomaterials. Nanomaterials in this thesis will encompass dimensions of  $\sim 1$  nm up to  $\sim 100$  nm, and present unique features in the THz regime. Phonons play a large role in the dielectric background of nanomaterials [71, 74], low-frequency free-carrier conduction is suppressed by the boundaries of nanomaterials [55, 69, 75–78], and trapping at surface states is significant [79–85]. More detail of the ultrafast carrier dynamics in semiconductors can be found in Chapter 2. Although dielectric background and surface trapping are important topics of nanomaterial conduction, the primary feature we will repeatedly observe is the low-frequency suppression of free carrier conduction.

Consider the complex conductivity in a ubiquitous semiconductor such as silicon at room temperature ( $T = 295$  K). The Drude model of conductivity works remarkably well in silicon, implying that electrons undergo isotropic scattering that randomizes electron momentum within an average time  $\tau$ . Given a moderate excess electron density of  $4 \times 10^{14}$  cm $^{-3}$ , it is known that  $\tau = 0.27$  ps, and the electron effective mass is  $m^* = 0.2m_e$ , where  $m_e$  is the free electron mass [86]. Free carriers excited in silicon will diffuse from regions of high density into regions of low density. Driving this diffusion with a THz wave at frequency of  $f = \omega/2\pi = 1$  THz displaces the carrier density by a distance  $\ell_D$ , given by

$$\ell_D = \sqrt{\frac{D}{\omega}} = \sqrt{\frac{\tau k_B T}{m^* \omega}} = 30 \text{ nm}, \quad (1.1)$$

where,  $k_B$  is the Boltzmann constant, and  $D$  is the electron diffusion constant of silicon. As the dimensions of the silicon crystal are reduced to  $\ell_D$ , free carriers are collectively accelerated by the electric field. Over time, some of these carriers will interact with boundaries. Since the boundary possesses a finite transmission probability, the charge carriers that do not pass through the will accumulate at the boundary. The diffusion force acts against the force from the electric field, and so the carriers are concentrated in a region near the boundary. There are two critical outcomes of this. First, the pile-up reduces the long-range conductivity

because some free carriers are unable to traverse the boundary. Second, the pile-up of charge causes a lag between the driving field and the current, which imposes capacitive features on the conductivity spectrum. As the nanomaterial dimensions decrease further, free carrier localization sets in, completely suppressing long-range conductivity.

This localization sequence is illustrated in Fig. 1.2 (a)-(c). On top of Fig. 1.2 (a), we show a square of bulk silicon that has dimensions significantly larger than  $\ell_D \sim 30$  nm. Below is the resultant complex conductivity of the Drude model. The real part ( $\sigma_1$ ) monotonically decreases as the frequency is increased. Furthermore,  $\sigma_1$  is greater than zero, indicating current losses due to the resistivity of bulk silicon. The imaginary part ( $\sigma_2$ ) has a maximum at  $\omega = 1/\tau$ , where it intersects  $\sigma_1$ . For silicon at room temperature, this results in a crossover between  $\sigma_1$  and  $\sigma_2$  at 0.6 THz. Indeed, for many semiconductors the crossover frequency falls within 0.5-3 THz [11, 86, 87]. The imaginary part is also greater than zero, indicating that the current leads the driving field in a fashion similar to an inductor. Figure 1.2 (b) shows the case for when the nanomaterial dimensions are close to  $\ell_D$  in size. Under these circumstances  $\sigma_1$  begins to drop for frequencies below 0.25 THz. Furthermore,  $\sigma_2$  turns negative at these frequencies, reflecting the aforementioned capacitive response. Finally, Fig. 1.2 (c) shows that when the nanomaterial has dimensions below  $\ell_D$ , the long range conductivity is zero, reflecting the complete localization of free carriers. The localization sequence presented here demonstrates the ability of THz radiation to probe the carrier dynamics of nanomaterials despite the associated wavelength of 1 THz  $\sim 300$   $\mu$ m.

Indeed, since far-infrared spectroscopy began, extensive technological developments have paved the way for new approaches to generating and detecting far-infrared radiation. Today one can find facilities dedicated to free-electron lasers (FEL) and synchrotrons that provide high-power, coherent, continuously tuneable sources of far-infrared radiation [88, 89]. On a more table-top scale, developments in mode-locking paved the way for near-infrared (wavelength  $\sim 800$  nm) pulses with 100 fs duration [90–92], and chirped-pulse amplification amplified the mode-locked pulses by over  $1000\times$  [93]. The short duration and high power near-infrared pulses can be used to generate phase-stable bursts of far-infrared radiation through photoconductive switches [94], optical rectification [95, 96], and air plasmas [97, 98].

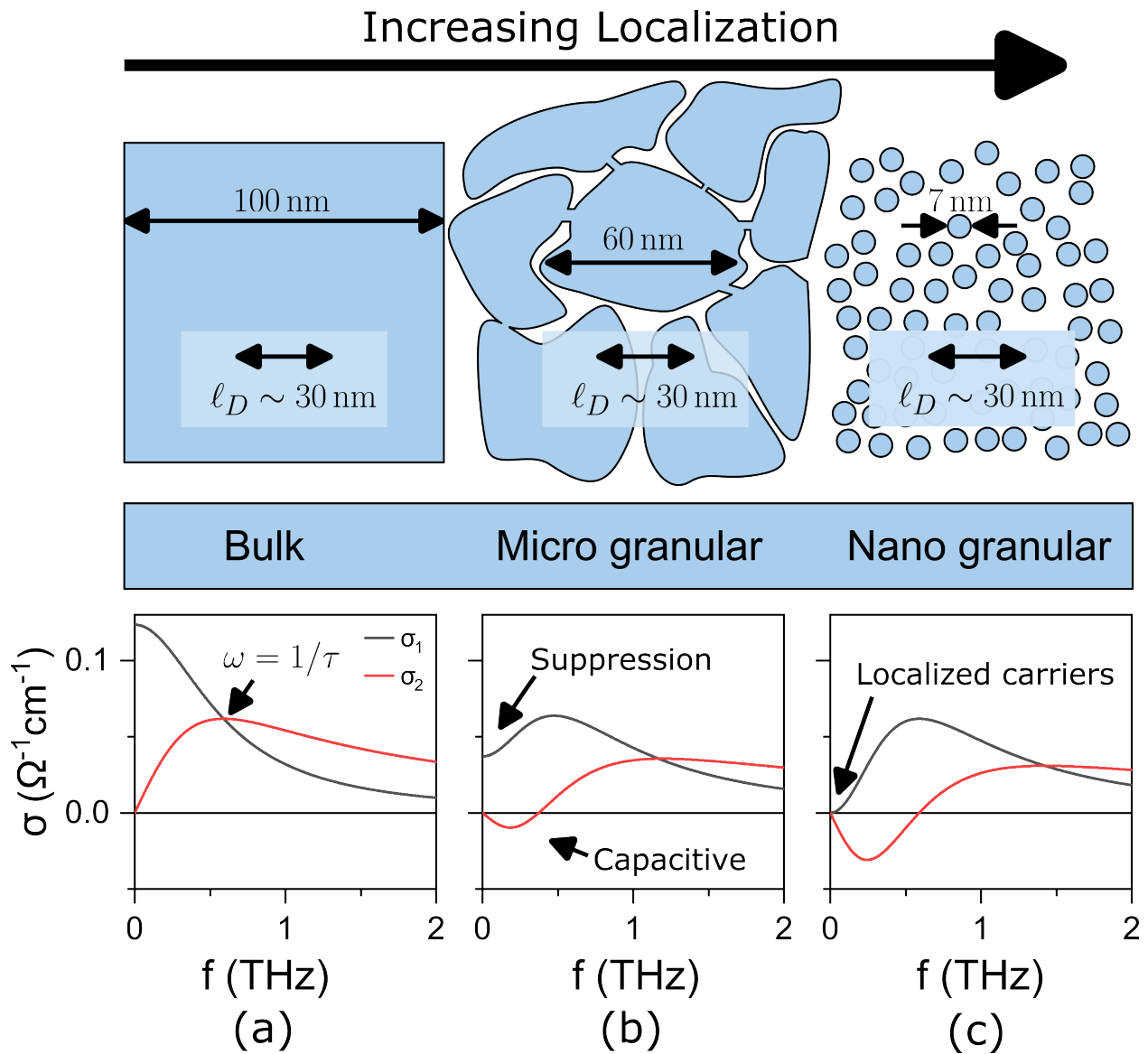


Figure 1.2: Charge-carrier localization modifies the conductivity. (a) Drude free carriers in silicon. (b) Semi-localized charge carriers yield suppressed low-frequency  $\sigma_1$ , and their capacitive behavior produces a negative  $\sigma_2$ . (c) Completely localized charge carriers with  $\sigma_1 = 0$  at  $\omega = 0$ .

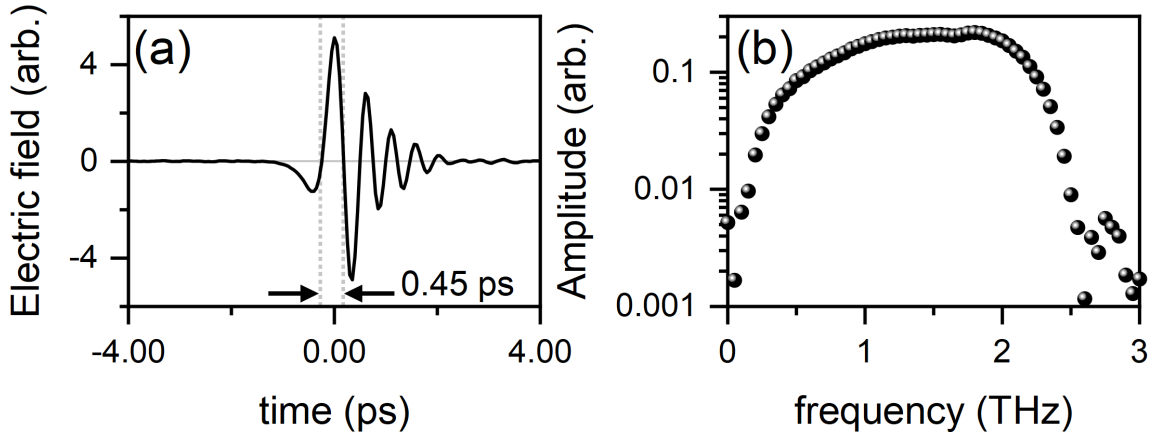


Figure 1.3: (a) Terahertz pulse with  $\sim 0.45$  ps half-cycle duration. The amplitude of the THz electric field is  $\sim 300$  V/cm. (b) Amplitude spectrum of the THz pulse in (a).

Figure 1.3 (a) shows a coherent measurement of a terahertz pulse generated via optical rectification in ZnTe. Perhaps the most important feature of Fig. 1.3 (a) is that it is a record of the electric field, not the intensity. As such, the phase and amplitude of the waveform are retained, eliminating the need for the Kramers-Kronig relations that were traditionally used in far-infrared spectroscopy. THz pulses in this thesis typically have half-cycle durations of  $\sim 0.45$  ps, which yields a  $\sim 1.1$  THz center frequency. Our THz pulses have a slight up-chirp due to normal dispersion in ZnTe. Our pulses also possess more than a single cycle oscillation, which is a result of the sharp cut off in the spectrum at 2.2 THz. The cut off is due to a phonon absorption at 2.2 THz [99]. Detection sensitivity reaches signal-to-noise ratios of  $\sim 2000$  owing to the noise reduction associated with gated-sampling and lock-in detection. Figure 1.3 (b) shows the corresponding amplitude spectrum. Due to strong phonon absorption above 2.5 THz in ZnTe, there is a sharp cutoff in the frequencies available for spectroscopy [32, 100].

Nonetheless, the phase stability of terahertz pulses provides access to coherent detection, which, in turn, permits time-domain spectroscopy. Terahertz time-domain spectroscopy (THz-TDS) is a powerful technique that provides direct access to the real and imaginary parts of the conductivity spectrum. Indeed this allows for direct observation of the  $\sigma_1$ - $\sigma_2$  crossover within the observable bandwidth, making THz-TDS an excellent approach to quantifying free-carrier density, mobility and scattering times in semiconductors and metals

[57, 101–106].

Furthermore, the synchronization of THz pulses (repetition rate  $\sim 1$  kHz) combined with the short pulse duration ( $\sim 2$  ps) yields the opportunity for a pump-probe configuration. In an optical-pump, terahertz-probe experiment, a 100 fs laser pulse is used to photoexcite a population of free charge carriers. Subsequently, terahertz spectroscopy can be performed on the photoexcited charge carriers, revealing how the carrier density, scattering time, and mobility evolve on ultrafast (picosecond) timescales. This time-resolved terahertz spectroscopy (TRTS) provides insight into recombination pathways, scattering mechanisms, and hot-carrier effects that evolve mere picoseconds after excitation [11, 32, 99, 107–110]. The pump-probe configuration is shown in Fig. 1.4. An optical excitation pulse (red) arrives at the nanomaterial film before the THz pulse (orange). The THz pulse transmitted through the nanomaterial film in equilibrium (blue,  $\mathcal{E}_{ref}$ ) is recorded along with the THz pulse transmitted through the photoexcited nanomaterial (burgandy,  $\mathcal{E}_{pump}$ ). The difference between  $\mathcal{E}_{ref}$  and  $\mathcal{E}_{pump}$  is the result of attenuation via the transient photoconductivity of the nanomaterial film. More detail of the time-resolved terahertz spectroscopy method can be found in Chapter 3, and the technical details used in this thesis can be found in Chapter 4.

Terahertz spectroscopy has become a central tool for exploring ultrafast charge carrier dynamics in various nanomaterials primarily because of the non-contact nature of the technique [31, 111–114]. Depositing clean contacts onto semiconductor nanowires is difficult, and has caused TRTS to become a premier tool for characterizing transport in nanowires. Free- and localized-carrier dynamics in semiconducting nanowires [67–69, 80–83, 110, 115] and internal exciton transition in CdSe nanorods [116] have been unveiled through TRTS experiments. CdS nanowires have great promise for use in photocatalytic water splitting [117], however, there may be transport mechanisms that limit charge carrier participation in surface chemistry. In Chapter 5 we investigate how wrapping CdS nanowires (diameter  $\sim 50$  nm, length  $\sim 1$   $\mu$ m) in atomically thin sheets of  $C_3N_5$  changes the photoconductivity of the nanowire [69]. The nanowires are grown in solution, and are deposited onto a substrate in a fashion similar to Fig. 1.5. Currently, wrapping nanowires in a core-shell configuration is a promising approach to enhancing photocatalytic applications of nanowires [69, 83]. We demonstrate, using TRTS, that CdS nanowires are best grown apart from the  $C_3N_5$  shell. If

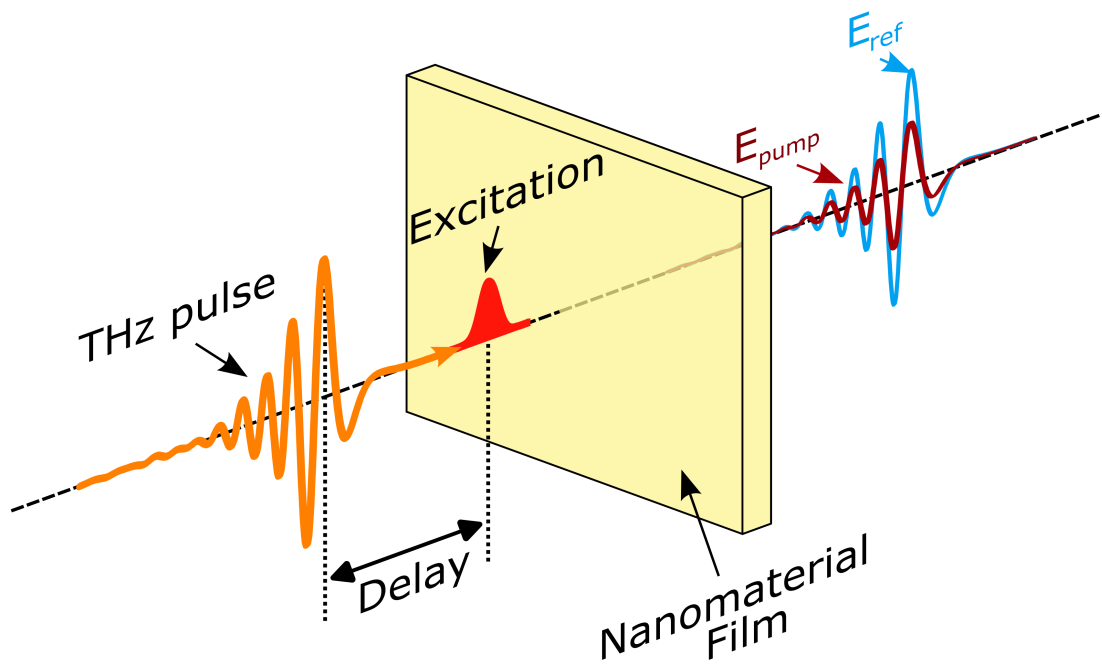


Figure 1.4: Pump-probe terahertz spectroscopy configuration.

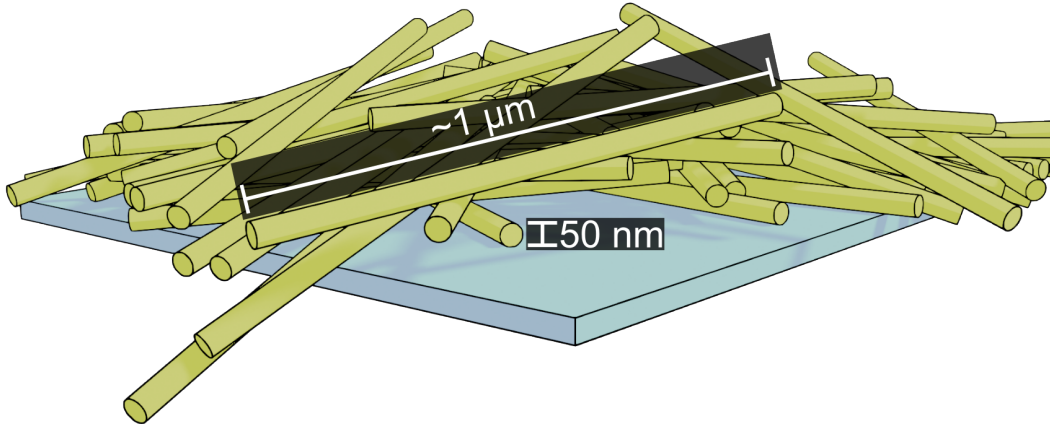


Figure 1.5: CdS nanowires on a substrate.

grown in-situ, the  $C_3N_5$  nanosheets appear to interfere with the growth of CdS nanowires, giving rise to a poor mobility and a short photoconductivity lifetime. When nanowires are wrapped after growth, the photoconductivity is nearly unaltered, yielding a bulk-like short-range mobility that maximizes charge carrier participation in surface chemistry.

Atomically thin transition metal dichalcogenides (TMDCs) have gathered a great deal of attention owing to the emergence of a direct band gap in monolayer form [118, 119]. To date, atomically thin ( $\sim 0.7$  nm) sheets can be grown with macroscopic dimensions of up to  $1\text{ cm} \times 1\text{ cm}$ . Atomically thin TMDCs begin as triangles that self-assemble into a monolayer over time when grown via metalorganic chemical vapor deposition (MOCVD). The orientation of the triangles impacts their optical properties, and so the orientation of these triangles has been imaged with optical techniques [120], similar to the schematic shown in Fig. 1.6. Atomically thin, direct gap semiconductors hold great promise for use in solar cells [121], photovoltaics [122], and optoelectronics [123]. Time-resolved terahertz spectroscopy has unveiled exciton formation dynamics [124], free carrier dynamics [125], and ultrafast transitions between exciton phases in TMDC heterostructures [126]. In Chapter 6, we contribute to this exploration by investigating the impact that photoexcitation density and temperature have on free charge carrier dynamics in the monolayer TMDC  $WSe_2$ .

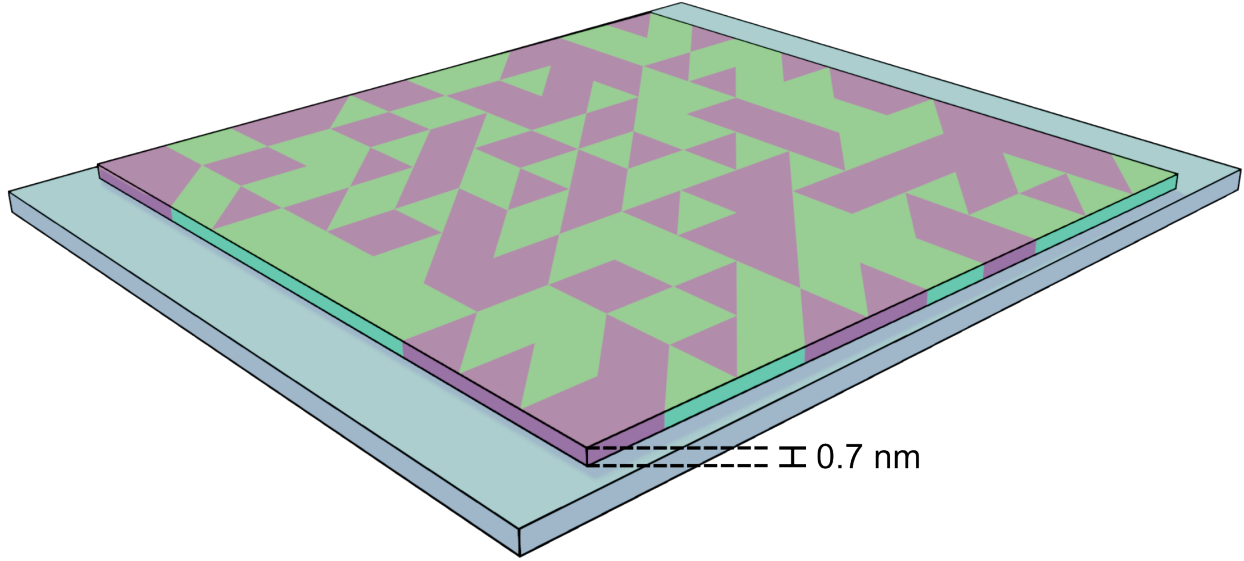


Figure 1.6: WSe<sub>2</sub> monolayer on a substrate.

Group 14 elemental semiconductors Si and Ge are essential in a broad range of applications such as optoelectronics, sensing, photovoltaic, and battery applications [127–133]. In the literature, one can find films comprised of nanowires, nanoparticles, and periodically porous nanostructures [130, 134–138], which have attracted attention due to their large surface area-to-volume ratios. Combining Group 14 elements (among others) with Group 1 or Group 2 elements yields a Zintl phase, a uniquely soluble semiconductor (and sometimes superconductor [139]) phase. Recently, Zintl phase germanium is finding new use in nanoscale templating [138]. Chapter 7 contains a study of picosecond charge carrier dynamics in a germanium inverse opal nanostructure fabricated via templating of Zintl phase germanium onto 300 nm PMMA beads. The inverse-opal structure consists of  $\alpha$ -phase germanium possessing spherical voids with a diameter of roughly 300 nm, as shown in Fig. 1.7. Owing to the chemistry of the Zintl phase, it is possible to remove germanium from the crystal and substitute it with silicon [138]. TRTS of pure inverse opal germanium was performed by Narreto et al. [140], and here we use TRTS to explore the consequences of substituting Ge with Si in an inverse-opal nanostructure.

Silicene is the silicon analog of graphene that has the potential for enhanced compati-

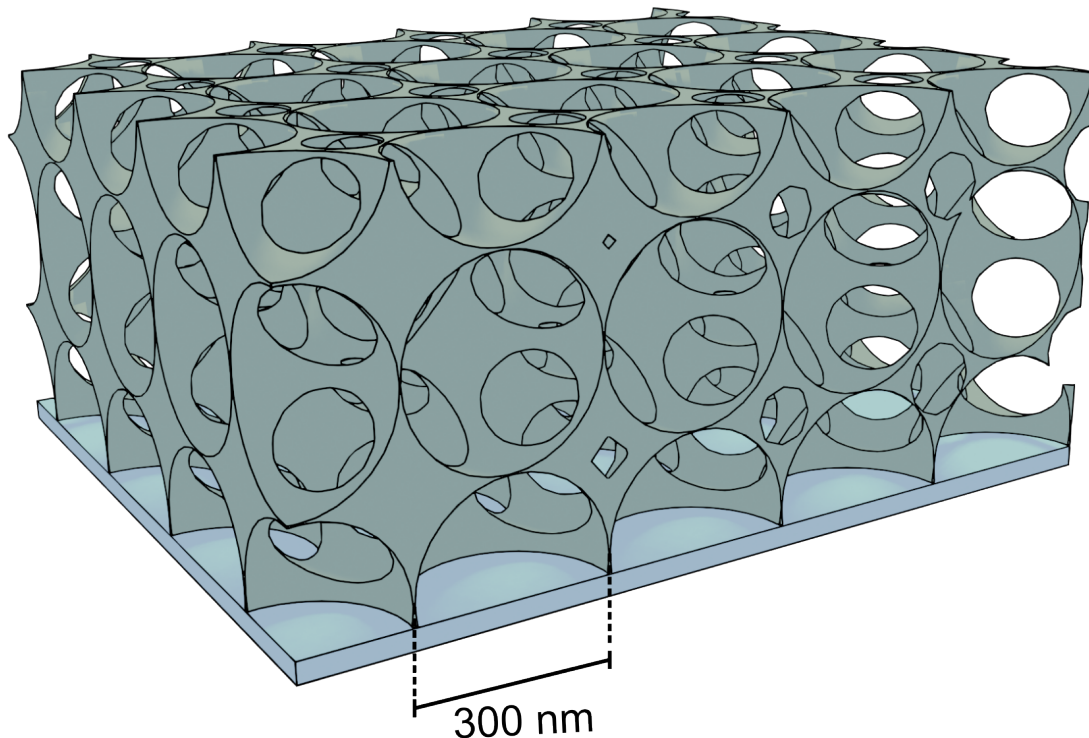


Figure 1.7: Inverse opal Ge on a substrate.

bility with current silicon technology. The silicon nanosheets possess a thickness of  $\sim 1$  nm [141], as shown in Fig. 1.8. The most significant obstacle in constructing next-generation silicene devices is oxidation. Preventing oxygen from bonding to the silicene can be achieved by bonding molecules to the silicene surfaces, forming a new class of materials called silicane. Hydride-terminated silicon nanosheets (SiNS-H) and 1-dodecene-functionalized silicon nanosheets (SiNS-dodecene) are the most thoroughly investigated passivations, and in Chapter 8 we extend the present knowledge with the first TRTS performed on silicon nanosheets. We find that excitation with 400 nm light results in a weak photoconductivity in SiNS-dodecene that may be robust to temperature. We find that the short-range mobility in SiNS-dodecene is  $400 \text{ cm}^2/\text{Vs}$ , which is comparable to the mobility seen in monolayer transition metal dichalcogenides [142] and high-mobility 2-dimensional polymers [143]. SiNS-H does not appear to exhibit a substantial photoconductivity.

Recently, group III-nitride materials such as GaN have gained considerable attention regarding photocatalytic water splitting. The alignment of the energy bands to many photocatalytic reactions has proven to be favorable, and the ability to remain stable in harsh

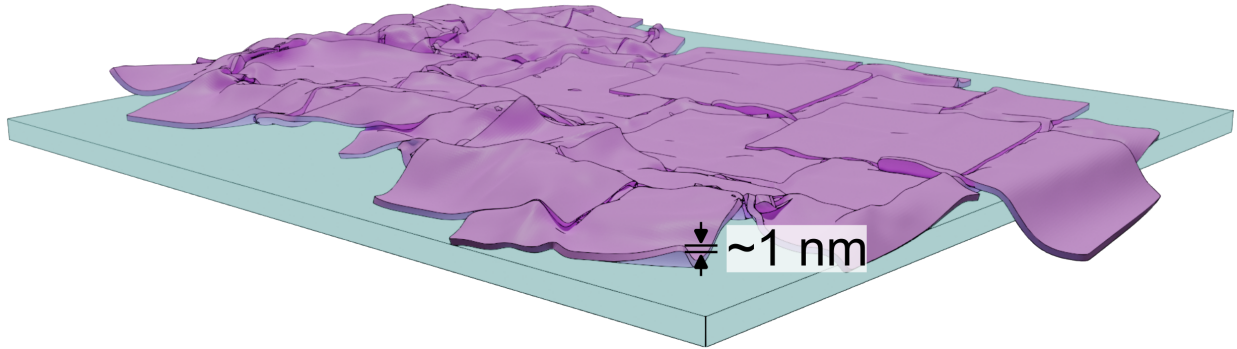


Figure 1.8: Silicon nanosheets on a substrate.

chemical environments makes them a valuable tool in photocatalysis [144, 145]. Increasing the surface area-to-volume ratio can be achieved by growing GaN nanowires and proves to be an excellent avenue to achieve increased molecular participation in surface chemistry. However, Kraut et al. showed that the nanowire growth exposes the crystallographic *m*-planes to photochemical etching, which erodes the GaN nanowires [146]. Fortunately, the crystallographic *c*-plane is stable [146]. Maximizing the *c*-plane exposure while minimizing *m*-plane exposure can be achieved by moving from a nanowire geometry to a nanowall configuration, as shown in Fig. 1.9. By utilizing selective area growth and molecular beam epitaxy, parallel nanowalls with highly tunable height, separation, and length can be grown, opening up many avenues for optimization [144]. In Chapter 9 we perform the first study of TRTS on GaN nanowalls (width  $\sim 270$  nm, height  $\sim 500$  nm, and pitch  $\sim 1$   $\mu\text{m}$ ) grown via selected area molecular beam epitaxy.

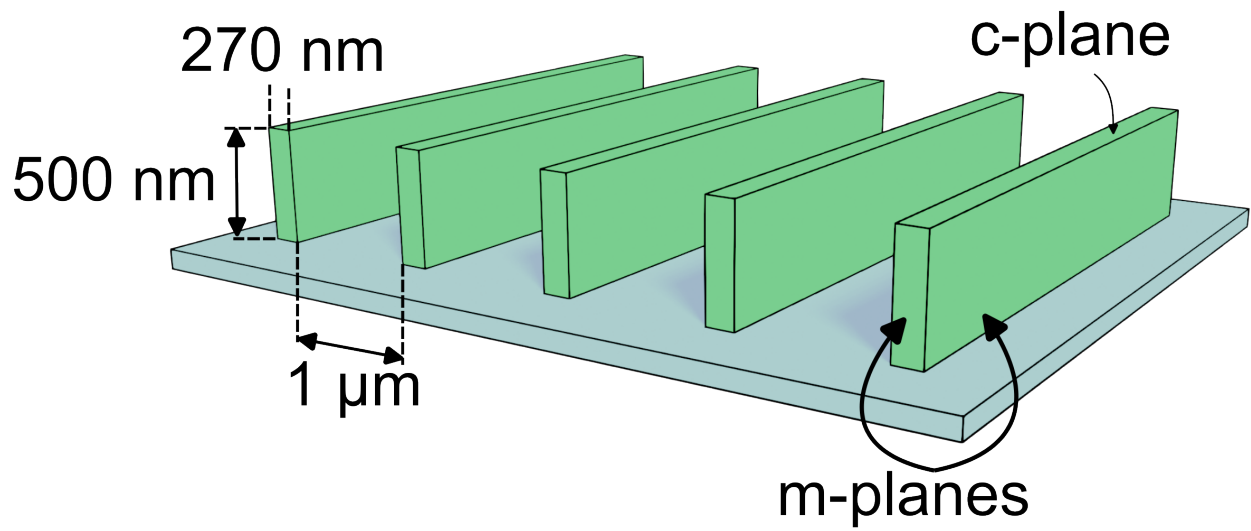


Figure 1.9: Gallium nitride nanowalls on a substrate.

# Chapter 2

## Ultrafast Carrier Dynamics in Semiconductors

### 2.1 Introduction

#### 2.1.1 Band Structure

In equilibrium, a semiconductor can be considered a periodic arrangement of atoms, each having their own local potential  $U_c$ . To find the electron wave function  $\psi_k(z)$  the Schrödinger equation must be solved. The Schrödinger equation for an electron in the periodic potential is given by

$$\left[ -\frac{\hbar^2}{2m_0} \frac{d}{dz} + U_c(z) \right] \psi_k(z) = E\psi_k(z), \quad (2.1)$$

where  $m_0$  is the free electron mass and  $E$  is the electrons total energy. A Bloch wave is a wave function that is a product of a function with the periodicity of the crystal  $u_k(z)$  and a plane wave  $e^{ikz}$ . Thus,

$$\psi_k(z) = u_k(z)e^{ikz} \quad (2.2)$$

where  $k$  is the electron wavevector. Given that  $u_k(z)$  contains the periodicity of the lattice, it follows that  $u_k(z) = u_k(z + a)$ , where  $a$  is the lattice constant. For any  $k$  we can solve for  $u_k(z)$  by inserting Eq. (2.2) into Eq. (2.1) and leveraging the periodic boundary condition. The energies of the  $k^{th}$  state is also found this way. Since, for each  $k$ , there is an infinite number of eigenvalues, we can denote each by introducing the band number  $n$ . The spacial

periodicity placed on the Bloch functions results in periodicity of the band  $E_n(k)$ . In general,

$$E_n(k) = E_n(k + k_\ell) \quad (2.3)$$

where  $k_\ell = 2\pi\ell/a$  ( $\ell = 1, 2, 3, \dots$ ) are the reciprocal lattice vectors. Because the band structure  $E_n(k)$  is periodic, all available energies can be found in the range of wave vectors  $-\pi/a \leq k \leq \pi/a$ , referred to as the Brillouin zone. It is convenient to work within the Brillouin zone, under what is called the reduced zone scheme. If the band structure is known,  $E_n(k)$  can be expanded in a Taylor series about  $k = 0$ , such that [147]

$$E_n(k) \approx E_n(0) + k \left[ \frac{\partial E_n(k)}{\partial k} \right]_{k=0} + k^2 \left[ \frac{1}{2} \frac{\partial^2 E_n(k)}{\partial k^2} \right]_{k=0} + \dots \quad (2.4)$$

The band minimum is an extrema by definition, and so the terms linear in  $k$  vanish. Defining the effective mass through

$$\frac{1}{m^*} = \frac{1}{\hbar^2} \left| \frac{\partial^2 E_n(k)}{\partial k^2} \right| \quad (2.5)$$

we can rewrite Eq. (2.4), in the form of the parabolic band approximation

$$E_n(k) \approx E_n(0) \pm \frac{\hbar^2 k^2}{2m^*} \quad (2.6)$$

where the  $\pm$  comes from the curvature of band  $n$ . Remarkably, crystals possess a dispersion relation similar to a free electron dispersion.

### 2.1.2 Semiclassical Absorption

The electronic band structure is inextricably linked to the index of refraction, which determines the amount of light that a semiconductor can absorb. A frequency-dependent, complex index of refraction  $\tilde{n}(\omega) = n(\omega) + i\kappa(\omega)$  provides a compact way to describe how the phase and amplitude of an electromagnetic wave  $\mathcal{E}$  (with angular frequency  $\omega$  and wave vector  $k$ ) are altered by propagating in a medium. For example, Beer's law states that an electric field propagating in a dielectric medium of thickness  $L$  is described by

$$\mathcal{E} = \mathcal{E}_0 e^{-\alpha L/2} e^{i(nkL - \omega t)} \quad (2.7)$$

where  $\alpha = 4\pi\kappa/\lambda$  is the absorption constant, and  $\mathcal{E}_0$  is the field amplitude. Bringing  $\alpha L/2$  into the exponent brackets we see that

$$\mathcal{E} = \mathcal{E}_0 e^{i(\tilde{n}kL - \omega t)} \quad (2.8)$$

which provides a compact way to encode the absorption of a medium into the index of refraction.

Equation 2.8 shows that only  $k$  is modified by  $\tilde{n}$ . The reason for this is that the index of refraction describes the microscopic interaction between the incident light wave and the atoms that compose the medium. The incident light wave does work on the electrons surrounding the atoms. Modelling the atoms as damped oscillators implies that after the work was done on the atoms, they will emit that energy as a re-radiated light. The inefficiency of the absorption/emission cycle gives rise to a net phase between the incident light wave and the re-emitted light. The phase causes interference between the incident and atom-radiated light, which results in an apparent wavelength that is different from the wavelength of the incident light [148]. This thought experiment demonstrates that the complex index of refraction links the microscopic behavior of electrons to observable changes in an electromagnetic wave. This is known as the Ewald-Oseen extinction theorem, and further detail can be found in Ref. [149].

To establish this connection, we begin with the definition of the absorption coefficient  $\alpha$ . The absorption coefficient is defined as the energy absorbed per unit time per unit volume divided by the energy flux. This gives [150]

$$\alpha = \frac{\hbar\omega W(\omega)}{I} = \frac{2\kappa\omega}{c} = \frac{4\pi\kappa}{\lambda} \quad (2.9)$$

where  $W(\omega)$  is the number of transitions per unit time per unit volume, and  $I$  is the energy crossing a unit area per unit time.  $I$  is given by the familiar relation [148, 151]

$$I = \frac{1}{2}\epsilon_0 n c \mathcal{E}_0^2, \quad (2.10)$$

where  $n$  is the real part of the refractive index, and  $c$  is the speed of light.

Fermi's golden rule establishes the transition rate between a state in the valence band to the conduction band  $W_{v \rightarrow c}$ . The transition rate is

$$W_{v \rightarrow c} = \frac{2\pi}{\hbar} |\mathbf{M}|^2 g(\hbar\omega), \quad (2.11)$$

where  $\mathbf{M}$  is the matrix element of the perturbation Hamiltonian between a conduction band state  $\psi_{c,k_c}$  and valence band state  $\psi_{v,k_v}$ , and  $g(\hbar\omega)$  is the joint density of states at photon energy  $\hbar\omega$ .  $\mathbf{M}$  follows the relation

$$\mathbf{M} = \int \psi_{c,k_c}^* H' \psi_{v,k_v} d^3 \mathbf{r}. \quad (2.12)$$

$H'$  is the perturbation Hamiltonian that arises from an electric field  $\mathcal{E}$ , given by

$$H' = -q\mathcal{E} \cdot \mathbf{r} = q\mathcal{E}_0 e^{i(\mathbf{k}_{light} \cdot \mathbf{r} - \omega t)} \mathbf{e} \cdot \mathbf{r}. \quad (2.13)$$

where  $\mathbf{e}$  is the polarization of the electric field.

In semiconductors, the photon momentum determines the relevant conduction/valence band states. Semiconductor band gaps are  $\sim 2$  eV, which gives

$$k_{light} \approx \frac{2\pi}{620 \text{ nm}} = \frac{2\pi}{6200 \text{ \AA}}. \quad (2.14)$$

Considering the maximum momentum within the Brillouin zone ( $k_{max}$ ) is

$$k_{max} = \frac{2\pi}{a} \sim \frac{2\pi}{1 \text{ \AA}}, \quad (2.15)$$

it is clear that the light wave momentum is small by comparison. Therefore the states that satisfy energy conservation correspond to vertical transitions in the band structure.

Due to the photon-induced vertical transition of the electrons and holes, conservation of energy in the parabolic band approximation requires that

$$\hbar\omega = E_g + \frac{\hbar^2 k^2}{2m_e^*} + \frac{\hbar^2 k^2}{2m_h^*}, \quad (2.16)$$

where,  $E_g$  is the band gap energy,  $m_e^*$  is the electron effective mass in the conduction band,  $m_h^*$  is the hole effective mass in the valence band. Equation (2.16) can be simplified by introducing the reduced electron-hole mass ( $\mu^*$ ), such that

$$\frac{1}{\mu^*} = \frac{1}{m_e^*} + \frac{1}{m_h^*}. \quad (2.17)$$

The joint density of states  $g(\hbar\omega)$  determines the density of optical transitions as a function of energy. The joint density of states is related to the density of states ( $g(k)$ ) through

$$g(\hbar\omega) = \frac{2g(k)}{dE/dk}, \quad (2.18)$$

where  $dE/dk$  is the gradient of the E-k dispersion curve, and the extra factor of two comes from having two allowed spin states for each allowed  $k$ -state. The density of states is found by considering the density of states in a sphere of radius  $k + dk$  in momentum space. This gives

$$g(k)dk = \frac{4\pi k^2}{(2\pi)^3} dk = \frac{k^2}{2\pi^2} dk \implies g(k) = \frac{k^2}{2\pi^2}. \quad (2.19)$$

Substituting Eq. (2.16) into Eq. (2.18) (with  $E = \hbar\omega$ ), and also using Eq. (2.16) to define  $k$ , we find that [150, 151]

$$g(\hbar\omega) = \frac{1}{\hbar^3\pi^2} \sqrt{\frac{\mu^3(\hbar\omega - E_g)}{2}}. \quad (2.20)$$

The absorption coefficient can now be constructed by substituting Eqs. (2.20), (2.11), and (2.10) into Eq. (2.9), giving

$$\alpha(\omega) = \frac{4\omega}{n\pi\epsilon_0 c \hbar^3 E_0^2} \mu^* \sqrt{2\mu^*(\hbar\omega - E_g)}. \quad (2.21)$$

Admittedly this approach has brought us to a situation where the absorption is defined in terms of the real part of the refractive index  $n$ . Casting this in terms of the relative dielectric constant (defined by  $\tilde{\epsilon}(\omega) = \sqrt{\tilde{n}} = \epsilon_1 + i\epsilon_2$ ) allows us to use the identity  $\alpha = \omega\epsilon_2/nc^*$  to find the imaginary part of  $\tilde{\epsilon}$

$$\epsilon_2(\omega) = \frac{4}{\pi\epsilon_0 \hbar^3 E_0^2} \mu^* \sqrt{2\mu^*(\hbar\omega - E_g)}. \quad (2.22)$$

---

\*Since  $\epsilon_2 = 2n\kappa$ , it follows from Eq. (2.9) that  $\alpha = \omega\epsilon_2/nc$ .

The real part of  $\tilde{\epsilon}$  can be retrieved with the help of the Kramers-Kronig relation

$$\epsilon_1(\omega) = 1 + \frac{2}{\pi} \mathcal{P} \int_0^{\infty} \omega' \epsilon_2(\omega') \frac{1}{(\omega')^2 - \omega^2} d\omega'. \quad (2.23)$$

where  $\mathcal{P}$  denotes the principle part of the integral. Equations (2.22) and (2.23) link the quantum mechanical behavior of electrons to measurable optical properties such as the absorption, transmission, and reflection coefficients.

### 2.1.3 Carrier Dynamics

Immediately after a photon is absorbed, electrons (holes) occupy a non-thermal distribution in the conduction (valence) band. Next, electrons and holes relax spatially and temporally over timescales that depend on the available energy dissipation pathways [152]. The process of dissipating excess energy from photoexcitation is referred to as carrier cooling, and the excited carriers are generally referred to as hot carriers until they reach thermal equilibrium with the crystal lattice temperature. Note that we choose to present the relaxation mechanisms in chronological order, which may lead to the presumption that certain mechanisms turn on at later times. This is not true, as there is a non-zero probability that any of the relaxation mechanisms we discuss occur at any time after excitation. Figure 2.1 (a) shows the band structure of a semiconductor in equilibrium. The Fermi energy ( $E_f$ ) resides within the band gap, and the thermal smearing of the Fermi-Dirac distribution  $f_e(E)$  causes some electrons to occupy the conduction band.

In Fig. 2.1 b, we show the moment a photon is absorbed by the semiconductor, with energy  $\hbar\omega$  above the band gap. Within 10 fs ( $10^{-14}$  s) momentum relaxation occurs through elastic and inelastic scattering, randomly distributing electron (hole) occupancy among states in the conduction (valence) band (Fig. 2.1 c). On this timescale electrons may interact with long wavevector phonons, resulting in a population of carriers that are scattered into satellite valleys of the Brillouin zone [153].

Coulomb thermalization then occurs over 100 fs ( $10^{-13}$  s), and allows the electron (hole) distribution to be described by the Fermi-Dirac distribution with a temperature  $T_e$  ( $T_h$ ) significantly higher than the lattice temperature ( $T_e \sim 1000$  K) [152, 154]. Electron-hole

scattering transfers energy between the two populations, and brings  $T_e$  and  $T_h$  to a shared temperature  $T_{e-h}$  over 1 ps ( $10^{-12}$  s) [155] (Fig. 2.1 d).

In  $<10$  ps, energy relaxation occurs through emission of small-wavevector polar-optical phonons which gradually shifts  $T_{e-h}$  toward the lattice temperature  $T_L$  (Fig. 2.1 e). For times  $> 10$  ps, the electrons and holes occupy states near the band extrema, which will gradually dissipate according to the various mechanisms of recombination [156]. The most important recombination mechanism in this thesis is photoluminescence, where an electron and hole recombine and emit a photon with energy equal to the electron-hole energy difference. Photoluminescence is shown in Fig. 2.1 f. Typically, photoluminescence occurs on timescales beyond 10 ps.

### 2.1.4 Photoluminescence

Photoluminescence (PL) is a broad term that denotes the spontaneous emission of light after photoexcitation. Radiative (R) and non-radiative (NR) transitions dictate the timescale of PL. The probability of electron-hole recombination per unit time ( $1/\tau$ ) follows the relation

$$\frac{1}{\tau} = \frac{1}{\tau_R} + \frac{1}{\tau_{NR}}, \quad (2.24)$$

where  $\tau_R$  and  $\tau_{NR}$  are the radiative and non-radiative times, respectively. The radiative efficiency  $\eta_R$  is the fraction of recombination events that contribute to photoluminescence and is written

$$\eta_R = \frac{\tau}{\tau_R} = \frac{1}{1 + \tau_R/\tau_{NR}}. \quad (2.25)$$

Due to the non-radiative recombination events, it is clear that  $\eta_R \leq 1$ .

Recombination across a semiconductor band gap depends strongly on the band-gap alignment. Direct transitions present the simplest case, where the valence and conduction band extrema share a common momentum  $k$ . The transition rate follows from Fermi's golden rule

$$W_{c \rightarrow v} = \frac{2\pi}{\hbar} |\mathbf{M}|^2 g(E(\mathbf{k})),$$

where  $\mathbf{M}$  is the aforementioned matrix element, with  $v$  and  $c$  exchanged.  $g(E)$  is the joint

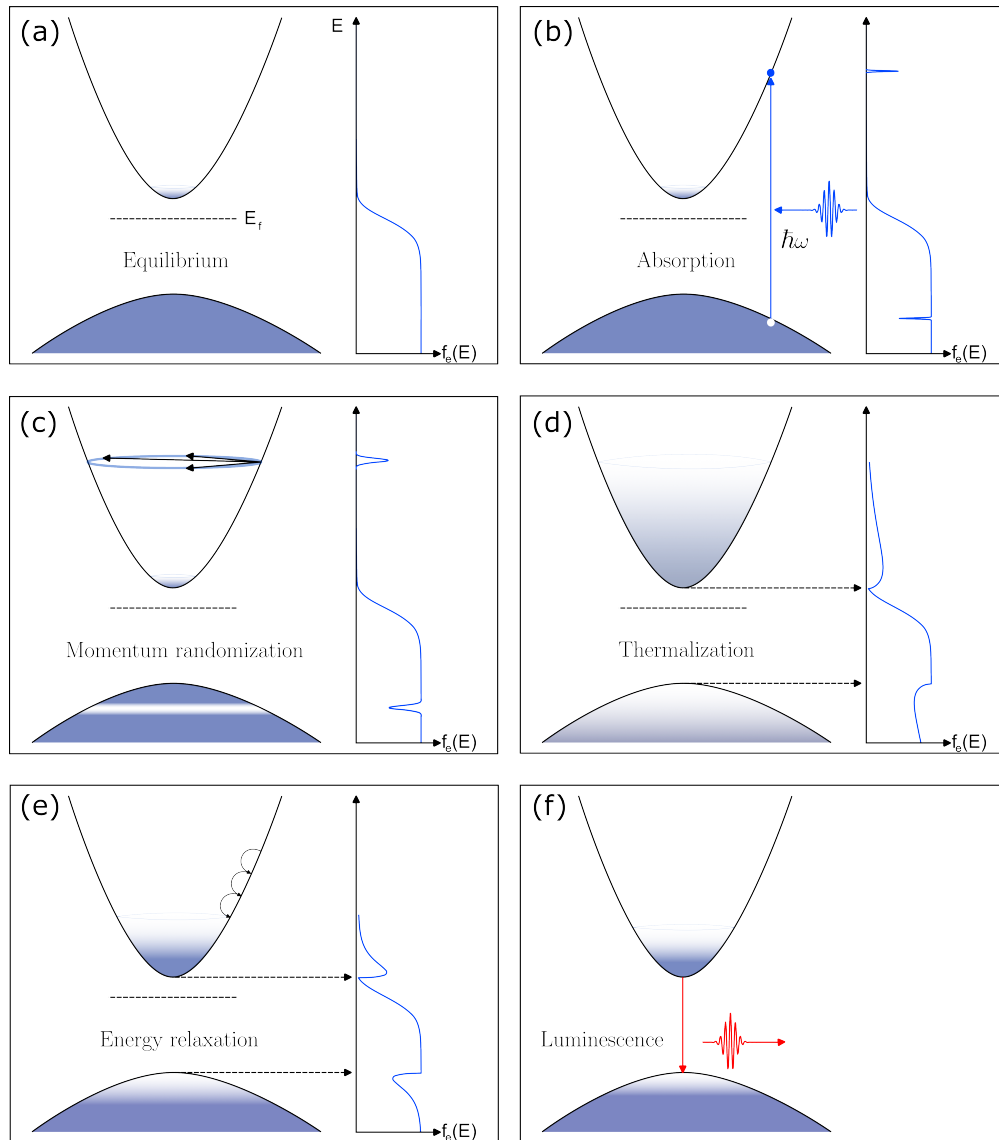


Figure 2.1: Schematic of relaxation timeline after photoexcitation. (a) Semiconductor in equilibrium. (b) Photons arrive with energy  $\hbar\omega$  (blue arrow) and create electrons (holes) in the conduction (valence) band. (c) Momentum relaxation randomizes carrier momentum (black arrows) throughout states with equal energy. (d) Thermalization of like-carriers occurs on  $\sim 100$  fs timescales, while electron-hole thermalization occurs on  $\sim$  ps timescales. (e) Phonon emission occurs on timescales of  $< 10$  ps, and lowers the average energy of the distribution. Photoexcited free-carriers occupy states near the band-edge. (f) Photoluminescence occurring from electron-hole recombination at the band extrema.

density of states given earlier. The amount of PL emitted with energy  $\hbar\omega$  is directly proportional to the rate and availability of transitions. The intensity of direct transitions ( $I_{dir}$ ) thus follows the relation

$$I_{dir}(\hbar\omega) \propto W_{c \rightarrow v} f(\hbar\omega) = |\mathbf{M}|^2 g(\hbar\omega) \times f(\hbar\omega) \quad (2.26)$$

where  $f(\hbar\omega)$  is the distribution of electrons and holes. Consider an electron with energy  $E_2$  and a hole with energy  $E_1$ . Upon recombination a photon will be emitted with energy  $\hbar\omega = E_2 - E_1$ . The total occupancy  $f(\hbar\omega)$  is given by the product of the electron and hole distributions [151, 156],

$$f(\hbar\omega) = f_e(E_2) \times f_h(E_1) = \frac{1}{\exp\left(\frac{E_2 - E_f}{k_B T}\right) + 1} \times \left(1 - \frac{1}{\exp\left(\frac{E_1 - E_f}{k_B T}\right) + 1}\right) \quad (2.27)$$

where  $E_f$  denotes the Fermi energy. At low excitation density, low temperature, and close vicinity to the band edge,

$$f_e(E_2) \approx \exp\left(-\frac{E_2 - E_f}{k_B T}\right), \quad (2.28)$$

and

$$f_h(E_1) = \frac{\exp\left(\frac{E_1 - E_f}{k_B T}\right)}{\exp\left(\frac{E_1 - E_f}{k_B T}\right) + 1} \approx \exp\left(\frac{E_1 - E_f}{k_B T}\right). \quad (2.29)$$

Substituting into Eq. (2.27) we find

$$f(\hbar\omega) \approx \exp\left(-\frac{\hbar\omega}{k_B T}\right). \quad (2.30)$$

Finally, substitution into Eq. (2.26), the distribution of energies emitted by direct recombination is given by

$$I_{dir}(\hbar\omega) \propto \exp\left(-\frac{\hbar\omega - E_g}{k_B T}\right) \sqrt{\hbar\omega - E_g}. \quad (2.31)$$

### 2.1.5 Models of Charge-Carrier Recombination

Modeling the photoluminescence lifetime is a complicated process often quantified with empirical models. Mechanisms like carrier-carrier interactions, traps, Pauli blocking, and sur-

face recombination all contribute to the lifetime of recombination in measurable ways. Here, we describe the three main processes used in this thesis.

### Monomolecular, Bimolecular, and Auger Recombination

The recombination rate  $R$  can be expanded into a power series in carrier density  $n$  such that

$$R = \frac{dn}{dt} = An + Bn^2 + Cn^3, \quad (2.32)$$

where  $A$  is the monomolecular recombination coefficient (often the definition  $A = 1/\tau$  is used),  $B$  is the bimolecular recombination coefficient, and  $C$  is the Auger recombination coefficient. The exponent of each term in this power series corresponds to the number of carriers involved in a recombination event, since the probability of  $m$  scatterings occurring simultaneously is proportional to the product of  $m$  densities. This gives rise to the monomolecular, bimolecular and trimolecular interpretations of this power series.

A monomolecular process requires only a single carrier for a recombination event. Thus it describes a nonradiative recombination pathway, and includes mechanisms such as trap states and lattice defects. Bimolecular recombination is the result of an electron and hole recombining directly across the band-gap, and as such bimolecular recombination is radiative. Auger recombination requires 3 charge carriers (eg, 2 holes, one electron), and via energy conservation this recombination is non-radiative [156, 157].

### Multilevel Systems

In some systems, the equation that describes recombination is presented as a set of coupled rate equations [158, 159]. Such a system is used to describe phenomena such as hot carrier cooling and saturable trapping. The lifetime of the carrier density  $n$  is governed by

$$\begin{aligned} \frac{dn_{hot}}{dt} &= G(t) - \frac{n_{hot}}{\tau_{cool}} \\ \frac{dn}{dt} &= \frac{n_{hot}}{\tau_{cool}} - \frac{n}{\tau_{trap}} \\ \frac{dn_{trap}}{dt} &= \frac{n}{\tau_{trap}} \end{aligned} \quad (2.33)$$

where the hot carriers  $n_{hot}$  cool through a monomolecular process with time-constant  $\tau_{cool}$ , and the cool carriers  $n$  fall into saturable trap states over the time-constant  $\tau_{trap}$ .  $G$  is the charge-carrier generation function. The saturable nature of the trapping occurs through the simple model [158]

$$\tau_{trap} = \frac{\tau_0}{1 - n_{trap}/n_{max}} \quad (2.34)$$

where  $n_{max}$  is the maximum density of carriers lost to trap states,  $n_{trap}$  is the density of carriers occupying trap states, and  $\tau_0$  is the average time between trapping events when no carriers are in the trap states. Equation (2.34) models trap saturation because filling the traps ( $n_{trap} \rightarrow n_{max}$ ) results in the trapping time diverging to positive infinity<sup>†</sup>.

### Surface Recombination

The surface of semiconductors terminates the periodicity of the crystal, which changes the energy landscape near the surface. At the surface, bonds remain unbound, and seek alternative arrangements to minimize the free energy. As such the electronic structure near the surface becomes disordered, forming defect states that act as monomolecular recombination centers. Surface recombination is the monomolecular recombination at these surface states.

Surface recombination is characterized by the surface recombination velocity  $S_0$ , which is defined as the number of carriers recombining at a semiconductor surface per unit area per unit time per unit volume of excess bulk carriers at the boundary between the quasi-neutral and space-charge regions [160]. The critical range for device purposes is bounded between  $10^3$  cm/s and  $10^7$  cm/s. In the lower limit,  $S_0$  is dominated by bulk recombination, and in the upper limit,  $S_0$  occurs at a rate governed by the charge carrier thermal velocity.

Surface recombination is treated as a boundary condition to the ambipolar diffusion equation

$$\frac{\partial n(x, t)}{\partial t} = G(x, t) - R(x, t) - qD^* \frac{\partial^2 n(x, t)}{\partial x^2}, \quad (2.35)$$

where  $x$  is position,  $G(x, t)$  is the source of free carriers,  $R$  is the recombination mechanisms captured by Eq. (2.32),  $q$  is the elementary charge, and  $D^*$  is the ambipolar diffusion constant. Equation (2.35) expresses the conservation of charge in semiconductors after pho-

---

<sup>†</sup>Since  $n_{trap} < n_{max}$ ,  $\tau_{trap}$  approaches positive infinity.

to excitation. The ambipolar diffusion coefficient is given by

$$D^* = \frac{2D_e D_h}{D_e + D_h} \quad (2.36)$$

where  $D_e$  and  $D_h$  are the diffusion coefficients of electrons and holes, respectively. More detail about  $D_e$  and  $D_h$  can be found in section 2.2.3. Since surface recombination occurs in the first few layers ( $\sim 5 \text{ \AA}$ ) of the semiconductor, surface recombination is handled as a boundary condition of Eq. (2.35). The boundary undergoing surface recombination (typically at  $x = 0$ ) states that the charge density is governed by the condition [161, 162]

$$\frac{\partial n(x, t)}{\partial x} = \frac{S_0}{D^*} n(x = 0, t). \quad (2.37)$$

Equation (2.35) can be solved numerically to unveil the evolution of  $n(x, t)$ . A numerical solution to the continuity equation with surface recombination is provided in Appendix A along with sample code from a working implementation.

## 2.2 Transient Conductivity

After photoexcitation, the semiconductor is in a state of quasi-equilibrium. Applying an electric field to the photoexcited charge carriers will result in the formation of a drift current  $J_{drift}$ . Furthermore, the act of photoexcitation results in a nonuniform distribution of charge (cf. Beer's law) that can manifest a diffusive current  $J_{diff}$ . As such, the net current density  $J$  is well described by

$$J = J_{drift} + J_{diff}, \quad (2.38)$$

where  $J_{drift}$  and  $J_{diff}$  are the subjects of this section.

### 2.2.1 Conductivity Spectrum

When an electric field  $\mathcal{E}$  is applied to an electron gas, it generates an electric current  $J_{drift}(\mathbf{x}, t)$  which, when the field is weak, is assumed to be linearly related to the field. Despite intuition, this does not imply that we may write  $J_{drift}(\mathbf{x}, t) = \sigma \mathcal{E}(\mathbf{x}, t)$  [163]. The issue at hand is one of locality, since the electric field at a particular space-time coordinate  $(\mathbf{x}, t)$  determines  $J_{drift}$  at the same coordinate. This is not true when the mean free path of

electrons is long compared to the distances over which the field changes appreciably (wavelength, penetration depth, etc.). Alternatively, locality is not satisfied when the mean time between collisions is long compared to times over which the pulse varies significantly (period of oscillation, pulse duration, etc.). Under these conditions an electric field at  $(\mathbf{x}', t')$  can generate a current density at different space-time points  $(\mathbf{x}, t)$ . To allow for such an effect,  $J_{drift}$  and  $\mathcal{E}$  are related by a linear and non-local integral [163]

$$J_{drift}(\mathbf{x}, t) = \int K(\mathbf{x}, t; \mathbf{x}', t') \mathcal{E}(\mathbf{x}', t') d^3 \mathbf{x}' dt' = -nev(\mathbf{x}, t) \quad (2.39)$$

where the rightmost identity comes from charge conservation, such that  $n$  is the free carrier density and  $v$  is the velocity. In the central identity,  $K(\mathbf{x}, t; \mathbf{x}', t')$  is the kernel of the integral, often referred to as the response function. Although kernels are not often a subject of direct study in the terahertz community, integrals of this kind appear often, including the path integral formulation of quantum mechanics (where it is referred to as the propagator) [164], and the mathematical expression of Huygen's principle (Huygen's integral) [165]. The kernel determines the contribution  $\mathcal{E}(\mathbf{x}', t')$  makes to the current density at  $(\mathbf{x}, t)$ . The role of the integral is to sum up the non-local contributions, giving rise to the net current density at the desired coordinates  $(\mathbf{x}, t)$ .

In general, Eq. (2.39) provides little insight as to how it can be used. Under the assumption of translational invariance, the kernel becomes a simpler function of the relative space-time coordinates

$$K = K(\mathbf{x} - \mathbf{x}', t - t').$$

Taking the Fourier transforms of the current density and electric field gives

$$\begin{aligned} \tilde{J}_{drift}(\mathbf{k}, \omega) &= \int J_{drift}(\mathbf{x}, t) \exp(-i\mathbf{k} \cdot \mathbf{x} + i\omega t) d^3 \mathbf{x} dt \\ \tilde{\mathcal{E}}(\mathbf{k}, \omega) &= \int \mathcal{E}(\mathbf{x}, t) \exp(-i\mathbf{k} \cdot \mathbf{x} + i\omega t) d^3 \mathbf{x} dt \end{aligned} \quad (2.40)$$

from which it can be shown that

$$\tilde{J}_{drift}(\mathbf{k}, \omega) = \tilde{\sigma}(\mathbf{k}, \omega) \tilde{\mathcal{E}}(\mathbf{k}, \omega) = -ne\tilde{v}(\mathbf{k}, \omega) \quad (2.41)$$

where

$$\tilde{\sigma}(\mathbf{k}, \omega) = \int K(\mathbf{x}, t) \exp(-i\mathbf{k} \cdot \mathbf{x} + i\omega t) d^3\mathbf{x} dt = -ne \frac{\tilde{v}(\mathbf{k}, \omega)}{\tilde{\mathcal{E}}(\mathbf{k}, \omega)} \quad (2.42)$$

is the Fourier transform of the kernel.

Because of the notational similarity between Eq. (2.41) and the elementary relationship at the very beginning of this section, Eq. (2.41) is referred to as Ohm's law, and  $\tilde{\sigma}$  is the conductivity at wave vector  $\mathbf{k}$  and frequency  $\omega$ . The tilde on  $\tilde{\sigma}$  denotes a complex number (ie,  $\tilde{\sigma} = \sigma_1 + i\sigma_2$ ), which is a notationally compact way to encode the resistive, capacitive and inductive behaviours into the conductivity. Under a weak electric field,  $\Delta\mathbf{k} \approx 0$ , which simplifies Eq. (2.42) to a more common form [163, 166–169]

$$\tilde{\sigma}(\mathbf{k}, \omega) \approx \tilde{\sigma}(\omega) = \int_{-\infty}^{\infty} K(t) \exp(i\omega t) dt = -ne \frac{\tilde{v}(\omega)}{\tilde{\mathcal{E}}(\omega)}. \quad (2.43)$$

The problem of understanding the optical conductivity spectrum can thus be solved in two ways. First, one may directly Fourier transform the local current density  $K(t)$ . Alternatively, one may Fourier transform  $v$ , and so long as  $\tilde{v}(\omega) \propto \tilde{\mathcal{E}}(\omega)$ , the conductivity spectrum will remain independent of the incident field. We will use both approaches in the following section.

## 2.2.2 Conductivity Models

The models in this section achieve the most important aim of time-resolved terahertz spectroscopy: accurately cataloguing the relaxation mechanisms of new materials to enable future optoelectronic technologies. Through the models discussed below, signatures of free carrier dynamics, quasiparticle resonances (plasmons, trions, excitons, biexcitons), diffusive back-action, and percolative resonances will enable discussion of carrier dynamics in cutting edge nanomaterials.

### Drude Model

In the Drude model, charge carriers move freely under the influence of an electric field. Any net motion of charge carriers is damped by collisions that are assumed to isotropically randomize the carrier momentum with an average time between collisions  $\tau$  [167]. The

semiclassical equation of motion for this is given by

$$m^* \frac{dv}{dt} + \frac{m^*}{\tau} v = -e\mathcal{E}(t). \quad (2.44)$$

Fourier transforming both sides gives a solution for  $v$  in the frequency domain,

$$\tilde{v}(\omega) = -\frac{e}{m^*} \frac{\tau}{1 - i\omega\tau} \tilde{\mathcal{E}}(\omega). \quad (2.45)$$

Since

$$\tilde{J}(\omega) = \sigma(\omega) \tilde{\mathcal{E}}(\omega) = -ne\tilde{v}(\omega), \quad (2.46)$$

it is straightforward to show that the Drude conductivity is given by

$$\tilde{\sigma}_D(\omega) = \frac{ne^2\tau}{m^*} \frac{1}{1 - i\omega\tau} = \frac{\sigma_{DC}}{1 + \omega^2\tau^2} + i \frac{\sigma_{DC}\omega\tau}{1 + \omega^2\tau^2}. \quad (2.47)$$

where  $\sigma_{DC} = ne^2\tau/m^* = \epsilon_0\omega_p^2\tau = ne\mu$ ,  $\omega_p$  is the plasma frequency, and  $\mu$  is the mobility.

Performing the inverse Fourier transform of  $\tilde{\sigma}_D$  gives the impulse response function

$$K_D(t) = \frac{ne^2}{m^*} e^{-t/\tau} \Theta(t), \quad (2.48)$$

where  $\Theta(t)$  is the Heaviside step function.

GaAs is a direct gap semiconductor ( $E_g = 1.4$  eV [170]) frequently used as a benchmark because  $\tilde{\sigma}$  is well described by a Drude model with  $\tau = 0.251$  ps [87]. Figure 2.2 (a) shows  $K_D(t)$  for GaAs. In the time-domain, a burst of current occurs at  $t = 0$ , strong enough to invoke a state where electrons shed their phonon dressing [171]. This results in a free current density  $K_D(0) = ne^2/m^*$  that exponentially decays in time according to the momentum relaxation timescale  $\tau$ . Figure 2.2 (b) shows the real and imaginary parts of the Drude conductivity spectrum [87]. The real and imaginary parts crossover at a frequency governed by the collision time scale  $\omega = 1/\tau$ , which, for many semiconductors, falls within the THz spectrum [11, 87, 172].

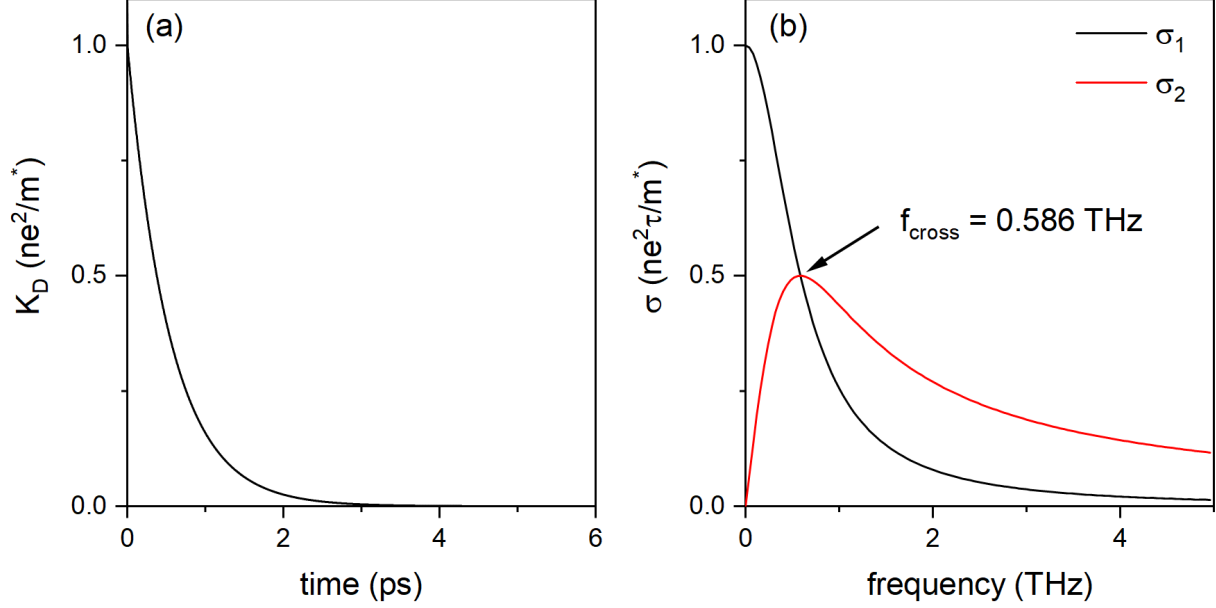


Figure 2.2: Simulated Drude model impulse response and conductivity spectrum of GaAs. (a) Impulse response function.  $K_D(t)$  instantaneously rises at  $t = 0$  and exponentially decays over time with time constant  $\tau$ . (b) Real (black) and imaginary (red) part of the Drude conductivity spectrum. A crossover occurs at  $f_{\text{cross}} = 1/2\pi\tau$ .

## Lorentz Oscillator Model

The Lorentz oscillator encompasses a response that is also isotropically damped by collisions (similar to the Drude model); however, after being driven by an impulse electric field, the local current oscillates. This model follows the equation of motion of a driven-damped harmonic oscillator. Newton's second law gives the equation of motion for an electron in a sinusoidal electric field,

$$m^* \frac{d^2v}{dt^2} + \frac{m^*}{\tau} v + \omega_0^2 m^* x = -e\mathcal{E}(t), \quad (2.49)$$

where  $\tau$  is the damping time constant,  $m^*$  is the effective mass, and  $\omega_0$  is the resonance frequency. Fourier transforming Eq. (2.49) allows us to algebraically solve for the equation of motion in the frequency domain. This gives

$$m^*(-i\omega)\tilde{v}(\omega) + \frac{m^*}{\tau}\tilde{v}(\omega) + \omega_0^2 m^* \frac{\tilde{v}(\omega)}{-i\omega} = -e\tilde{\mathcal{E}}(\omega). \quad (2.50)$$

Therefore,  $\tilde{v}(\omega)$  is

$$\tilde{v}(\omega) = -\frac{e}{m^*} \frac{\omega}{\omega/\tau + i(\omega_0^2 - \omega^2)} \tilde{\mathcal{E}}(\omega). \quad (2.51)$$

Using our definition of the current density,

$$\tilde{J}(\omega) = \sigma(\omega) \tilde{\mathcal{E}}(\omega) = -nev(\omega) \quad (2.52)$$

it is straightforward to show that

$$\tilde{\sigma}(\omega) = \frac{ne^2}{m^*} \frac{\omega}{\omega/\tau + i(\omega_0^2 - \omega^2)}. \quad (2.53)$$

An example of the Lorentz oscillator model can be found in Fig. 2.3. The Lorentz oscillator model was used to quantify surface plasmon resonances in GaAs nanowires, where it was found that the nanowires possess a bulk-like scattering time, and a centre frequency  $\omega_0/2\pi \sim 1$  THz [115]. In Fig. 2.3 (a) we show the impulse response associated with the surface plasmon, and in (b) we show the conductivity spectrum.

## Drude-Smith Model

The Drude-Smith model is a relatively new model that is often used to describe conductivity in disordered systems. In disordered systems it is common to find deviations from the Drude model such as a low-frequency suppression of  $\sigma_1$ , and a transition from positive to negative  $\sigma_2$ . To describe these features, Smith modified the Drude model to encompass the effect of carrier back-scattering [168, 169]. Smith used Poisson statistics to describe the current response function as

$$K_{DS}(t) = \frac{ne^2}{m^*} e^{-t/\tau} \left[ 1 + \sum_{n=1}^{\infty} c_n \left( \frac{t}{\tau} \right)^n \frac{1}{n!} \right], \quad (2.54)$$

where  $c_n$  is the fraction of velocity a carrier retains after the  $n^{\text{th}}$  collision,  $m^*$  is the effective mass, and  $\tau$  is the mean time between scattering events. The Fourier transform of this gives

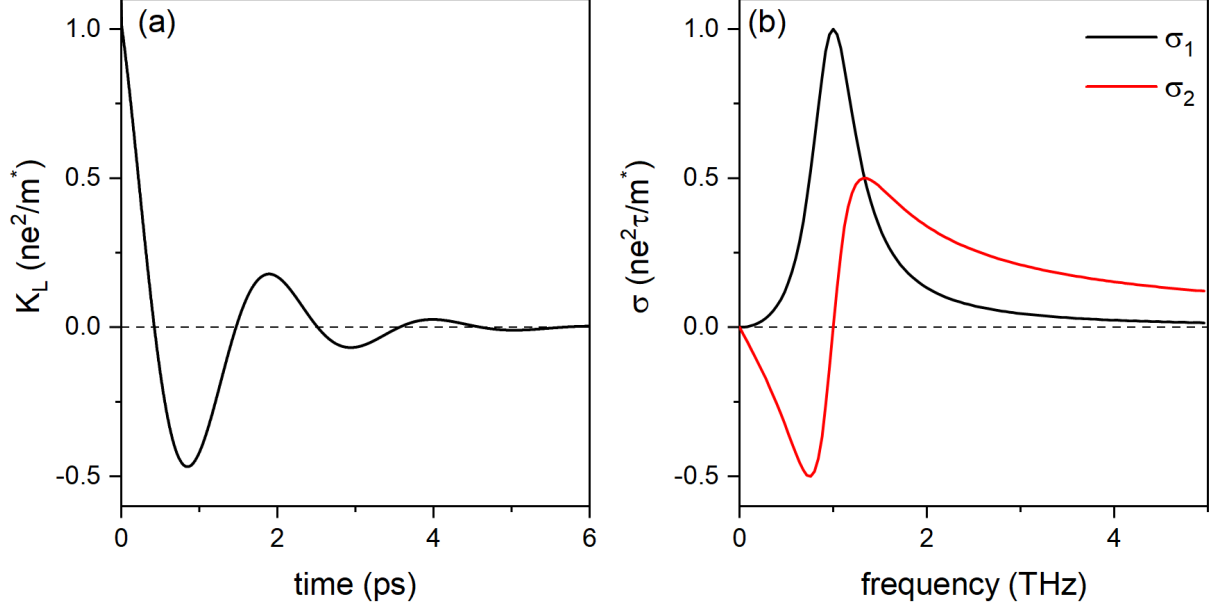


Figure 2.3: Lorentz oscillator model impulse response and conductivity spectrum for GaAs nanowires. (a) Impulse response function.  $K_L(t)$  instantaneously rises at  $t = 0$  and exponentially decays over time with time constant  $\tau$ , oscillating with a frequency  $\omega_0/2\pi = 1$  THz. (b) Real (black) and imaginary (red) part of the conductivity spectrum.  $\sigma_1$  is peaked at  $\omega_0/2\pi = 1$  THz, and the full-width at half-maximum is given by  $1/\tau = 0.543$  THz.

the photoconductivity

$$\tilde{\sigma}(\omega) = \frac{ne^2\tau}{m^*} \frac{1}{1 - i\omega\tau} \left[ 1 + \sum_{n=1}^{\infty} \frac{c_n}{(1 - i\omega\tau)^n} \right]. \quad (2.55)$$

Normally this series is truncated to include only the first order correction, implying that only one scattering event deviates from the typical isotropic scattering that is assumed in the Drude model. Truncating the series and labelling  $c_1$  as  $c$  gives the phenomenological Drude-Smith equation

$$\tilde{\sigma}_{DS}(\omega) = \frac{ne^2\tau}{m^*} \frac{1}{1 - i\omega\tau} \left( 1 + \frac{c}{1 - i\omega\tau} \right). \quad (2.56)$$

The  $c$  parameter is a phenomenological parameter that encompasses the degree of carrier backscattering. When  $c = -1$ , the charge carrier is completely backscattered by the boundary, while in the limit that  $c \rightarrow 0$  we retrieve the Drude model.

It is difficult to make high-quality semiconductor-metal interfaces on the nanoscale, since

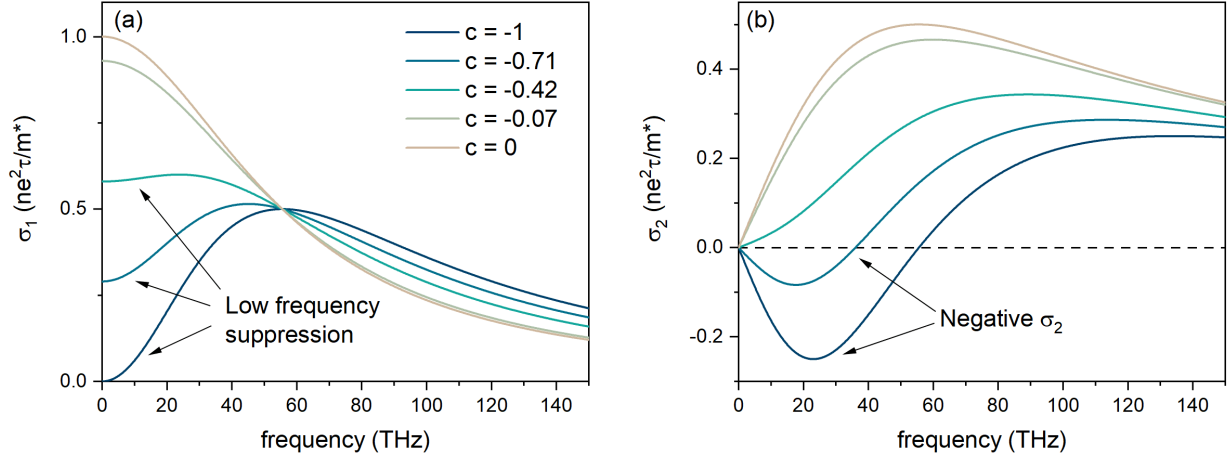


Figure 2.4: Example of Drude-Smith model on gold thin films following the results of Ref. [55], where  $\tau = 0.018$  ps. (a) Low-frequency suppression of the real conductivity. (b) Transition from positive to negative in the imaginary conductivity.

nanogranularity can result in a percolative photoconductivity. The Drude-Smith model was essential in parameterizing a percolation transition gold thin films deposited on silicon [55]. It was found that by increasing the film thickness from 4 nm to 28 nm, a transition to non-percolative dynamics occurred at  $\sim 6$  nm. By  $\sim 9$  nm, the transition was complete, and the thin films behaved as bulk gold films [55]. In Fig. 2.4 we show the transition from bulk carrier dynamics to localized carrier dynamics. In Fig. 2.4 (a) we show the real part of the conductivity ( $\sigma_1$ ), where a suppression of the low frequency conductivity can be seen as  $c \rightarrow -1$ , which stems from THz-driven charge carriers backscattering at nanogranular interfaces [55]. In Fig. 2.4 (b) we show the imaginary part of the conductivity ( $\sigma_2$ ), where a transition from positive to negative is seen as  $c \rightarrow -1$ . The transition arises from a charge-carrier pile-up at the nanogranular interfaces, which results in a capacitive response.

### Modified Drude-Smith Model

Recent criticism of the Drude-Smith model revealed that it insufficiently describes Monte Carlo simulations of free charge-carrier scattering in nanoparticles [173]. Later, Cocker et al. reconciled this issue by showing that diffusive back-action plays a large role in the transient photoconductivity of confined carriers, and results in a photoconductivity that has a form that is nearly identical to the Drude-Smith model [167].

To accommodate the accumulation of charge at the boundary of a square well, the diffu-

sive back-action impulse current  $K_{DB}$  is given by

$$K_{DB}(t) = K_D(t) - a \int_0^t K_{DB}(t') dt', \quad (2.57)$$

where  $K_D$  is the Drude response, and the rightmost term represents the amount of charge accumulated over the time  $t$ .  $a$  is the rate of charge accumulation (also called the diffusion current rate). In general,  $a$  depends on the geometry of the system under study. Cocker et al. found that in a perfectly reflective square well, with a constant carrier density gradient,

$$a = 12D/L^2 = \frac{12}{t_o} \left( \frac{\tau}{t_o + 2\tau} \right), \quad (2.58)$$

where  $L$  is the width of the well,  $D$  is the diffusion constant for the free carrier, and  $t_o = L/v_{th}$ , where  $v_{th}$  is the thermal velocity. An important consequence of this model is that in situations where carrier confinement is evident, the diffusion coefficient takes the form

$$D = \frac{\tau' k_B T}{m^*}, \quad (2.59)$$

where  $\tau'$  is the scattering time that encompasses the momentum relaxation time  $\tau$  and the boundary scattering time  $\tau_{Bound}$ .  $\tau'$  follows Matthiessen's rule, whereby

$$\frac{1}{\tau'} = \frac{1}{\tau} + \frac{1}{\tau_{Bound}}. \quad (2.60)$$

Differentiating both sides of Eq. (2.57) gives

$$\frac{dK_{DB}}{dt} = \frac{dK_D}{dt} - aK_{DB}(t), \quad (2.61)$$

which, after Fourier transform, allows us to algebraically solve for the conductivity spectrum

$$\tilde{\sigma}_{DB}(\omega) = \frac{ne^2\tau'}{m^*} \frac{1}{1 - i\omega\tau'} \left( 1 - \frac{1}{1 - i\omega/a} \right). \quad (2.62)$$

In systems where there is non-perfect reflection at the interface, a phenomenological ansatz

is provided by Cocker et al., where

$$\tilde{\sigma}_{DB}(\omega) = \frac{ne^2\tau'}{m^*} \frac{1}{1 - i\omega\tau'} \left( 1 - \frac{c(R)}{1 - i\omega/a} \right). \quad (2.63)$$

The exact nature of how  $c$  depends on the reflectance  $R$  is an open question, but  $c(R)$  is expected to be less dependent on the box size ( $L$ ) than the Drude-Smith model discussed above [167]. Monte Carlo results further support these conclusions [167].

## Plasmon Model

As we saw in the Drude model, free carriers possess a plasma frequency  $\omega_p$ . The Debye length is the length scale over which a free carrier plasma appears electrically neutral, and so it is common to refer to the free carrier plasma as being quasi-neutral. Upon perturbation, a plasma will restore quasi-neutrality on timescales of  $\sim 1/\omega_p$ . Driving the free carriers at frequencies above the plasma frequency results in the separation of charge that loosely resembles ionization of the quasi-neutral plasma. This ‘ionization’ gives rise to a coherent oscillation of the free carrier plasma which is referred to as a plasmon.

Localized plasmon resonances occur in semiconductor nanomaterials, and can be understood in the framework of the Bergman effective medium theory (EMT). The Bergman EMT is the most general EMT that uses dielectric functions of two materials ( $\tilde{\epsilon}_1$  and  $\tilde{\epsilon}_2$ ) to construct a net dielectric function  $\tilde{\epsilon}_r$ . The net dielectric function can be calculated by summing contributions of percolation and depolarization through

$$\tilde{\epsilon}_r = V_1\tilde{\epsilon}_1 + V_2\tilde{\epsilon}_2 + \int_0^1 \frac{g(L)\tilde{\epsilon}_1\tilde{\epsilon}_2}{L\tilde{\epsilon}_1 + (1-L)\tilde{\epsilon}_2} dL, \quad (2.64)$$

where  $V_i$  is the percolation strength of the  $i^{th}$  medium, and  $g(L)$  is the spectral function that encompasses the contribution of inclusions at a particular depolarization factor  $L$ . Integration is performed over all depolarization factors, encompassing nonpercolative modes of transport [31, 174].

The spectral function can be computed numerically, and in most practical cases the spectral function is sharply peaked near a particular depolarization  $L_0$ , which allows us to

approximate  $g(L) \approx g_0\delta(L - L_0)$  [174]. Under this assumption,  $\tilde{\epsilon}_r$  becomes

$$\tilde{\epsilon}_r \approx V_1\tilde{\epsilon}_1 + V_2\tilde{\epsilon}_2 + \frac{g_0\tilde{\epsilon}_1\tilde{\epsilon}_2}{L_0\tilde{\epsilon}_1 + (1 - L_0)\tilde{\epsilon}_2}. \quad (2.65)$$

The transient permittivity is then given by the difference between photoexcited and unphotoexcited permittivities. In the photoexcited state we assume that only medium  $\epsilon_2$  is excited, and so one can make the substitution  $\tilde{\epsilon}_2 \rightarrow \tilde{\epsilon}_2 + \Delta\tilde{\epsilon}_2$ . This gives a net relative permittivity of [174]

$$\begin{aligned} \Delta\tilde{\epsilon} &= \tilde{\epsilon}_{phot} - \tilde{\epsilon}_r \\ &= V_2\Delta\tilde{\epsilon}_2 + \frac{g_0\tilde{\epsilon}_1(\tilde{\epsilon}_2 + \Delta\tilde{\epsilon}_2)}{L_0\tilde{\epsilon}_1 + (1 - L)(\tilde{\epsilon}_2 + \Delta\tilde{\epsilon}_2)} - \frac{g_0\tilde{\epsilon}_1\tilde{\epsilon}_2}{L_0\tilde{\epsilon}_1 + (1 - L)\tilde{\epsilon}_2} \\ &= \Delta\tilde{\epsilon}_2 \left[ V_2 + \frac{B}{1 + D\Delta\tilde{\epsilon}_2} \right] \end{aligned} \quad (2.66)$$

where,

$$B = \frac{L\tilde{\epsilon}_1^2 g_0}{[(1 - L)\tilde{\epsilon}_2 + L\tilde{\epsilon}_1]^2}, \quad (2.67)$$

and<sup>‡</sup>

$$D = \frac{1 - L}{(1 - L)\tilde{\epsilon}_2 + L\tilde{\epsilon}_1}. \quad (2.68)$$

The differential photoconductivity ( $\Delta\tilde{\sigma}$ ) is found by noting that  $\Delta\tilde{\epsilon} = i\Delta\tilde{\sigma}/\epsilon_0\omega$ , so that the transient differential photoconductivity is given by

$$\Delta\tilde{\sigma}(\omega) = \Delta\tilde{\sigma}_2 \left[ V + \frac{B}{1 + iD\Delta\tilde{\sigma}_2/\epsilon_0\omega} \right], \quad (2.69)$$

where  $V_2 = V$ . This is referred to as the VBD formula [31], and  $V$ ,  $B$ , and  $D$  are treated as fit parameters.

So far we have not given a functional form to  $\Delta\tilde{\sigma}_2$ . For nanomaterials it is often convenient to assume that the microscopic conductivity is given by the Drude model described above. We can get a feel for how the model behaves by substituting Eq. (2.47) into  $\Delta\tilde{\sigma}_2$ . Substituting

---

<sup>‡</sup>Not to be confused with the diffusion coefficient.

directly we find

$$\Delta\tilde{\sigma}(\omega) = \left( V\omega_p^2\epsilon_0\tau \frac{1}{1-i\omega\tau} \right) + \left( \frac{B\omega_p^2\epsilon_0\tau/(1-i\omega\tau)}{1+iD\frac{\omega_p^2\epsilon_0\tau}{\omega\epsilon_0} \frac{1}{1-i\omega\tau}} \right). \quad (2.70)$$

Factoring out  $\tau/\omega$  and  $1/(1-i\omega\tau)$ , and substituting  $\omega_p^2 = ne^2/\epsilon_0m^*$ , we can rewrite Eq. (2.70) as

$$\Delta\tilde{\sigma}(\omega) = \underbrace{\left( V\frac{ne^2\tau}{m^*} \frac{1}{1-i\omega\tau} \right)}_{\text{Drude}} + \underbrace{\left( \frac{Bne^2}{m^*} \frac{\omega}{\omega/\tau + i[D\omega_p^2 - \omega^2]} \right)}_{\text{Lorentz}}. \quad (2.71)$$

We can see that this definition neatly separates into one term that follows a Drude-like conductivity and another that follows a Lorentz oscillator [cf. Eq. (2.53)]. The width of the resonance is characterized by  $1/\tau$ , while the resonance frequency is given by  $\omega_{res} = \sqrt{D\omega_p^2}$ . The resonance frequency thus follows a  $\omega_{res} \propto \sqrt{n}$  dependence that can be experimentally verified by recording the resonance at various photoexcitation densities.

It is interesting that the Drude term is modified by percolation, while the Lorentz term sees modification from depolarization. The first observation comes from the fact that only medium  $\tilde{\epsilon}_2$  was photoexcited, and so the free carrier percolation is only relevant for  $\tilde{\epsilon}_2$ . Depolarization results from interactions between  $\tilde{\epsilon}_1$  and the free carriers in  $\tilde{\epsilon}_2$ , and so both host mediums make an appearance in the depolarization factors  $B$  and  $D$  defined above.

## Bruggeman Effective Medium Theory

The Bruggeman effective medium theory has found use in describing the photoconductivity of heterogenous materials in situations where the fill fraction ( $f$ ) is large [31, 55, 175]. The dielectric function of a heterogenous medium  $\epsilon_{eff}$  can be found by solving

$$f \frac{\epsilon_{loc} - \epsilon_{eff}}{\epsilon_{loc} + \epsilon_{eff}} + (1-f) \frac{\epsilon_{host} - \epsilon_{eff}}{\epsilon_{host} + \kappa\epsilon_{eff}} = 0 \quad (2.72)$$

where  $\kappa \approx 1$  is related to the depolarization factor,  $\epsilon_{host} \approx 1$  is the dielectric function of the host medium when the material is immersed in vacuum,  $\epsilon_{loc}$  is the dielectric function of the particulates immersed in the host medium. As in the plasmon model,  $\epsilon_{loc}$  is assumed to follow a Drude model according to Eq. (2.47).  $\epsilon_{loc}$  can then be found by noting that

$$\epsilon_{loc} = 1 + i\tilde{\sigma}/\epsilon_0\omega.$$

## Disordered Metals

In disordered metals, the conductivity is discussed in terms of empirical power laws that are applicable near metal-insulator phase transitions. The power law changes depending on the amount of disorder. For all types of disorder, the high-frequency roll-off for  $\sigma_1$  is always of the form

$$\sigma_1(\omega) \propto \frac{1}{\omega^2}, \quad (2.73)$$

because the charge carriers are expected to experience Drude-like transport at high frequencies. Under weak disorder  $\sigma_1$  follows the power law

$$\sigma_1(\omega) \propto A\omega^\alpha + B, \quad (2.74)$$

where  $A$  and  $B$  are constants, and the power  $\alpha$  is a constant that depends on the strength of the electron-electron interaction [176]. Under conditions of weak disorder, the system retains a finite  $\sigma_1(0)$  parameterized by  $B$ . At the metal-insulator transition  $\sigma_1$  follows a similar power law

$$\sigma_1(\omega) \propto A\omega^\alpha, \quad (2.75)$$

where  $\sigma_1$  converges on 0 as  $\omega \rightarrow 0$ . On the insulator side of the metal-insulator transition,  $\sigma_1$  follows

$$\sigma_1(\omega) \propto A\omega^\alpha - B, \quad (2.76)$$

and even more localized electrons in the insulating phase follow the relation

$$\sigma_1(\omega) \propto \omega^\beta \ln\left(\frac{1}{\omega}\right), \quad (2.77)$$

where  $\beta$  depends on the strength of the electron-electron interaction [176].

### 2.2.3 Diffusion

Diffusion is a non-equilibrium process that arises from a nonuniform distribution of charge carriers. A diffusive current is formed opposite to the gradient of the distribution following

Fick's first law (flux-gradient relation) [177],

$$J_{diff} = -eD^* \frac{\partial n(x, t)}{\partial x}, \quad (2.78)$$

where  $D^*$  is the ambipolar diffusion coefficient

$$D^* = \frac{2D_e D_h}{D_e + D_h}, \quad (2.79)$$

and  $D_e$  and  $D_h$  are the electron and hole diffusivities, respectively [162]. The diffusion coefficient of the  $i^{th}$  species ( $i = e, h$ ) is related to the mobility ( $\mu_i = e\tau_i/m_i^*$ ) through the Einstein relation

$$D_i = \mu_i k_B T / e, \quad (2.80)$$

where  $T$  is the temperature and  $k_B$  is the Boltzmann constant.

Earlier in section 2.1.5 the continuity equation was introduced. The continuity equation for charge carriers expresses the balance of the temporal change in the charge per volume element [178]. Alternatively, the continuity equation expresses the fact that the change in number of carriers within a region is entirely determined by the rate of carriers flowing into and out of the region [14]. Consider an infinitesimal diffusive current density  $dJ_{diff}$ . The current density will be proportional to the infinitesimal density of charge  $dn$ , and the velocity of carriers  $dx/dt$  [177], such that

$$dJ_{diff} = -dn e \frac{dx}{dt}. \quad (2.81)$$

Rearranging Eq. (2.81) and making use of Eq. (2.78) yields the diffusion equation (Fick's second law, local diffusion equation)

$$e \frac{\partial n(x, t)}{\partial t} = -eD^* \frac{\partial^2 n(x, t)}{\partial x^2}. \quad (2.82)$$

Solutions of the diffusion equation can be achieved using some basic assumptions. Since the diffusion is driven by the scattering of free carriers, the relaxation timescale is the scattering time  $\tau$ . Over  $\tau$ , the carrier density  $n$  will have a  $1/e$  fall of of  $\ell_D$ . Assuming that the

carrier density has the form

$$n \propto e^{-x/\ell_D} e^{-t/\tau}, \quad (2.83)$$

and inserting this solution into Eq. (2.82) yields a relationship between  $\ell_D$  and  $\tau$

$$\ell_D = \sqrt{D^* \tau}. \quad (2.84)$$

The diffusion length ( $\ell_D$ ) is a measure of the distance it takes for the density to relax back to its equilibrium value [14]. This is important for nanomaterials, where  $L_D \sim 10 \text{ nm}$ <sup>§</sup>, since carriers may be driven by an electric field into a boundary. If a large amount of carriers are localized to the boundary, then a diffusive back current will occur as explained by the Modified Drude-Smith model (Section 2.2.2). Under an alternating electric field, the appreciable timescale becomes the period of oscillation. This led to a commonly used estimate for an alternating field is

$$\ell_D = \sqrt{\frac{D^*}{\omega}} \quad (2.85)$$

which was discussed in Chapter 1 (Eq. (1.1)) [71, 167]. To characterize the expansion of the carrier distribution, one can compute the average width of  $n(x, t)$  at each time step [179]. The width of  $n(x, t)$  is then

$$L_{ave}(t) = \frac{\int_0^L n(x, t) |x| dx}{\int_0^L n(x, t) dx}. \quad (2.86)$$

Intrinsic GaAs has an electron mobility of  $\sim 3300 \text{ cm}^2/\text{Vs}$  and a hole mobility of  $\sim 400 \text{ cm}^2/\text{Vs}$  at room temperature [180]. The ambipolar diffusion coefficient at room temperature is then  $D_{GaAs}^* \approx 18.46 \text{ cm}^2/\text{s}$ . In section 2.2.2 we noted that  $\tau = 0.2716 \text{ ps}$  [180], which gives

$$L_D = 22.39 \text{ nm}. \quad (2.87)$$

Solving Eq. (2.82) on a  $1.5 \text{ }\mu\text{m}$  domain with perfectly reflecting boundaries (see Appendix A), no recombination, and an initial carrier distribution of  $n(0, 0) = 1$ , yields the behavior shown in Fig. 2.5 (a). The red, blue, and green curves are the distribution at 0.5 ps, 5

---

<sup>§</sup>Estimating  $\tau \sim 0.1 \text{ ps}$ , and  $D^* \sim 10 \text{ cm}^2/\text{s}$ .

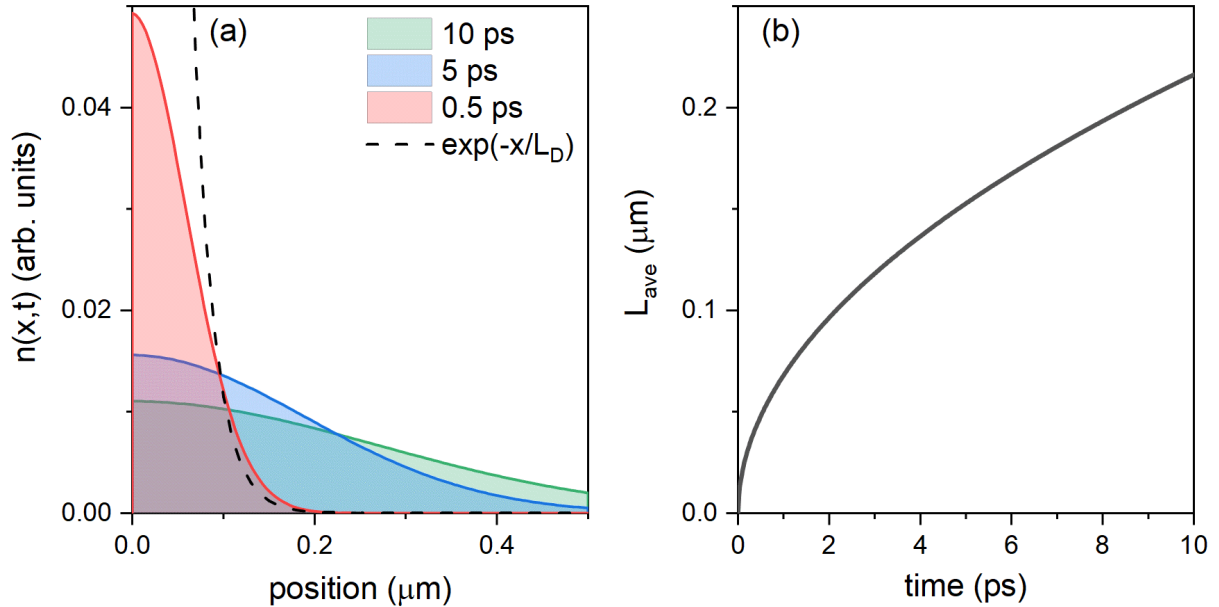


Figure 2.5: Diffusion simulation for GaAs. (a) Carrier distribution at 0.5 ps (red), 5 ps (blue), and 10 ps (green). The exponential profile of  $\exp(-x/L_D)$  is shown as the black dashed line. (b) Expansion of the distribution into the bulk as time increases. The width of the distribution is computed at each time step using Eq. (2.86).

ps, and 10ps. Initially the distribution changes quickly, and over time the expansion slows down. By  $\sim 0.5$  ps the carrier distribution has already expanded to  $\sim 0.5 \mu\text{m}$ , and the growth slows down rapidly afterwards. This is seen in the calculations of  $L_{ave}$  shown in Fig. 2.5 (b), where it follows the behavior  $L_{ave} \sim \sqrt{t}$ .

## 2.3 Summary

In summary, this chapter has introduced the fundamentals of ultrafast carrier dynamics in semiconductors. We began with a semiclassical description of absorption at a semiconductor interface, followed by a discussion of relaxation, cooling dynamics, recombination, and luminescence. The drift and diffusion currents were discussed as a consequence of the quasi-equilibrium of the photoexcited state, and microscopic models of conductivity were described.

# Chapter 3

## Terahertz Spectroscopy

### 3.1 Terahertz Pulses

#### 3.1.1 Generation via Optical Rectification

Here, we outline the important physics that underpins the generation of phase stable picosecond bursts of electromagnetic radiation (THz pulses). Terahertz pulses are a form of electromagnetic radiation, and according to Maxwell's wave equation, they can be created by either a transient current or a transient polarization. These options can be seen in the variety of sources that are available. Inspired by Hertz's original experiments with dipole radiation, photoconductive antennas rely on a transient current density to generate THz radiation [94, 181]. Techniques such as optical rectification are rooted in transient polarizations of atomic bonds and breaking of symmetry [95]. Two-color plasma sources even combine the two techniques to produce THz radiation through four-wave mixing inside a laser produced plasma [97, 182, 183]. In this thesis THz radiation is generated through optical rectification in a ZnTe crystal, as demonstrated by Rice et al. in 1994 [95], and will hence be the focus of this section.

It is common to start a discussion of optical rectification with the standard tensor formalism [95, 99, 184–186], and here we take a less abstract approach by considering how light interacts with electrons in a Zn-Te bond. In ZnTe the electron cloud is distributed primarily around the Te atoms because Te has a larger electronegativity than Zn (2.10 and 1.65 respectively [187]). Intuitively this results in an asymmetric potential energy landscape

in ZnTe [188], and hence the motion of an electron driven by a light wave will be described by a nonlinear equation of motion. In particular, due to the asymmetric tilt in the energy landscape, an electron driven by an oscillating electric field will spend more (less) time in areas where the potential is shallower (steeper) than a perfectly parabolic potential. The asymmetry in the electron motion introduces low frequency components to the light emitted from the crystal. The high frequency light is then filtered, and the low frequency (THz) radiation is used for spectroscopy. This section aims to cover this process in more detail, following a classical approach.

Shining an ultrafast laser pulse onto ZnTe greatly perturbs the electron distribution from equilibrium. To first order the energy landscape is parabolic, however when the incident electric fields are strong enough to drive the electrons far from equilibrium anharmonic terms are needed. Consider the case of an electron being driven by a Gaussian optical pulse where the electric field is given by

$$\mathcal{E}_{opt} = \mathcal{E}_0 \cos(\omega t) e^{-\xi t^2} \quad (3.1)$$

with the field amplitude  $\mathcal{E}_0$ , angular frequency  $\omega$ , and the  $1/e^2$  pulse duration is related to  $\xi$  through  $\tau_{1/e^2} = \sqrt{2/\xi}$ . We can describe the microscopic dynamics classically by solving for the motion of an electron along the Zn-Te bonds ( $x(t)$ ) via

$$\frac{d^2x}{dt^2} + 2\gamma \frac{dx}{dt} + \omega_0^2 x + ax^2 = -\frac{e}{m} \mathcal{E}_{opt}(t), \quad (3.2)$$

where  $\gamma$  is the dipole damping rate,  $\omega_0$  is the natural frequency of the potential, and  $a$  characterizes the degree of nonlinearity. The nonparabolic nature of the potential can be found by observing that the restoring force in this system is given by

$$F_{res} = -m\omega_0^2 x - max^2 \quad (3.3)$$

such that the potential energy is given by

$$U_{res} = -\int F_{res} dx = \frac{1}{2}m\omega_0^2 x^2 + \frac{1}{3}max^3. \quad (3.4)$$

For optical rectification to occur the material must be *non-centrosymmetric*, which indicates that there must be odd powers of  $x$  in Eq. 3.4 because even powers do not break spatial symmetry. As we discussed above, this is indeed the case for ZnTe crystals since the potential is shifted towards the Te atoms.

From Maxwell's wave equation for light propagation in a non-magnetic dielectric medium it is known that the motion of bound currents generates electromagnetic radiation. Assuming no free currents are present, Maxwell's wave equation in 1-D is given by

$$\frac{\partial^2 \mathcal{E}}{\partial x^2} - \epsilon_0 \mu_0 \frac{\partial^2 \mathcal{E}}{\partial t^2} = \mu_0 \frac{\partial^2 P}{\partial t^2}, \quad (3.5)$$

where  $P$  is the polarization,  $\mathcal{E}$  is the incident electric field,  $\mu_0$  is the permeability of free space and  $\epsilon_0$  is the permittivity of free space. The right hand side of Eq. (3.5) contains the source term, which, under the assumptions above, only depends on  $P$ . We now connect this to Eq. (3.2) by noting that the net polarization of a medium is given by

$$P = \sum_i e x_i(t), \quad (3.6)$$

where  $i$  denotes an individual Zn-Te bond. Therefore, by analyzing a single Zn-Te bond under a classical approximation, the profile of electromagnetic radiation generated through optical rectification will be given by

$$\mathcal{E}_{THz} \propto \frac{\partial^2 x_i}{\partial t^2}. \quad (3.7)$$

Figure 3.1 shows a numerical simulation of THz generation via optical rectification, and the simulation parameters are given in Table 3.1. The values in Table 3.1 are not chosen arbitrarily in this example. In Fig. 3.1 (a) we show the slight non-centrosymmetric nature of the potential well. Under the strong electric field of  $\mathcal{E}_{opt}$ , the bound electrons are driven high into the well, which results in an asymmetric trajectory for the electron in the ZnTe bond. This can be seen in Fig. 3.1 (b), where nonlinearity of  $x(t)$  appears at the peak field of  $\mathcal{E}_{opt}$ . Taking the second derivative of  $x(t)$  results in the green curve in Fig. 3.1 (b), where the difficulty of viewing the rectified motion can be explained. Consider the motion of an

$m$	$\omega$	$\omega_0$	$\gamma$	$q$	$\mathcal{E}_0$	$\tau_{1/e^2}$
( $m_e$ )	(THz)	(THz)	(THz)	( $10^{-19}\text{C}$ )	(MV/cm)	(ps)
1	$100\pi$	5	1.5	-1.6	1	0.5

Table 3.1: Parameters used in the THz generation simulation shown in Fig. 3.1.

electron that contains two frequencies, one that oscillates at frequency  $\omega_1 = 1 \times 2\pi$  THz, and the other oscillates at frequency  $\omega_2 = 50 \times 2\pi$  THz. The total displacement will have the form  $x(t) = A \sin(\omega_1 t) + B \sin(\omega_2 t)$ , where  $A$  and  $B$  are constants. Differentiating this twice shows that  $d^2x/dt^2 = -A\omega_1^2 \sin(\omega_1 t) - B\omega_2^2 \sin(\omega_2 t)$ . Therefore, even under circumstances where  $A$  and  $B$  are equal, we find that the high-frequency term contains the largest amplitude, which, for the simulation shown here, is larger by a factor of  $50^2 = 2500$ .

After Fourier transforming to the frequency domain in Fig. 3.1 (c), we find that there are two significant peaks in the amplitude spectrum.  $\mathcal{E}_{opt}$  is seen at the driving frequency, while closer to zero frequency there is a peak that corresponds to the THz pulse. Isolating these components and inverting the Fourier transform allows us to separate  $\mathcal{E}_{opt}$  and  $\mathcal{E}_{THz}$ , as shown in Fig. 3.1 (d), where we find a distinct THz pulse that looks similar to routine measurements.

There are important consequences that arise from generating THz radiation via optical rectification. First, the emitted pulse is phase-stable, meaning that the pulses emitted via optical rectification have identical phases with respect to the carrier envelope. Phase stability guarantees the shot-to-shot repeatability that is necessary for detecting of THz through electro-optic sampling.

Second, from Eq.(3.6) we can see that summing over all of the ZnTe bonds gives rise to the net polarization response of the crystal. As such, the profile of the THz radiation depends on the number of bonds in the crystal, or alternatively, the crystal thickness. Given the incredible number of bonds in a material of macroscopic size ( $\sim 10^{21}\text{mm}^{-3}$  [187]), the total field can be represented as an integral over the length of the crystal. Under ideal circumstances the THz radiation travels at the same speed as the optical pulse, where it can be shown that the strength of the generated field is directly proportional to the thickness of the nonlinear crystal [99].

In practise, the optical and THz refractive indices do not match. In situations where the

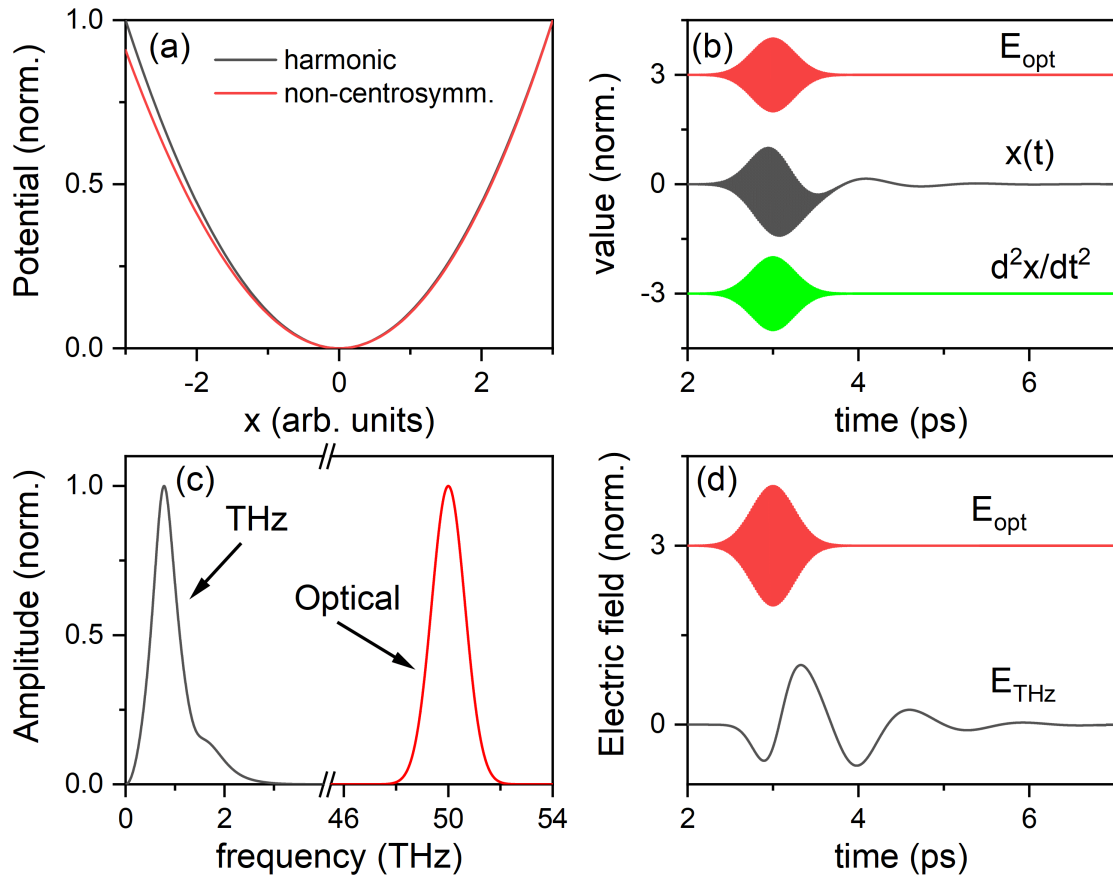


Figure 3.1: Simulation of THz generation via optical rectification. (a) Anharmonic (red) potential compared to just the harmonic component (black). (b) Optical driving field (red), electron position  $x$  (black), and  $d^2x/dt^2$  (green). (c) Normalized amplitude spectrum of  $d^2x/dt^2$  with terahertz spectrum in black and the optical spectrum in red. (d) Waveforms extracted by isolating the individual pulses and inverting the Fourier transform.

optical index is smaller than the THz index the optical pulse leads the THz pulse generation, and so each  $x_i$  in Eq. (3.6) is shifted in phase relative to one another. The interference of between each  $x_i$  thus accumulates over the length of the crystal and may result in destruction of the field amplitudes. The walk-off length ( $\ell_w$ ) is the distance over which one pulse duration  $\tau_p$  of phase is accumulated. Therefore two THz pulses generated with a separation of  $\ell_w$  will destructively interfere.  $\ell_w$  is thus given by [99]

$$\ell_w = \frac{c\tau_p}{n_{THz} - n_0}. \quad (3.8)$$

where  $n_{THz}$  is the THz index and  $n_0$  is the optical index.

Alternatively, the coherence length defines the distance over which the carrier wave of the optical pulse accumulates a  $\pi/2$  phase relative to the THz pulse, and is directly related to the degree of velocity matching in a crystal. Writing the pulse duration in terms of the THz bandwidth via the uncertainty principle ( $\tau_p \rightarrow 1/2\nu_{THz}$ ) and substituting  $n_0$  with the optical group index  $n_{gr}$  transforms the walk-off length into the coherence length  $\ell_c$  such that

$$\ell_c = \frac{c}{2\nu_{THz}|n_{gr} - n_{THz}|}. \quad (3.9)$$

It is clear that  $\ell_c$  of ZnTe has a pole where the optical group index matches the THz refractive index, hinting that a certain combination of THz and optical wavelengths can theoretically yield an infinite coherence length. Using the dispersion relations from Ref. [185] the optical group index ( $n_{gr}(\lambda)$ ) and THz index ( $n_{THz}(\nu_{THz})$ ) are shown for ZnTe in Fig. 3.2. At an optical wavelength of  $\sim 812.2$  nm and a THz frequency of 1.68 THz, index matching occurs with the common index of 3.216. Given that modern Ti:sapphire lasers can easily generate intense optical pulses that satisfy index matching requirements, optical rectification in ZnTe has remained one of the most common ways to generate THz radiation for nearly 30 years.

Nonlinearity and coherence are important aspects of terahertz generation, and so too is the orientation of the nonlinear crystal. Figure 3.3 (a) shows the arrangement of Zn and Te atoms when viewed along the [110] direction with the [001] direction pointing upwards. The Zn (Te) atoms are denoted by red (blue) circles. One might expect that light polarized parallel to [001] will generate THz radiation since the lightwave could drive a polarization

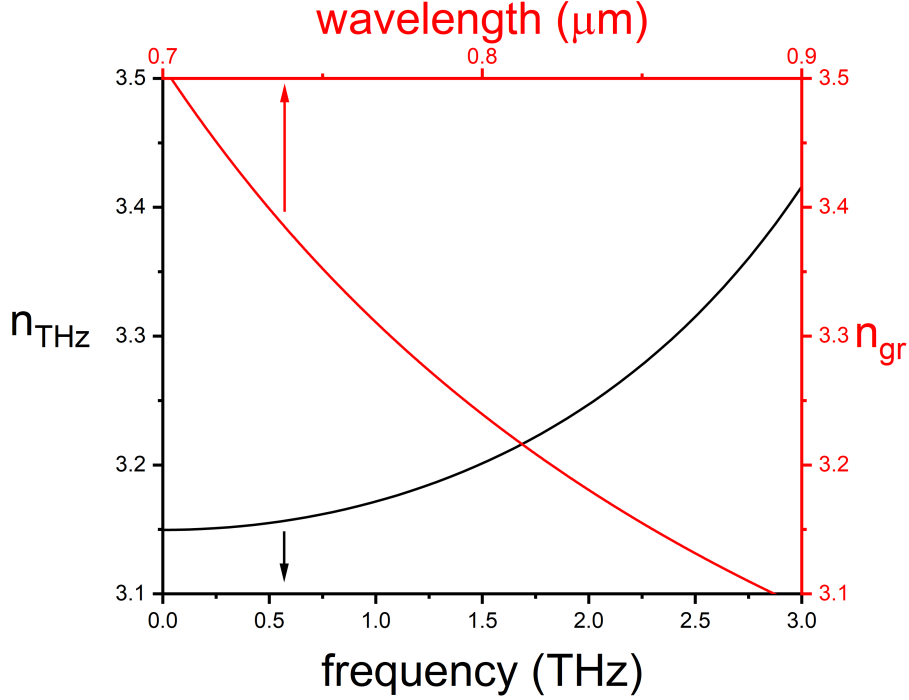


Figure 3.2: Optical group index ( $n_{gr}$ , red) and THz refractive index ( $n_{THz}$ , black) for ZnTe crystal.

along the Zn-Te bonds parallel to this axis, however this is not the case because inversion symmetry is not broken. Still looking down  $[110]$  we can rotate the crystal in Fig. 3.3 (a) until the  $[\bar{1}11]$  axis is pointing upwards. This brings us to the orientation shown in Fig. 3.3 (b) where inversion symmetry is broken, and hence optical rectification will occur. THz generation is maximized along this axis, which is correlated with the fact that the polarization of the lightwave is pointing directly along the Zn-Te bond, maximizing the coupling between the optical field and the electron motion.

### 3.1.2 Detection via Electro-Optic Sampling

Electro-optic sampling (EOS) is a process pioneered by Zhang and Wu [186] in 1995 that allows us to measure the transient electric field of a THz pulse  $\mathcal{E}_{THz}(\Delta t_{EOS})$ . In electro-optic sampling, an electric field is repeatedly sampled by an optical pulse, and forms the backbone of the sections that follow. EOS is similar to stroboscopic imaging of crankshaft rotation. The period of revolution is fixed by the geometry of the system, and by synchronously flashing the crankshaft with short bursts of light, you can repeatedly capture one instant of

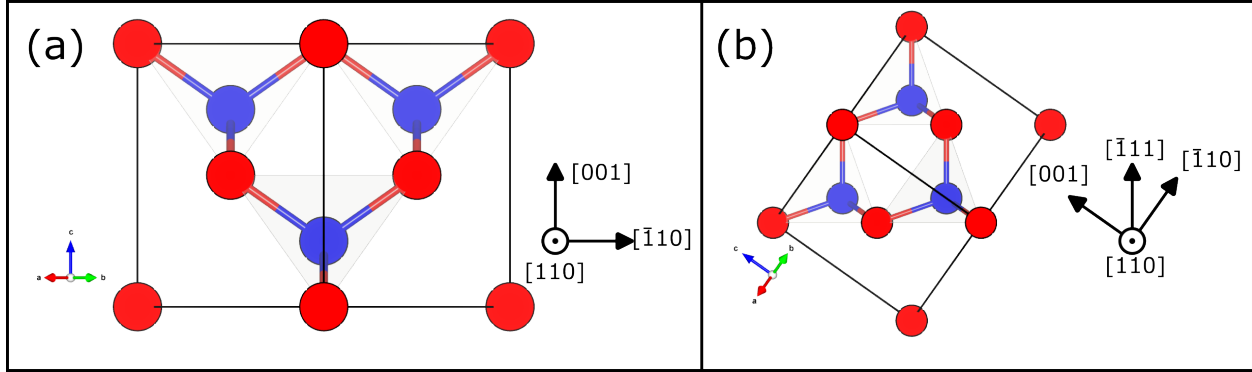


Figure 3.3: Orientations of the ZnTe crystal. Zinc atoms are given by blue spheres, and Te atoms are red. The primitive vectors of the x,y, and z direction are given by the orientation of a,b, and c, respectively. (a) Looking into the [110] direction with the [001] direction pointing upwards. Along this axis the crystal is centrosymmetric. (b) Rotating the crystal in (a) such that the  $[\bar{1}11]$  axis is pointing upwards we see that the inversion symmetry is broken making this the optimal direction for THz generation. The *Vesta 3* software package was used to generate these crystallographic images [189]. ZnTe crystallographic data can be retrieved from the Springer Materials and Phases Data System [190].

the rotation [191]. Changing the phase between the flash and the crankshaft allows you to image other moments of the rotation. Recording many of these images allows you to make a movie of the crankshaft rotation, which would otherwise be impossible with a video camera.

The stroboscopic technique hinges on two important features. First, the rotation must be reproducible, with a well defined period. This is the reason that phase-stability was an important criteria for THz generation. Second, the flash must be much shorter than the period of rotation. The process of electro-optic sampling consists essentially of using a 100 fs, 800 nm flash of light to record one instant of a THz pulse. Due to the phase stability of optical rectification and the precisely defined laser repetition rate, THz pulses are nearly identical, which satisfies the need for repeatability. Since a THz pulse lasts on the order of  $\sim 2$  ps, and the optical sampling pulse is smaller by a factor of  $\sim 20$ , the flash is clearly shorter than the period of oscillation, and hence the criteria for a stroboscopic technique are satisfied. EOS can thus be summarized by repetition of the following steps: (1) sampling one instant of a THz electric with an optical pulse and (2) changing the relative phase of the optical pulse. The process of sampling a picosecond electric field is the primary focus of this section, since changing the relative phase of the optical pulse is done by introducing a gold retroreflector mounted on a motorized delay stage. To describe the sampling process

we will take the less conventional, but more intuitive, approach of building upon an optical element referred to as a Pockels Cell.

A Pockels cell consists of two crossed polarizers with an electro-optic crystal between them. The intensity of light transmitted through two linear polarizers with angle  $\theta$  between their transmission axes will follow Malus' law

$$I_{out} = I_{in} \cos^2(\theta), \quad (3.10)$$

where  $I_{in}$  is the incoming intensity and  $I_{out}$  is the outgoing intensity. In a Pockels cell  $\theta$  is fixed to  $\pi/2$ , and the electro-optic crystal that resides between the polarizers introduces an additional phase  $\phi$  such that the relationship between incoming and outgoing intensity is given by

$$I_{out} = I_{in} \cos^2\left(\frac{\pi}{2} + \frac{\phi}{2}\right) = I_{in} \sin^2\left(\frac{\phi}{2}\right). \quad (3.11)$$

The phase  $\phi$  consists of contributions from the intrinsic and extrinsic birefringence of the chosen electro-optic crystal. The intrinsic phase comes from internal stresses that accumulate during the growth of the electro-optic crystal, and owing to advances in crystal growth techniques this contribution is negligible. The largest contribution to the phase is the extrinsic term. The Pockel's effect is a second order nonlinear polarization phenomena that determines the phase induced by an externally applied electric field [99]. The externally induced phase accumulated by travelling through an electro-optic crystal is given by [99, 184]\*

$$\phi = \frac{2\pi d n_0^3 r_{41}}{\lambda} \mathcal{E}_{ext}, \quad (3.12)$$

where  $d$  is the crystal thickness,  $n_0$  is the index of refraction for the modulated light,  $\lambda$  is the wavelength of the modulated light,  $\mathcal{E}_{ext}$  is the magnitude of the external electric field,  $r_{41}$  is the electro-optic coefficient and  $c$  is the speed of light in vacuum. Therefore, by applying an electric field to the electro-optic crystal in a Pockels cell we may control the intensity of light that exits. Inversely, we can measure the intensity of light exiting a Pockels cell and infer the square of the external electric field using Eq. (3.11). This inference is the core of

---

\*The electro-optic coefficient that appears in this relation depends strongly on the conditions upon which symmetry is broken. See Nonlinear Optics by R. W. Boyd for further details [184].

how electro-optic sampling is performed on the electric field of THz pulses.

In electro-optic sampling we aim to measure a quantity that is directly proportional to the external electric field. To this end, a quarter waveplate is inserted before the final polarizer which adds an additional  $\pi/4$  to the phase. The output intensity now has the form

$$I_{out} = I_{in} \cos^2\left(\frac{3\pi}{4} + \frac{\phi}{2}\right) \approx I_{in} \left(\frac{1}{2} + \frac{\phi}{2}\right). \quad (3.13)$$

where the rightmost approximation is the first order Taylor series. To first order, Eq. (3.13) is linear in  $\phi$ , but does not discriminate a positive field from a negative field. In order to retrieve the polarity of the applied field a Wollaston prism replaces the exit polarizer (Fig. 3.4). A Wollaston prism separates the vertical ( $I_A$ ) and horizontal ( $I_B$ ) polarizations of the incident light. It can be shown that the externally applied field is thus given by [99]

$$\mathcal{E}_{ext} = \frac{I_A - I_B}{I_A + I_B} \frac{\lambda}{2\pi dn_0^3 r_{41}} \quad (3.14)$$

which is not subject to the  $I_{in}/2$  offset in Eq. (3.13), and thus retains the polarity of  $\mathcal{E}_{ext}$ .

The electro-optic sampling system of the Ultrafast Spectroscopy Laboratory is built on the principles outlined above. Inspired by the pioneering work of Nahata et al. [185], Wu et al. [192], and Winnewisser et al. [193], the EOS system uses 800 nm pulses to sample the instantaneous electric field of THz pulses using a ZnTe crystal, as shown in Fig. 3.4. The intensity of the vertical and horizontal components of the elliptically polarized 800 nm pulse ( $I_A$  and  $I_B$ ) are recorded using silicon photodiodes. The difference in the photodiode output voltage pulses are then measured using a Stanford Research Systems SR-830 Lock-In Amplifier, where a signal-to-noise ratio (SNR) of  $>1000$  is achieved. This allows us to precisely measure the instantaneous THz electric field  $\mathcal{E}_{THz}$  through

$$\mathcal{E}_{THz}(\Delta t_{EOS}) \propto \frac{I_A - I_B}{I_A + I_B}, \quad (3.15)$$

where  $\Delta t_{EOS}$  is the relative delay between the THz pulse and the 800 nm electro-optic sampling pulse. Repeating this measurement for a series of delays allows us to construct the temporal profile of many identical THz pulses, which provides the phase and amplitude in-

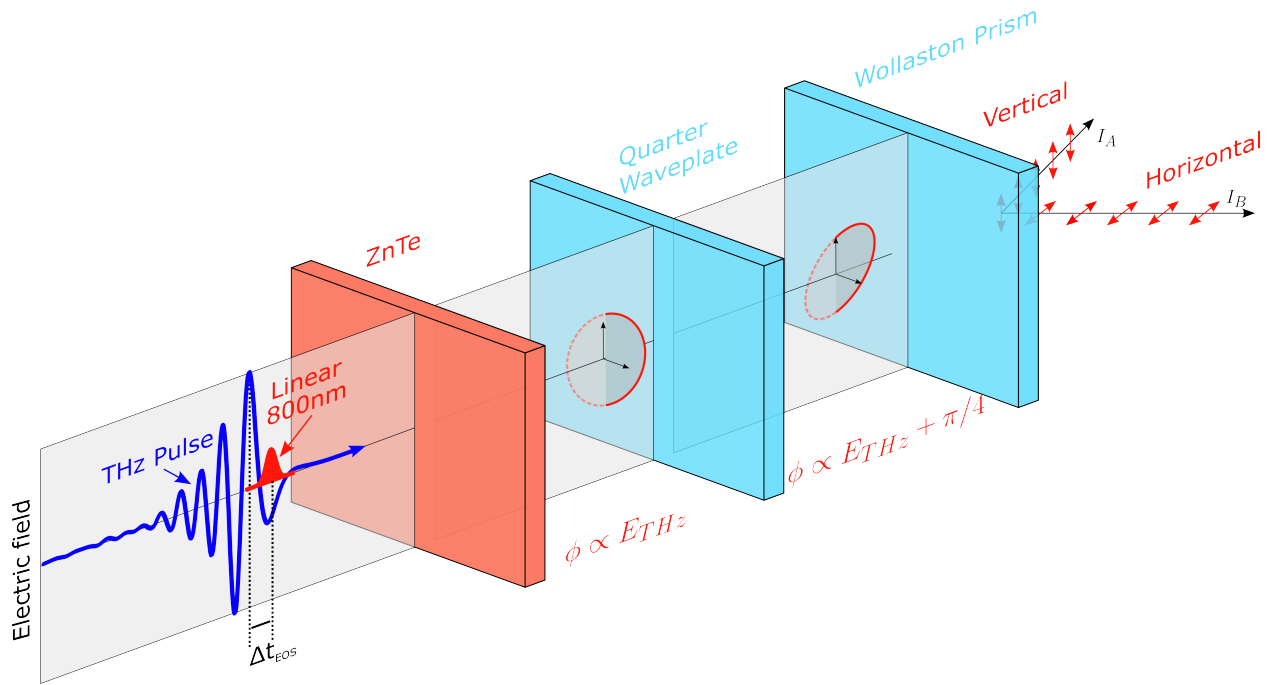


Figure 3.4: Schematic of electro-optic sampling. A THz pulse (blue) and 100 fs, 800 nm sampling pulse (red) arrive at a ZnTe crystal with relative delay  $\Delta t_{EOS}$ . The THz pulse modulates the index of refraction in the ZnTe crystal, inducing an ellipticity to the 800 nm laser pulse. The quarter waveplate ensures that the sign of the electric field is retained by introducing a phase of  $\pi/4$ . A Wollaston prism separates the horizontal and vertical components of the 800 nm laser pulse, which are used to quantify  $\mathcal{E}_{THz}(\Delta t_{EOS})$ .

$r_{41}$	$d$	$\lambda$	$n_0$
(pmV <sup>-1</sup> )	(mm)	(nm)	
4	1	800	2.85

Table 3.2: Parameters of the electro-optic sampling system in the Ultrafast Spectroscopy Laboratory for a 1 mm thick ZnTe crystal electro-optic sampling setup [99].

formation that is crucial to performing time-resolved THz spectroscopy. Table (3.2) provides the constants used to calibrate the electric field in this thesis, and more details about the Lock-In amplification are given in Appendix B.

## 3.2 Terahertz Time-Domain Spectroscopy

THz time-domain spectroscopy (THz-TDS) is an all-optical approach to measuring the equilibrium conductivity spectrum ( $\tilde{\sigma}(\omega)$ ). First used in 1989 by Grischkowsky et al. to measure the absorption modes of water vapour [8], THz time-domain spectroscopy (THz-TDS) was quickly applied to a host of insulators and semiconductors that stand as benchmarks of the field today [172].

THz-TDS retrieves the complex index of refraction by comparing a THz pulse propagating through free space  $\mathcal{E}_{ref}(t)$  to a THz pulse that has transmitted through the material of interest  $\mathcal{E}_{samp}(t)$ , as shown in Fig. 3.5. Fourier transforming these waveforms provides access to a broad range of frequencies ( $\sim 0.5 - 2.5$  THz) that can be used for spectroscopy. Under Fourier transformation  $\mathcal{E}_{ref}(t) \rightarrow \tilde{\mathcal{E}}_{ref}(\omega)$  and  $\mathcal{E}_{samp}(t) \rightarrow \tilde{\mathcal{E}}_{samp}(\omega)$ , so that the net transmission  $\tilde{T}(\omega)$  is given by the ratio

$$\tilde{T}(\omega) = \frac{\tilde{\mathcal{E}}_{samp}(\omega)}{\tilde{\mathcal{E}}_{ref}(\omega)}. \quad (3.16)$$

Since  $\tilde{\mathcal{E}}_{samp}(\omega)$  passed through the sample, it can be written as

$$\tilde{\mathcal{E}}_{samp} = \tilde{t}_{12}\tilde{t}_{23}e^{i(\tilde{n}_2-1)\frac{\omega d}{c}}\tilde{\mathcal{E}}_{ref}, \quad (3.17)$$

as shown in Fig. 3.5.  $\tilde{t}_{ij}$  are the Fresnel transmission coefficient of each interface, given by

$$\tilde{t}_{ij} = 2\tilde{n}_i/(\tilde{n}_i + \tilde{n}_j). \quad (3.18)$$

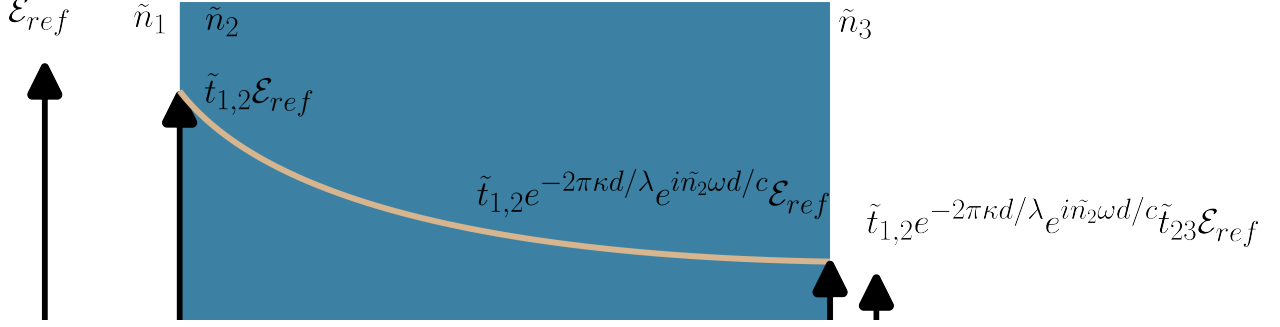


Figure 3.5: Diagram of the THz-TDS geometry. The arrows represent electric field strength.  $\tilde{\mathcal{E}}_{ref}(\omega)$  is incident onto the first face of the sample, and as the field passes through the material it is modified by the complex Fresnel transmission coefficients at the interfaces.

The complex exponential in Eq. (3.17) expresses the attenuation and phase shift of the electromagnetic wave caused by transmission through the semiconductor bulk, and naturally depends on the sample thickness  $d$ , and complex index of refraction  $\tilde{n}_2 = n_2 + i\kappa_2$ . Equation (3.16) can be written as

$$\tilde{T} = \tilde{t}_{12}\tilde{t}_{23}e^{i(\tilde{n}_2-1)\omega d/c}, \quad (3.19)$$

which can be simplified by assuming vacuum on either side of the semiconductor (where  $n = 1$ ), and so

$$\tilde{T}(\omega) = \frac{4\tilde{n}_2}{(1 + \tilde{n}_2)^2} e^{i(\tilde{n}_2-1)\frac{\omega d}{c}}. \quad (3.20)$$

Equation (3.20) can be split into the magnitude  $|T(\omega)|$  and phase  $\phi(\omega)$  components, which yields a set of coupled nonlinear equations

$$|T(\omega)| = \frac{4\sqrt{n_2^2 + \kappa_2^2}}{(n_2 + 1)^2 + \kappa_2^2} e^{-\kappa_2 \frac{\omega d}{c}} \quad (3.21)$$

and

$$\phi(\omega) = (n_2 - 1)\frac{\omega d}{c} + \tan^{-1} \left( \frac{\kappa_2^2(n_2^2 + \kappa_2^2 - 1)}{n_2(n_2 + 1)^2 + \kappa_2^2(n_2 + 2)} \right) \quad (3.22)$$

that must be solved numerically. Equations (3.21) and (3.22) can be decoupled when the absorption is weak ( $\kappa_2 \approx 0$ ). When  $\kappa_2 \approx 0$ , the  $\tan^{-1}$  term in Eq. (3.22) vanishes, and so

$$n_2(\omega) \approx 1 + \frac{c}{\omega d} \phi(\omega). \quad (3.23)$$

Expanding the exponential on the right hand side of Eq (3.21) to  $\mathcal{O}(1)$  in  $\kappa_2$ , and noting that  $\kappa_2^2 \approx 0$  gives the imaginary part of the complex index of refraction via

$$\kappa_2(\omega) = \frac{c}{\omega d} \left( 1 - \frac{|T(\omega)|(n_2(\omega) + 1)^2}{4n_2(\omega)} \right). \quad (3.24)$$

Finally, the complex index of refraction is connected to the equilibrium conductivity  $\tilde{\sigma}_{eq}$  through

$$\tilde{n}_2(\omega) = \sqrt{\tilde{\epsilon}(\omega)} = \sqrt{1 + i \frac{\tilde{\sigma}_{eq}(\omega)}{\epsilon_0 \omega}}, \quad (3.25)$$

which provides direct access to the equilibrium conductivity spectrum.

An example of THz-TDS follows, where a  $(1.03 \pm 0.01)$  mm thick crystal of intrinsic silicon is used as a sample. Figure 3.6 contains each step of the analysis, starting with the reference ( $\mathcal{E}_{ref}$ ) and sample ( $\mathcal{E}_{samp}$ ) waveforms in Fig. 3.6 (a). The amplitudes of  $\tilde{\mathcal{E}}_{ref}$  and  $\tilde{\mathcal{E}}_{samp}$  are shown in Fig. 3.6 (b) where we can clearly see the majority of the bandwidth lies in the region of  $\sim 0.5 - 2.5$  THz. From  $\tilde{\mathcal{E}}_{ref}$  and  $\tilde{\mathcal{E}}_{samp}$  we can then calculate the complex transmission function  $\tilde{T}$ . The amplitude and phase of  $\tilde{T}$  are shown in Figs. 3.6 (c) and (d), respectively. Equations (3.21) and (3.22) are then solved numerically for each frequency, producing the measured  $n$  and  $\kappa$  shown in Fig. 3.6 (e). Finally, using Eq. (3.25) it is possible to then extract other optical parameters such as the dielectric function (shown in Fig. 3.6 (f)) and the equilibrium conductivity (not shown).

The complex index can be modelled by a simple Drude model. In this model, the free-carrier dynamics arise from the intrinsic population of free carriers. Fitting  $\tilde{\epsilon}$  to a Drude model results in the parameters given in Table 3.3. The real index of  $n \sim 3.415$  agrees very well with the results of Grischkowsky et al., where they found  $n \sim 3.419$ [172]. The discrepancy can easily be explained by our ability to determine the crystal thickness, which has a direct impact on the extracted index of refraction (cf. Eq. 3.23)<sup>†</sup>.

### 3.3 Time-Resolved Terahertz Spectroscopy

Time-resolved Terahertz Spectroscopy (TRTS) is a technique used to measure the conductivity of a material mere picoseconds after photoexcitation. Excitation is performed using

---

<sup>†</sup>If  $n = 1 - c/\omega d$ , then the uncertainty is given by  $\delta(n) = c\delta(d)/\omega d^2 \approx 0.001$  for a frequency of 0.5 THz.

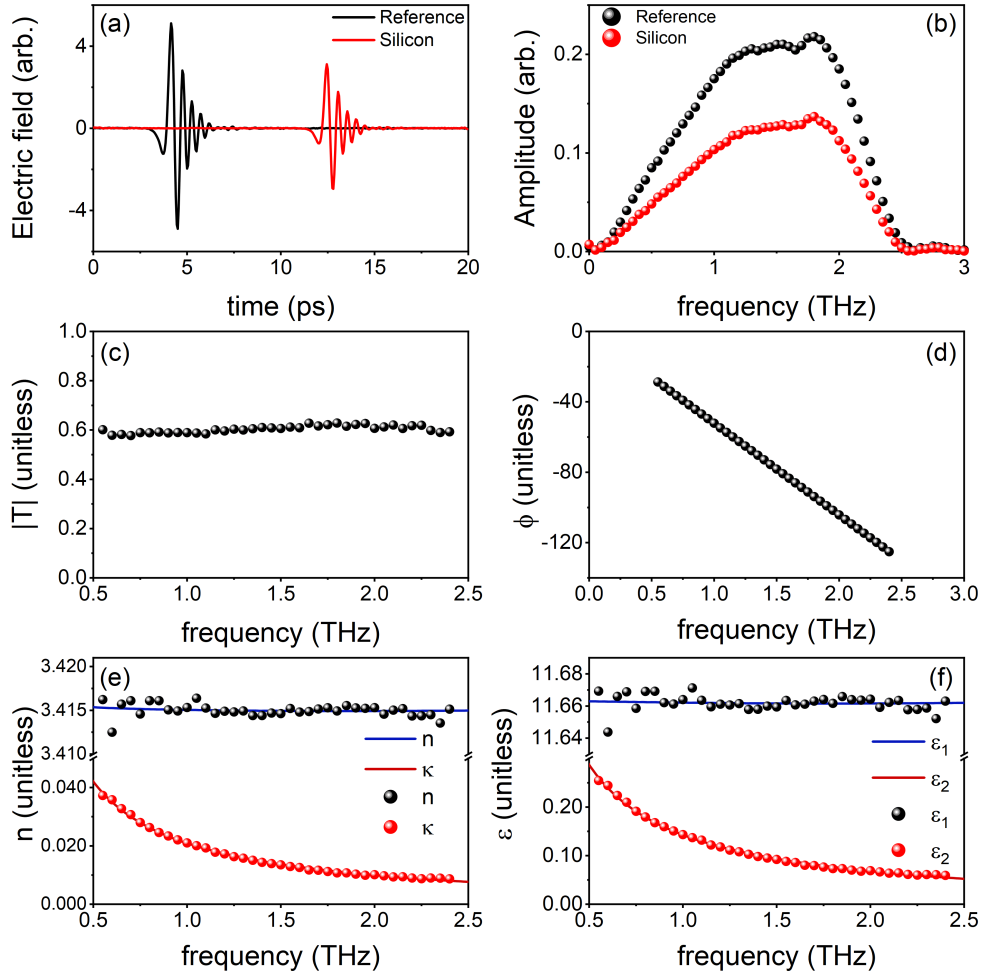


Figure 3.6: THz-TDS on intrinsic silicon. (a) Reference (black) and sample (red) waveforms. (b) Amplitude spectrum of the reference (black) and sample (red) waveforms. (c) Transmission spectrum and (d) unwrapped phase spectrum. (e) Complex index of refraction found by numerically solving Eq. (3.21) and Eq. (3.22). (f) Complex dielectric function computed using Eq. (3.25).

$n_e$ ( $10^{14} \text{ cm}^{-3}$ )	$\tau_e$ (ps)	$\epsilon(\infty)$	$\sigma_{DC}$ ( $\Omega^{-1} \text{ cm}^{-1}$ )
$5 \pm 1$	$0.040 \pm 0.006$	$11.675 \pm 0.002$	$0.031 \pm 0.005$

Table 3.3: Drude fit parameters from THz-TDS of intrinsic silicon crystal.

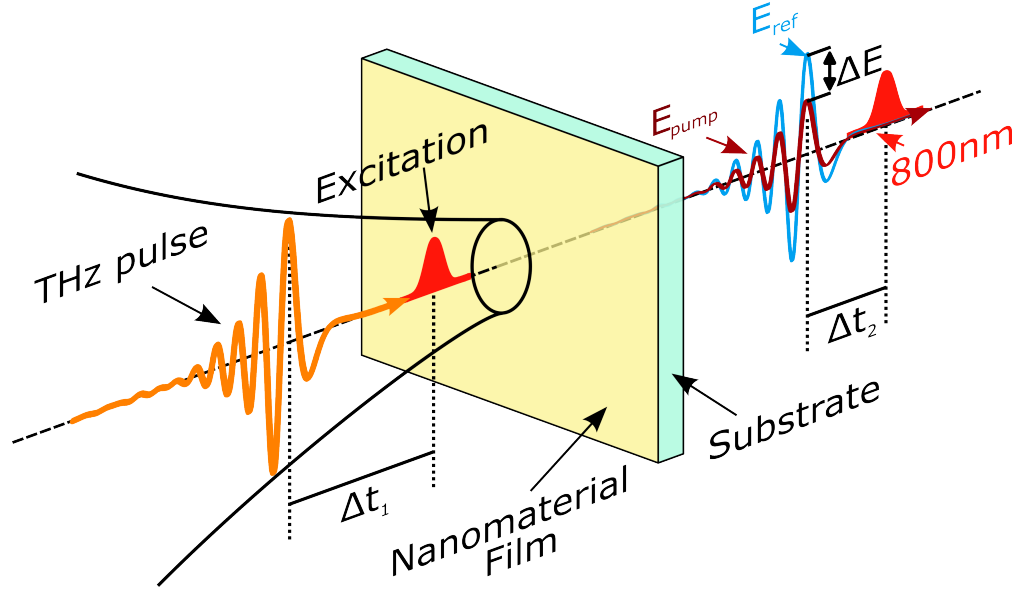


Figure 3.7: Schematic of TRTS experiment.

100 fs laser pulses, and the wavelength is chosen based on the band gap of the material under study. After photoexcitation, a wide variety of processes including carrier-carrier scattering, phonon scattering, electron-hole recombination, localization, intervalley scattering, and quasi-particle formation occur before the sample returns to equilibrium. Studies containing time-resolved terahertz spectroscopy thus aim to document these processes, providing fundamental insight for future electronic and optoelectronic applications.

The process of TRTS is captured by the schematic given in Fig. 3.7. A femtosecond excitation pulse (red) arrives at the nanomaterial film creating a large population of photoexcited charge carriers. At time  $\Delta t_1$  after photoexcitation, a THz pulse (orange) is incident onto the sample. Through free carrier screening, the amplitude of the incident THz is attenuated, forming  $\tilde{\mathcal{E}}_{pump}$  (burgandy).  $\tilde{\mathcal{E}}_{pump}$  is measured through electro-optic sampling at controlled intervals  $\Delta t_2$ . Using two optical choppers and Lock-in amplification (details in Appendix B),  $\tilde{\mathcal{E}}_{ref}$  (blue) and  $\tilde{\mathcal{E}}_{pump}$  are acquired simultaneously<sup>‡</sup>.

$\tilde{\mathcal{E}}_{pump}$  can be written as a product of the pump-induced Fresnel transmission coefficient

<sup>‡</sup>Simultaneous implies that  $\tilde{\mathcal{E}}_{ref}$  and  $\tilde{\mathcal{E}}_{pump}$  are measured milliseconds apart, as opposed to the  $\sim 5$  min. timescale of alternative methods.

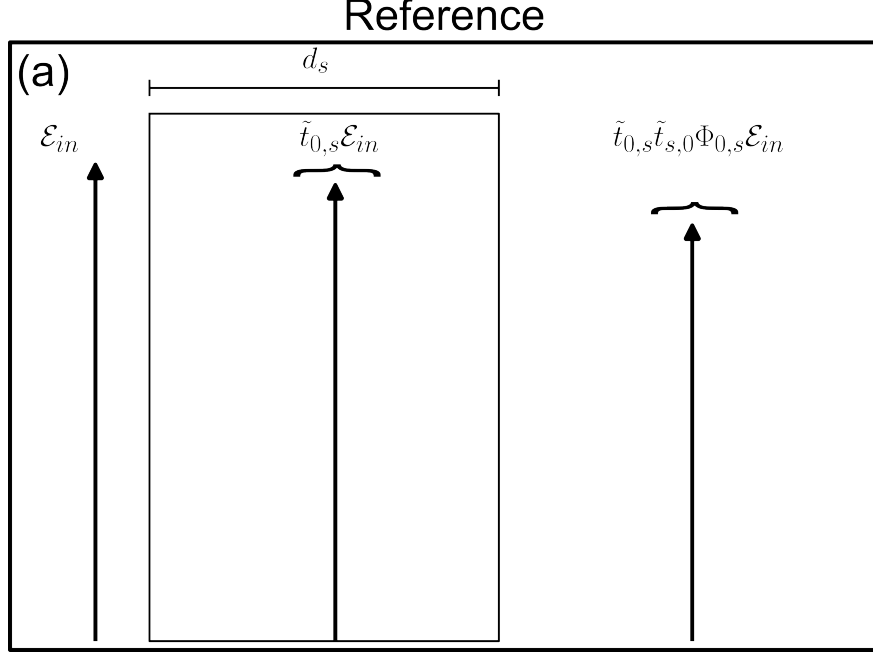


Figure 3.8: Schematic of reference transmission in TRTS experiment. The arrows indicate electric field strength. The reference electric field is incident on the left of the figure. It then transmits through the sample,

$(\tilde{t}_{pump})$  and the reference field  $\tilde{\mathcal{E}}_{ref}$

$$\tilde{\mathcal{E}}_{pump} = \tilde{t}_{pump} \tilde{\mathcal{E}}_{ref}. \quad (3.26)$$

Note that in a TRTS experiment the reference waveform  $\tilde{\mathcal{E}}_{ref}$  has already passed through the unexcited film, whereas in THz-TDS the reference waveform is the incident field  $\tilde{\mathcal{E}}_{in}$ . The reference spectrum is given by

$$\tilde{\mathcal{E}}_{ref} = \tilde{t}_{0,s} \tilde{t}_{s,0} \Phi_{s,0} \tilde{\mathcal{E}}_{in}, \quad (3.27)$$

where  $\Phi_{s,0} = \exp(i\omega d_s (\tilde{n}_s)/c)$ ,  $\tilde{n}_s$  is the substrate index,  $d_s$  is the substrate thickness,  $\tilde{t}_{0,s} = 2/(1 + \tilde{n}_s)$  is the Fresnel transmission coefficient at the vacuum-substrate interface, and  $\tilde{t}_{s,0} = 2\tilde{n}_s/(1 + \tilde{n}_s)$  is the Fresnel transmission coefficient at the substrate-vacuum interface, as shown in Fig. 3.8. A list of symbols can be found at the end of this section in table 3.4.

When the sample is photoexcited, a small  $\sim 100$  nm conducting film exists on top of the substrate as shown in 3.9. The field transmitted through the pumped sample  $\tilde{\mathcal{E}}_{pump}$  is given

by

$$\tilde{\mathcal{E}}_{pump} = \tilde{t}_{0,f} \tilde{t}_{f,s} \tilde{t}_{s,0} \Phi_{f,s} \Phi_{0,f} FP_{f,s} \tilde{\mathcal{E}}_{in}, \quad (3.28)$$

where  $\tilde{t}_{0,f} = 2/(1 + \tilde{n}_f)$  is the Fresnel transmission coefficient at the vacuum-film interface,  $\tilde{n}_f$  is the film index of refraction,  $\tilde{t}_{f,s} = 2\tilde{n}_f/(\tilde{n}_f + \tilde{n}_s)$  is the Fresnel transmission coefficient for the film-substrate interface,  $\Phi_{0,f} = \exp(i\omega d_f(\tilde{n}_f)/c)$  is the phase induced by the film, and  $\Phi_{f,s} = \exp(i\omega(d_s - d_f)(\tilde{n}_s)/c)$  is the phase induced by the remainder of the substrate.  $FP_{f,s}$  accommodates the thin-film interference that arises from reflections within the thin film.  $FP_{f,s}$  is given by

$$FP_{f,s} = \sum_{j=1}^{\infty} \left( r_{f,s} r_{f,0} \exp\left(\frac{2i\omega d_f \tilde{n}_f}{c}\right) \right)^j = \frac{1}{1 - r_{f,s} r_{f,0} \exp\left(\frac{2i\omega d_f \tilde{n}_f}{c}\right)}, \quad (3.29)$$

where  $r_{f,s} = (\tilde{n}_f - \tilde{n}_s)/(\tilde{n}_f + \tilde{n}_s)$  is the Fresnel reflection coefficient for the film-substrate interface, and  $r_{f,0} = (\tilde{n}_f - 1)/(\tilde{n}_f + 1)$  is the Fresnel reflection coefficient for the film-vacuum interface.

Substituting Eq. (3.27), (3.28), and (3.29) into Eq. (3.26) gives [32, 71, 74, 194, 195]

$$\tilde{t}_{pump} = \frac{\tilde{\mathcal{E}}_{pump}}{\tilde{\mathcal{E}}_{ref}} = \frac{2\tilde{n}_f[1 + \tilde{n}_s] \exp\left(i\left(\frac{\omega d_f \tilde{n}_f}{c} + \frac{\omega(d_s - d_f)\tilde{n}_s}{c} - \frac{\omega d_s \tilde{n}_s}{c}\right)\right)}{[\tilde{n}_f + \tilde{n}_s][\tilde{n}_f + 1] - [\tilde{n}_f - \tilde{n}_s][\tilde{n}_f - 1] \exp\left(\frac{2i\omega d_f \tilde{n}_f}{c}\right)}. \quad (3.30)$$

Equation (3.30) provides us with a recipe for extracting the optical properties of the photoexcited film index  $\tilde{n}_f$  on the condition that a measurement of  $\tilde{t}_{pump}$  is acquired. Equation (3.30) can, in general, be numerically inverted if the substrate index is known [32]. However, in the limit of a weakly absorbing thin-film, the complex exponentials can be approximated by their first-order Taylor series, yielding the remarkably simple analytic result [71, 74, 157, 195, 196]

$$\tilde{t}_{pump} = \frac{\tilde{n}_s + 1}{\tilde{n}_s + 1 + Z_0 \tilde{\sigma} d_f}, \quad (3.31)$$

where  $\tilde{\sigma}$  is the conductivity of the photoexcited film and  $Z_0 = 1/c\epsilon_0$  is the impedance of free space. More detail on the expansions needed to arrive at Eq. (3.31) can be found in Refs. [74, 195]. Interestingly, Eq. (3.31) could have been easily deduced on the assumption

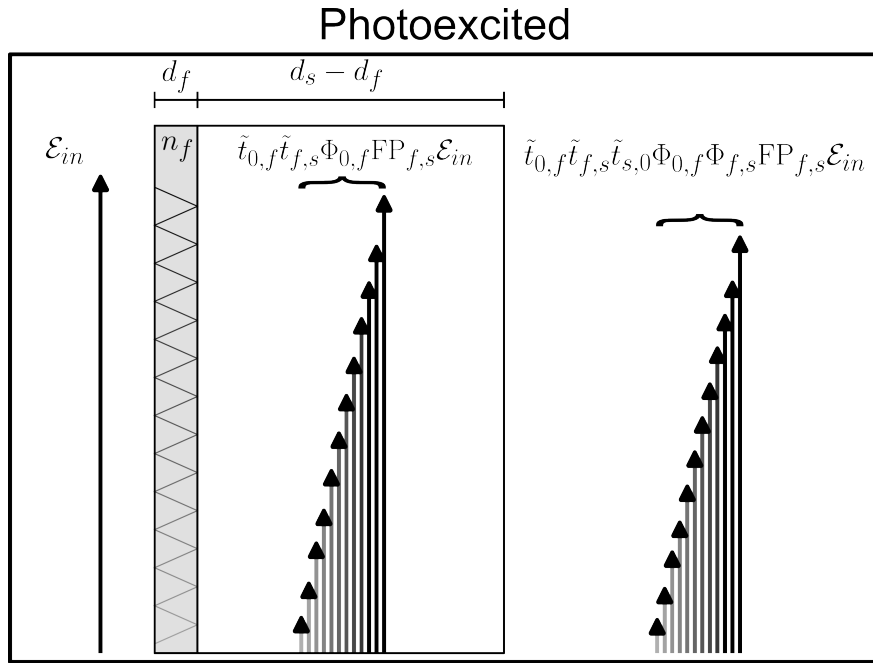


Figure 3.9: Schematic of pump-induced transmission in TRTS experiment. The vertical arrows indicate electric field strength. The reference electric field is incident on the left of the sample. The electric field first enters the photoexcited film. The multiple reflections inside the photoconducting film are denoted by the zig-zag lines, and their corresponding field strengths are also shown with supplementary arrows.

Symbol	Defintion
$\tilde{n}_s$	Substrate refractive index
$\tilde{n}_f$	Photoexcited film refractive index
$\Phi_{s,0}$	Substrate induced phase shift
$\Phi_{f,s}$	Film-Substrate induced phase shift
$\Phi_{0,f}$	Film induced phase shift
$\text{FP}_{f,s}$	Fabry-Perot reflection term
$\tilde{t}_{0,f}$	Fresnel transmission from vacuum into film
$\tilde{t}_{f,s}$	Fresnel transmission from film into substrate
$\tilde{t}_{s,0}$	Fresnel transmission from substrate into vacuum
$\tilde{t}_{0,s}$	Fresnel transmission from vacuum into substrate

Table 3.4: Symbols and definitions in TRTS experiment.

that only the transmission at the vacuum-film interface is modified by photoexcitation. This gives  $t_{0,f} \sim 2/(\tilde{n}_s + 1 + Z_o \tilde{\sigma} d_f)$ , from which Eq. (3.31) easily follows. Rearranging Eq. (3.31), we arrive at an expression of the photoconductivity

$$\tilde{\sigma} = \frac{\tilde{n}_s + 1}{Z_o d} \left( \frac{1}{\tilde{t}_{pump}} - 1 \right). \quad (3.32)$$

### Photoconductivity Dynamics

Measurement of photoconductivity dynamics is performed by electro-optically sampling the peak of  $\mathcal{E}_{ref}$  (i.e.  $\Delta t_2 = 0$ ).  $\Delta t_1$  is then varied using an optical delay stage, and using the technique in Appendix B.2.4,  $\Delta \mathcal{E} = \mathcal{E}_{pump} - \mathcal{E}_{ref}$  is recorded. From Eq. (3.32) it is possible to measure the photoconductivity dynamics by expanding  $\frac{1}{\tilde{t}_{pump}}$  into a power series<sup>§</sup>. This gives

$$\tilde{\sigma}(\Delta t_1) \propto \left( \frac{1}{\tilde{t}_{pump}} - 1 \right) \approx -\frac{\Delta \mathcal{E}(\Delta t_1)}{\mathcal{E}_{ref}(\Delta t_1)}, \quad (3.33)$$

which allows direct measurement of the photoconductivity dynamics, provided that the modulation follows  $\Delta \mathcal{E}/\mathcal{E}_{ref} \lesssim 0.2$ . When  $\Delta \mathcal{E}/\mathcal{E}_{ref} \gtrsim 0.2$ , the error in this technique can exceed  $\sim 5\%$ , resulting in a poor approximation of the photoconductivity dynamics [157, 197].

---

<sup>§</sup>  $\frac{1}{x} \approx 1 - (x - 1) + \mathcal{O}(x^2)$

## Photoconductivity Spectroscopy

Many signatures of charge-carrier dynamics in nanomaterials can be found by investigating the complex conductivity spectrum. To gain access to the photoconductivity spectrum, the pump-probe delay ( $\Delta t_1$ ) is fixed. The reference ( $\mathcal{E}_{ref}$ ) and pump ( $\mathcal{E}_{pump}$ ) waveforms are then recorded for the specified pump-probe delay.

Once the reference and pump waveforms are recorded, they may be Fourier transformed to yield the complex amplitude spectra  $\tilde{\mathcal{E}}_{ref}(\omega)$  and  $\tilde{\mathcal{E}}_{pump}(\omega)$ , respectively. These complex amplitude spectra can then be inserted into Eq. (3.32) in order to extract the real and imaginary parts of the photoconductivity spectrum via

$$\tilde{\sigma}(\omega) = \sigma_1(\omega) + i\sigma_2(\omega) = \frac{n_s + 1}{Z_0 d} \left( \frac{\tilde{\mathcal{E}}_{ref}(\omega)}{\tilde{\mathcal{E}}_{pump}(\omega)} - 1 \right). \quad (3.34)$$

### Bulk germanium

Germanium is an indirect-gap semiconductor with a mobility of  $\sim 3000 \text{ cm}^2/\text{Vs}$ . In Fig. 3.10, we demonstrate an example of TRTS being applied to study a bulk germanium crystal. The germanium studied here was photoexcited with 400 nm pulses at a fluence of  $F = 6 \text{ } \mu\text{J}/\text{cm}^2$ . The penetration depth and reflection coefficient of Ge at 400 nm are  $\delta = 14 \text{ nm}$  and  $R = 0.47135$ , respectively [198]. From this, we estimate the photoexcited charge-carrier density as

$$n = \frac{(1 - R)F}{\delta} = 4.457 \times 10^{18} \text{ cm}^{-3}. \quad (3.35)$$

The room temperature photoconductivity lifetime was measured by recording the differential transmission ( $-\Delta\mathcal{E}/\mathcal{E}_{ref}$ ) for many pump-probe delays, as shown in Fig. 3.10 (a) [cf. Eq. (3.33)]. The pump-probe delay of  $\Delta t_1 = 13 \text{ ps}$  was chosen for photoconductivity spectroscopy, and is identified in Fig. 3.10 (a) as the red sphere. A reference and pump waveform was recorded at  $\Delta t_1 = 13 \text{ ps}$ , and Fourier transformed for spectroscopy. The Fourier transformed waveforms were used to calculate the complex transmission spectrum, which was then used to determine the complex conductivity through the Tinkham formula [Eq. (3.31)]. The extracted real and imaginary photoconductivity spectra are shown as the black and red spheres in Fig. 3.10 (b), respectively. The complex conductivity data are then

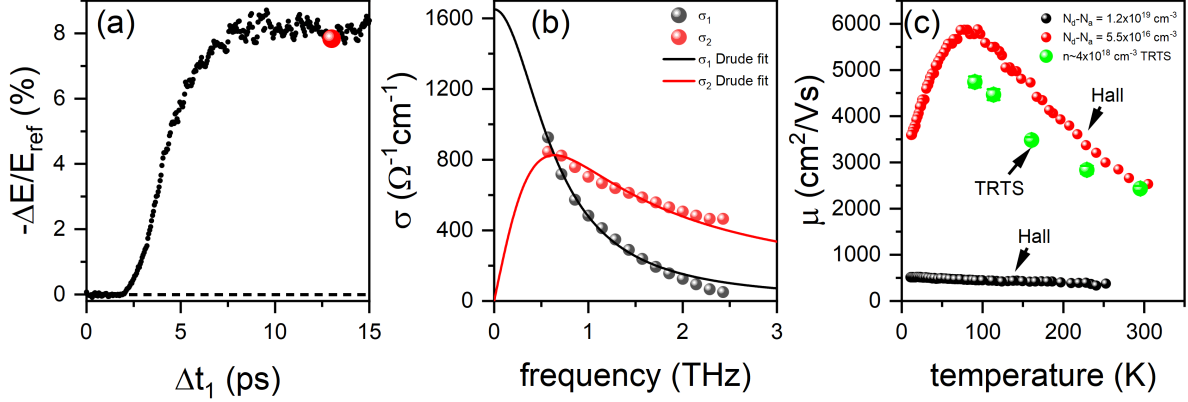


Figure 3.10: Example of TRTS on Ge crystal. The Ge crystal is photoexcited with 100 fs, 400 nm laser pulses at a fluence of  $6 \mu\text{J}/\text{cm}^2$ . (a) The photoconductivity lifetime is measured by fixing the electro-optic sampling time-delay to record the differential transmission of the peak THz electric field. The pump-probe time delay that was chosen for the time-resolved spectroscopy is indicated by the red sphere ( $\Delta t_1 = 13$  ps). (b) The photoconductivity spectrum extracted at  $\Delta t_1 = 13$  ps. The extracted real (black) and imaginary (red) conductivity are shown as colored spheres, and the data are fit to a Drude model of conductivity (solid lines). (c) Temperature dependent mobility of n-type Ge and results from TRTS. Mobilities measured via TRTS reside between Hall mobilities in n-type Ge with an excess carrier density of  $N_d - N_a = 5.5 \times 10^{16} \text{ cm}^{-3}$  and  $N_d - N_a = 1.2 \times 10^{19} \text{ cm}^{-3}$ . Hall mobility data are from Ref. [199].

fit to the Drude model [cf. Eq. (2.47)], which is shown as the solid lines in Fig. 3.10 (b).

From the Drude fit in Fig. 3.10 (b), we find that the charge-carrier density is  $(4.23 \pm 0.05) \times 10^{18} \text{ cm}^{-3}$ , which is consistent with the fluence  $\sim 4.5 \times 10^{18} \text{ cm}^{-3}$  that was estimated above. We find the scattering time is  $\tau = 250 \pm 6$  fs, which yields a mobility of  $\mu = e\tau/m^* = 2340 \pm 60 \text{ cm}^2/\text{Vs}$ . The mobility we extract is consistent with measurements of  $\sim 2500 \text{ cm}^2/\text{Vs}$  which have been routinely observed in literature [199]. With the system calibrated, we are then able to proceed to measure various dependencies such as fluence and temperature. Figure 3.10 (c) shows the temperature dependent mobility that was extracted by performing TRTS using the same conditions as above. The mobilities we observe reside between measurements of mobility in n-type Ge for excess carrier densities of  $N_d - N_a = 5.5 \times 10^{16} \text{ cm}^{-3}$  and  $N_d - N_a = 1.2 \times 10^{19} \text{ cm}^{-3}$  [199], where  $N_d$  is the donor density and  $N_a$  is the acceptor density.

## 3.4 Summary

This Chapter covers how to use terahertz time-domain spectroscopy (THz-TDS) to measure the equilibrium conductivity of a material. We explain how to use time-resolved terahertz spectroscopy (TRTS) to extract the ultrafast photoconductivity and the photoconductivity dynamics. We provide an example of TRTS performed on bulk Ge, which shows that carrier densities extracted from fits to the photoconductivity spectrum are consistent with estimates based on photoexcitation fluence. Further, we show that temperature dependent mobilities can be extracted that agree with measurements of mobility in n-type Ge crystals.

# Chapter 4

## Experimental Details

### 4.1 Introduction

In the experiments conducted in this thesis, time-domain terahertz spectroscopy, time-resolved terahertz spectroscopy, and time-resolved photoluminescence are used to inform us of the ultrafast evolution of the photoexcited state. Terahertz spectroscopy informs us of the evolution of the photoconductivity, while photoluminescence contains information about the rate of charge carrier recombination. In this chapter we review the technical details of the laser systems used, generation of THz pulses, measuring THz pulses, THz spectroscopy, and photoluminescence.

### 4.2 Time-Resolved Terahertz Spectroscopy

Time-resolved Terahertz Spectroscopy (TRTS) was performed using a pulsed laser that operates at 1040 Hz, emitting 800 nm pulses with 100 fs duration. The laser system shown in Fig. 4.1 is comprised of a KMLabs Oscillator, followed by an Odin amplifier. The oscillator is comprised of a  $\text{Ti:Al}_2\text{O}_3$  gain medium that is pumped by a 532 nm continuous wave (CW) laser source. The oscillator cavity is designed to support modes of the 800 nm spontaneous emission that occurs in the gain medium. Along the axis of the cavity 800 nm radiation lases, and through a process known as mode-locking the CW lasing is transformed into a pulsed output, with normal average powers of 400 mW, and a repetition rate of 76 MHz.

The 76 MHz pulse train is directed into the Odin amplifier, where they are stretched temporally to reduce the instantaneous power per pulse. From the pulse train, one pulse is

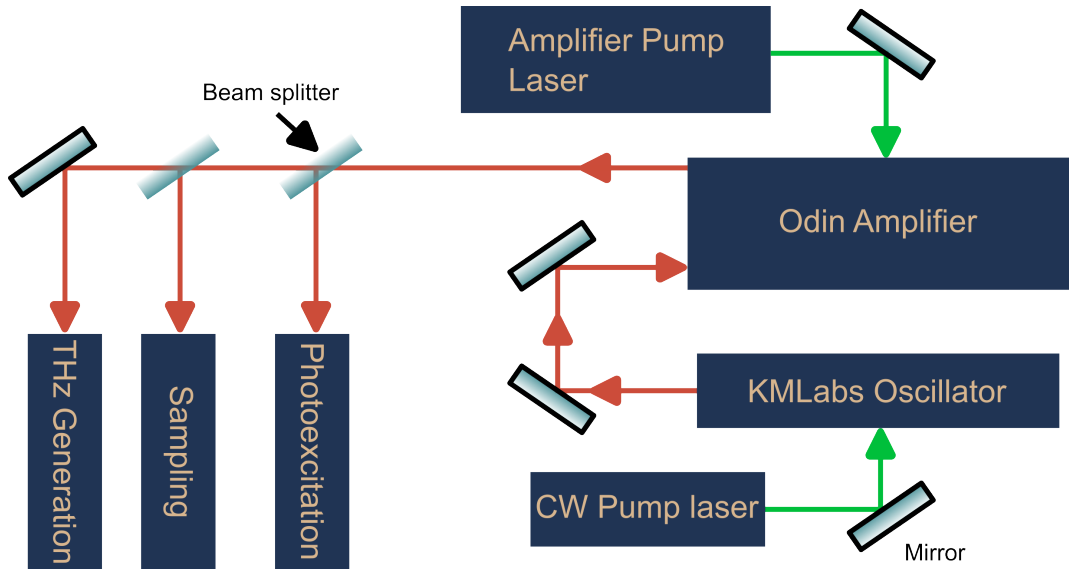


Figure 4.1: Overview of Ultrafast Spectroscopy Laboratory. 100 fs, 800 nm pulses exit the KMLabs Oscillator at 76 MHz. One pulse is selected to enter the Odin Amplifier, where it undergoes chirped-pulse amplification. The amplified pulse is compressed, and exits the amplifier. The high-power pulse is split into the photoexcitation, electro-optic sampling, and THz generation pathways.

selected every 1 ms for injection into the multipass amplifier. This pulse is referred to as the seed pulse. Inside the Odin Amplifier, the seed completes 8 circuits, passing through a photoexcited  $\text{Ti:Al}_2\text{O}_3$  crystal each time. The seed initiates stimulated emission on each pass, which increases the intensity of the seed. A mirror selects the 8th pass, ejecting the pulse from the amplifier. After ejection the pulse is temporally compressed to  $\sim 100$  fs having an average power of  $\sim 650$  mW. Comprehensive information about the detailed settings for the Odin multipass system can be found in the user manual located in the Ultrafast Spectroscopy Laboratory [200].

After exiting the multipass amplifier, the pulse train is split up into 3 different paths. 75% (487.5 mW) is for photoexciting samples, and the remaining 25% (162.5 mW) is used to generate and measure THz pulses. 48.75 mW is allocated for generating THz pulses, and 113.75 mW is reserved for electro-optic sampling THz pulses. For reasons that are outlined in Appendix B, the photoexcitation line is chopped at a frequency of 520 Hz, and the electro-optic sampling line is chopped at 260 Hz.

In Fig. 4.2 we show a schematic of how the photoexcitation, THz generation, and sam-

pling lines are combined to form the time-resolved terahertz spectroscopy (TRTS) system. An 800 nm pulse on the THz generation line enters the vacuum chamber on the top-right corner of Fig. 4.2, and is immediately incident onto a ZnTe crystal. A burst of THz radiation is emitted from the ZnTe crystal and is focused onto a sample by way of off-axis parabolic mirrors. The photoexcitation line enters from the top-center of Fig. 4.2, and is focused onto the sample, arriving in time with the THz pulse. A small hole is drilled into the off-axis parabolic mirror, which allows the excitation beam to arrive at the sample collinear to the THz pulse. The THz radiation is attenuated by the photoexcited sample and collected by off-axis parabolic mirrors for electro-optic sampling. The electro-optic sampling line is shown in the bottom-left of Fig. 4.2, and arrives at a second ZnTe crystal collinear with the attenuated THz pulse.

Under normal circumstances, the vacuum chamber pressure is evacuated to pressures of  $\sim 10^{-6}$  Torr to remove water line contamination in the spectroscopy. The vacuum chamber can also be purged with dry gasses such as nitrogen if samples are susceptible to photodegradation in vacuum. Samples are mounted on a cold finger cryostat which can be used to lower the sample temperature to  $\sim 20$  K. Mounting the sample to the cryostat is usually performed in ambient conditions, however the sample holder can be placed in a glove box if samples are sensitive to air or water vapour. Samples are affixed over 1.5 mm apertures using Elmer's rubber cement, which has been found to securely hold samples to the cryostat at 20 K. The 1.5 mm holes are chosen so that the excitation fluence can be calibrated, and THz transmission through the hole is not affected by spatial filtering of the low THz frequencies. The sample temperature is monitored using a Lakeshore Cryotronics temperature controller. It is important to record the temperature at the sample as well as the temperature at the cold-finger because a  $\sim 10$  K difference may arise from the thermal radiation of the vacuum chamber. The flow rate may be increased to lower the sample temperature, however this may induce unnecessary waste of the liquid cryogen. Calibrated silicon diodes are used to record the temperature.

Electro-optic sampling is performed using a 1 mm ZnTe crystal, a quarter waveplate, a Wollaston prism, and two switchable gain amplified silicon photodiodes. The terahertz electric field is mapped onto the ellipticity of the 800 nm pulse via the linear electro-optic

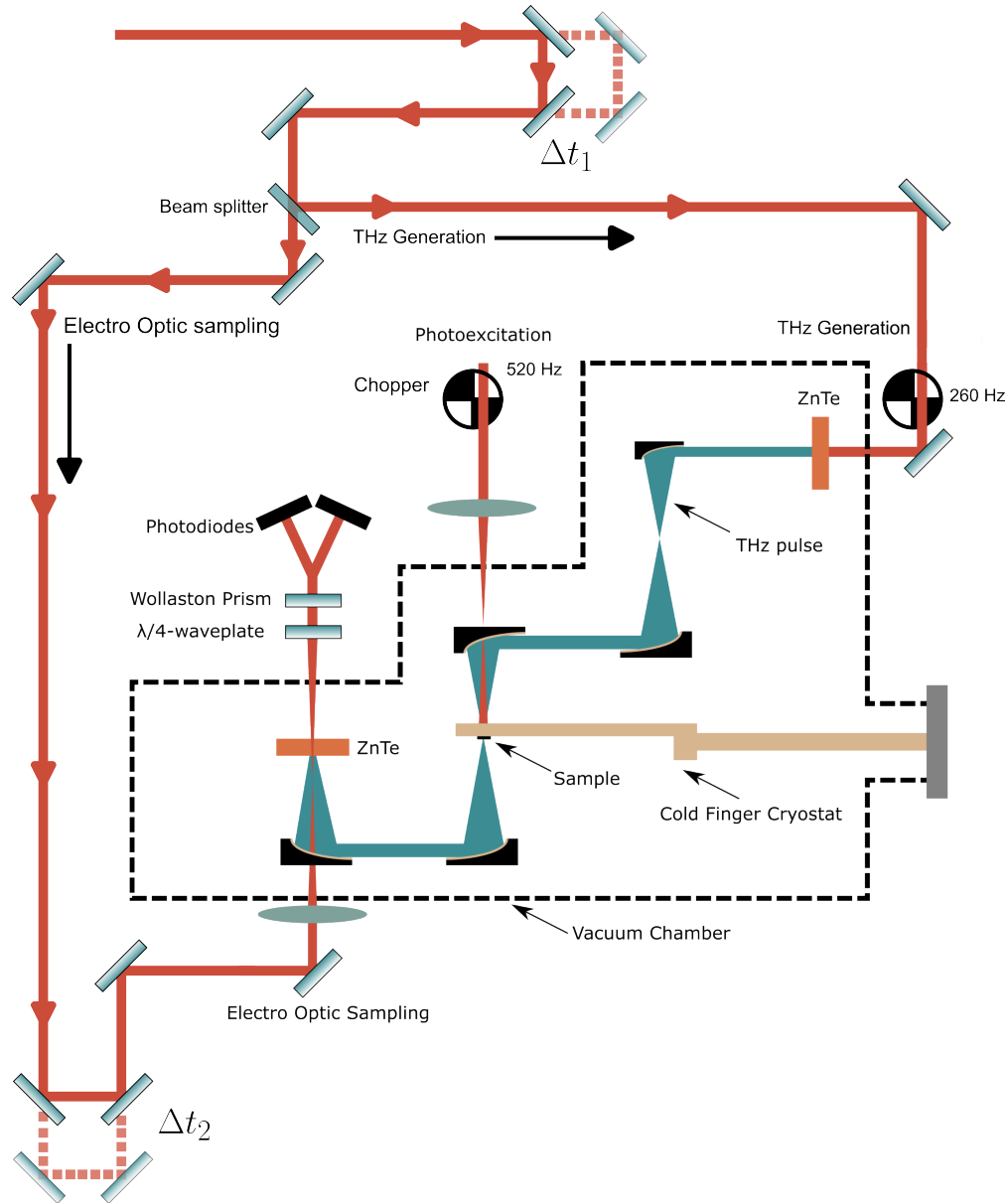


Figure 4.2: Experiment chamber for TRTS. THz generation beam (red) enters from the top-right of the figure. THz radiation (green) is generated in a 1 mm thick ZnTe crystal. The photoexcitation beam enters from the top-center. It is focused such that it is able to pass through a small hole in the parabolic mirror. The samples are mounted on a cold-finger cryostat, where they are exposed to THz radiation and photoexcitation. The transmitted THz radiation is collected, and shined onto a second ZnTe crystal in the bottom left. The electro-optic sampling beam enters from the bottom left, and the THz waveforms are recorded using the quarter-wave ( $\lambda/4$ ) wave plate, Wollaston prism, and two silicon photodiodes. The electro-optic sampling delay ( $\Delta t_2 + \Delta t_1$ ) is shown in the bottom left, and is achieved using a retroreflector mounted on a motorized translation stage. The pump-probe delay is realized by delaying the electro-optic sampling and the THz generation by  $\Delta t_1$ . The THz generation delay is shown in the top right.

effect in ZnTe. The Wollaston prism separates the horizontal and vertical polarizations, and directs them onto independent switchable gain amplified silicon photodiodes. The photodiodes convert the intensity of these components into an electrical signal that is analyzed by an SR-830 Lock-In Amplifier [201]. Since the difference between the horizontal and vertical intensities is directly proportional to the THz electric field, and the voltages of the photodiodes are directly proportional to the intensities, the Lock-in amplifiers are set to the “A-B” setting to perform the necessary subtraction. There are two lock-in amplifiers employed in TRTS measurements.

One lock-in is set to a reference frequency of 260 Hz, and records the sum of the reference and photoexcited electric fields. The output is given by

$$V_{out,260} = \frac{2}{260 \text{ Hz}} (V_1 + V_2) \frac{1}{\sqrt{2}} \propto \mathcal{E}_{ref} + \mathcal{E}_{pump}, \quad (4.1)$$

where  $V_1$  is proportional to the reference THz field  $\mathcal{E}_{ref}$ , and  $V_2$  is proportional to the photoexcited THz field  $\mathcal{E}_{pump}$ . Since  $\mathcal{E}_{ref} = \mathcal{E}_{pump}$  under conditions of no excitation, the 260 Hz lock-in amplifier is used for routine electro-optic sampling. Before daily measurements are taken, the photodiode signals are balanced by setting this lock-in to R mode, blocking the THz generation line, and lightly rotating the quarter waveplate until the signal is minimized.

The second lock-in amplifier is set to a reference frequency of 520 Hz, and records the difference between the reference and photoexcited electric fields. The output voltage is given by

$$V_{out,520} = \frac{2}{520 \text{ Hz}} (V_1 - V_2) \propto \mathcal{E}_{ref} - \mathcal{E}_{pump}. \quad (4.2)$$

Since  $\mathcal{E}_{ref} - \mathcal{E}_{pump} \propto \sigma(\delta t_1)$ , this lock-in amplifier is used to measure photoconductivity lifetimes and “2-Chop” waveforms. Further details about lock-in amplification can be found in Appendix B.

Combining these lock-in amplifiers allows for the simultaneous acquisition of  $\mathcal{E}_{ref}$  and  $\mathcal{E}_{pump}$ . From Eqs. (4.1) and (4.2), it is easy to show that

$$\mathcal{E}_{ref} = \frac{1}{2} \left( \frac{1}{\sqrt{2}} V_{out,260} + V_{out,520} \right) \quad (4.3)$$

and

$$\mathcal{E}_{pump} = \frac{1}{2} \left( \frac{1}{\sqrt{2}} V_{out,260} - V_{out,520} \right). \quad (4.4)$$

Equations (4.3) and (4.4) make it possible to compute  $-\Delta\mathcal{E}/\mathcal{E}_{ref}$ , which provides direct access to the conductivity via Eq. (3.31). The choppers are triggered by the injection timing, and the frequency dividing features of the chopper controller are used to generate reference signals for the lock-in amplifiers.

### 4.3 Time-Resolved Photoluminescence

Time-integrated photoluminescence (TIPL) and time-resolved photoluminescence (TRPL) studies were carried out using a time-correlated single-photon counting (TCSPC) system in the Ultrafast Nanotools Laboratory. Figure 4.3 shows a schematic of the system that is used to perform both TIPL and TRPL. A Coherent RegA ultrafast laser emits 100 fs, 800 nm laser pulses at a 250 kHz repetition rate. These pulses are directed into an optical parametric amplifier (OPA) containing a  $\beta$ -barium borate crystal, which halves the wavelength to 400 nm via second harmonic generation. The 400 nm pulses are reflected off of a beam splitter (glass slide) onto the sample through an objective lens (20x Mitutoyo M Plan Apo). The sample undergoes photoluminescence, and the light is coupled back through the objective lens, passing through the beam splitter, and onto a 435 nm long-pass filter. After the 400 nm light has been filtered, the PL is focused onto a multimode optical fiber with core size of 550  $\mu\text{m}$  that is optimized for wavelengths ranging from 400 - 2200 nm. The optical fiber is connected to a Princeton Instruments Acton SP2500 Spectrometer, where the PL is directed onto a 1200 g/mm grating blazed at 750 nm (Grating number 3 on the turret). The PL is dispersed by the grating, and is then directed onto a controllable flip-mirror that reflects the PL onto a CCD array (Acton Pixis 400 CCD) for TIPL, or onto a monochromator for TRPL.

#### 4.3.1 Time-Integrated Photoluminescence

Figure 4.3 shows the internal workings of the spectrometer. Time-integrated photoluminescence (TIPL) can be obtained by using a CCD to image the distribution of light captured by the spectrometer. The Acton Pixis 400 is a CCD array with a size of 26.8 mm  $\times$  8

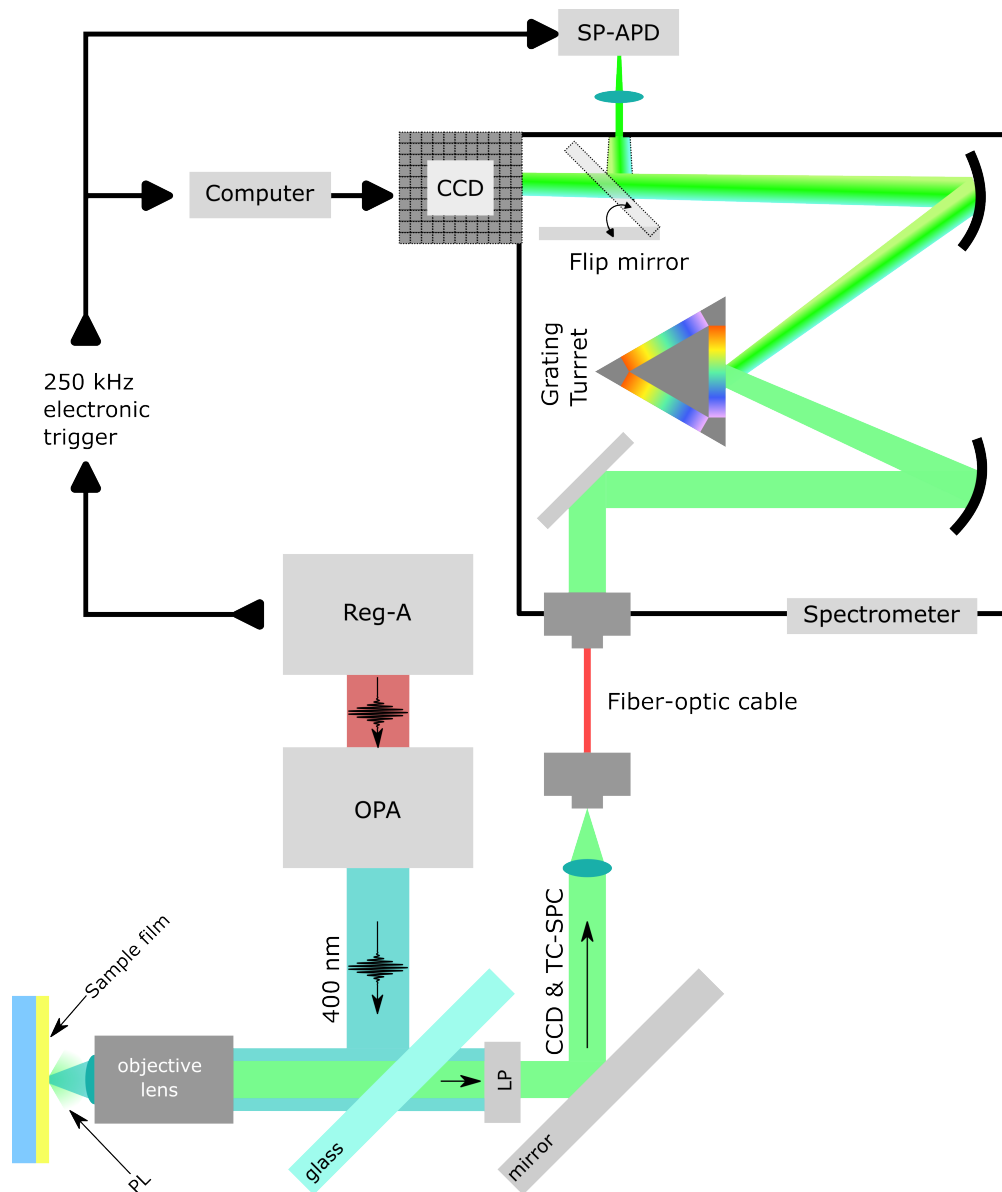


Figure 4.3: Schematic of photoluminescence system. A Coherent RegA ultrafast laser generates 800nm, 100 fs pulses that are directed into an optical parametric amplifier containing BBO. The 400 nm output is directed onto the sample through an objective lens. The PL is collected by the objective, and is directed into the spectrometer after filtering out the excitation wavelengths.

mm, containing  $1340 \times 400$  pixels. All measurements were taken using an entrance slit of  $\Delta\ell = 0.2$  mm. The grating has an angular dispersion of  $D = 300$  rad/mm, and the focal length within the monochromator is  $f = 500$  mm. The wavelength resolution  $\Delta\lambda$  is thus found to be

$$\Delta\lambda = \frac{\Delta\ell}{fD} = 1.3 \text{ nm.} \quad (4.5)$$

It is generally recommended to use  $\Delta\ell \lesssim 0.2$  mm, so that the light shining onto the grating has the profile of a top-hat, preserving the integrity of the spectrum. When the signal is weak, and  $\Delta\ell \sim 0.2$  mm, simply increase the exposure time using the Labview interface. The flip-mirror must be out of the way in the TIPL configuration. The motion of the mirror can be heard by the user after it has been set in the Labview interface.

The PL spectrum that arrives at the CCD is summed vertically, such that the total intensity per wavelength is recorded by a Labview program. A spectral correction must be made when converting the PL distribution from wavelength to energy. It is not enough to simply transform the domain via  $E = hc/\lambda$ , one must also multiply the range by  $\lambda^2$  [156]. To see why, note that the total intensity of light ( $I$ ) is independent of the chosen representation. Thus,

$$I = \int_0^{\infty} I(E)dE = \int_0^{\infty} I(\lambda)d\lambda. \quad (4.6)$$

It is clear that the integrands must be equal, and so one may now write

$$I(E) = I(\lambda) \left| \frac{d\lambda}{dE} \right| = \frac{\lambda^2}{hc} I(\lambda). \quad (4.7)$$

This correction factor is accommodating the fact that when a spectrum is sampled in bins of equal width in  $\lambda$ , the width of each bin is not equal in  $E$ . As such, properly converting into the energy domain will boost the long-wavelength end of the spectrum, and slightly red-shifts spectral peaks [156].

### 4.3.2 Time-Resolved Photoluminescence

To perform time-resolved photoluminescence, the flip mirror in Fig. 4.3 is flipped into a position that directs the diffracted PL spectrum onto a monochromator slit, allowing the

user to view the lifetime at a single wavelength. This light is focused onto a single-photon avalanche-photodiode (SP-APD) which converts the incident photon energy into an electric current. Time-correlated single photon counting (TC-SPC) allows us to measure the current over nanosecond timescales, with  $\sim 30$  ps time resolution. The SP-APD is connected to the PicoQuant 300 TC-SPC module that is triggered by the 250 kHz pulse train of the RegA laser. Referencing the arrival of a single-photon pulse to the pulse train of the RegA allows the TC-SPC module to discriminate the incoming PL pulses from the laser pulse train. The time delays between the single photon and trigger pulse are binned to create a histogram that represents the time-resolved PL decay.

The general workflow of the photon counting system is to take the output pulse-train from the SP-APD, pass it through a filter and amplifier, use a voltage threshold to discriminate signal pulses from dark noise, and then count how many pulses satisfy the discrimination. An ideal system satisfies 4 critical design criteria. (1) The pulses must be short enough to be identified by the discriminator as unique pulses. (2) A high quantum efficiency is desirable for the SP-APD, so that the maximum number of photons is converted into useful signal. (3) The discriminator pulse-height should be selected as the local minimum of the counts vs. pulse-height curve. The local minimum exists because at the lowest pulse heights, the signal is mostly noise. As the height is increased, more of the dark noise is filtered out, until a maximum signal is achieved. The minimum between these two regimes acts as a natural threshold between the dark signal and the real signals, and should be chosen as the threshold. (4) Once the discriminator voltage threshold has been set, the bias of the SP-APD is chosen based on the ratio of dark/signal counts. As the bias is increased, the ratio will increase as you achieve more and more signal counts. At a certain voltage, the ratio will saturate, forming a plateau. The desired bias is anywhere in this plateau region.

Now that single-photon pulses are being discriminated from dark noise, they can be sampled to obtain the luminescence rise and decay curve. TC-SPC is outlined in Fig. 4.4, where a voltage is linearly increased from 0 to some maximum value. The ramping is triggered by the laser system, and the ramping is stopped when a discriminated voltage pulse arrives from the SP-APD. The voltage at which the stop was triggered is therefore directly correlated to the time at which the photon arrived (hence the name time-correlated). These voltages

are recorded in a histogram through a multichannel analyzer. Random, repeated sampling of the single-photon histogram thus allows us to construct the lifetime of the PL, since the probability of emitting a single-photon in a chosen solid-angle is directly proportional to the number of luminescence centres in the excited state. The voltage bins can then be converted into time bins, and the lifetime is retrieved. Two or more photons detected by the SP-APD can distort the binning of the photon counts. To maintain a low probability of registering more than one photon, a generally accepted rule of thumb is to keep the number of counts below 10% of the laser repetition rate. In turn, the statistical error in the histogram is less than 10% [202]. For the RegA system, the repetition rate is 250,000 Hz, and so the counts should be kept below 25,000. In practise, one will find that 10,000 counts is sufficient.

Figure 4.4 (a) shows an example of TC-SPC. A discriminated single-photon pulse (red pulse) arrives in bin  $\Delta t_5$ , which corresponds to a voltage bin  $V_5$ . From this occurrence, one count (+1) is added to the  $V_5$  bin. The histogram is displayed on the voltage axis, and it is clear to see that there is a larger rate of occurrence in the  $\Delta t_2$  bin, corresponding to bin  $V_2$ . As time (Voltage) increases, the number of counts in each voltage bin decreases because the number of luminescence centers is decreasing. One specific benefit of this technique is that voltages can be recorded with extreme precision, reminiscent of how a similar voltage - time correlation is used in streak cameras. Figure 4.4 (b) shows a lifetime measured on a 1 mm thick wurtzite CdS crystal. Inset is the PL showing a peak at  $\sim 508$  nm, where the TRPL was recorded. We see at the PL lifetime is  $< 1$  ns. The CdS sample was photoexcited with 100 fs, 400 nm pulses at a fluence of  $100 \mu\text{J}/\text{cm}^2$ .

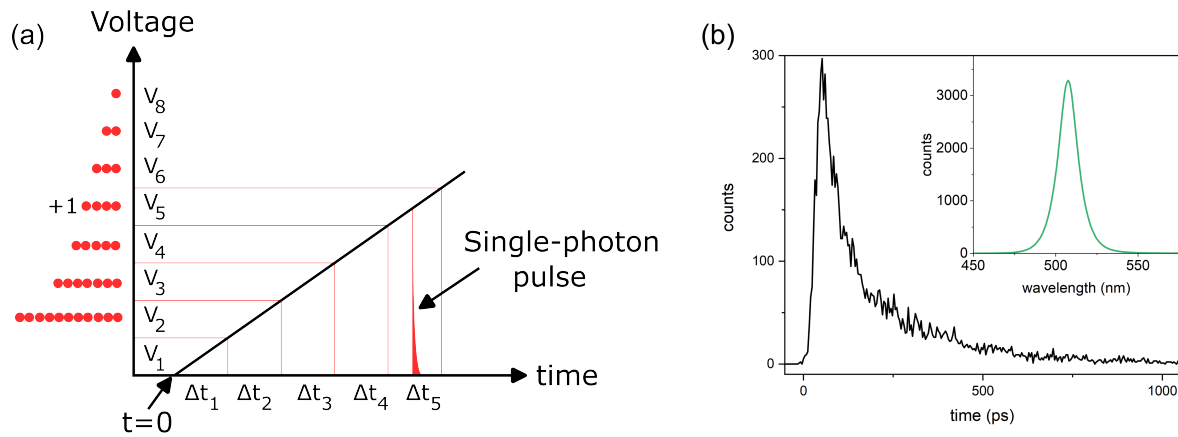


Figure 4.4: (a) Schematic of a single time-correlated binning event. A trigger pulse from the RegA triggers start of a collection event. A voltage is increased linearly over time. The linear increase is stopped when a pulse from the SP-APD arrives (at  $\Delta t_5$ ), and one count is added to the voltage bin corresponding to the stop voltage ( $V_5$ ). The histogram of binned voltages is shown as circles on the left, where we see that  $V_2$  contains the most counts, and as  $V$  is increased, the corresponding number of counts falls off. Owing to the detection event in  $\Delta t_5$ , +1 counts has been added to  $V_5$ . (b) TRPL measured from 1 mm CdS crystal. Inset is the PL spectrum of the CdS crystal. TRPL was recorded at the PL peak which occurs at  $\sim 508$  nm.

# Chapter 5

## CdS Nanowires wrapped in $C_3N_5$ Nanosheets

### 5.1 Introduction

CdS is a semiconductor with a direct bandgap of 2.4 eV that is suitable for the absorption of visible light and possesses a moderate electron mobility of  $\sim 440 \text{ cm}^2/\text{Vs}$  [203, 204]. Together, these properties have encouraged optoelectronic applications such as thin-film solar cells [205], photocatalysts [117], lasers [206], and waveguides [207]. Recent advances in solution-based growth of CdS nanomaterials [49, 208, 209] yield highly crystalline CdS nanowires (NWs), which has stimulated wide interest in nanoscale optoelectronic applications of CdS [208].

Although CdS nanowires can readily absorb visible light, they suffer from unfavorable band alignment because the alignment of the conduction/valence bands to the levels of the photochemistry is not tuneable. Fortunately, favorable band alignment can be achieved by encapsulating CdS nanowires in two-dimensional nanosheets [69, 210]. In particular, Alam, Jensen et al. wrapped CdS nanowires in  $C_3N_5$  nanosheets and found that the interface formed a type-I heterojunction that enabled control of the photocatalytic pathway and provided a significant enhancement to the photocatalytic degradation of 4-nitrophenol and rhodamine B [69]. However, charge-carrier participation in surface chemistry is limited by the transport properties of CdS nanowires.

Alam, Jensen et al. performed preliminary measurements using time-resolved terahertz spectroscopy (TRTS), and revealed that free-carrier localization limits long-range mobility in these samples because the nanowires possess dimensions near the diffusion length in bulk CdS ( $\sim 25$  nm) [69]. It was found that the mobility within the CdS nanowires remained bulk-like, with  $\mu \sim 400$  cm<sup>2</sup>/Vs, which is encouraging because highly mobile carriers are more available for photocatalysis. It was also found that the photoconductivity lifetimes in these nanowires are long, lasting more than 500 ps. This is also encouraging, because the mobile carriers are available for longer times, which correlates with higher photocatalytic yield. The preliminary measurements and results that were published in Ref. [69] can be found in Section 5.3.1.

Despite the promise of the preliminary results, a detailed study of the mechanisms driving the prolonged photoconductivity lifetime and charge-carrier localization has yet to be performed. In the later sections of this chapter, we extend our preliminary study by performing TRTS for a variety of photoexcitation fluences. This yields valuable information about the photoconductivity spectrum, and photoconductivity lifetimes that is used to understand the mechanisms limiting charge-carrier transport in CdS nanowires wrapped in C<sub>3</sub>N<sub>5</sub> nanosheets. Furthermore, we use time-resolved photoluminescence to reveal the transient recombination dynamics, and construct a model of charge-carrier dynamics that simultaneously describes the photoconductivity and photoluminescence lifetimes.

## 5.2 Experimental Details

### 5.2.1 Wrapping CdS Nanowires in C<sub>3</sub>N<sub>5</sub> nanosheets

Azo-linked carbon nitride (C<sub>3</sub>N<sub>5</sub>) nanosheets were fabricated prior to nanowire wrapping following the method in Ref. [211] and Ref. [69]. Briefly, melamine was heated for an extended period at 450 °C, and then crushed into a yellow powder. The powder was dispersed into deionized (DI) water and refluxed for several hours to remove impurities and unreacted materials. The result was melem (2,5,8-triamino-s-heptazine) which was reacted with hydrazine hydrate to form the monomeric unit melem hydrazine (2,5,8-trihydrazino-s-heptazine). This was heated in a teflon-lined autoclave for 24 hours at 140 °C. After filtering, several cycles of HCl and NaOH, washing with DI water, methanol wash, the system was left to dry overnight

in a vacuum oven. A melem hydrazine polymer (MHP) was then obtained by controlled heating of the melem hydrazine [69, 211]. Synthesizing few-layered MHP nanosheets (MHP-NS) began by placing 500 mg of the MHP into a flask immersed in an ice bath. 50 mL of  $\text{HNO}_3$  (65 wt. %) was added in the flask very slowly for 15 minutes under magnetic stirring. The flask was then removed from the ice bath and the suspension was refluxed for 3 hours at 80 °C. The milky-white solution indicated formation of MHP-NS. After dilution with DI water and several washes, the unwanted material was removed leaving behind MHP-NS that can be vacuum dried and saved for wrapping CdS nanowires.

Wurtzite cadmium sulfide nanowires were synthesized following a solvothermal protocol with minimal modifications to Refs. [69, 209]. 2.5 mM of cadmium dichloride hemipentahydrate ( $\text{CdCl}_2 \cdot 2\text{H}_2\text{O}$ ) and 7.48 mM of thiourea ( $\text{NH}_2\text{CSNH}_2$ ) were mixed in a solution containing 20 mL of ethylenediamine, followed by magnetic stirring until the solution became transparent. This solution was poured into a teflon-lined autoclave and sealed prior to heating at 170 °C for 36 hours. Afterwards, the solution was washed with methanol, ethanol, and DI water many times to separate out the unreacted material. The bright yellow, highly crystalline CdS nanowires were then dried in a vacuum oven overnight at 80 °C. This yielded a hard solid that was then crushed into a powder using a mortar and pestle. Nanowires were then suspended in a solvent, and dropcast onto 0.5 mm c-cut sapphire for ultrafast spectroscopy.

CdS nanowire – MHP heterojunctions were made in two ways. The first method takes an ex-situ (ES) approach to wrapping the CdS nanowires. For the ES method, CdS nanowires were grown according to the method outlined above. Then the nanowires were mixed with the dry powder of MHP-NS (5 wt. %) in a glass vial with methanol. After magnetic stirring for 36 hours, the MHP-NS spontaneously wrap around the CdS nanowires via an electrostatic attraction, forming the ex-situ wrapped nanowires (ES-WNW). The second method takes an in-situ approach to wrapping the CdS nanowires. In this method, nanowires are grown according to the protocol above, however, an addition of MHP-NS (5 wt. %) occurs at the mixing stage of the precursor materials, prior to the hydrothermal reaction. These nanowires will be referred to as the in-situ wrapped nanowires (IS-WNWs). After growth, ES-WNWs and IS-WNWs were separately suspended in a solvent and dropcast onto separate 0.5 mm

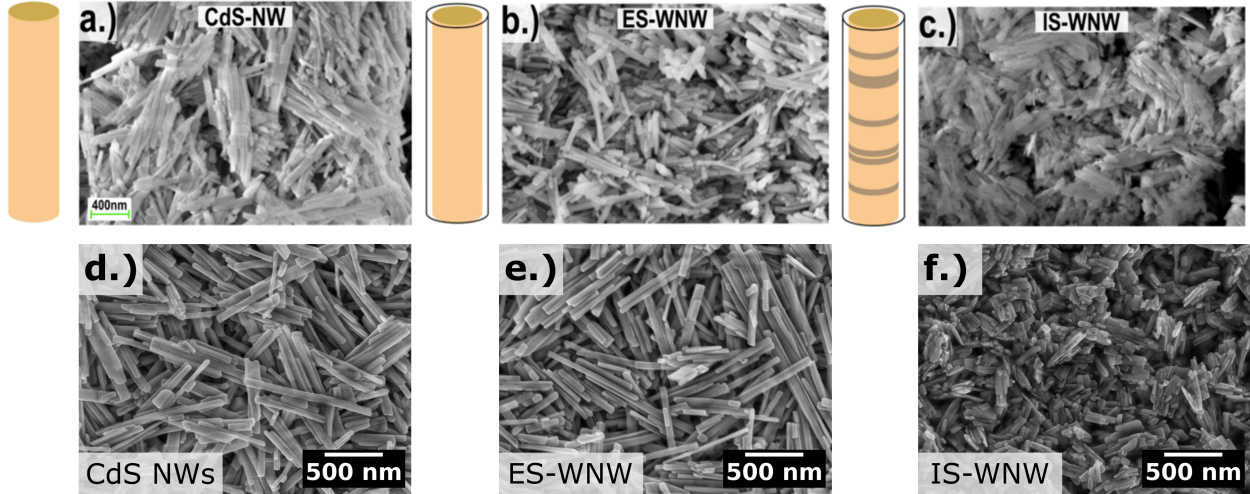


Figure 5.1: FESEM images of (a,d) CdS nanowires, (b,e) Ex-situ wrapped nanowires, and (c,f) In-situ wrapped nanowires. Images (a-c) courtesy of Kazi M. Alam, Navneet Kumar, and Karthik Shankar. The CdS NWs and ES-WNWs have diameters  $\sim 50$  nm, and lengths of  $\sim 1$   $\mu\text{m}$ . The IS-WNWs have diameters  $\sim 50$  nm, and lengths  $< 500$  nm. Schematics of the nanowires are shown above the SEM images. The nanowires are indicated by the yellow cylinder, while the  $\text{C}_3\text{N}_5$  nanosheets are indicated by the transparent cylinder. Defects along the nanowires are indicated by grey bands on the CdS nanowire.

c-cut sapphire wafers for ultrafast spectroscopy.

Field emission scanning electron microscope (FESEM) images of the samples described above are shown in Fig. 5.1. Generally, the CdS nanowires are found to have a diameter of 50 nm and lengths of  $\sim 1$   $\mu\text{m}$ . Figure 5.1 (a) shows the FESEM micrograph of CdS nanowires, Fig. 5.1 (b) shows the ES-WNWs, and Fig. 5.1 (c) shows the IS-WNWs. The IS-WNWs appear to be much shorter in length than the ES-WNWs. This is likely caused by the MHP nanosheets interfering with the growth process of the NWs.

## 5.2.2 Sample Thickness

Terahertz spectroscopy is very sensitive to the thickness of the sample under study [212]. The film thickness was measured by scanning the focus of a Witek confocal microscope from the substrate to the top of the film. Images of the samples are shown in Fig. 5.2. Figures 5.2 (a), (c), and (e) are captured in the region where spectroscopy was performed. We find that the samples are flat in these regions, with nanowires uniformly dispersed across the surface.

To determine the film thickness, we deliberately scratched the edge of the nanowire film

CdS-NWs	ES-WNWs	IS-WNWs
$12 \pm 1 \text{ }\mu\text{m}$	$12 \pm 1 \text{ }\mu\text{m}$	$5 \pm 1 \text{ }\mu\text{m}$

Table 5.1: Table of CdS nanowire film thicknesses.

so that the substrate could be exposed. The scratch was on the edge of the sample, so that the region of spectroscopy could be preserved. Figures 5.2 (b), (d), and (f) show the scratches in the nanowire films. These images are composite images that are formed using a technique called focus stacking, which can be used to extend the depth of field of an imaging system [213]. We used an ImageJ plugin of this technique to create the composite image\*. Extending the depth of field was necessary to produce a clear image of the scratches. Scanning the focus from the substrate provided the thicknesses of the samples. The thicknesses are provided in Table 5.1. The uncertainty of the thickness was found by moving the focus in small increments, and finding displacements that defocused the image.

### 5.2.3 Terahertz Time-Domain Spectroscopy

THz time-domain spectroscopy (THz-TDS) can elucidate the presence of intrinsic charge-carriers in the samples, which can have a significant effect on the transient photoconductivity [71, 110]. To this end, THz-TDS was performed on the CdS nanowires under study, as well as a bulk  $1 \text{ cm} \times 1 \text{ cm} \times 1 \text{ mm}$  Wurtzite CdS crystal<sup>†</sup> for reference. The CdS crystal is charge-compensated to semi-insulating state where the resistivity is  $R > 10^6 \text{ }\Omega\text{cm}$ . The samples were placed in the vacuum chamber shown in Fig. 4.2 at a pressure of  $10^{-6}$  Torr. Briefly, the reference and sample waveforms were measured using electro-optic sampling. The waveforms were Fourier transformed, and the complex index of refraction was extracted by solving the coupled nonlinear equations Eq. (3.21) and Eq. (3.22). More information about how THz-TDS is performed can be found in Section 3.2.

### 5.2.4 Time-Resolved Terahertz Spectroscopy

The 1 kHz, 100 fs, 800 nm ultrafast laser system used in these TRTS experiments has explored charge-carrier transport in a wide variety of nanomaterials [55, 78, 167, 214]. Further details can be found in Section 4.2. Briefly, a transient photoconductivity is induced by a 400 nm,

\*The plugin can be found at the following URL: <http://bigwww.epfl.ch/demo/edf/>

<sup>†</sup>Purchased from MTI Incorporated.

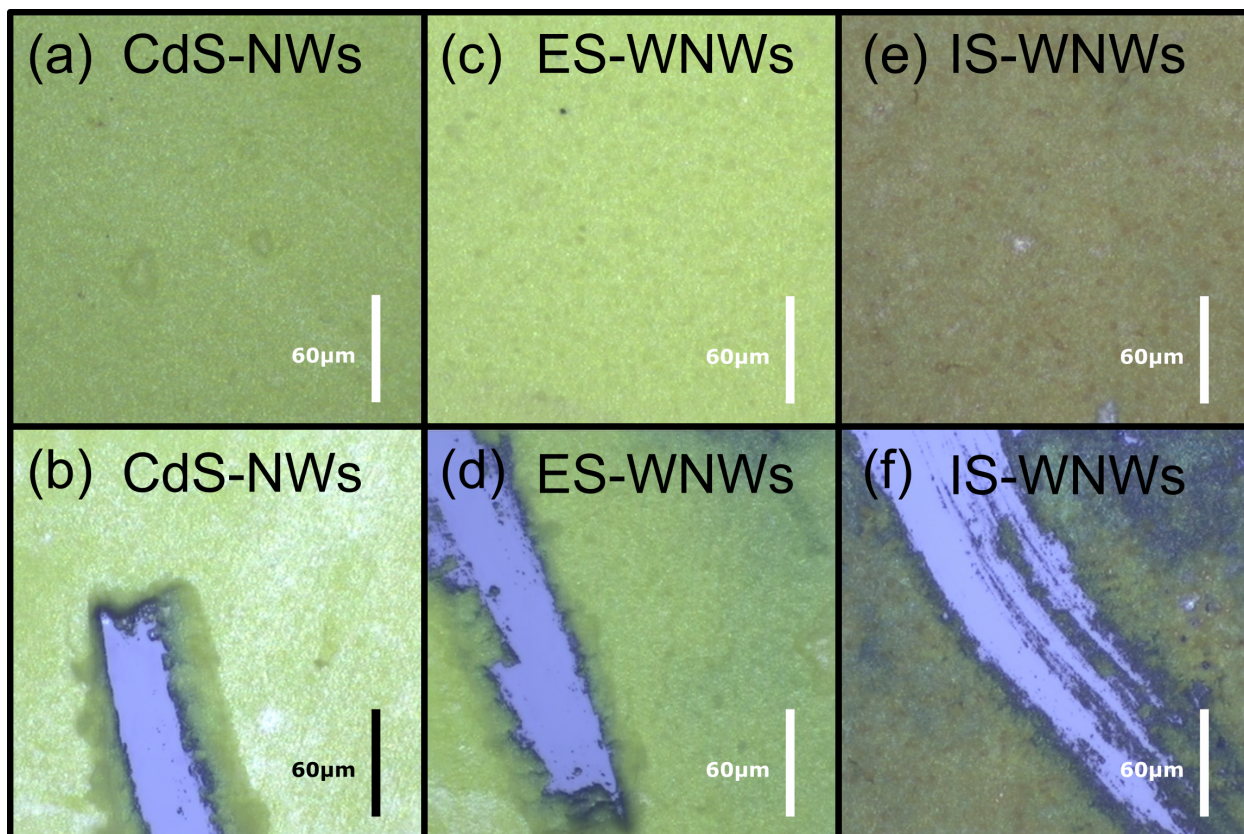


Figure 5.2: Imaging nanowire film morphology with a Witek confocal microscope. (a) Image of CdS-NW sample where spectroscopy was performed. (b) Image of the CdS-NW sample near the scratch where the thickness was measured. The CdS-NW film has a thickness of  $12 \pm 1 \mu\text{m}$ . (c) Image of the ES-WNW sample where the spectroscopy was performed. (d) Image of the ES-WNW sample near the scratch where the thickness was measured. The sample thickness was  $12 \pm 1 \mu\text{m}$ . (e) Image of the IS-WNW sample where the spectroscopy was performed. (f) Image of the IS-WNW sample near the scratch where the thickness was measured. The thickness of the IS-WNWs is  $5 \pm 1 \mu\text{m}$ .

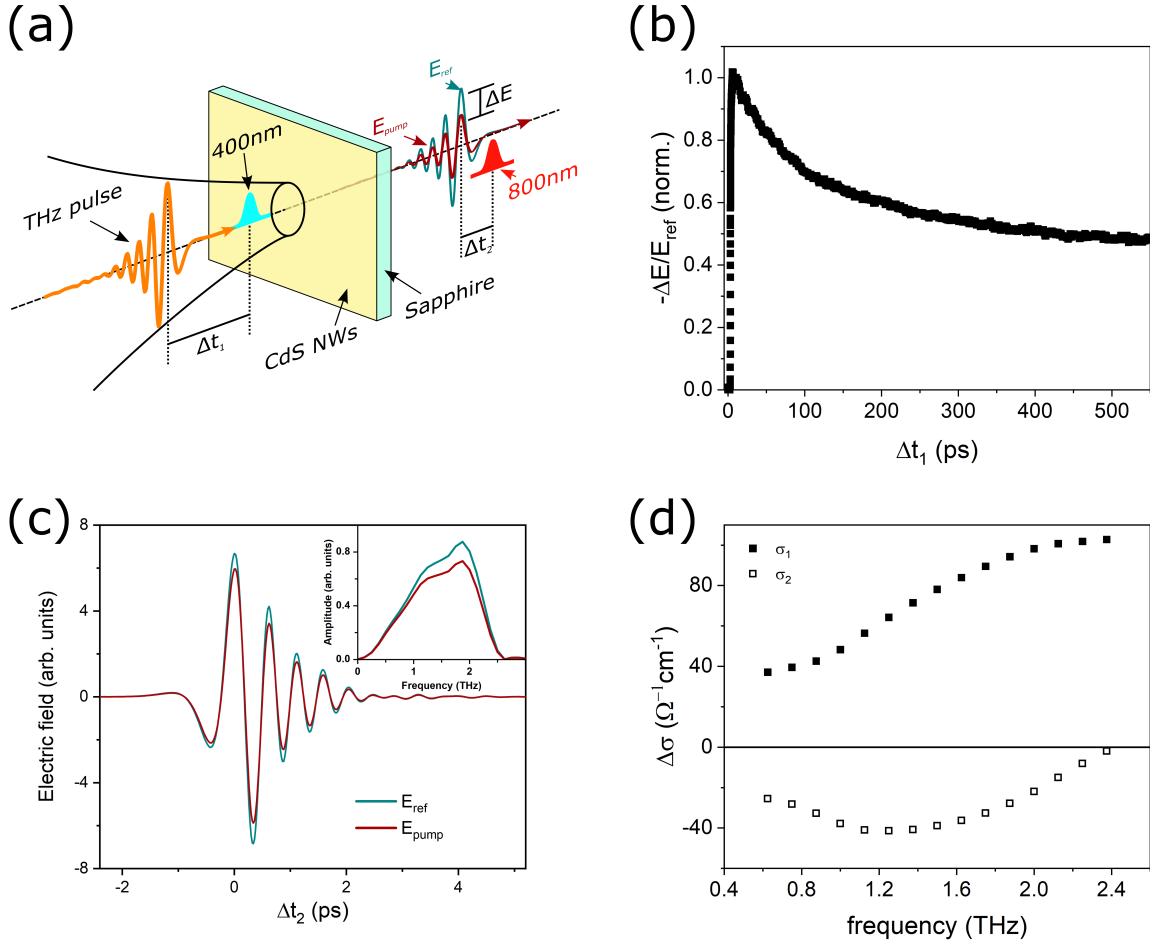


Figure 5.3: (a) Schematic of a time-resolved terahertz spectroscopy experiment. (b) Photoconductivity lifetime measured on CdS NWs at  $400 \mu\text{J}/\text{cm}^2$ . (c) Reference ( $\mathcal{E}_{ref}$ ) and photoexcited ( $\mathcal{E}_{pump}$ ) waveforms taken at a delay of  $\Delta t_2 = 10$  ps. (d) Complex photoconductivity spectrum extracted from (b) at  $\Delta t_1 = 10$  ps. Filled (hollow) squares represent the real (imaginary) part of the photoconductivity.

100 fs laser pulse and then probed by a THz pulse, as shown in Fig. 5.3 (a). The transient photoconductivity is encoded onto the THz pulse via the complex transmission coefficient, bypassing the need to deposit physical contacts on fragile nanodevices. The electric field of the THz pulse is measured through free-space electro-optic sampling, recording the phase and amplitude of the THz pulse. In turn this provides access to the real and imaginary parts of the conductivity spectrum [55, 71, 78].

To study charge carrier transport, we measure the carrier lifetimes and conductivity spectra of the CdS-NWs, ES-WNWs and IS-WNWs, at excitation densities of 25, 100, 200,

300, 400  $\mu\text{J}/\text{cm}^2$ . The 400 nm pump pulse arrives at the sample with a fixed pump-probe time delay,  $\Delta t_1$ , with respect to the THz pulse. The reference ( $\mathcal{E}_{ref}$ ) and photoexcited ( $\mathcal{E}_{pump}$ ) electric fields are measured through electro-optic sampling, using an 800 nm, 100 fs gate pulse at a delay time  $\Delta t_2$ . Transient photoconductivity lifetimes are measured by fixing the electro-optic gate delay to  $\Delta t_2 = 0$ , varying the pump delay  $\Delta t_1$ , and measuring the negative differential transmission  $-\Delta\mathcal{E}/\mathcal{E}_{ref}$ , which (as shown in Section 3.3) is proportional to the instantaneous conductivity [55, 71, 78, 110, 197]. Fig. 5.3 (b) shows a transient photoconductivity lifetime measured on CdS nanowires at a fluence of 400  $\mu\text{J}/\text{cm}^2$ .

Conductivity spectra are measured by fixing  $\Delta t_1$ , scanning  $\Delta t_2$ , and simultaneously measuring  $\mathcal{E}_{ref}$  and  $\mathcal{E}_{pump}$ . Further details can be found in Section 3.3. Example waveforms can be seen in Fig. 5.3 (c), where the amplitude spectra are shown in the inset.  $\mathcal{E}_{ref}$  and  $\mathcal{E}_{pump}$  are then Fourier transformed ( $\tilde{\mathcal{E}}_{pump}(\omega)$  and  $\tilde{\mathcal{E}}_{ref}(\omega)$ ) to compute the complex, frequency domain transmission function  $\tilde{t}(\omega)$  which is linked to the differential photoconductivity  $\Delta\tilde{\sigma}(\omega) = \sigma_1(\omega) + i\sigma_2(\omega)$  through the Tinkham equation [55, 69, 78, 167, 197],

$$\tilde{t} = \frac{\tilde{\mathcal{E}}_{pump}(\omega)}{\tilde{\mathcal{E}}_{ref}(\omega)} = \frac{N + 1}{N + 1 + Z_o\tilde{\sigma}(\omega, \Delta t_1)d} \quad (5.1)$$

where  $N = 3.079$  is the refractive index of c-cut sapphire [172],  $Z_o$  is the impedance of free space ( $377\Omega$ ), and  $d$  is the thickness of the photoexcited region ( $\sim 90$  nm) [170]. An example photoconductivity spectrum for CdS-NWs is given in Fig. 5.3 (d) where  $\Delta t_1 = 10ps$ , under the same fluence as in Fig. 5.3 (b) and (c).

### 5.2.5 Time-Resolved Photoluminescence

We perform TRPL by photoexciting nanowires with 400 nm, 100 fs pulses that were generated via second-harmonic generation of an 800 nm, Coherent RegA Ti:sapphire laser source operating at a repetition rate of 250 kHz, as explained in Ref. [215] and Section 4.3. We use a single photon avalanche photodiode attached to a monochromator to monitor the wavelength-resolved photoluminescence lifetime using a time-correlated single-photon counting unit that provides 40 ps time resolution, and  $\sim 1$  nm wavelength specificity. The  $1/e^2$  diameter of the excitation beam was estimated to be  $\sim 781$  nm. Since the excitation beam

was focused using an objective lens, the spot size was near the diffraction limit of 400 nm light. It is challenging to measure these small spot sizes, and so we estimate the diameter via  $D \sim 0.82 * \lambda / NA$ , where  $D$  is the  $1/e^2$  diameter at the focus,  $\lambda = 400$  nm, and  $NA$  is the numerical aperture. From the Mitutoyo data sheet,  $NA = 0.42$ , and so  $D \sim 781$  nm. This allowed for fluences of 25, 100, 200, 300, and 400  $\mu\text{J}/\text{cm}^2$ . Time-integrated PL spectra are collected using a thermoelectrically cooled CCD array coupled to the monochromator with  $\sim 1$  nm resolution.

## 5.3 Results

### 5.3.1 Photoconductivity for Photocatalytic Applications

In 2021, Alam, Jensen et al. published a detailed study of CdS nanowires wrapped in  $\text{C}_3\text{N}_5$ . In their work, Alam, Jensen et al. investigated the efficacy of CdS-MHP nanowires as candidates for photocatalysis [69]. The time-resolved photoconductivity in that paper was performed as part of this thesis, and here we show those findings.

Alam, Jensen et al. studied three types of CdS nanowire -  $\text{C}_3\text{N}_5$  heterojunctions. Bare CdS NWs were used as a reference, and CdS NW -  $\text{C}_3\text{N}_5$  heterojunctions were grown following an ex-situ protocol (ES-WNWs), and an in-situ protocol (IS-WNWs) [69]. Figure 5.1 shows scanning electron microscope (SEM) images of the CdS nanowires. Figures. 5.1 (a), (b), and (c) were taken by Kazi M. Alam, Navneet Kumar, and Karthi Shankar to demonstrate the nanowire morphology in Ref. [69]. Figure 5.1 (a) shows the bare CdS nanowires, and a schematic of a single nanowire is shown to the left of the image. The nanowires are densely packed, have lengths of  $\sim 1 \mu\text{m}$ , and diameters of  $\sim 50$  nm. Figure 5.1 (b) shows the ex-situ wrapped nanowires (ES-WNWs), and (c) shows the in-situ wrapped nanowires (IS-WNWs). The outer shell on the schematic indicates the shell of  $\text{C}_3\text{N}_5$  nanosheets. Alam, Jensen et al. found that wrapping the nanowires after growth (ES-WNWs) yields nanowires with superior crystallinity compared to the nanowires that were wrapped during growth (IS-WNWs). The disorder is indicated in Fig. 5.1 (c) as the grey banding on the nanowire schematic.

Measuring the transport properties of CdS nanowires is challenging because it is difficult to deposit electrical contacts onto a single nanowire. To this end, TRTS was chosen to study the charge-carrier dynamics of the CdS nanowires because it is intrinsically a non-

contact approach to measuring the optical conductivity (see Section 3.3) [69]. The nanowires were excited with 400 nm, 100 fs pulses, at an excitation density of 400  $\mu\text{J}/\text{cm}^2$ . The photoconductivity lifetime was measured using Eq. 3.33; the results are shown in Fig. 5.4. Figure 5.4 shows the photoconductivity ( $\sigma \propto -\Delta\mathcal{E}/\mathcal{E}_{ref}$ ) as a function of pump-probe delay time ( $\Delta t_1$ ). The photoconductivity of the bare CdS nanowires is shown as black dots, the ES-WNWs are shown as red dots, and the IS-WNWs are shown as blue dots. The transient photoconductivity of the CdS-NWs and the ES-WNWs are significantly larger than the IS-WNWs. Alam, Jensen, et al. noted that this is the result of a low carrier mobility and fast initial trapping. The inset of Fig. 5.4 shows the normalized lifetimes, which reveals a faster recombination in the IS-WNWs and also a faster rise time. This indicates that the hot carrier dynamics are suppressed in the IS-WNWs, which is likely a consequence of ultrafast trapping.

Alam, Jensen et al. quantify the charge-carrier relaxation using fits to a biexponential decay model,

$$-\Delta\mathcal{E}/\mathcal{E}_{ref} = A_1 e^{-\Delta t_1/\tau_1} + A_2 e^{-\Delta t_1/\tau_2} + A_3 \quad (5.2)$$

where  $A_1$  and  $A_2$  are the weights associated with the short and long decay processes,  $\tau_1$  and  $\tau_2$  are the short and long decay constants, and  $A_3$  is a constant term that corresponds to a lifetime much greater than the 500 ps measurement window [69]. The biexponential fits are shown as grey lines in Fig. 5.4, and the best-fit parameters are provided in Table 5.2. No mechanisms are assigned to these lifetimes; however, the shorter lifetime of the IS-WNWs is very likely to be the result of extensive trapping induced by disorder. This is supported by the findings from optical and structural characterizations, which also indicate the presence of structural and energetic disorder in the IS-WNWs [69]. Also, a significant photoconductivity is found to last longer than the 500 ps measurement window for all samples. This long-lived photoconductivity is an asset for photocatalysis applications, as it provides more charge carriers an opportunity to participate in surface chemistry. It is interesting that the IS-WNWs also possess a long-lived photoconductivity, despite the initially fast decay. To date, no mechanism has been reported for this behaviour in CdS nanowires. We find that the rise-time of the CdS-NWs is 1.14 ps. For the ES-WNWs and the IS-WNWs we find rise

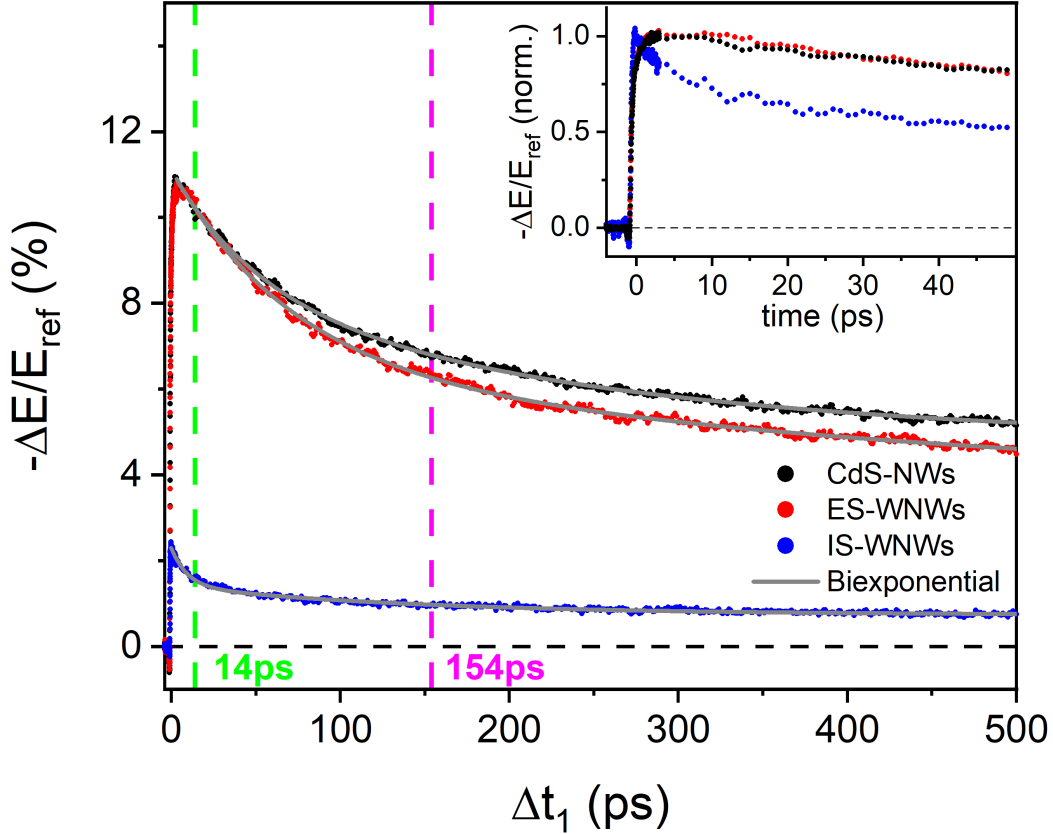


Figure 5.4: Photoconductivity lifetimes of CdS nanowires (black), ES-WNWs (red), and IS-WNWs (blue) (after Alam, Jensen et al. [69]). Biexponential fits to the lifetimes are shown as grey lines. Inset: Normalized photoconductivity lifetimes of the nanowires under study. It is clear that the IS-WNWs possess a significantly faster rise and decay compared to the CdS-NWs and the ES-WNWs. The green and magenta vertical dashed lines represent the times at which the photoconductivity spectra were measured (14 and 154 ps, respectively).

Sample	$A_1$ (%)	$A_2$ (%)	$A_3$ (%)	$\tau_1$ (ps)	$\tau_2$ (ps)
CdS-NWs	$3.0 \pm 0.1$	$3.6 \pm 0.1$	$4.73 \pm 0.01$	$53 \pm 2$	$252 \pm 13$
ES-WNWs	$4.7 \pm 0.2$	$3.2 \pm 0.1$	$3.5 \pm 0.3$	$87 \pm 3$	$500 \pm 100$
IS-WNWs	$1.32 \pm 0.02$	$0.69 \pm 0.01$	$0.735 \pm 0.005$	$9.6 \pm 0.4$	$150 \pm 5$

Table 5.2: Table of biexponential fit parameters from Alam, Jensen et al. [69].

times of 1.1 ps and 0.38 ps, respectively.

As indicated by the vertical dashed lines in Fig. 5.4, the photoconductivity spectrum was measured at pump-probe delay times of 14 ps and 154 ps. The transmission function is related to the photoconductivity through (see Section 3.3)

$$\tilde{\sigma}(\omega) = \frac{n_s + 1}{Z_o d} \left( \frac{\tilde{\mathcal{E}}_{ref}}{\tilde{\mathcal{E}}_{pump}} - 1 \right), \quad (5.3)$$

where,  $n_s = 3.079$  is the refractive index of the c-cut sapphire substrate [172],  $Z_o$  is the impedance of free space ( $377 \Omega$ ), and  $d = 90$  nm is the thickness of the photoexcited film [170]. Alam, Jensen et al. fit the photoconductivity to a Drude-Smith model, shown as the solid/dashed lines in Fig. 5.5. The Drude-Smith model has been used in other studies of CdS nanomaterials [216, 217], and indicates that interactions with the boundaries of the CdS nanowires result in charge carrier localization (see Section 2.2.2 for more details). The conductivity of the Drude-Smith model is given by

$$\tilde{\sigma}(\omega) = \frac{ne^2\tau}{m^*} \frac{1}{1 - i\omega\tau} \left( 1 + \frac{c}{1 - i\omega\tau} \right), \quad (5.4)$$

where,  $n$  is the charge carrier density,  $m^* = 0.19m_e$  is the effective mass [69],  $\tau$  is the scattering rate, and  $c$  is the localization coefficient that exists between 0 and -1. The long-range mobility  $\mu_{l.r.} = e\tau(1 + c)/m^*$  signifies the macroscopic mobility one would measure across the nanowire film, while the short-range mobility  $\mu_{s.r.} = e\tau/m^*$  represents the mobility within CdS nanowires themselves. The photoconductivity spectrum and the fits to the Drude-Smith model are shown in Fig. 5.5, and the results are given in Table 5.3.

Alam, Jensen et al. found that mobilities of the samples did not significantly vary between 14 and 154 ps [69]. The highest long-range mobility belongs to the bare CdS nanowires, and

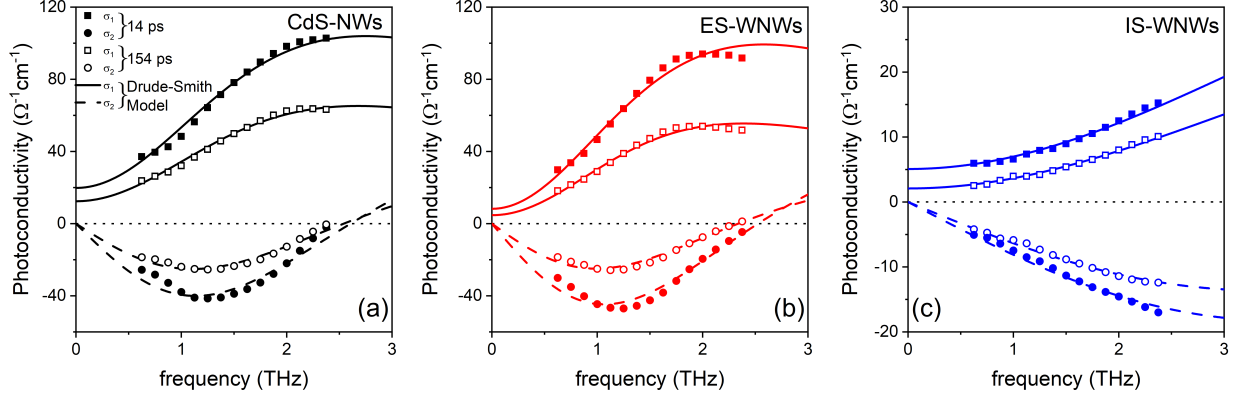


Figure 5.5: Complex photoconductivity of (a) CdS-NWs, (b) ES-WNWs, and (c) IS-WNWs. The real part of the photoconductivity is shown as squares, and the imaginary part is shown as circles. Photoconductivity spectra are measured at  $\Delta t_1 = 14$  ps (filled squares and circles) and 154 ps (hollow squares and circles).

the lowest belongs to the in-situ wrapped nanowires. The long-range mobility of the bare CdS nanowires agrees well with FET measurements of solution grown CdS nanowires, which found  $\mu_{l,r} \sim 62$  cm<sup>2</sup>/Vs [49]. Interestingly, the long-range mobility of the ex-situ wrapped nanowires is half the mobility of the bare nanowires. This implies that the C<sub>3</sub>N<sub>5</sub> wrapping may be impeding the long-range transport of the nanowire network. This sentiment is echoed in the localization parameter of the wrapped nanowires. We find that the localization constants are significantly lower for the wrapped nanowires than the bare nanowires. This implies that charge carriers are being localized to the nanowire core by the C<sub>3</sub>N<sub>5</sub> film. The quality of the nanowires is reflected in the short range mobility. The short range mobility of the IS-WNWs is the lowest, owing to a much shorter scattering time. This could be the result of increased impurity scattering brought about by the disorder in the nanowire observed by Alam, Jensen et al. [69]. The short-range mobility of the CdS-NWs and the ES-WNWs agrees well with measurements of the bulk mobility of CdS [170], as well as band-gap graded CdS<sub>x</sub>Se<sub>1-x</sub> nanowires [217]  $\sim 400$  cm<sup>2</sup>/Vs.

Although the initial results presented by Alam, Jensen et al. are promising, there are avenues that can be taken to refine our understanding of charge-carrier dynamics in CdS nanowires. For example, measuring the fluence dependence of the photoconductivity spectrum has become an important metric for ruling out other interpretations of the conductivity spectrum, such as plasmons and effective medium theories. Furthermore, it has also become

Sample	$\Delta t_1$ (ps)	$\mu_{l.r.}$ (cm <sup>2</sup> /Vs)	$\mu_{s.r.}$ (cm <sup>2</sup> /Vs)	$c$ (unitless)	$\tau$ (ps)
CdS-NWs	14	40 ± 3	420 ± 50	-0.905 ± 0.009	55 ± 1
	154	41 ± 3	430 ± 40	-0.905 ± 0.007	56 ± 1
ES-WNWs	14	19 ± 4	461 ± 155	-0.96 ± 0.01	60 ± 1
	154	21 ± 5	498 ± 160	-0.96 ± 0.01	65 ± 1
IS-WNWs	14	8.1 ± 0.3	137 ± 7	-0.941 ± 0.002	17.9 ± 0.7
	154	5.1 ± 0.2	146 ± 8	-0.965 ± 0.002	19.1 ± 0.5

Table 5.3: Table of Drude-Smith fit parameters from Alam, Jensen et al. [69].

increasingly important to compare the photoconductivity lifetimes to the photoluminescence lifetimes, because the complimentary information about the rate of change of charge carrier density can provide insight into mechanisms such as charge separation. In this chapter we extend the work of Alam, Jensen et al. by measuring the fluence dependant photoconductivity and photoluminescence in CdS-C<sub>3</sub>N<sub>5</sub> nanowires. Drawing inspiration from existing literature on bulk CdS, we construct a model of the charge carrier lifetimes that describes both the transient conductivity and the transient photoluminescence in CdS-C<sub>3</sub>N<sub>5</sub> nanowires.

### 5.3.2 Terahertz Time-Domain Spectroscopy

#### Background Conductivity of Bulk CdS Crystal

Figure 5.6 contains the result of the THz-TDS experiment. The reference waveform (red,  $\mathcal{E}_{ref}$ ) and sample waveform (black,  $\mathcal{E}_{samp}$ ) are shown in Fig. 5.6 (a). The amplitude spectra of the waveforms are shown in Fig. 5.6 (b). The measured transmission function is then calculated as the ratio of the amplitude spectra, as shown in Fig. 5.6 (c).

It is clear from Fig. 5.6 (c) that the transmission contains spectral features within our detector bandwidth. A neutron scattering experiment performed on a wurtzite CdS crystal [24] found that the optically active ( $\mathbf{k} \approx \Gamma$ ) phonon modes occur at frequencies  $\sim 1 - 10$  THz. However, there are only a few available modes within the observable bandwidth of our THz spectroscopy. The first phonon mode occurs at  $\sim 1.22$  THz and the next is 4 THz, which lies outside the bandwidth of our detector. To explain the features we observe, we propose that they arise from difference frequency modes, similar to those observed in ZnTe [100]. Starting with the optically active modes of Ref. [24], we compute the available difference frequency

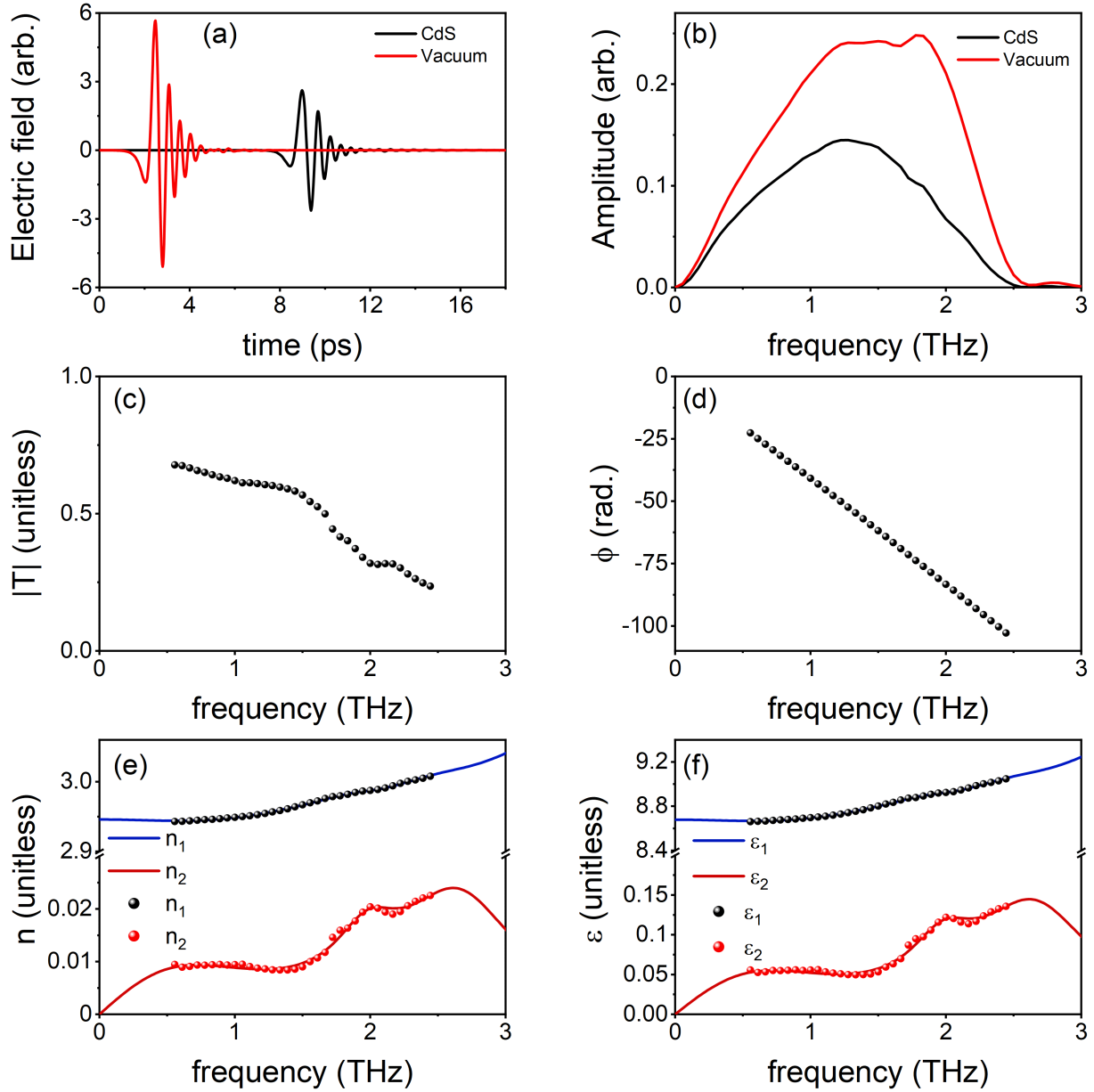


Figure 5.6: (a) Vacuum (red) and CdS (black) waveforms. (b) Vacuum (red) and CdS (black) amplitude spectra. (c) Measured transmission function (black dots) and model transmission function (red line). (d) Complex index of refraction used in the model transmission function. The filled areas indicate the contribution of each difference frequency mode.

$j$	$\omega_{0,j}/2\pi$ (THz)	$\omega_{p,j}/2\pi$ (THz)	$\gamma$ ( $2\pi$ THz)
1	0.4	0.26	2.41
2	1.1	0.19	4.46
3	2.0	0.33	4.02
4	2.7	0.70	2.19

Table 5.4: Parameters used in modelling the transmission function.

modes. The modes that lie within the detector bandwidth (0.5 - 2.5 THz) are listed in Table 5.4. The transmission spectrum can then be modelled using a linear combination of Lorentz Oscillators. The equilibrium conductivity is thus given by

$$\tilde{\sigma}(\omega) = \sum_{j=1}^4 \frac{\omega_{p,j}^2 \epsilon_0 \omega}{\omega \gamma_j + i(\omega_{0,j}^2 - \omega^2)}, \quad (5.5)$$

where  $\omega_{0,j}$  is the resonance frequency of the  $j^{\text{th}}$  mode,  $\gamma_j$  is the damping rate of the  $j^{\text{th}}$  mode, and  $\omega_{p,j}$  is the plasma frequency of the  $j^{\text{th}}$  mode.

The transmission function is modelled according to Eq. (3.21),

$$|T(\omega)| = \frac{4\sqrt{n_2^2 + \kappa_2^2}}{(n_2 + 1)^2 + \kappa_2^2} e^{-\kappa_2 \frac{\omega d}{c}},$$

where

$$\tilde{n}_2(\omega) = n_2 + i\kappa = \sqrt{\epsilon_{st} + 1 + i \frac{\tilde{\sigma}(\omega)}{\epsilon_0 \omega}},$$

and  $\epsilon_{st} = 8.9$  [170]. With the  $\omega_{0,j}$  fixed by the difference frequency modes,  $\omega_{p,j}$  are then adjusted until a reasonable agreement is found between the data and the model. Further investigations would fit the spectrum using this model, but here we aim to simply document our findings. The complex index that best represented our results is shown in Fig. 5.6 (d). The contribution of each difference frequency mode is shown as the filled region beneath the imaginary part of the index. It is clear that the 2.7 THz mode is much stronger than the other modes nearby, leading to the large decrease in transmission near the edge of our bandwidth.

To verify the nature of these modes, a temperature dependence is necessary. Cooling the

sample temperature results in a suppression of the available phonon modes, which, in turn, reduces the probability of interaction between said modes. The reduction of this probability thus results in a suppression of the difference frequency modes, as shown in Ref. [100].

## Background Conductivity of CdS Nanowires

Terahertz time-domain spectroscopy (THz-TDS) was performed on CdS nanowire films that were deposited onto 1 mm thick fused silica substrates. Quartz substrates were initially chosen so that the sample could be customized to allow for the reference waveforms to be measured on the same wafer as the CdS nanowires. An example of the THz-TDS can be found in Fig. 5.7. Fig. 5.7 (a) contains waveforms taken in vacuum (black), with a fused silica substrate (red), and with a CdS-NW film on top of the fused silica substrate (blue). For clarity, the Quartz and CdS-NW waveforms are shown in the inset of Fig. 5.7 (a). To further help, the CdS-NW waveform is shown as blue circles, which shows that it is very slightly shifted to later times.

The vacuum waveform looks dramatically different from the waveforms that passed through fused silica. This is because fused silica is known to have a large absorption in the THz band [172]. This can be seen in Fig. 5.7 (b), where the amplitudes of the Fourier transforms are shown. Due to the large suppression of the amplitudes, the spectroscopy on these films is limited to a maximum frequency of  $\sim 1.5$  THz. The amplitudes are used to calculate the transmission spectra using  $|T| = |\tilde{\mathcal{E}}_{samp}|/|\tilde{\mathcal{E}}_{ref}|$  (cf. Eq. (3.16)).

The transmission coefficients of the fused silica substrate (red) and CdS-NW films (black) are shown in Fig. 5.7 (c). The transmission of the CdS nanowires is flat, with an average of  $100 \pm 1$  %. In contrast, the transmission of the fused silica substrate starts near 0.5 and monotonically decreases in our bandwidth. The flatness of the CdS nanowire transmission indicates that there is no free-carrier absorption in our films, because free-carrier absorption attenuates the the low frequency amplitudes.

This trend of flat transmission continues for the wrapped nanowires as well. The results of THz-TDS performed on these samples is shown in Fig. 5.8. Figures 5.8 (a) and (b) show the waveforms of the ES-WNWs and the IS-WNWs, respectively. Figures 5.8 (c) and (d) show the transmission functions of the ES-WNWs and the IS-WNWs, respectively. For

the ES-WNWs we find an average transmission of  $98.1 \pm 0.7 \%$ , and the IS-WNWs we find  $96.7 \pm 0.8 \%$ . Due to the lack of free-carrier absorption in these nanowire films, we conclude that there is no significant presence of background carriers. A transmission function of nearly 1 implies that the extracted index of refraction is also  $\tilde{n} \approx 1 + 0i$ .

The transmission of the nanowire films can be modelled using the transmission function

$$\tilde{T} = \frac{\tilde{\mathcal{E}}_{samp}}{\tilde{\mathcal{E}}_{ref}} = \frac{\tilde{t}_{v,f}\tilde{t}_{f,s}\Phi_f}{\tilde{t}_{v,s}} \frac{1}{1 - \tilde{r}_{f,s}\tilde{r}_{f,v}exp(2i\omega d_f/c)} \quad (5.6)$$

where  $\tilde{t}_{v,f}$  is the Fresnel transmission coefficient for the vacuum - nanowire film interface,  $\tilde{t}_{f,s}$  is the Fresnel transmission coefficient of the film-substrate interface,  $\tilde{t}_{v,s}$  is the Fresnel transmission of the vacuum-substrate interface,  $\tilde{r}_{f,s}$  is the Fresnel reflection coefficient of the film-substrate interface,  $\tilde{r}_{f,v}$  is the Fresnel reflection coefficient of the film-vacuum interface,  $\Phi_s = exp(i(\tilde{n}_f - 1)\omega d_f/c)$ ,  $d_f$  is the film thickness,  $\omega$  is the angular frequency, and  $c$  is the speed of light. Equation (5.6) allows us to numerically determine the index of refraction of the thin films. For all of the films under study we find that the index of refraction is given by  $n = 1 + 0i$  across the 0.5 THz - 1.5 THz region of the spectrum. The sample thicknesses were measured using a Mitutoyo micrometer. The CdS-NW film thickness was  $35 \pm 6 \mu\text{m}$ , while the ES-WNW and IS-WNW films were  $19 \pm 3 \mu\text{m}$  and  $38 \pm 8 \mu\text{m}$ , respectively. The thicknesses were measured in 4 locations on the sample, and the uncertainty is found by calculating the standard error of the mean.

### 5.3.3 Time-Resolved Terahertz Spectroscopy

#### Ultrafast Photoconductivity Dynamics of CdS Crystal

Photoconductivity lifetimes of bulk CdS excited with 400 nm, 100 fs excitation pulses are shown in Fig. 5.9. The sample was photoexcited at fluences of 6, 25, 100, and 200  $\mu\text{J}/\text{cm}^2$ . The lifetimes in (a) and (b) are shown on a linear and logarithmic scale, respectively. More discussion on the features of the lifetimes will follow. For now we wish to note that the maximum  $-\Delta\mathcal{E}/\mathcal{E}_{ref}$  exceeds 20 % at the fluence of 100  $\mu\text{J}/\text{cm}^2$ , as shown in Fig. 5.9 (c). The dashed line in Fig. 5.9 (c) is a guide-to-the-eye, which suggests a saturation of the maximum differential transmission that may be due to a departure from the linear regime

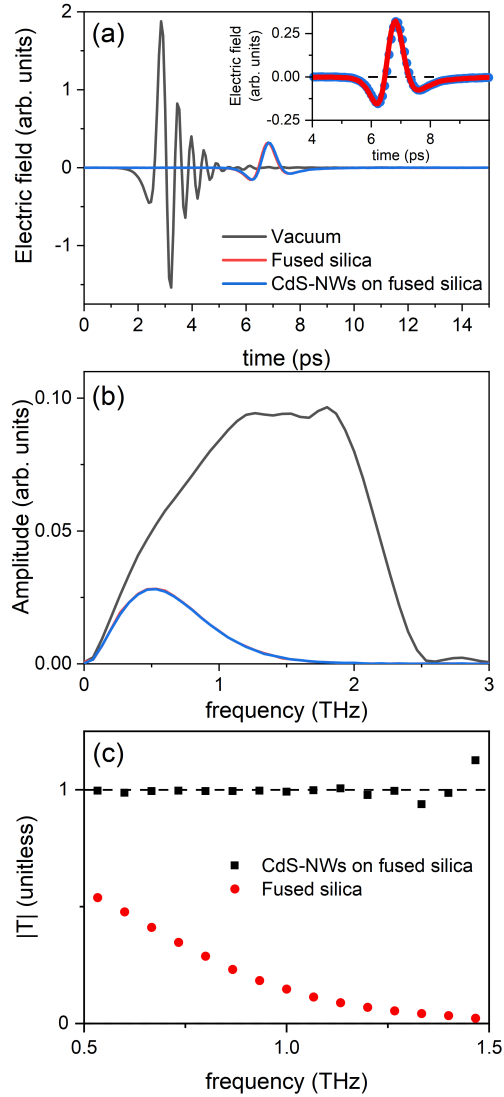


Figure 5.7: (a) Vacuum waveform (black), waveform transmitted through 1 mm thick fused silica substrate (red), and waveform transmitted through CdS nanowire film on fused silica substrate (blue). Inset: Close-up of the region around the fused silica waveform. The CdS-NW waveform is shown as circles for clarity. (b) Amplitude spectra of the waveforms in (a). The amplitude spectra are used to calculate the transmission function in (c). (c) Transmission spectra of the CdS-NW film and the fused silica substrate. The absorption of the CdS-NW film is flat, indicating a lack of free carrier absorption.

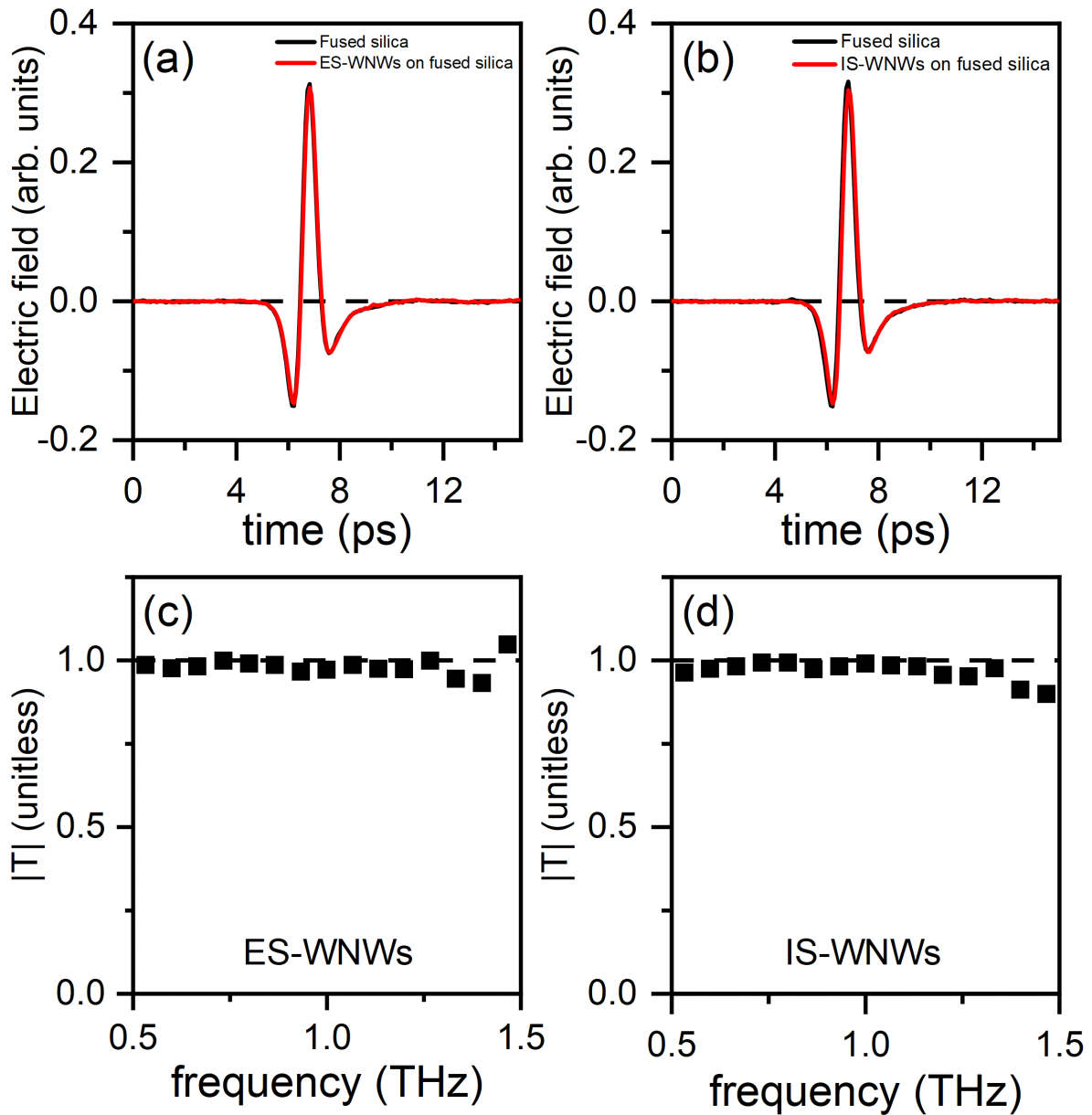


Figure 5.8: THz-TDS of wrapped CdS nanowires on a 1 mm thick Quartz substrate. (a) Ex-situ wrapped nanowire waveforms. Quartz is black, and ES-WNWs is red. (b) In-situ wrapped nanowire waveforms. Quartz is black, and IS-WNWs is red. (c) Transmission function of the ES-WNWs. (d) Transmission function of the IS-WNWs.

of Eq. 3.33. Departure from the linear regime indicates a significant amount of absorption in the bulk crystal, which is not shared by the CdS-NW films shown later. These fluences are thus a subset of the fluences used in the TRTS of the CdS-NW films.

### Ultrafast Photoconductivity Dynamics of CdS Nanowires

The ultrafast photoconductivity dynamics were measured for the CdS-NW films, as shown in Fig. 5.10. The samples were excited with 400 nm, 100 fs laser pulses at a fluences of 25, 100, 200, 300, and 400  $\mu\text{J}/\text{cm}^2$ . Figure 5.10 (a) contains the fluence dependent lifetimes of the CdW-NWs, and (d) contains the same normalized lifetimes. Figure 5.10 (b) contains the fluence dependent lifetimes of the ES-WNWs and (e) contains the normalized lifetimes. Figure 5.10 (c) contains the fluence dependent lifetimes of the IS-WNWs and (f) contains the normalized lifetimes. Only the 100, 200, 300, and 400  $\mu\text{J}/\text{cm}^2$  lifetimes are shown in Fig. 5.10 (f) because the 25  $\mu\text{J}/\text{cm}^2$  data was quite close to the noise floor of the detector, which significantly reduced the readability of the figure. In the bulk CdS lifetimes, the differential transmission exceeded 20 % at a fluence of 100  $\mu\text{J}/\text{cm}^2$ . Figure 5.11 shows that the CdS nanowires do not approach the region of nonlinearity, even at the maximum fluence of 400  $\mu\text{J}/\text{cm}^2$ . This indicates that the signal is a good representation of the transient photoconductivity (cf. Eq. (3.33)). The dashed lines in Fig. 5.11 are guides to the eye, and demonstrate slight saturation of the photoconductivity.

The results from the normalized curves indicate that the photoconductivity lifetime shortens as the fluence is increased. More rigorous modelling of the normalized lifetimes will come later in Section 5.4; for now, a biexponential function was fit to the lifetimes in Fig 5.10 (a)-(c) so that a comparison can be made to the work of Alam, Jensen et al.. Results of the present biexponential fits are shown in Table 5.5.

Our biexponential fits agree with the results of Alam, Jensen et al. (cf. Table 5.2) [69]. For the CdS-NWs the short lifetime at 400  $\mu\text{J}/\text{cm}^2$  is  $\tau_1 = 52 \pm 3$  ps, which agrees well with the  $53 \pm 2$  ps measured by Alam, Jensen et al. [69]. Furthermore, we measure a long lifetime of  $\tau_2 = 250 \pm 10$  ps, which also agrees well with the  $252 \pm 13$  ps reported by Alam, Jensen et al. [69]. We find equal agreement among the other samples, and conclude that the samples did not change between the initial measurements made by Alam, Jensen et al. and

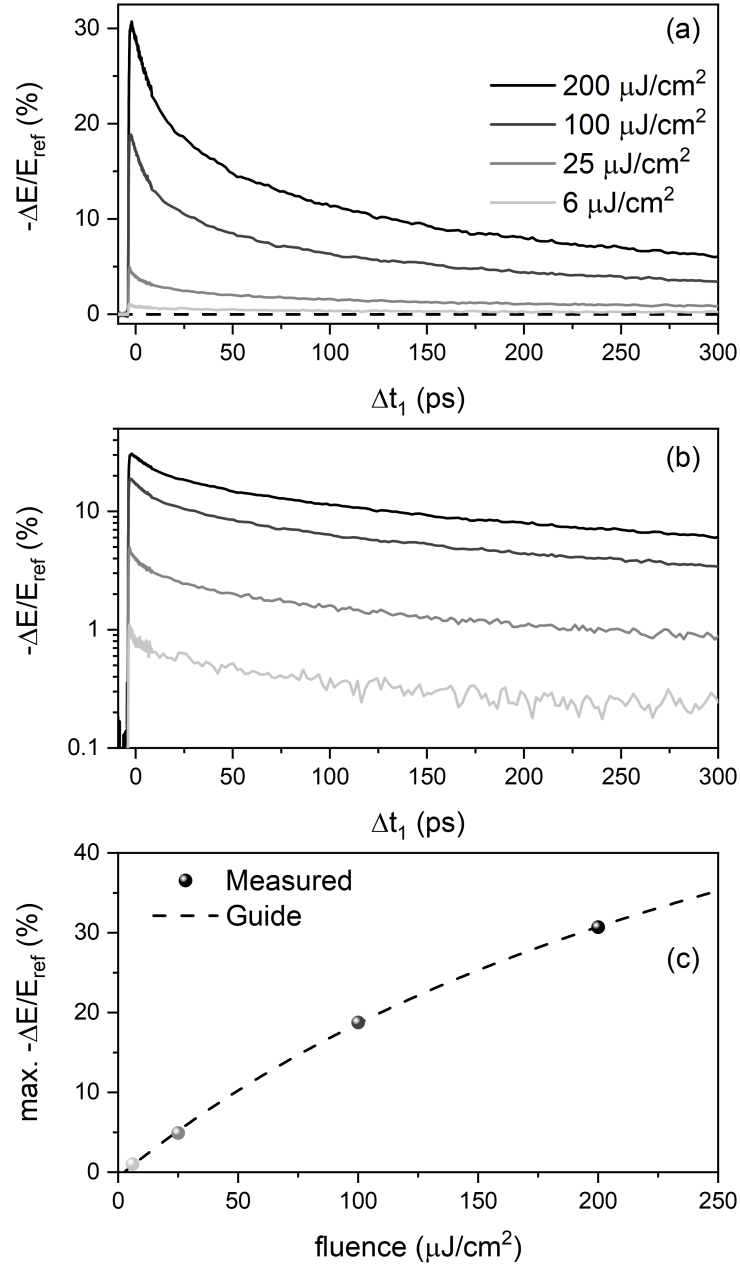


Figure 5.9: (a) and (b) show the photoconductivity lifetimes of bulk CdS on a linear and logarithmic scale, respectively. (c) Maximum  $-\Delta\mathcal{E}/\mathcal{E}_{ref}$  as a function of fluence. The black dashed line is a guide to the eye that suggests saturation of the differential transmission.

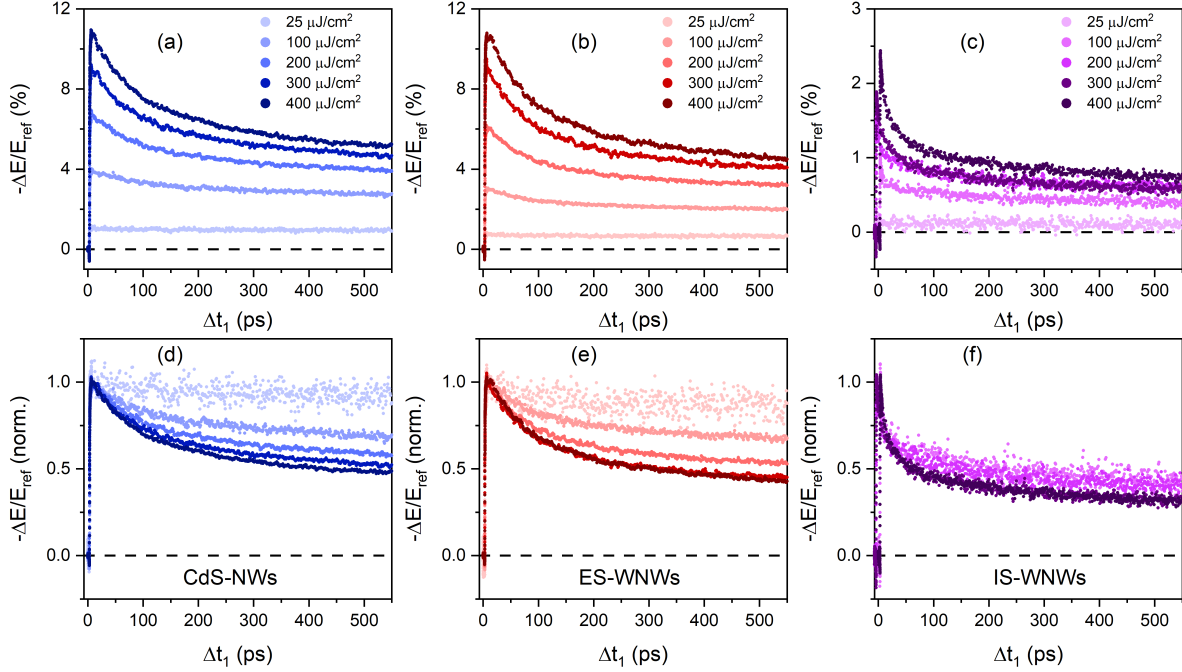


Figure 5.10: Photoconductivity lifetimes of the CdS-NW films. (a) Photoconductivity lifetime of the CdS nanowires. (b) Photoconductivity lifetime of the ES-WNWs. (c) Photoconductivity lifetime of the IS-WNWs. (d)-(f) Normalized lifetimes of (a)-(c), respectively.

the present measurements. Since the photoconductivity of some fluences was flat across our measurement window, it is difficult for the nonlinear fitting algorithm to estimate a complete biexponential model for every fluence. Because of this, certain parameters were neglected in order to produce an accurate fit of the lifetime. The neglected parameters are indicated by dashed lines in Table 5.5.

### Ultrafast Photoconductivity Spectra of CdS Crystal

The ultrafast photoconductivity spectrum of the bulk CdS crystal was measured at pump-probe delay times of  $\Delta t_1 = 61.45$  ps and  $\Delta t_1 = 201.45$  ps, and excitation densities of 6, 25, 100, and 200  $\mu\text{J}/\text{cm}^2$ . The photoconductivity spectra are extracted by measuring the THz waveforms transmitted through the CdS crystal ( $\mathcal{E}_{ref}$ ) and the photoexcited crystal ( $\mathcal{E}_{pump}$ ),

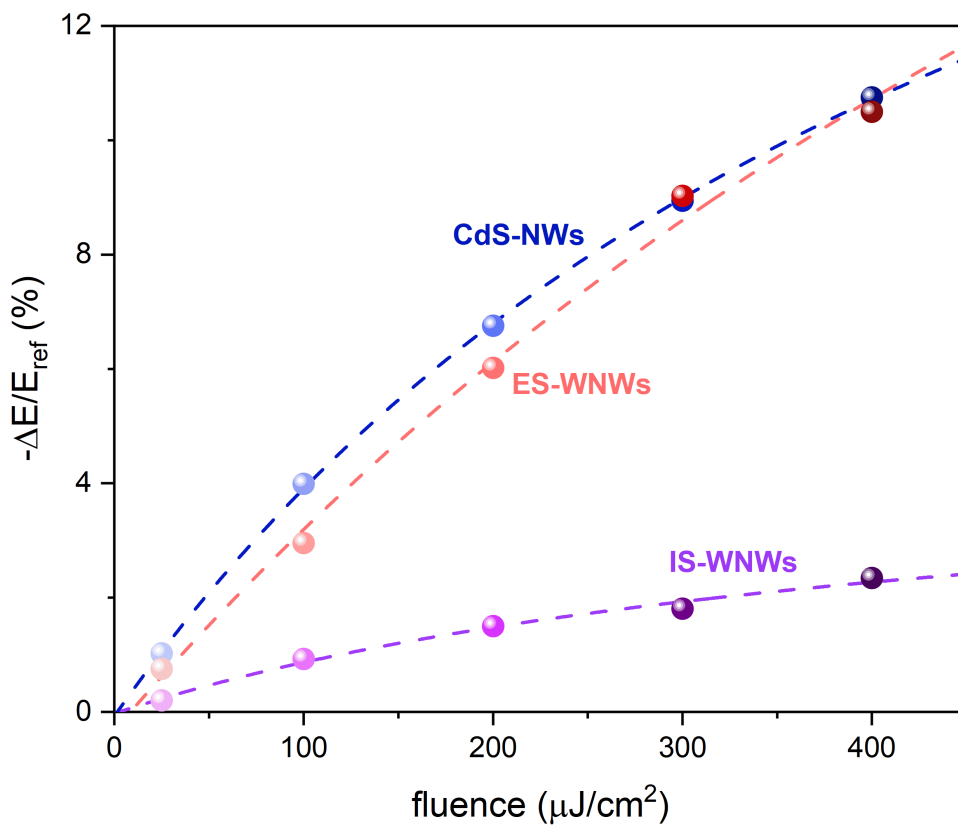


Figure 5.11: Maximum differential transmission of the CdS-NW films. Dashed lines are a guide to the eye, suggesting saturation of the differential transmission at high fluences. All films showed a maximum differential transmission well within 20 %, indicating a good representation of the photoconductivity.

Sample	Fluence $\mu\text{J}/\text{cm}^2$	$A_1$ (%)	$A_2$ (%)	$A_3$ (%)	$\tau_1$ (ps)	$\tau_2$ (ps)
CdS-NWs	25	--	--	$0.966 \pm 0.002$	--	--
	100	$1.17 \pm 0.01$	--	$2.731 \pm 0.007$	$158 \pm 4$	--
	200	$1.9 \pm 0.1$	$1.68 \pm 0.05$	$3.4 \pm 0.2$	$70 \pm 5$	$468 \pm 122$
	300	$2.7 \pm 0.1$	$2.6 \pm 0.08$	$4.21 \pm 0.08$	$56 \pm 3$	$310 \pm 30$
	400	$3.0 \pm 0.1$	$3.6 \pm 0.1$	$4.73 \pm 0.04$	$52 \pm 2$	$250 \pm 10$
ES-WNWs	25	--	--	$0.666 \pm 0.002$	--	--
	100	$0.69 \pm 0.06$	$0.56 \pm 0.03$	$1.90 \pm 0.04$	$55 \pm 5$	$321 \pm 70$
	200	$2.0 \pm 0.1$	$1.42 \pm 0.06$	$2.91 \pm 0.07$	$64 \pm 3$	$346 \pm 60$
	300	$3.4 \pm 0.2$	$2.4 \pm 0.1$	$3.69 \pm 0.08$	$62 \pm 3$	$290 \pm 40$
	400	$4.7 \pm 0.2$	$3.17 \pm 0.09$	$3.5 \pm 0.3$	$69 \pm 3$	$477 \pm 100$
IS-WNWs	25	$0.20 \pm 0.06$	--	$0.110 \pm 0.002$	$4 \pm 1$	--
	100	$0.81 \pm 0.09$	$0.250 \pm 0.007$	$0.399 \pm 0.005$	$3.3 \pm 0.3$	$160 \pm 12$
	200	$1.03 \pm 0.05$	$0.45 \pm 0.01$	$0.607 \pm 0.005$	$4.7 \pm 0.3$	$138 \pm 7$
	300	$1.02 \pm 0.02$	$0.56 \pm 0.01$	$0.577 \pm 0.005$	$9.1 \pm 0.5$	$140 \pm 6$
	400	$1.32 \pm 0.02$	$0.69 \pm 0.01$	$0.765 \pm 0.005$	$9.6 \pm 0.4$	$148 \pm 5$

Table 5.5: Table of biexponential fit parameters from fits to the CdS nanowire films. Dashed lines indicate that this parameter was neglected in order to accurately fit the lifetime.

Fourier transforming them, and using the Tinkham equation <sup>‡</sup>

$$\tilde{\sigma}(\omega) = \frac{n_s + 1}{Z_o d} \left( \frac{\tilde{\mathcal{E}}_{ref}}{\tilde{\mathcal{E}}_{pump}} - 1 \right) \quad (5.7)$$

where  $n_s$  is the index of refraction of the CdS crystal measured with THz-TDS,  $Z_o = 377 \Omega$  is the impedance of free space, and  $d = 90 \text{ nm}$  is the  $1/e$  penetration depth of 400 nm radiation in CdS [170]. The results of the TRTS performed at  $\Delta t_1 = 61.45 \text{ ps}$  are shown in Fig. 5.12. Figures 5.12 (a), (b), (c), and (d) correspond to the excitation densities of 6, 25, 100, and 200  $\mu\text{J}/\text{cm}^2$ , respectively.

Since CdS is a direct gap semiconductor, and we are photoexciting carriers into the conduction band, it is expected that the photoconductivity follows the Drude model. Thus, the photoconductivity spectra in Fig. 5.12 are fit to a Drude model (cf. 2.2.2)

$$\tilde{\sigma}(\omega) = \frac{ne^2\tau}{m^*} \frac{1}{1 - i\omega\tau} \quad (5.8)$$

<sup>‡</sup>For more information on the Tinkham equation, see Section 3.3.

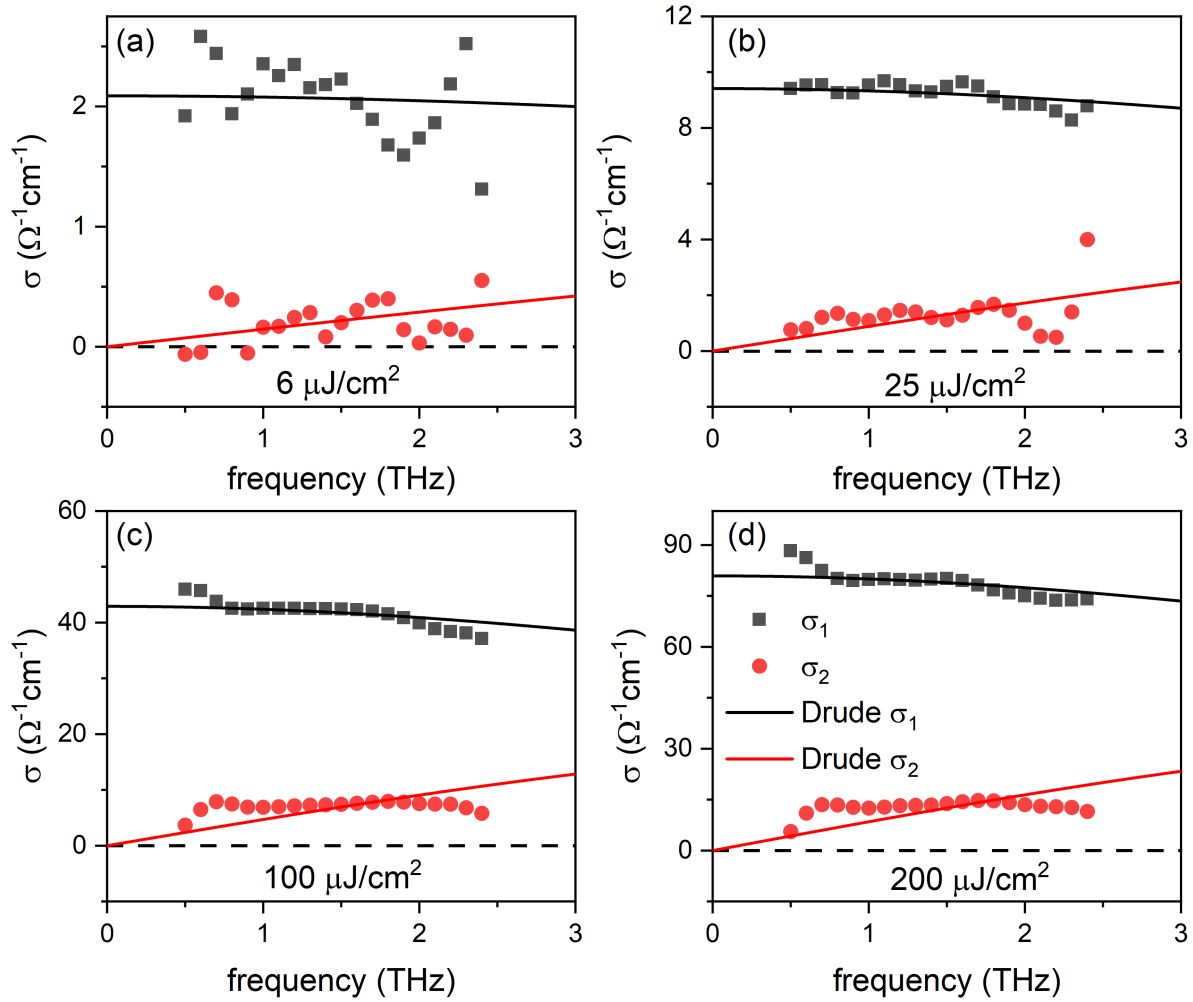


Figure 5.12: TRTS of bulk CdS crystal. The measured real conductivity are shown as black squares, and the measured imaginary part are shown as red circles. The real and imaginary conductivities of the Drude fits are shown as black and red lines, respectively. (a) Photoconductivity spectrum at  $6 \mu\text{J}/\text{cm}^2$ . (b) Photoconductivity spectrum at  $25 \mu\text{J}/\text{cm}^2$ . (c) Photoconductivity at  $100 \mu\text{J}/\text{cm}^2$ , and (d) is the photoconductivity at  $200 \mu\text{J}/\text{cm}^2$ . The black dashed line indicates  $\tilde{\sigma} = 0 \Omega^{-1}\text{cm}^{-1}$ .

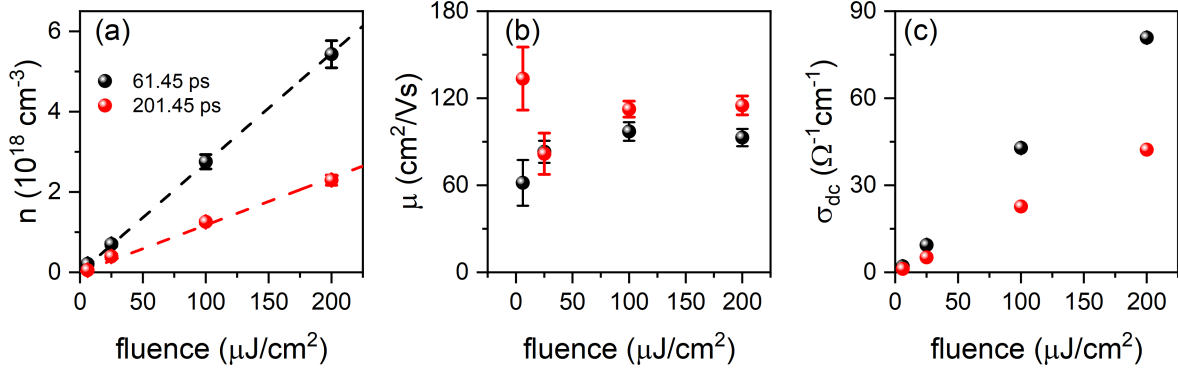


Figure 5.13: Results of fitting bulk CdS photoconductivity to a Drude model. Results taken at  $\Delta t_1 = 61.45$  ps and  $\Delta t_1 = 201.45$  ps are indicated as black and red circles, respectively. (a) Carrier density ( $n$ ), (b) mobility ( $\mu$ ), and (c) DC conductivity. Dashed lines are guides to the eye.

where  $n$  is the carrier density,  $m^* = 0.21m_e$  is the effective electron mass [180], and  $\tau$  is the scattering time. The mobility of the Drude-model is calculated through  $\mu = e\tau/m^*$ . The results of the Drude fits are shown in Fig. 5.13. The carrier density, mobility, and  $\omega = 0$  (DC) conductivity are shown in Fig. 5.13 (a), (b), and (c), respectively. Results from spectroscopy at  $\Delta t_1 = 61.45$  ps and  $\Delta t_1 = 201.45$  ps are shown as black and red circles, respectively. Dashed lines are a guide to the eye.

In Fig. 5.13 (a) and (c) we see that the carrier density and DC conductivity increase linearly with fluence. The carrier densities are  $\sim 10^{18} \text{ cm}^{-3}$ . The mobility is shown in Fig. 5.13 (b), and we find that it does not possess a clear dependence on excitation density. The measured mobility of  $\sim 100 \text{ cm}^2/\text{Vs}$  is low compared to the  $\sim 440 \text{ cm}^2/\text{Vs}$  measured in other CdS crystals [203]. A similar mobility of  $140 \text{ cm}^2/\text{Vs}$  was found by Mics et al. using TRTS and 400 nm excitation, however no explanation was provided for the low mobility [218]. Measurements of the mobility in CdS thin-films show that diffuse scattering off the vacuum - CdS surface can reduce the mobility of carriers. The average scattering rate is given by

$$\frac{1}{\bar{\tau}} = \frac{1}{\tau_b} + \frac{1}{\tau_s}, \quad (5.9)$$

where  $\tau_b$  is the bulk scattering time, and  $\tau_s$  is the surface scattering time. The average mobility is then given by

$$\bar{\mu} = \frac{e\bar{\tau}}{m^*}, \quad (5.10)$$

where  $m^*$  is the effective mass of electrons in CdS. The surface scattering rate can be estimated as the time it takes an electron to travel to the surface within one bulk scattering interval, weighted by the mean free path of the electron ( $\lambda$ ) [219, p. 307–208]. This gives the relation

$$\tau_s \approx d \frac{\tau_b}{\lambda}, \quad (5.11)$$

where  $2d$  is the film thickness. This approximation only holds when the majority of electrons are within one mean free path of the surface, which has been measured to be  $\lambda = 111$  nm for CdS thin-films [220]. The final result is a relationship between the average mobility, the bulk mobility ( $e\tau_b/m^*$ ), the film thickness, and the mean free path

$$\bar{\mu} = \mu_b \frac{1}{1 + \lambda/d}. \quad (5.12)$$

Since  $\sim 70$  % of 400 nm photons are absorbed within 90 nm of the CdS surface [170], the majority of photoexcited charge carriers fall within one mean-free path of the CdS surface. Inserting the known values into Eq. (5.12) gives a mobility of  $\sim 128$  cm<sup>2</sup>/Vs, which agrees well with our mobility  $\mu \sim 100$  cm<sup>2</sup>/Vs and the mobility of  $\sim 140$  cm<sup>2</sup>/Vs seen by Mics et al [218].

## Ultrafast Photoconductivity Spectra of CdS Nanowires

The photoconductivity spectra of the CdS-NW films were measured at pump-probe delays of  $\Delta t_1 = 10$  ps and 150 ps. The reference ( $\mathcal{E}_{ref}$ ) and photoexcited ( $\mathcal{E}_{pump}$ ) waveforms were recorded, and Fourier transformed yielding  $\tilde{\mathcal{E}}_{ref}(\omega)$  and  $\tilde{\mathcal{E}}_{pump}(\omega)$ , respectively. The conductivity was then extracted using the Tinkham equation

$$\tilde{\sigma}(\omega) = \frac{n_s + 1}{Z_o d} \left( \frac{\tilde{\mathcal{E}}_{ref}}{\tilde{\mathcal{E}}_{pump}} - 1 \right) \quad (5.13)$$

where  $n_s = 3.097$  is the c-cut sapphire substrate index [172], and  $d = 90$  nm is the photoexcited film thickness. The extracted photoconductivities at  $\Delta t_1 = 10$  ps are shown in Fig. 5.14. The photoconductivity of the CdS-NWs is shown in Fig. 5.14 (a) and the photoconductivity of the ES-WNWs and IS-WNWs are shown in Fig. 5.14 (b) and (c), respectively.

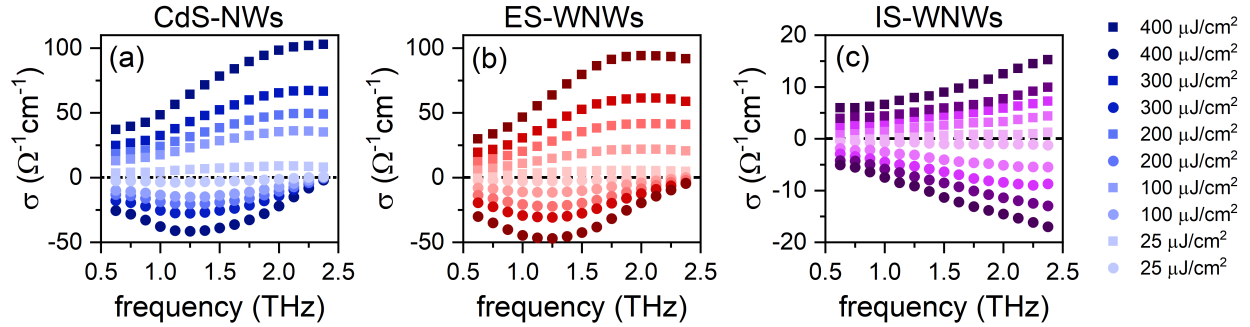


Figure 5.14: Photoconductivity spectra of CdS-NW films. The real (square) and imaginary (circle) parts of the conductivity measured at  $\Delta t_1 = 10$  ps are shown for the three nanowire samples. Going from darkest to lightest, the spectroscopy are taken at fluences of 400, 300, 200, 100, 25  $\mu\text{J}/\text{cm}^2$ , respectively. (a) Photoconductivity of CdS-NW film. (b) Photoconductivity of ES-WNW film. (c) Photoconductivity of the IS-WNW film. The dashed line represents  $\sigma = 0 \text{ } \Omega^{-1}\text{cm}^{-1}$ .

In 5.4 we will fit these curves to a Drude-Smith model.

### 5.3.4 Time-Resolved Photoluminescence

In Fig. 5.15 we show the results of our photoluminescence (PL) spectroscopy. PL spectra are shown in Fig. 5.15 (a), (c), and (e). PL spectra have a peak at  $\sim 2.4$  eV that is consistent with previous measurements on CdS nanowires [162, 221, 222]. Furthermore, the peak of the spectra weakly blueshifts as the fluence is increased from 25  $\mu\text{J}/\text{cm}^2$  to 400  $\mu\text{J}/\text{cm}^2$ , which has also been observed in CdS nanowires [222]. Wrapping the NWs in  $\text{C}_3\text{N}_5$  is found to make no significant change to the PL, as shown in Fig. 5.15. There is an extended tail of states residing at energies below the band gap. In CdS these are common, likely the result of disorder and surface states residing in the band gap, consistent with other measurements of PL performed on CdS Nanowires [221, 222].

Corresponding PL lifetimes measured at 2.46 eV are shown in Fig. 5.15 (b), (d), and (f), and the lifetime of  $\sim 500$  ps is also consistent with previous measurements in CdS nanowires, and bulk CdS crystals [162, 221]. We find that fluence does not significantly alter the lifetimes at moderate fluences. Interestingly, at 25  $\mu\text{J}/\text{cm}^2$  the lifetime is shorter, which implies the possibility of fluence-dependent quenching.

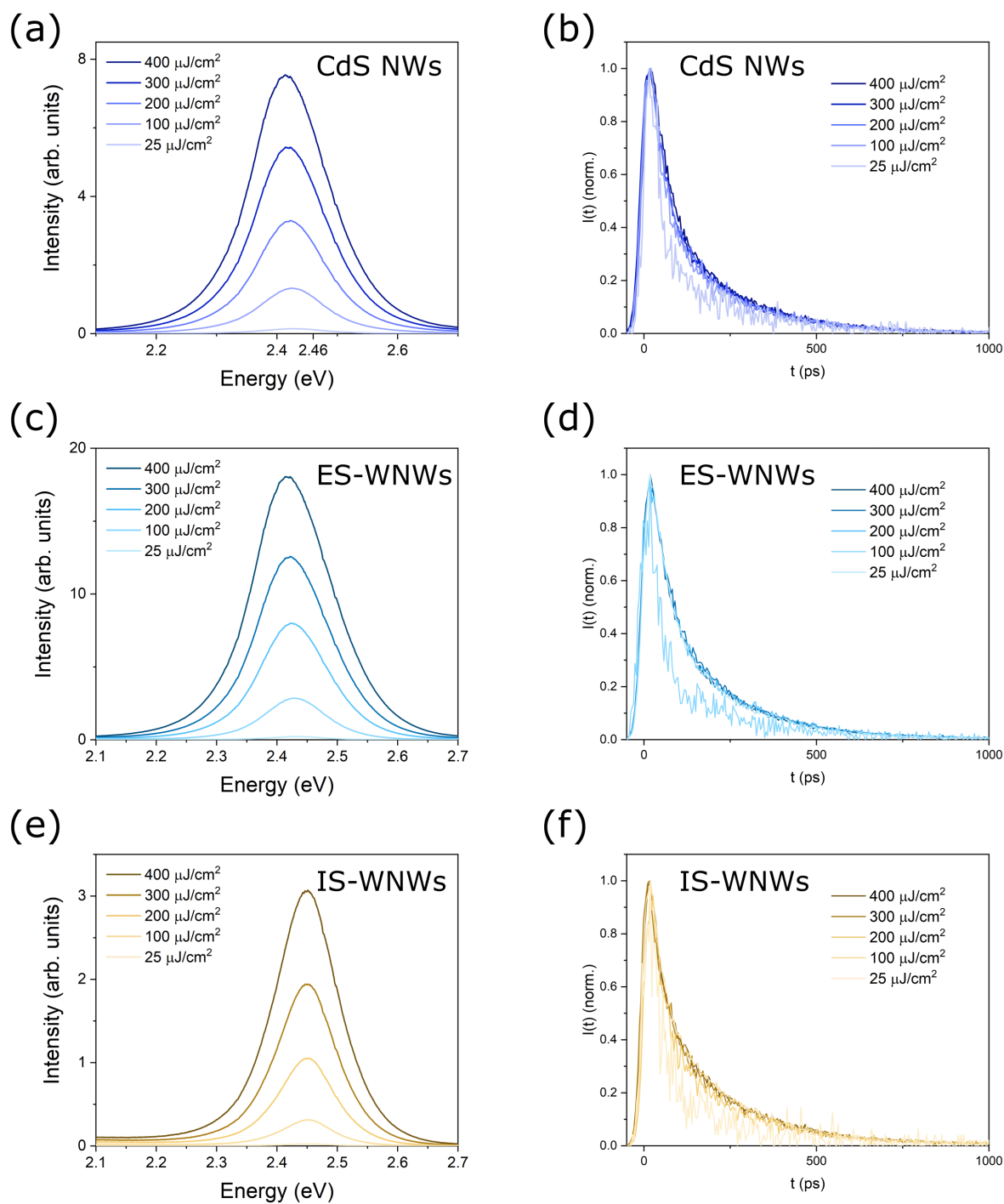


Figure 5.15: Fluence dependence of PL spectra and lifetimes. Lifetimes are acquired near the band-edge at 2.46 eV [170]. (a) Photoluminescence spectrum of CdS NWs. (b) Photoluminescence lifetime of CdS NWs. (c) Photoluminescence spectrum of ES-WNWs. (d) Photoluminescence lifetime of ES-WNWs. (e) Photoluminescence spectrum of IS-WNWs. (f) Photoluminescence lifetime of IS-WNWs.

### 5.3.5 Summary of Results

So far there have been many different results presented in this chapter. Here we wish to briefly summarize these results, and draw attention to observations that will be important later in this chapter.

Terahertz time-domain spectroscopy was performed to establish the equilibrium charge carrier density of bulk CdS and the CdS nanowires. Bulk CdS possesses an index of refraction of  $n \sim 2.95$  that monotonically increases in the THz spectrum. The imaginary part possesses peaks in the THz spectrum, with  $k \sim 0.02$ . The spectrum may be explained by absorption from phonon difference frequency modes, which may be explored in the future by measuring the temperature dependent absorption of the modes. For now, we note that there is no contribution from free charge carriers, as there is no significant Drude component to the fits. We draw a similar conclusion about the CdS nanowires under study. Our THz-TDS revealed a flat transmission spectrum in the THz regime, which indicates that there is no significant free-carrier absorption in any of the CdS nanowires under study. Later we will discuss the appropriate model of the conductivity spectra, and the lack of equilibrium free charge-carriers will play an important role.

Transient absorption of the THz pulses allowed us to measure the photoconductivity lifetime of a bulk CdS crystal and the CdS-NW films. In bulk CdS, the photoconductivity lifetimes exceed  $-\Delta\mathcal{E}/\mathcal{E}_{ref} \sim 20\%$  at a fluence of  $100 \mu\text{J}/\text{cm}^2$  due to the large absorption of the CdS crystal. For fluences above  $100 \mu\text{J}/\text{cm}^2$ , we observe saturation in the maximum  $-\Delta\mathcal{E}/\mathcal{E}_{ref}$ . The photoconductivity of CdS nanowires behaved differently than bulk. In all of the nanowire films, the lifetime was estimated using a biexponential fit, and the results at  $400 \mu\text{J}/\text{cm}^2$  agree well with the published results of Alam, Jensen et al. [69]. The fast lifetimes are  $\tau_1 \sim 50$  ps for the CdS-NWs and the ES-WNWs. For the IS-WNWs the fast lifetime is  $< 10$  ps. The long lifetimes of the CdS-NWs and ES-WNWs are  $\tau_2 \sim 300 - 400$  ps, while for the the IS-WNWs  $\tau_2 \sim 150$  ps. Later, in Section 5.4, we will compare the bulk and nanowire photoconductivity lifetimes to try and investigate how the morphology of CdS changes charge-carrier recombination.

Time-resolved terahertz spectroscopy was performed on a bulk CdS crystal and the CdS

nanowire films. In bulk, we fit the conductivity spectrum to a Drude model in order to estimate the mobility of charge carriers. We extract mobilities of  $\sim 100 \text{ cm}^2/\text{Vs}$ , which disagree with literature mobilities of  $\sim 440 \text{ cm}^2/\text{Vs}$  [203]. We believe the discrepancy arises from surface scattering because the  $\sim 110 \text{ nm}$  surface interaction length of the CdS crystal is larger than the  $\sim 90 \text{ nm}$  penetration depth of  $400 \text{ nm}$  radiation [170, 220]. We find that estimates provided by Kazmerski et al. yield a mobility of  $\sim 129 \text{ cm}^2/\text{Vs}$  which are the same order as our measurements of  $\sim 100 \text{ cm}^2/\text{Vs}$  [220]. As mentioned earlier, the photoconductivity spectra of the CdS nanowires will be discussed in more detail later. So here we showed only the extracted photoconductivity of the CdS-NWs, ES-WNWs, and the IS-WNWs taken at  $10 \text{ ps}$  after excitation. Although it is not immediately obvious, the photoconductivity in bulk CdS excitation densities of  $100 \mu\text{J}/\text{cm}^2$  was larger than the CdS nanowire samples at the same fluence. This is due to the  $100 \%$  fill fraction of the bulk.

The results of time-resolved photoluminescence spectroscopy of the CdS-NWs was also shown. We find luminescence spectra with maxima  $\sim 2.4 \text{ eV}$  which agree well with literature values of  $2.4 \text{ eV}$ . The PL lifetimes were measured at the band edge of  $2.46 \text{ eV}$  for all CdS nanowire samples. Comparing the photoluminescence and photoconductivity lifetimes of the nanowires will be an important part of the following section, as it will constrain the mechanisms involved in the charge-carrier lifetimes. Ultimately we will construct a model of charge carrier lifetimes that satisfies both the photoluminescence and photoconductivity lifetimes for the first time.

## 5.4 Discussion

### 5.4.1 Ultrafast Photoconductivity Spectra

#### Terahertz Photoconductivity in CdS Nanomaterials

In Chapter 2 we reviewed the various models of photoconductivity in this thesis. In the literature on CdS one finds many models are used to explain the terahertz photoconductivity in various CdS nanomaterials, and here we present a short review of these models. Briefly, these models fall into three categories: Drude-Smith, Monte-Carlo, and effective medium theories.

The Drude-Smith model has played a significant role in the interpretation of photoconductivity of CdS nanomaterials. In work by Li et al. the Drude-Smith model led to an understanding that band bending in CdS nanobelts can push photoexcited electrons to the center of the nanobelt and holes to the surface [216]. A Drude-Smith model was used on bandgap graded  $\text{CdS}_x\text{Se}_{1-x}$  nanowires and revealed that the grading can yield a bulk-like mobility of  $\sim 400 \text{ cm}^2/\text{Vs}$  [217]. As mentioned in the introduction to this chapter, the ultrafast photoconductivity in solution-grown CdS nanowires wrapped in  $\text{C}_3\text{N}_5$  nanosheets was recently reported by Alam et al., where it was found that charge-carrier localization can greatly reduce the long-range mobility [69]. Agreeing with high-resolution transmission electron micrographs (HR-TEM), the high crystallinity of the nanowires gave rise to a bulk-like short-range mobility of  $\sim 450 \text{ cm}^2/\text{Vs}$  (cf. Table 5.3). Due to charge-carrier localization, the long-range mobilities of the nanowire films were found to range from  $\sim 40 \text{ cm}^2/\text{Vs}$  in the highly crystalline films, and  $\sim 10 \text{ cm}^2/\text{Vs}$  in the disordered nanowire film.

The Maxwell-Garnett effective medium theory was used to study photoconductivity in CdS nanorods with a CdSe nanocrystal embedded in them [223]. They modelled the photoconductivity using a Maxwell-Garnett effective medium theory for prolate spheroids and report an incredibly high mobility of  $700 \pm 30 \text{ cm}^2/\text{Vs}$ . This is believed to be the result of suppressed electron-phonon scattering and quantum confinement induced mixing of the lowest conduction band states which alters the band structure.

Monte-Carlo simulations have played an important role in understanding the relevant interaction length scales in CdS nanocrystals. Mics et al. performed TRTS on films of 10 nm CdS nanocrystals and fit their photoconductivity to a Debye relaxation formula that was found to agree well with Monte-Carlo simulations [218]. They also fit their photoconductivity lifetimes to a Monte-Carlo model that takes into account the existence of two length scales for the interaction of electrons with the boundaries of the 10 nm CdS nanocrystal. They find that the probability of transferring across a nanocrystal barrier is dependent on charge-carrier density, going from 3 % to 34 % across their fluence range of  $\sim 40 - 170 \mu\text{J}/\text{cm}^2$ . Modelling the charge carrier lifetimes Mics et al. find that the initially-hot carrier mobility is  $\sim 33 \text{ cm}^2/\text{Vs}$  and the carrier mobility at the conduction band edge is  $\sim 96 \text{ cm}^2/\text{Vs}$ . [218].

## Modelling Photoconductivity in CdS Nanowires

Modelling the photoconductivity in CdS nanowires is difficult because there are many models that can fit our photoconductivity spectra, but they possess different physical interpretations. The goal of this section is to reduce the candidate models of photoconductivity, and so we will focus our attention to only the bare CdS nanowires for now. Figure 5.16 shows the photoconductivity spectra for CdS NWs taken at 25, 100, 200, 300, and 400  $\mu\text{J}/\text{cm}^2$ , at 10 ps after peak  $-\Delta\mathcal{E}/\mathcal{E}_{ref}$ .

Figure 5.16 (a) shows the results of fitting the spectra to the plasmon model [110, 224, 225]. The optical conductivity ( $\tilde{\sigma}(\omega)$ ) in the plasmon model is given by

$$\tilde{\sigma}(\omega) = \frac{(N_p + N_{eq})e^2}{m^*} \frac{i\omega}{\omega^2 - \omega_p^2 + i\omega\gamma} - \frac{N_{eq}e^2}{m^*} \frac{i\omega}{\omega^2 - \omega_{0,N_{eq}}^2 + i\omega\gamma}, \quad (5.14)$$

where  $N_{eq}$  is the equilibrium carrier density,  $N_p$  is the photoexcited carrier density,  $g$  is a geometric factor,  $\epsilon_0$  is the dielectric permittivity of free space,  $m^* = 0.23m_e$  is the electron conduction band mass where  $m_e$  is the free electron mass [226, 227],  $\gamma$  is the scattering rate,  $\omega_{p,PM}^2 = g(N_p + N_{eq})e^2/\epsilon_0m^*$ , and  $\omega_{(0,N_{eq})}^2 = gN_{eq}e^2/\epsilon_0m^*$ . This model has been used to determine the equilibrium carrier concentrations of InAs nanowires, InP nanowires, shell-doped GaAs nanowires, and n-doped Si nanowires [81, 228, 229], and can provide access to the charge-carrier mobility through  $\mu_{pl} = e/m^*\gamma$ .

Although the plasmon model fits our data well ( $\chi_{red}^2 \sim 2$ ), there are issues with this model that center around the fluence dependent plasma frequency. The plasma frequency in the plasmon model is proportional to the square root of the carrier density ( $\omega_{p,PM} \propto \sqrt{N_p + N_{eq}}$ ), yet, as shown in Fig. 5.16 (b) we see that  $\omega_{p,PM}$  (red spheres) does not increase significantly as the fluence is raised. This may be due to a significant density of equilibrium charge-carriers [110, 224, 225], however, our THz time-domain spectroscopy revealed no significant equilibrium charge-carrier density. This leads us to believe that another model is more appropriate.

The modified Drude-Smith model can be used to describe systems where nanoscale localization suppresses the low frequency (DC) conductivity of a material [167, 169]. Cocker et al. showed that the microscopic origin of the Drude-Smith model is diffusive back-action

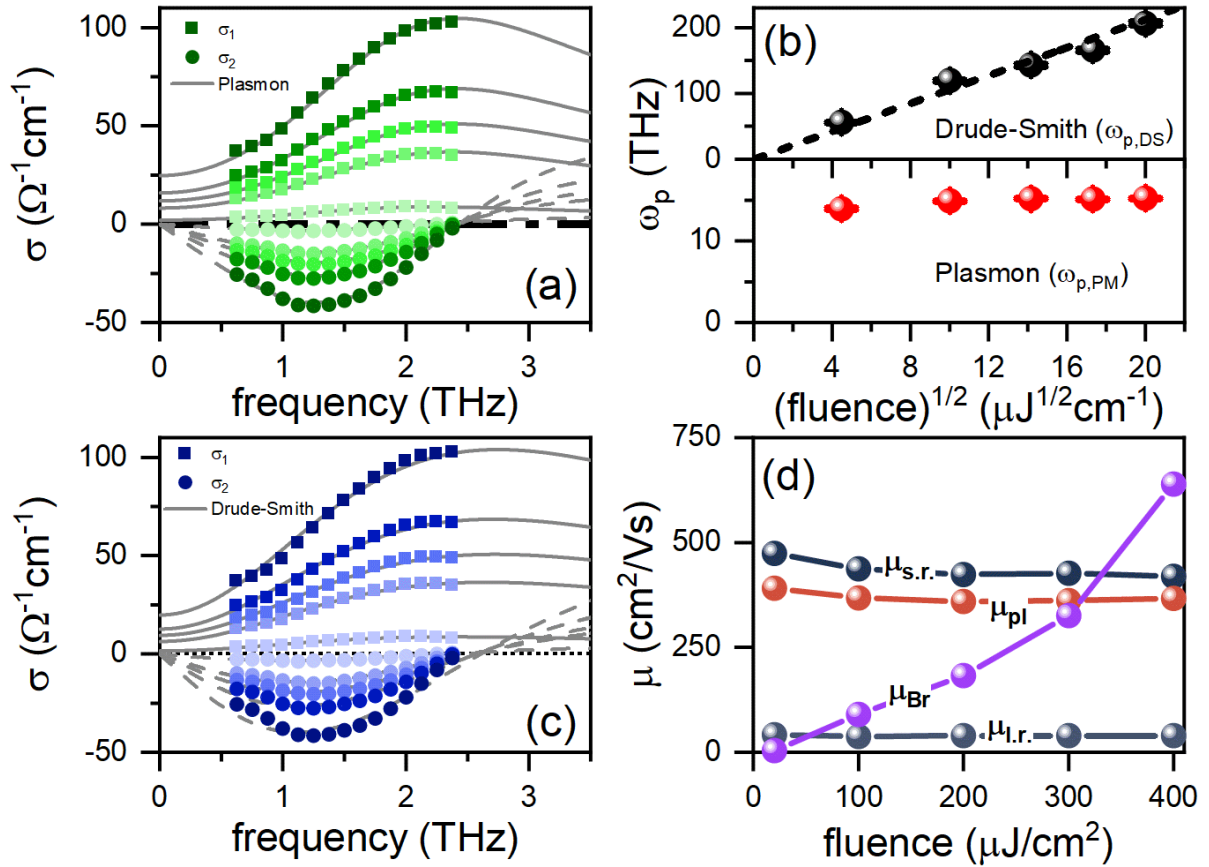


Figure 5.16: Modelling the THz photoconductivity for CdS NWs. (a) Fitting results to a Plasmon model. (b) Plasma frequency fluence dependence. Drude-Smith plasma frequency ( $\omega_{p,S}$ , black spheres) are shown to increase linearly with  $\sqrt{\text{fluence}}$ , as indicated by the dashed line. The plasma frequency of the Plasmon model ( $\omega_{p,PM}$ , red spheres) does not appear to increase linearly with  $\sqrt{\text{fluence}}$ . (c) Fitting results to the Drude-Smith model. (d) Fluence dependence of the Plasmon (red), Drude-Smith long-range (light green), Drude-Smith short-range (dark green), and Bruggeman mobilities (magenta). The photoconductivity spectra were measured at fluences of 400  $\mu\text{J}/\text{cm}^2$  (darkest), 300  $\mu\text{J}/\text{cm}^2$ , 200  $\mu\text{J}/\text{cm}^2$ , 100  $\mu\text{J}/\text{cm}^2$ , and 25  $\mu\text{J}/\text{cm}^2$  (lightest).

induced by a local density gradient from charge-carrier accumulation at the boundary of a finite square well [167].  $\tilde{\sigma}(\omega)$  is given by a phenomenological ansatz,

$$\tilde{\sigma}(\omega) = \frac{ne^2\tau}{m^*} \left( \frac{1}{1 - i\omega\tau} \right) \left( 1 + \frac{c}{1 - i\omega\tau'} \right) \quad (5.15)$$

where  $n$  is the charge-carrier density,  $\tau$  is the scattering time,  $\tau'$  is the effective scattering time,  $c$  is a function of the boundary reflectivity, and is bounded by 0 and -1.  $m^*$  is the conduction band electron effective mass and  $e$  is the elementary charge. The plasma frequency in the Drude-Smith model is given by  $\omega_{p,DS}^2 = ne^2/\epsilon_0 m^*$ . As shown in Fig. 5.16 (b), we find that  $\omega_{p,DS} \propto \sqrt{n} \propto \sqrt{\text{fluence}}$ . We also find that the Drude-Smith model fits the measurements well ( $\chi_{red}^2 \sim 3$ ), as shown in Fig. 5.16 (c). Furthermore, the plasma frequency extracted from this model scales proportional to the square root of the photoexcitation fluence, as indicated in Fig. 5.16 (b). At  $\omega = 0$ , the short-range mobility is given by  $\mu_{s.r.} = e\tau'/m^*$ , while the long-range mobility (suppressed by the diffusive back-action) is given by  $\mu_{l.r.} = \mu_{s.r.}(1 + c)$ . Our fits of the CdS-NWs to the modified Drude-Smith model are shown in Fig. 5.16 (c). For all of the fits, we found that  $\tau' = \tau$  within the fit certainty, which collapses the modified Drude-Smith model to the Drude-Smith model.

It can be shown that the Bruggeman effective medium theory reduces to the Maxwell-Garnett effective medium theory in the limit of small volume fill fraction [230]. The Bruggeman effective medium theory has found use in describing the photoconductivity of heterogeneous materials in situations where the fill fraction is large ( $f > 0.1$ ), similar to our CdS nanowire films [31, 55, 231–233]. The dielectric function for the heterogeneous nanowire system ( $\epsilon_{eff}$ ) can be found by solving

$$f \frac{\epsilon_{NW} - \epsilon_{eff}}{\epsilon_{NW} + \kappa\epsilon_{eff}} + (1 - f) \frac{\epsilon_h - \epsilon_{eff}}{\epsilon_h + \kappa\epsilon_{eff}} = 0 \quad (5.16)$$

where  $\kappa \approx 1$  is related to the depolarization factor for infinitely long oblate spheres,  $\epsilon_h = 1$  is the relative dielectric constant for the host medium when the nanowires are immersed in vacuum, and  $\epsilon_{eff}$  is the dielectric constant of the composite medium. The photoexcited nanowire is assumed to be conductive, following a Drude model  $\epsilon_{NW} = 1 + i \frac{ne^2\tau}{\epsilon_0\omega m^*} \frac{1}{1 - i\omega\tau}$  where  $1/\tau$  is the scattering rate and  $n$  is the charge carrier density. The charge-carrier mobility

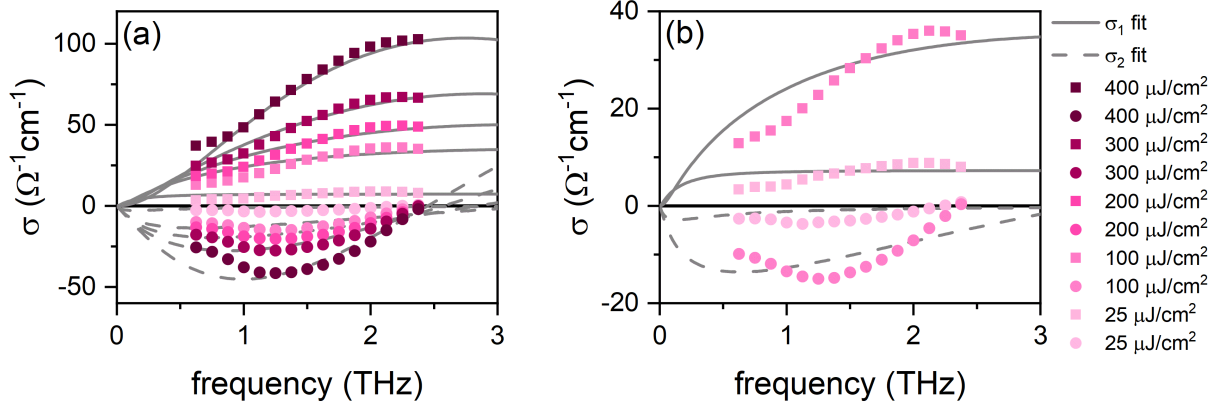


Figure 5.17: Real (square) and imaginary (circles) conductivity are fit to the real (grey line) and imaginary (dashed grey line) parts of the Bruggeman model. (a) Plot containing all of the fits performed on the bare CdS-NWs. (b) Only the 25  $\mu\text{J}/\text{cm}^2$  and 100  $\mu\text{J}/\text{cm}^2$  fits are shown because they are obscured in (a).

( $\mu_{Br}$ ) within the nanowire is then found via  $\mu_{Br} = e\tau/m^*$ . Since the dielectric function is related to the optical conductivity through  $\epsilon_{eff} = 1 + i\tilde{\sigma}(\omega)/\epsilon_0\omega$ , we can fit our THz conductivity spectra to the Bruggeman effective medium theory. The fits to the Bruggeman model are shown in Fig. 5.17. Figure 5.17 (a) contains the full set of fitted data for the CdS nanowires. Figure 5.17 (b) shows only the fits to the 25  $\mu\text{J}/\text{cm}^2$  and 100  $\mu\text{J}/\text{cm}^2$  data because they are obscured in Fig. 5.17 (a). Overall we find that the fit quality is very poor.

### Localized Carrier Dynamics in CdS Nanowires

In the previous section we showed the results of fitting the CdS nanowire photoconductivity to three important models of conductivity in nanomaterials. First, the plasmon model showed very good agreement with our data. However, we found that the plasma frequency is not increasing as the excitation density is increased. If plasmons were responsible for the measured dispersion, then the relation  $\omega_p \propto \sqrt{N_p}$  should hold, especially since our measurements from THz-TDS indicated no significant presence of background free carriers. Given the benefit of the doubt, and assuming that there is a background carrier density of  $N_{eq} = 4 \times 10^{18} \text{ cm}^{-3}$ , we still found that the expected scaling  $\omega_p \propto \sqrt{N_p + N_{eq}}$  did not hold. We therefore conclude that the plasmon model is not a suitable representation of our data, since the plasma frequency does not obey the predicted scaling.

Fitting the photoconductivity to the Bruggeman model resulted in poor fits. The poor

fit quality comes from the fact that the Bruggeman model requires a unique combination of fill fraction and carrier density to provide the desired spectral shape; an effect that has been observed in other densely packed nanowire systems [71]. Since the fill fraction was treated as a global parameter in the Bruggeman fits, and the carrier density was varied by changing the fluence, the model was not able to fit our data for all fluences. Furthermore, we find that the best-fit fill fraction for this sample is  $f \sim 0.203$ , which seems low compared to the dense packing we see in the SEM image in Fig. 5.1 (a). Finally, the mobilities from the Bruggeman fits are shown in Fig. 5.16 (d), and seem to exponentially rise as the fluence is increased. It is unclear how to interpret this result. We thus conclude that the Bruggeman model does not provide an accurate representation of our data.

The Drude-Smith model provided good fits to our data, while remaining self-consistent. The Drude-Smith model predicts that the entire photoconductivity spectrum scales as the fluence is increased, and this agrees well with the extracted carrier densities shown in Fig. 5.18 (a). Also, the results show that as the fluence approaches  $0 \mu\text{J}/\text{cm}^2$ , the carrier density goes to  $0 \text{ cm}^{-3}$ . This is consistent with our THz-TDS, which showed that there are no measurable free charge carriers in the CdS nanowires. The localization constant ( $c$ ) of the Drude-Smith model has received criticism for permitting a density-dependence that may be unphysical [115]. However, in Fig. 5.18 (b) we show that our localization constants agree within error for all of the fluences measured. The scattering time seems to be initially be  $\tau \sim 62 \text{ fs}$  at the fluence of  $25 \mu\text{J}/\text{cm}^2$ , but as the fluence is raised it quickly settles into a fairly constant value of  $\tau \sim 56 \text{ fs}$ . The Drude-Smith model is also supported by the dimensions of the CdS-NWs under study. As was found by Alam, Jensen et al., the time required for carriers to diffuse one radius of the nanowires was estimated to be  $\tau_D \approx 0.6 \text{ ps}$ . Therefore, in one cycle of THz radiation, it is expected that charge-carriers will accumulate near nanowire boundaries, forming a diffusive back-action that limits charge-carrier transport [167].

Finally, the Drude-Smith results agree well with measurements from literature. The short-range mobilities we extract are  $\mu_{s,r} \sim 400 \text{ cm}^2/\text{Vs}$ , which agrees very well with the mobility of  $\mu \sim 440 \text{ cm}^2/\text{Vs}$  seen in bulk CdS [203]. The long-range mobilities extracted from the Drude-Smith model ( $\sim 40 \text{ cm}^2/\text{Vs}$ ) agree well with field-effect transistor (FET) measurements of the long-range ( $\sim 1 \mu\text{m}$ ) mobilities in single solution-grown CdS nanowires

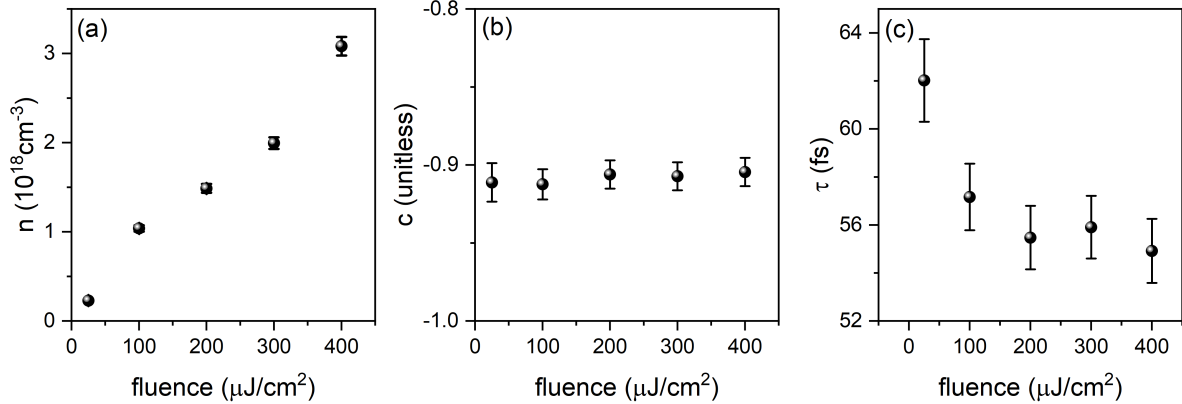


Figure 5.18: Drude-Smith fit parameters for the CdS-NWs. (a) Carrier density  $n$ , (b) localization parameter  $c$ , and (c) scattering time  $\tau$ .

( $\sim 62 \text{ cm}^2/\text{Vs}$ ) [49], providing consistency with alternative measurements of the mobility. Furthermore, inserting the nanowire diameter ( $2d = 50 \text{ nm}$ ) into the empirical relation Eq. (5.12) yields a nanowire mobility of  $\sim 80 \text{ cm}^2/\text{Vs}$ , which is the same order of magnitude as the long-range mobility (cf. Fig. 5.16 (d)). It is interesting that the mobility along a single nanowire is the same as the average mobility of the CdS nanowire film. However, as we saw earlier in TRTS on bulk CdS, diffuse surface scattering plays a significant role in limiting transport in CdS thin films [219, 220]. Therefore, the reduction in mobility is likely a consequence of the 50 nm nanowire diameter. Due to the quality of the fits, the self-consistency of the model, and the agreement with established literature, we will use the Drude-Smith model to fit the photoconductivity of the bare CdS-NWs as well as the wrapped CdS nanowires (ES-WNWs, and IS-WNWs).

The ex-situ wrapped nanowire (ES-WNW) and in-situ wrapped nanowire (IS-WNW) photoconductivities were fit to the Drude-Smith model. The fits are shown in Fig. 5.19 (a) and (b). The ES-WNW fits have a similar quality of fit as the CdS-NWs, with  $\chi_{red}^2 \sim 2$ . The IS-WNWs are well fit by the Drude-Smith model, where  $\chi_{red}^2 \sim 0.03$ .

The parameters of the Drude-Smith fits in Fig. 5.19 are shown in Fig. 5.20. Results of the ES-WNWs are shown as burgundy spheres, and the IS-WNWs are shown as purple spheres. Figure 5.20 (a) shows the carrier densities. We find that the carrier densities are higher in the IS-WNWs than in the ES-WNWs, which is the result of the large filling fraction of the IS-WNWs. Since the IS-WNWs are much shorter than the ES-WNWs, there are more nanowires

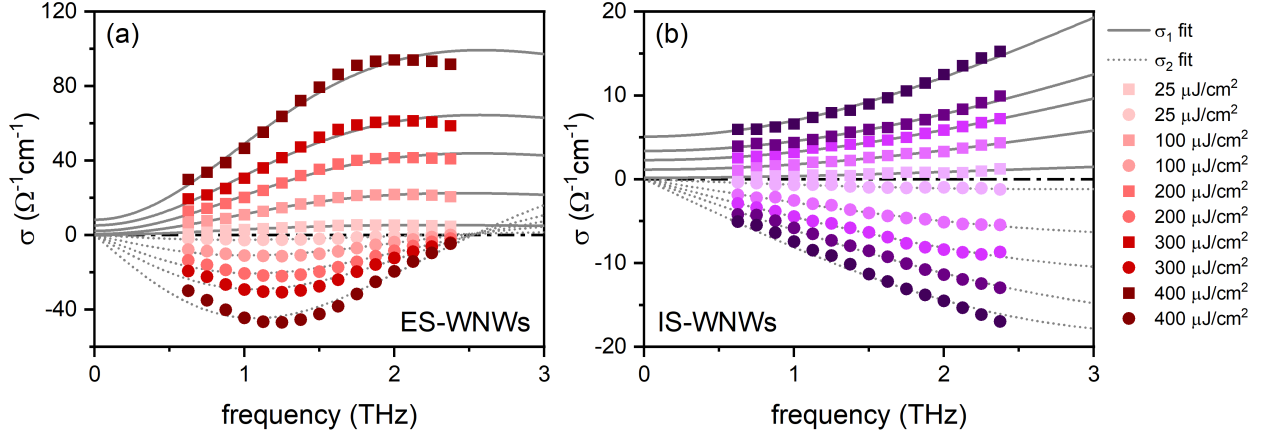


Figure 5.19: Drude-Smith fits of the ES-WNWs and the IS-WNWs. The real (square) and imaginary (circle) conductivities are fit to the real (solid grey lines) and imaginary (dotted grey lines) parts of the Drude-Smith model. (a) Drude-Smith fits of the ES-WNW photoconductivity. (b) Drude-Smith fits of the IS-WNWs.

per unit volume in the IS-WNW film (cf. Fig. 5.1). This would naturally raise the charge carrier densities. Initially, one might expect that the charge carriers in the IS-WNW film would also experience enhanced localization compared to the ES-WNWs, simply because the IS-WNWs are smaller. However, the fluence-dependent localization parameters in Fig. 5.20 (b) show that they agree within one error interval for some fluences, and two intervals for most fluences. The reason they agree is because although the IS-WNWs are smaller, the electrons in the ES-WNWs have a longer scattering time than carriers in the IS-WNWs. Localization in the wrapped nanowires is stronger than the unwrapped nanowires. This may be due to the van der Waals bond that attaches  $C_3N_5$  nanosheets to the surface of the nanowire. This may be altering the surface field in a way such that electrons and holes experience further localization. The scattering times are shown in Fig. 5.20 (c), where we find a scattering time of  $\sim 60$  fs in the ES-WNWs and  $\sim 20$  fs in the IS-WNWs. Compared to the unwrapped CdS nanowires, we find that the localization parameters in the wrapped nanowires are more than three error intervals from the unwrapped nanowires. The enhanced localization seen in the wrapped nanowires may be implying that wrapping the CdS-NWs in  $C_3N_5$  lowers the long range conductivity by creating insulating barriers between the CdS NWs. This is reflected in the long-range mobility of the wrapped nanowires ( $\mu_{l.r.} = (1 + c)e\tau/m^*$ ) shown in Fig. 5.20 (d). The long-range mobility of the bare CdS nanowires was found earlier to be  $\mu_{l.r.} \sim 40$

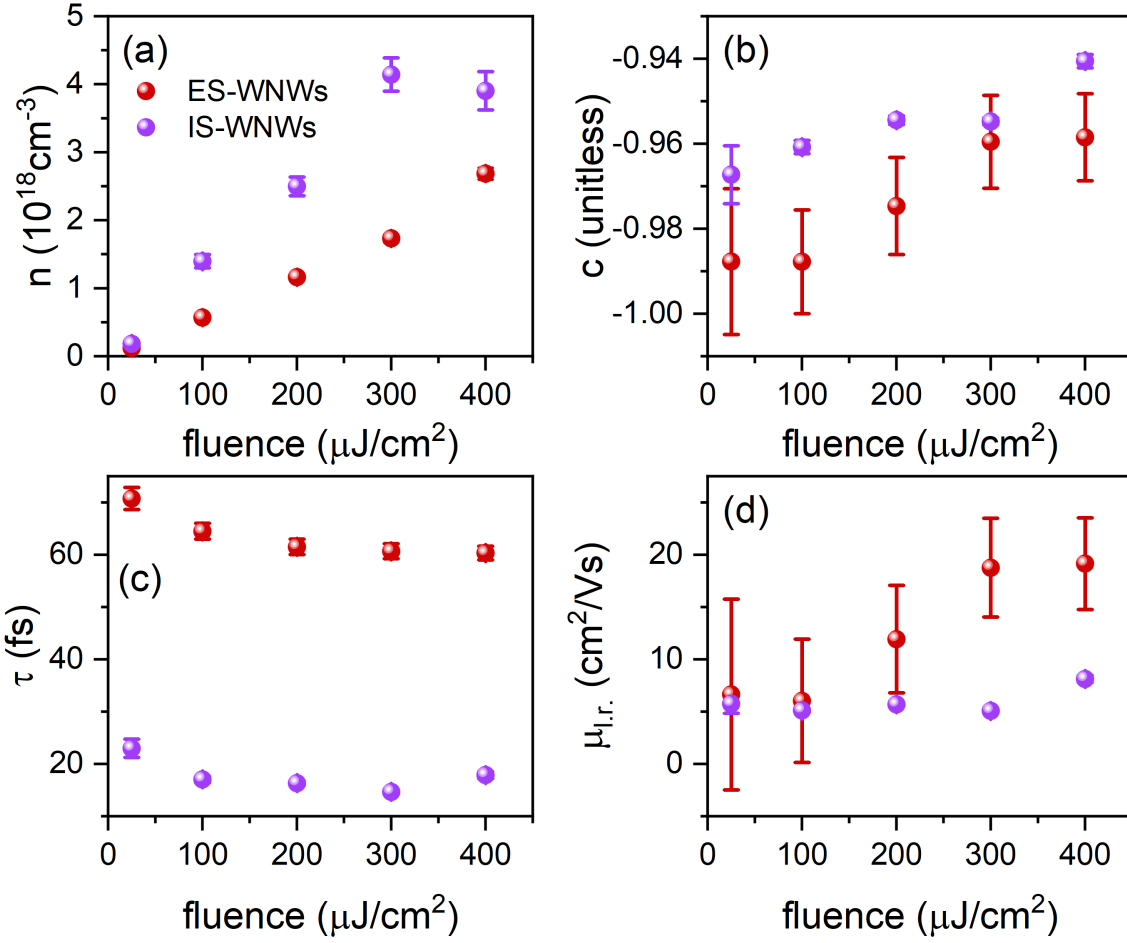


Figure 5.20: Best-fit parameters of the Drude-Smith fits on the wrapped CdS nanowires. Ex-situ wrapped nanowire results are shown in burgundy, and in-situ wrapped nanowire results are shown in purple. (a) Carrier density  $n$ , (b) localization constant  $c$ , (c) scattering time  $\tau$ , and long-range mobility  $\mu_{l,r} = (1 + c)\mu_{s,r}$ .

cm<sup>2</sup>/Vs, but in Fig. 5.20 (d) we find that the wrapped nanowires have  $\mu_{l,r} \sim 10$  cm<sup>2</sup>/Vs.

Our evidence from TRTS of bulk CdS and the CdS-NW films indicates that surfaces play a large role in the ultrafast carrier dynamics of CdS. Along with a suppressed mobility [219, 220], surface interactions also induce surface recombination [162]. Surface recombination can be modelled by solving the 1-D diffusion equation (cf. Section 2.2.3) [162]

$$\frac{\partial n(x,t)}{\partial t} = G(x,t) + D^* \frac{\partial^2 n(x,t)}{\partial x^2} - \frac{n(x,t)}{\tau_{rec}}, \quad (5.17)$$

where  $n(x,t)$  is the charge carrier density,  $G$  is the charge carrier excitation profile,  $D^*$  is the

ambipolar diffusion coefficient, and  $\tau_{rec} = 20$  ns is the recombination lifetime in CdS [162]. Surface recombination is then modelled as a boundary condition

$$\left. \frac{\partial n(x, t)}{\partial x} \right|_{x=0} = \frac{S_0}{D^*} n(x = 0, t), \quad (5.18)$$

where  $S_0$  is the surface recombination velocity. In the following sections we will solve the diffusion equation to model the charge-carrier lifetimes, but for now we note that the diffusion equation and the boundary conditions are directly dependent on the ambipolar diffusion coefficient  $D^*$ . From our fits to the photoconductivity, we are able to extract  $D^*$  for each nanowire film and bulk CdS.

In bulk CdS the ambipolar diffusivity is  $D^* = 1.2$  cm<sup>2</sup>/s [162]. From our spectroscopy,  $D^*$  can be found via Eq. (2.79), such that

$$D^* = \frac{\mu_e \mu_h}{\mu_e + \mu_h} \frac{k_B T}{q}, \quad (5.19)$$

where  $\mu_e$  and  $\mu_h$  are the electron and hole mobilities in CdS,  $T = 300$  K is the temperature,  $k_B$  is the Boltzmann constant, and  $q$  is the elementary charge. Using a hole mass that of  $m_h = 0.6m_e$  [5], and assuming that the scattering time is equal for holes and electrons, our TRTS yields the diffusivities in Fig. 5.21. We find that our results ( $\sim 1.3$  cm<sup>2</sup>/s) are in moderate agreement with the literature value of 1.2 cm<sup>2</sup>/s.

For the diffusivities of the CdS nanowire films, we follow the work of Cocker et al. [167]. In the modified Drude-Smith model, the effective scattering rate  $\tau'$  is given by a sum of contributions from bulk scattering ( $\tau$ ) and boundary scattering ( $\tau_{Bound}$ ), such that

$$\frac{1}{\tau'} = \frac{1}{\tau} + \frac{1 + c}{\tau_{Bound}}. \quad (5.20)$$

In the limit that  $\tau$  becomes large compared to  $\tau_{Bound}$ ,  $\tau'$  is dominated by interactions with the boundary. In CdS it is known that the holes are significantly heavier than the electrons, and as a result the holes lower the ambipolar diffusivity of the nanowire network [226, 227]. When boundary scattering dominates the diffusivity of the holes within a single NW, the

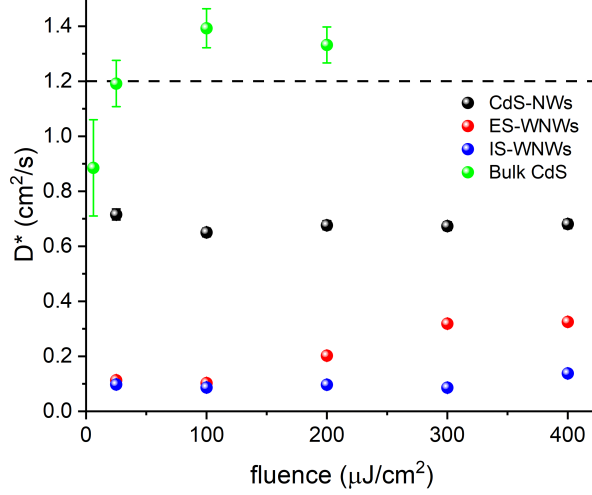


Figure 5.21: Ambipolar diffusivity of the CdS-NWs (black), ES-WNWs (red), and IS-WNWs (blue) calculated from the Drude-Smith fits via Eq. (5.22). Green spheres are the measured  $D^*$  from bulk CdS, and the dashed line is the accepted value for bulk CdS in literature.

short-range hole diffusivity can be expressed as [167]

$$D_{s.r.}^* = \frac{\tau' k_B T}{m_h^*} \approx \frac{k_B T}{m_h^*} \left( \frac{\tau_{Bound}}{1 + c} \right) \quad (5.21)$$

where  $T$  is the temperature of the carriers,  $k_B$  is the Boltzmann constant, and  $m_h^* = 0.6m_e$  is the hole effective mass [227]. The long-range diffusion constant can be determined from  $D_{s.r.}^*$  through  $D_{l.r.} = (1 + c)D_{s.r.}^*$ . Since holes dominate the diffusivity, we now make the approximation

$$D^* = \frac{2D_e D_h}{D_e + D_h} \approx 2D_h = 2D_{l.r.} \quad (5.22)$$

Figure 5.21 shows the fluence dependence of  $D^*$  for the CdS NWs, ES-WNWs, and IS-WNWs. We find that the ambipolar diffusivity in the wrapped nanowire networks is significantly lower than the unwrapped nanowires, implying that the wrapping layer serves to insulate transport across the nanowire boundary [167]. The diffusion constants for the CdS nanowire films will play a significant role in the diffusion simulations that govern the charge-carrier lifetimes.

## 5.4.2 Modelling Charge-Carrier Lifetimes

### Charge-Carrier Lifetimes in CdS and CdS Nanomaterials

In this section we will model the charge carrier lifetimes in our CdS nanowire films. To begin, let us compare our measurements of photoconductivity lifetimes against the corresponding photoluminescence lifetimes. Figure 5.22 shows the photoconductivity (blue) and the photoluminescence (orange) lifetimes in bare CdS nanowires at a fluence of  $400 \mu\text{J}/\text{cm}^2$ . The inset shows the first 50 ps of the photoconductivity lifetime. From Fig. 5.22 it is clear that the two lifetimes behave dramatically different, despite the fact that they are both related to the charge carrier lifetimes. In the early photoconductivity we see a slow rise that takes  $\sim 5$  ps for the photoconductivity to reach its maximum. For both of the lifetimes we see a fast initial recombination in the first  $\sim 100$  ps. Afterwards the photoconductivity begins to plateau, while the photoluminescence continues to quickly decay. The slow rise of the photoluminescence is the result of the 40 ps time resolution of our time-correlated single photon counting system (see Section 4.3 for more details). We find similar features in all of the recorded lifetimes.

To begin formulating a model to describe the charge-carrier lifetimes, we will examine the current understanding of photoluminescence in CdS crystals. Measurements of the band-edge ultrafast time-resolved photoluminescence were performed by Huppert et al. in the late 1980s and early 1990s [162, 234–236]. It is common to begin by describing the charge carrier lifetimes with a 1-D diffusion equation

$$\frac{\partial n(x, t)}{\partial t} = G(x, t) + D^* \frac{\partial^2 n(x, t)}{\partial x^2} - \frac{n(x, t)}{\tau_b} \quad (5.23)$$

where  $1/\tau_b$  is the bulk recombination rate,  $G(x, t)$  is the excitation profile, and  $D^*$  is the ambipolar diffusion constant [87, 161, 162]. Initially, there are no charge carriers, and so the initial condition is given by  $n(x, t = 0) = 0$ . Carriers are generated by modelling the photoexcitation as a gaussian distribution  $G(x, t)$ ,

$$G(x, t) = A \exp\left(-\frac{(t - t_0)^2}{w^2}\right) \exp\left(-\frac{x}{\delta}\right) \quad (5.24)$$

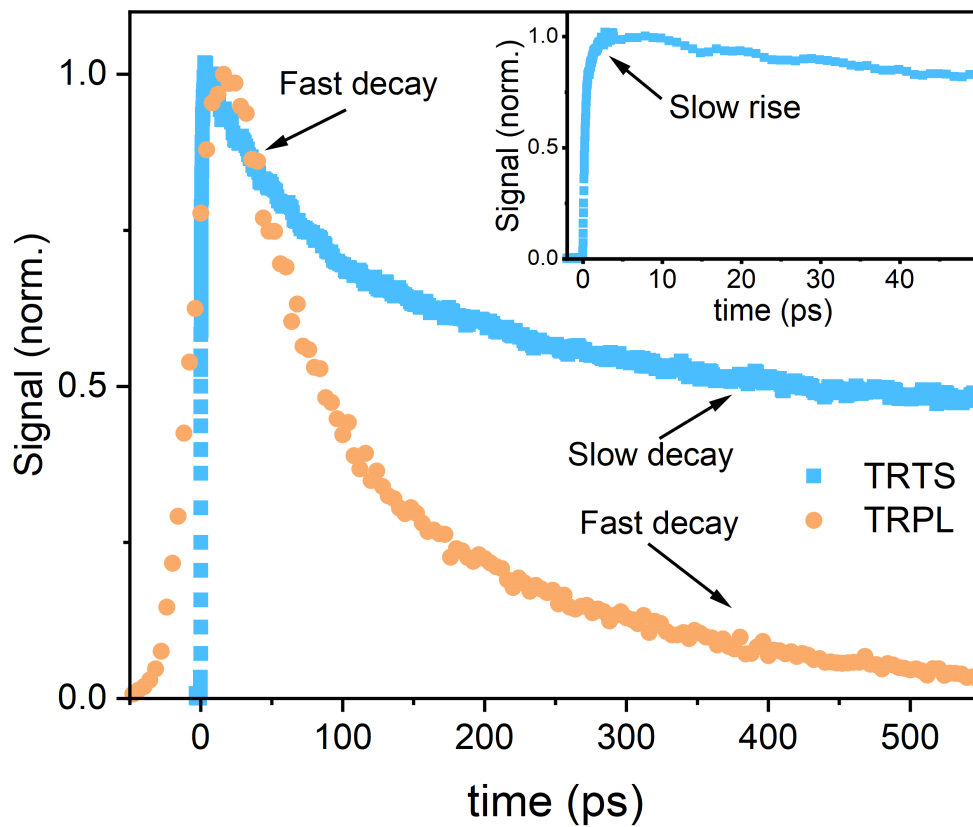


Figure 5.22: Comparing photoconductivity (blue) and photoluminescence (orange) lifetimes. The lifetimes both show an initially fast decay, but the photoconductivity outlasts the photoluminescence. Inset: First 50 ps after excitation shows a slow onset to the photoconductivity.

where  $\delta$  is the penetration depth of 400 nm radiation (90 nm [170]),  $A$  is the amplitude of the excitation pulse,  $w$  is the temporal duration of the excitation, and  $t_0$  is the time of excitation [162]. Since photoluminescence requires an electron and hole to recombine at the band edge, the probability of a recombination event is proportional to the product of the electron ( $n$ ) and hole densities ( $p$ ). When the excitation produces more electrons and holes than the background carriers,  $n \sim p$ , and so we may write [161]

$$I(t) \propto \int_0^{\infty} n^2(x, t) e^{-x/\delta} dx, \quad (5.25)$$

where the exponential decay comes from reabsorption of the luminescence within the crystal. As we found in our own work, surface physics is important when exciting CdS with 400 nm radiation. To model recombination at surface states, Huppert et al. use the boundary condition

$$\left. \frac{\partial n(x, t)}{\partial x} \right|_{x=0} = \frac{S_0}{D^*} n(x=0, t), \quad (5.26)$$

where  $S_0$  is the surface recombination velocity. Fitting the measured photoluminescence to this model allowed Huppert et al. to systematically study how changes in the CdS surface can impact recombination dynamics. An immediate benefit of this model is that it can be used to model the photoconductivity lifetime. Since  $\sigma \propto n$ ,  $\sigma$  can be modelled through

$$\sigma(t) \propto \int_0^{\infty} n(x, t) dx, \quad (5.27)$$

which provides an avenue to simultaneously model the photoconductivity and photoluminescence lifetimes. Initially, we attempted to fit our results to this model, however, it was not able to explain the slow rise in the photoconductivity or the long-lived photoconductivity.

To extend the surface recombination model, we will need to encompass hot carrier cooling. Since the band gap of CdS is 2.46 eV, and we are photoexciting the CdS with 3.1 eV photons, the photoexcited charge carriers have an excess energy of  $\sim 640$  meV. This is not enough energy for intervalley effects to become significant, and so we believe that the slow rise in conductivity is due to hot carriers cooling from a low mobility part of the conduction band.

However, the description of hot carrier cooling requires a multi-level rate equation of the form given in Refs. [158, 228] (cf. Section 2.1.5). Therefore, in order to encompass hot carrier cooling, the Eq. (5.23) will take on the modified form

$$\begin{aligned}\frac{\partial n_{hot}}{\partial t} &= G(x, t) - \frac{n_{hot}}{\tau_{cool}} \\ \frac{\partial n_{cool}}{\partial t} &= \frac{n_{hot}}{\tau_{cool}} + D^* \frac{\partial^2 n_{cool}}{\partial x^2}\end{aligned}\tag{5.28}$$

where  $n_{hot}$  are the hot carriers,  $n_{cool}$  are the carriers at the conduction band edge, and  $\tau_{cool}$  is the cooling time constant. This model would describe the early charge carrier lifetimes well, however, we find that the photoconductivity seems to flatten out at later times.

In recent work on semiconductor nanowires, side-by-side comparisons of  $I(t)$  and  $\sigma(t)$  have been used to elucidate the presence of twin defects in InP and GaAs nanowires [80, 82, 237]. The photoconductivity is found to far outlast the photoluminescence in these nanowires, and the most likely cause of such an observation is the discontinuous energy landscape caused by twin-defects [80, 82, 237]. The discontinuous energy landscape separates charge carriers, which, in turn, quenches the photoluminescence while sustaining the photoconductivity [82]. This observation is often corroborated with measurements of the nanowire crystallinity such as high resolution transmission electron microscopy (HR-TEM) [82, 238] which provides a very strong argument in favor of charge separation. To enable charge separation in Eq. (5.28), we introduce a monomolecular decay of charge carriers from the bottom of the conduction band into a separated state.

$$\begin{aligned}\frac{\partial n_{hot}}{\partial t} &= G(x, t) - \frac{n_{hot}}{\tau_{cool}} \\ \frac{\partial n_{cool}}{\partial t} &= \frac{n_{hot}}{\tau_{cool}} + D^* \frac{\partial^2 n_{cool}}{\partial x^2} - \frac{n_{cool}}{\tau_{sep}} \\ \frac{\partial n_{sep}}{\partial t} &= \frac{n_{cool}}{\tau_{sep}}\end{aligned}\tag{5.29}$$

where  $n_{sep}$  are the carriers in the separated state. Finally, since electron-hole recombination requires two species to interact, the cool carriers will recombine proportional to the square

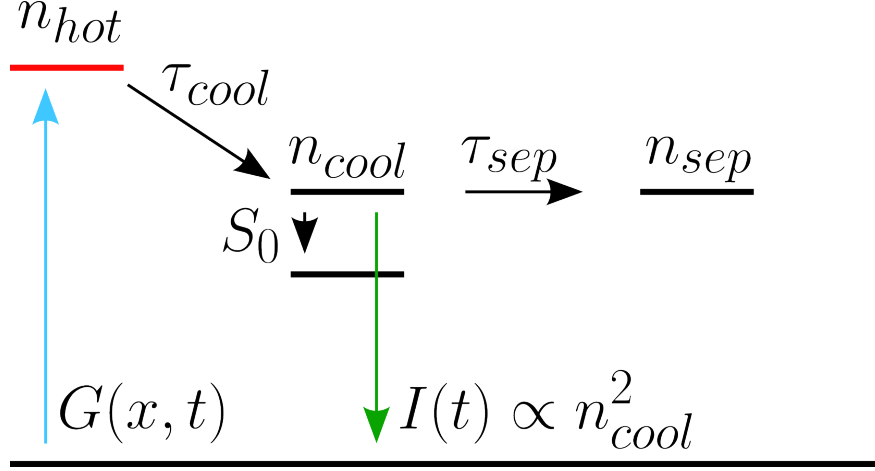


Figure 5.23: Schematic of carrier relaxation in CdS nanowires. Hot carriers are excited by the 400 nm excitation beam  $G$ . Hot carriers cool over the timescale  $\tau_{cool}$  to the bottom of the conduction band, where they join the population of cool carriers  $n_{cool}$ . Surface recombination occurs on the surfaces via midgap states. Cool carriers gradually become separated carriers ( $n_{sep}$ ) over the timescale  $\tau_{sep}$ .

of the carrier density. The final model will thus have the form

$$\begin{aligned}
 \frac{\partial n_{hot}}{\partial t} &= G(x, t) - \frac{n_{hot}}{\tau_{cool}} \\
 \frac{\partial n_{cool}}{\partial t} &= \frac{n_{hot}}{\tau_{cool}} + D^* \frac{\partial^2 n_{cool}}{\partial x^2} - \frac{n_{cool}}{\tau_{sep}} - \beta n_{cool}^2 \\
 \frac{\partial n_{sep}}{\partial t} &= \frac{n_{cool}}{\tau_{sep}}
 \end{aligned} \tag{5.30}$$

where,  $\beta$  is the bimolecular recombination coefficient. The decay pathways encompassed by Eq. (5.30) are shown schematically in Fig. 5.23.

It is assumed that the separated charge carriers and the hot carriers do not undergo surface recombination. Therefore we implement the Neumann boundary conditions for  $n_{hot}(x, t)$  and  $n_{sep}(x, t)$ . The Neumann boundary conditions give perfect reflection at the boundaries, and the conditions are stated as

$$\begin{aligned}
 \left. \frac{\partial n_{hot}(x, t)}{\partial x} \right|_{x=0, x=d} &= 0, \\
 \left. \frac{\partial n_{sep}(x, t)}{\partial x} \right|_{x=0, x=d} &= 0,
 \end{aligned} \tag{5.31}$$

where,  $d = 50$  nm is the diameter of the nanowires. For the carriers near the band edge we use a surface recombination boundary condition where

$$\begin{aligned} \left. \frac{\partial n_{cool}(x, t)}{\partial x} \right|_{x=0} &= -\frac{S_0}{D^*} n(x = 0, t) \\ \left. \frac{\partial n_{cool}(x, t)}{\partial x} \right|_{x=d} &= -\frac{S_0}{D^*} n(x = d, t) \end{aligned} \quad (5.32)$$

where  $S_0$  is the surface recombination velocity, and  $D^*$  is the ambipolar diffusivity. For numerical implementation of these conditions see Appendix A.

### Example Fit

Here we show a simultaneous fit of the photoconductivity and photoluminescence lifetimes shown in Fig. 5.22. The data in Fig. 5.22 are taken on the bare CdS nanowires, with an excitation density of  $400 \mu\text{J}/\text{cm}^2$ . The Drude-Smith fits yield an ambipolar diffusivity of  $D^* = 0.68 \pm 0.01 \text{ cm}^2/\text{s}$  (cf. Fig. 5.21). The only fit parameters are the cooling time scale,  $\tau_{cool}$ , the separation timescale,  $\tau_{sep}$ , the surface recombination velocity,  $S_0$ , and the bimolecular recombination coefficient,  $\beta$ . For this fit we found  $\tau_{cool} = 0.370 \pm 0.006$  ps,  $\tau_{sep} = 231 \pm 2$  ps,  $S_0 = (0.94 \pm 0.04) \times 10^4 \text{ cm/s}$ , and  $\beta = 0.01 \pm 0.002 \text{ cm}^2/\text{s}$ .

Figure 5.24 shows the evolution of the charge carrier distribution  $n(x, t)$ . In Fig. 5.24 (a) we show  $n(x, t)$  at the moment of excitation. Carriers are excited into the hot carrier state, which has an exponential fall off in  $x$ . Because of the 100 fs Gaussian excitation, some carriers were excited into  $n_{hot}$  before the maximum of the Gaussian distribution. Some of these carriers have already cooled into the bottom of the conduction band, and now occupy  $n_{cool}$ . Within 10 ps the hot carriers have cooled to the bottom of the conduction band, as seen in Fig. 5.24 (b). Figure 5.24 (b) also shows early signs of surface recombination, as the carrier density is lowered at the leftmost boundary ( $x = 0$ ). By 10 ps there is also a very small population of separated charge carriers. In Fig. 5.24 (c) we see that by 150 ps the band edge charge carriers,  $n_{cool}$ , are outnumbered by the separated charge carriers,  $n_{sep}$ .

Figure 5.25 shows how the carrier density is used to compute the conductivity and luminescence lifetimes. For each time step in the numerical solution of Eq. (5.30) we compute

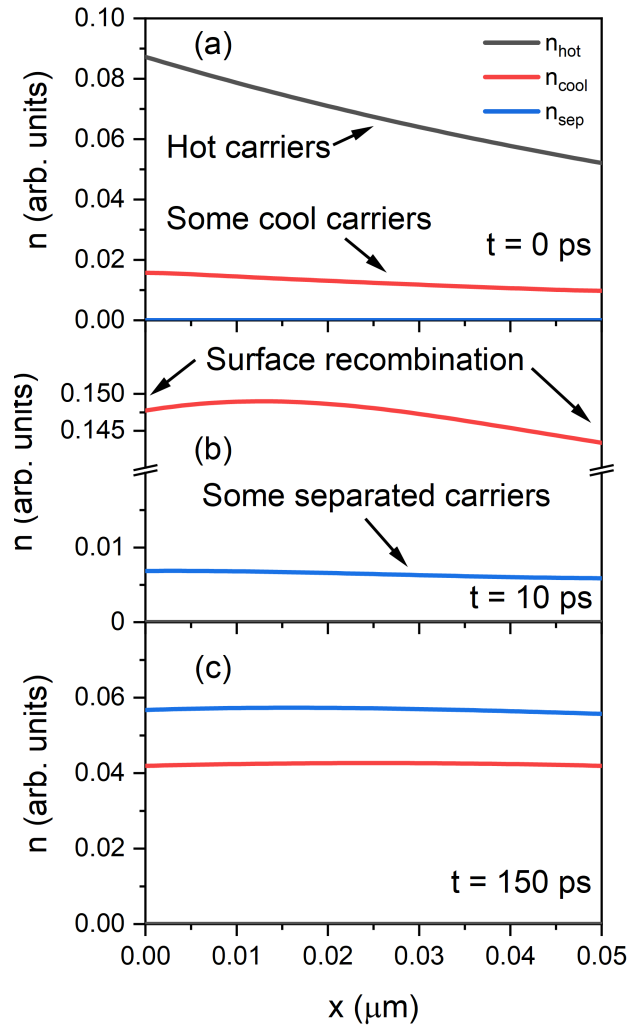


Figure 5.24: Spatial evolution for charge carriers in CdS NWs. (a) Carrier profile at the time of maximum excitation. The majority of carriers are hot carriers  $n_{hot}$ . (b) Carrier profile at 100 ps after excitation. At this point hot carriers have cooled to the bottom of the conduction band. (c) Carrier profile at 400 ps. At this stage some of the cool carriers have become separated. The effects of surface recombination are also visible, as the density of cool carriers near the surface is suppressed.

the total carriers contributing to the conductivity via

$$\sigma(t) \propto n_{tot}(t) = \int_0^L n_{cool}(x, t) dx + \int_0^L n_{sep}(x, t) dx. \quad (5.33)$$

To model the photoluminescence we use the relation [87, 161, 234]

$$I(t) \propto \int_0^\infty n_{cool}^2(x, t) e^{-x/\delta} dx. \quad (5.34)$$

where,  $\delta = 90$  nm is the penetration depth of 400 nm light in CdS [170]. To incorporate the 40 ps response time of the TRPL system, the simulated  $I(t)$  is convolved with a Gaussian function possessing a 40 ps FWHM. The photoluminescence and photoconductivity simulations are then normalized individually for the fitting process.

An example of the computed carrier lifetimes is shown in Fig. 5.25 (a). Carriers are excited into  $n_{hot}$  at  $t = 0$ . Within 2 ps the carriers cool into  $n_{cool}$ , as seen in the inset of Fig. 5.25 (a). Initially there is a fast decay of  $n_{cool}$ , and this is the result of surface recombination (cf. Fig. 5.24 (c)). There is a gradual increase in the separated charge carriers, which prolongs the total carrier density  $n_{tot}$ . The corresponding fit is shown in Fig. 5.25 (b). The conductivity (red dots) and luminescence (blue dots) are remarkably well described by the model ( $\chi_{red}^2 = 0.77$ ) given that it only contains four fit parameters.

## Fitting Lifetimes

Below we present the results of the simultaneous fitting of the photoconductivity and photoluminescence lifetimes in our CdS nanowire samples. The fluence dependent fits of the bare CdS-NWs are shown in Fig. 5.26. Figures 5.26 (a), (b), (c), (d), and (e) correspond to fluences of 400, 300, 200, 100, and 25  $\mu\text{J}/\text{cm}^2$ , respectively. Figure 5.27 contains the fits for the ex-situ wrapped nanowires (ES-WNWs). Figures 5.27 (a), (b), (c), (d), and (e) correspond to fluences of 400, 300, 200, 100, 25  $\mu\text{J}/\text{cm}^2$ , respectively. Figure 5.28 contains the fits for the ex-situ wrapped nanowires (ES-WNWs). Figures 5.28 (a), (b), (c), (d), and (e) correspond to fluences of 400, 300, 200, 100, 25  $\mu\text{J}/\text{cm}^2$ , respectively.

Figure 5.29 shows the results of the fluence-dependent lifetime fits. In Fig. 5.29 (a) we

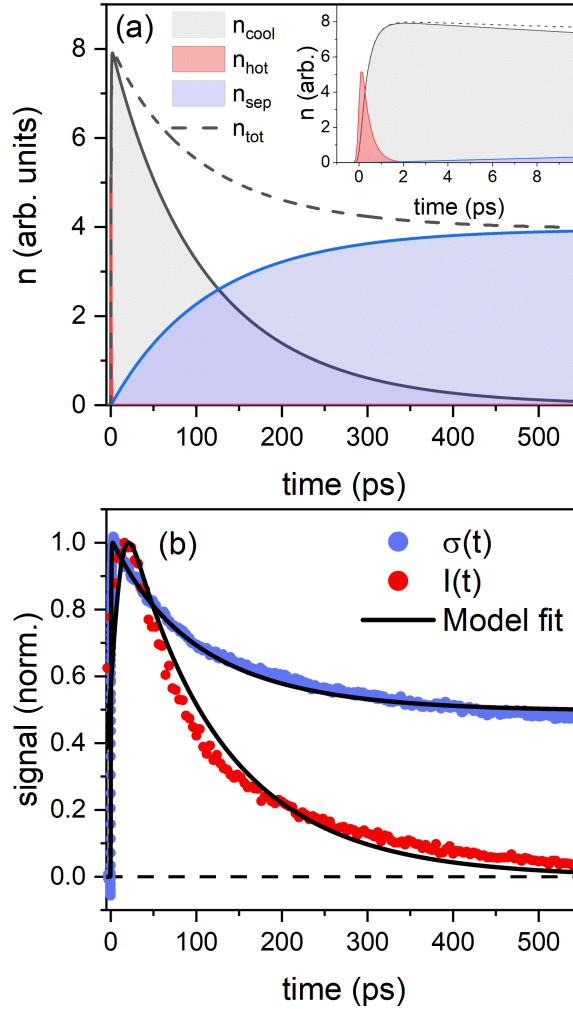


Figure 5.25: Simultaneous fit of the photoconductivity and photoluminescence lifetimes of CdS NWs excited at  $400 \mu\text{J}/\text{cm}^2$ . (a) Free carrier transients. Carriers are initially excited into  $n_{hot}$  (red), and quickly decay into  $n_{cool}$ . Surface recombination lowers  $n_{cool}$  steadily as charge separation slowly sustains the carrier population. (b) Photoluminescence  $I(t)$  and photoconductivity  $\sigma(t)$  fit to the model as discussed above.

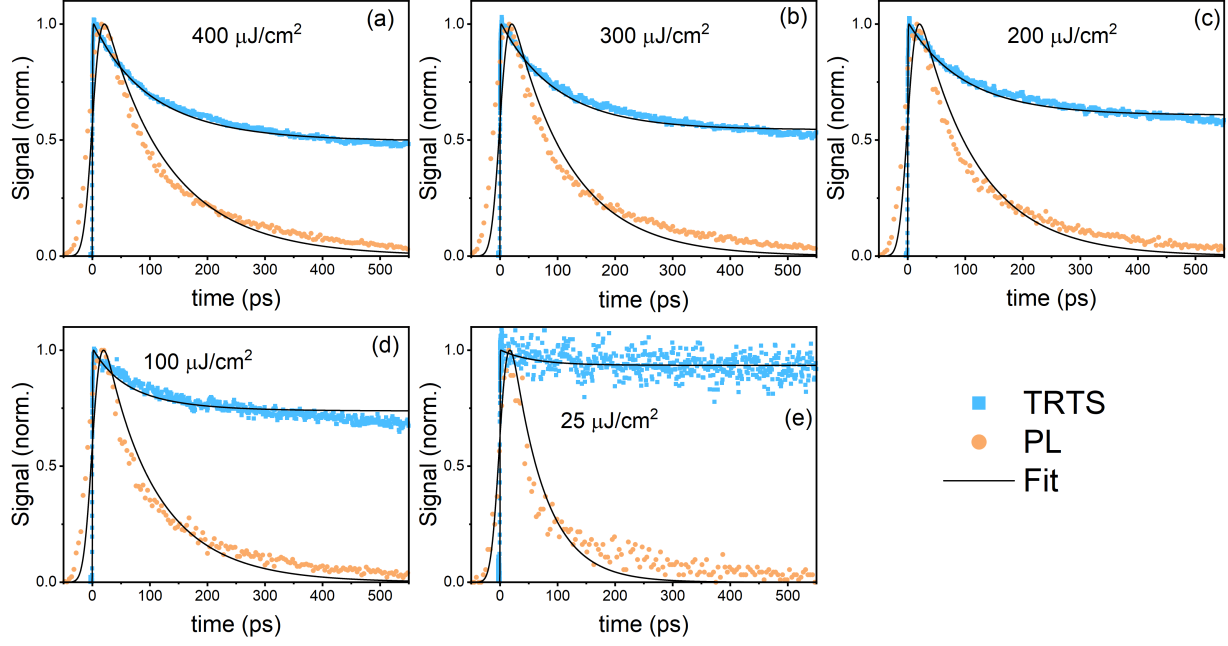


Figure 5.26: Fluence dependent fits of the bare CdS-NWs lifetimes. (a), (b), (c), (d), and (e) correspond to fluences of 400, 300, 200, 100, and 25  $\mu\text{J}/\text{cm}^2$ , respectively.

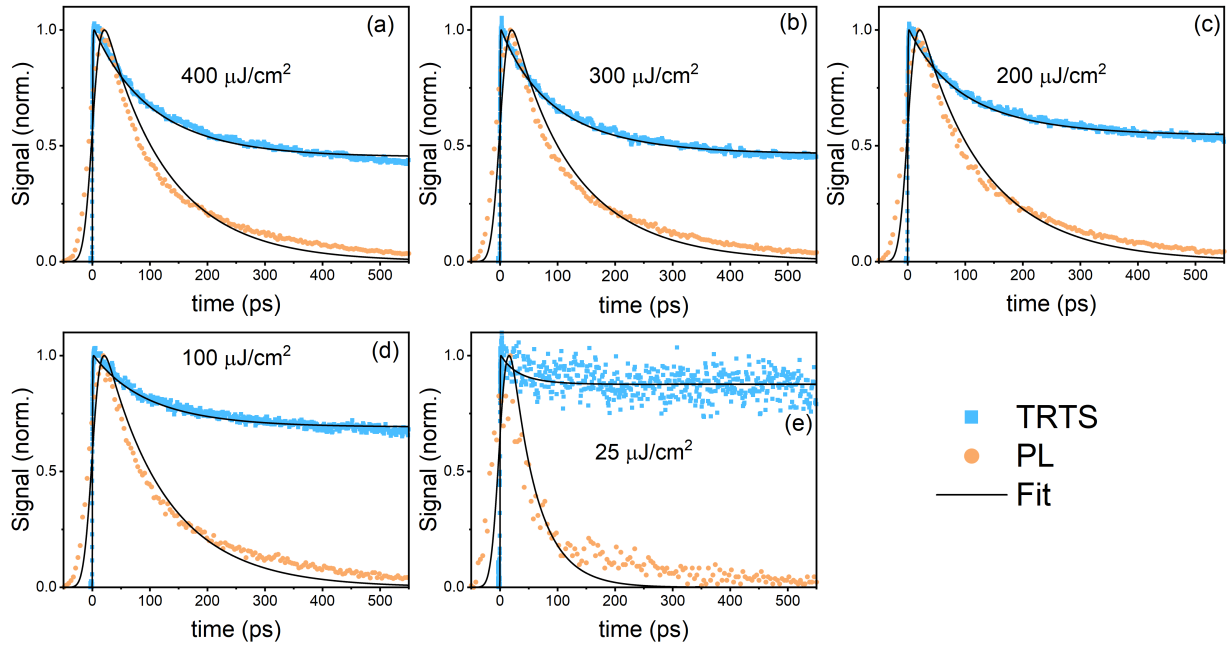


Figure 5.27: Fluence dependent fits of the ES-WNW lifetimes. (a), (b), (c), (d), and (e) correspond to fluences of 400, 300, 200, 100, and 25  $\mu\text{J}/\text{cm}^2$ , respectively.

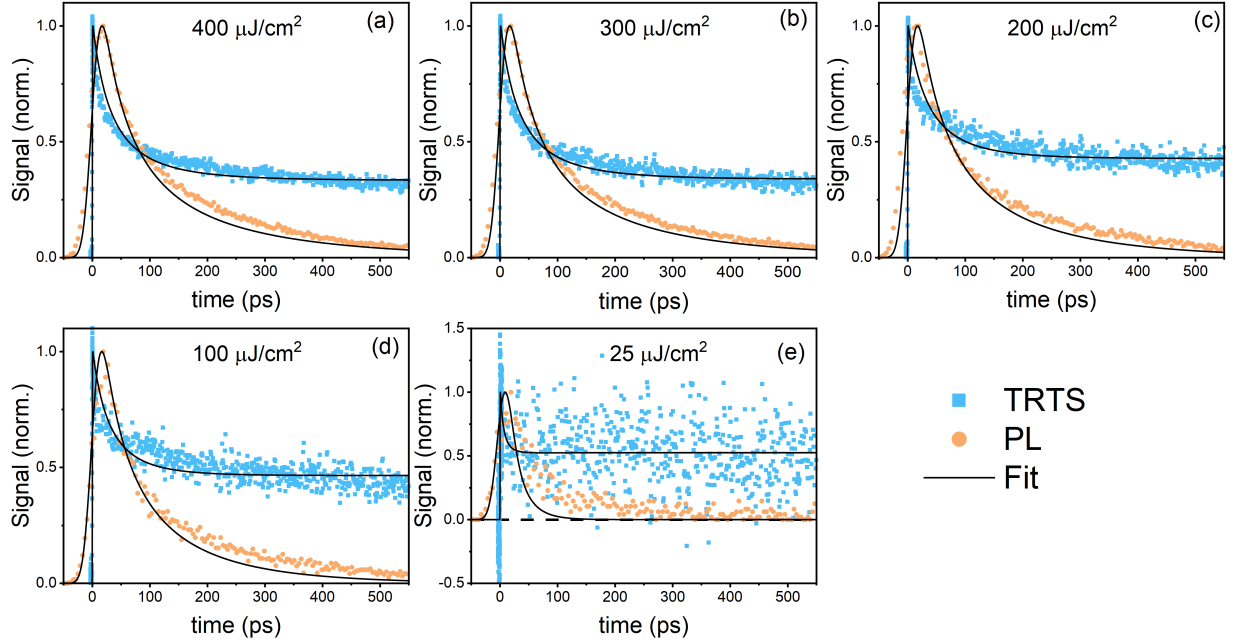


Figure 5.28: Fluence dependent fits of the IS-WNW lifetimes. (a), (b), (c), (d), and (e) correspond to fluences of 400, 300, 200, 100, and 25  $\mu\text{J}/\text{cm}^2$ , respectively.

show the surface recombination velocity for the samples under study. We find that as the fluence is raised,  $S_0$  increases for the CdS-NWs and the ES-WNWs, but not for IS-WNWs. An increasing surface recombination velocity,  $S_0$ , can be interpreted as a screening of the surface potential in the CdS nanowires. As the carrier density is raised, the photoexcited holes neutralize surface potential at the CdS nanowire surface. This results in faster surface recombination because charge carriers can more easily access the mid-gap states that are responsible for the surface recombination. Our measurements of  $S_0 \sim 10^4$  cm/s are in agreement with measurements in bulk CdS [162] despite the large surface-to-volume ratio of CdS nanowires [83, 229, 239].  $S_0$  is significantly smaller in the IS-WNW samples. In the IS-WNW sample it might be expected that  $S_0$  be larger because of the increased disorder observed by Alam, Jensen et al. [69]. However, it may be the case that  $S_0$  is so large that it occurs within the first picosecond of the charge carrier lifetime, leaving the rest of the lifetime to be dominated by bimolecular recombination. This is supported by the bimolecular recombination coefficients shown in Fig. 5.29 (b), where we find that  $\beta \sim 0.1$  cm<sup>2</sup>/s for the IS-WNWs, while it is an order of magnitude smaller for the ES-WNWs and the CdS-NWs.

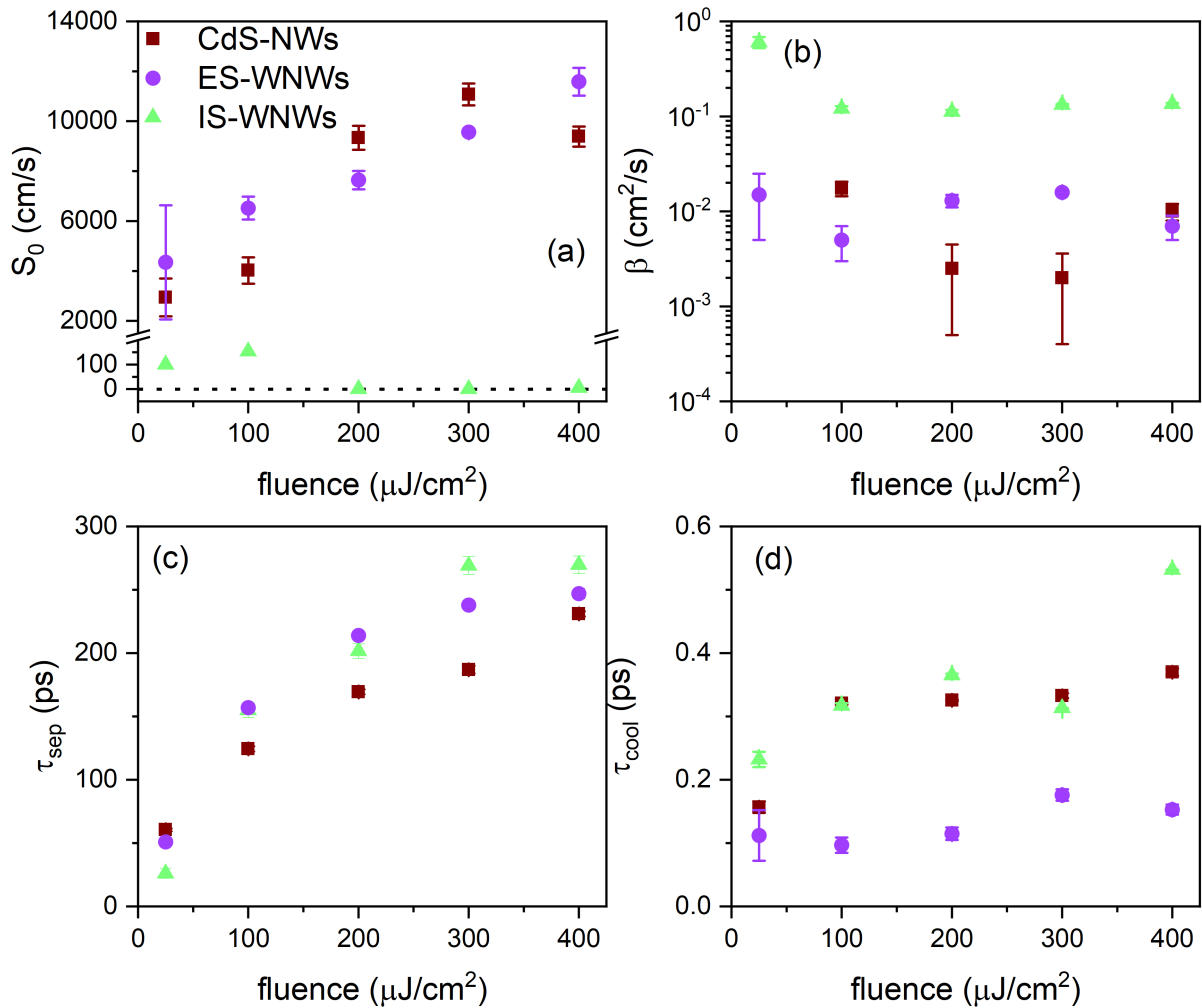


Figure 5.29: Fluence dependent surface recombination velocity, bimolecular recombination coefficient, separation lifetime, and cooling timescales in all three CdS nanowire samples. (a) Surface recombination velocity in CdS NWs (burgundy) and ES-WNWs (purple) and IS-WNWs (green). Note the the broken axes to increase readability of the CdS-NWs and ES-WNWs. (b) Bimolecular recombination coefficient,  $\beta$ , for all three samples. (c) Separation timescale,  $\tau_{\text{sep}}$ , for all three samples. (d) Hot carrier cooling timescale,  $\tau_{\text{cool}}$  for all three samples.

Often, an effective time-constant is associated with  $S_0$  so that the spatial component of the diffusion can be removed from the simulations. The surface recombination time constant,  $\tau_{SRV}$ , is related to the nanowire diameter,  $d$ , and diffusion constant,  $D^*$  [80] through

$$\tau_{SRV} = \frac{3\pi d^2}{D^*} \quad (5.35)$$

in the high SRV regime ( $S_0 \gg D^*/d$ , where  $d$  is the nanowire diameter) [240]. It is tempting to remove diffusion by substituting  $\tau_{SRV}$  into our rate equation. However, the convenient expression for  $\tau_{SRV}$  comes from an analytical solution of a 1-D diffusion equation and may not be valid within the multi-level system we have proposed.

The charge separation time constant also increases as the fluence is raised. This is shown in Fig. 5.29 (c). At low fluences,  $\tau_{sep} \sim 50$  ps, and increases to  $\sim 250$ . In 2012, Li et al. found that the surface potential in CdS nanobelts can spatially separate the holes and electrons [216]. Holes were found to migrate towards the surface, while electrons moved toward the core of the nanobelts [216]. In our nanowires, the surface potential is being screened by the large density of charge carriers, and so the timescale of charge carrier separation is longer because the charge carriers need to recombine in order to restore the surface potential.

An alternative mechanism of charge separation is the inhomogeneity of the energy landscape [80, 218]. Our CdS nanowires are predominantly Wurtzite phase, as indicated by the work of Alam et al. [69]. However, during nanowire growth it is possible that the nanowires possess intermittent locations where there the zinc-blende phase exists. This can produce inhomogeneity in the conduction and valence band energies of the nanowires. The CdS nanowires in this study are grown in such a way that the c-axis is aligned with the longest axis of the nanowire. However, it is also possible that there exist regions where the c-axis is not aligned to the growth axis, and this results in a stacking fault that can alter the energy landscape of the nanowire [80]. In both of these cases, a large carrier density can saturate the discontinuous energy landscape [218]. In turn, this may prolong the separation timescale because carriers will have to recombine before the PL is quenched by separation. However, this is not supported by our measurements because the separation timescale increases with fluence. In the case that charge separation is determined by the discontinuous

energy landscape of the nanowire, the separation timescale should remain constant because the localization of the charge-carriers is not limited by the screening of the surface potential. To determine if this is indeed the case, future work may encompass solutions of the coupled diffusion equations that lay beyond the scope of the present work [241].

The cooling time constant for all of the samples are  $\sim 0.3$  ps, which is consistent with the rapid 300 – 400 fs cooling times observed in transient absorption measurements performed on  $\sim 14$  nm diameter CdS nanowires [242]. The energy of LO phonons in CdS are  $37.7 \pm 1$  meV [243]. Furthermore, the photoexcited charge carriers possess an excess energy of approximately  $3.1 \text{ eV} - 2.46 \text{ eV} = 0.64 \text{ eV}$ . This means that approximately 21 LO phonon emissions need to occur before charge carriers reach equilibrium. This is in agreement with calculations of the electron-phonon scattering rates in CdS, which indicate that LO-phonon emission is expected to occur on timescales of  $\sim 10 \text{ fs}$ <sup>§</sup> for charge-carriers with an excess energy of  $\sim 0.6 \text{ eV}$  [244].

The rapid cooling time may also indicate that the model may be insensitive to the rise dynamics of the photoconductivity lifetime. The 40 ps response time of the time-resolved photoluminescence system is orders of magnitude larger than the cooling timescales, and since our model incorporates this response function, early dynamics are strongly obscured. In turn this reduces the sensitivity of the fit to the cooling time. Future measurements using time-resolved photoluminescence up-conversion spectroscopy can be used to gain access to timescales of 200 fs [80], which would greatly enhance the fit sensitivity to charge-carrier cooling.

Our model of the charge-carrier lifetime is summarized schematically in Fig. 5.30. Figure 5.30 (a) shows a CdS nanowire in equilibrium. In equilibrium, the conduction ( $E_c$ ) and valence ( $E_v$ ) bands are raised near the surface due to the negatively charged surface states [245]. Figure 5.30 (b) shows a 400 nm laser pulse photoexciting the nanowire, creating a large population of electrons in the conduction band and holes in the valence band. The electrons and holes extinguish the surface potential [245], which allows the charge-carriers to recombine, emitting a photon with an energy equal to the band gap energy  $E_g = 2.46 \text{ eV}$

---

<sup>§</sup>The cooling time is then approximately  $21 \times 10 \text{ fs} = 210 \text{ fs}$ . The LO phonon absorption timescales is roughly  $1/\omega_{LO} \approx 100 \text{ fs}$ [244]

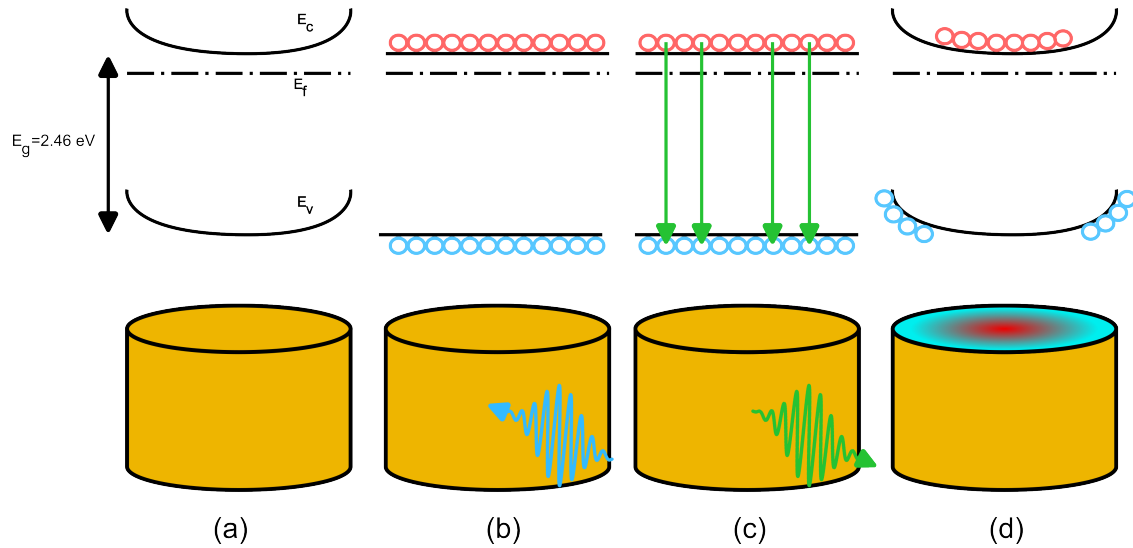


Figure 5.30: Schematic of charge-carrier lifetime in CdS nanowires. (a) CdS nanowire in equilibrium. (b) Photoexciting a CdS nanowire puts electrons (holes) in the conduction (valence) bands. (c) Holes are pushed to the surface by the surface field. (d) Surface field is neutralized. (e) Surface recombination occurs. (f) The surface potential restores due to the lower charge carrier density. The surface potential separates electrons and holes, quenching luminescence and prolonging photoconductivity.

[170]. After extensive bimolecular recombination, the surface potential is restored, and in doing so the electrons are localized to the nanowire core and the holes are localized towards the nanowire surface. The spatial separation of charge is shown in Fig. 5.30 (d), where the spatial distribution of electrons and holes is shown as the gradient on top of the nanowire.

## 5.5 Summary

In this chapter we investigated the photoconductivity and photoluminescence of CdS nanowires wrapped in  $C_3N_5$  nanosheets.

Our terahertz time-domain spectroscopy of bulk CdS and CdS nanowire films showed that our samples possess no significant density of equilibrium charge carriers. We performed TRTS on bulk CdS, and found that surface scattering significantly reduces the mobility in CdS. Our measurements of  $\sim 100 \text{ cm}^2/\text{Vs}$  agree well with estimates of  $\sim 128 \text{ cm}^2/\text{Vs}$  that come from a simple diffuse surface scattering model [219, 220].

We investigated three models of charge carrier dynamics in CdS nanowire films. The plasmon model was shown to not support our results due to inconsistencies in the fluence dependent behaviour of the plasma frequency. The Bruggeman model of conductivity did

not fit our data well because it requires a unique combination of charge carrier density and volume fill fraction to match the shape of our photoconductivity spectra. The fill fraction was kept as a global fit parameter, and the unique combination of fill fraction and carrier density was not always attainable. The Drude-Smith model was found to fit our data well, and provide meaningful insight into the charge carrier localization occurring in the CdS nanowire films. Our results suggest that the short range ( $< 25$  nm) charge-carrier mobilities ( $\sim 400$  cm<sup>2</sup>/Vs) are nearly bulk-like ( $\sim 440$  cm<sup>2</sup>/Vs [203]). Wrapping the nanowires in C<sub>3</sub>N<sub>5</sub> is shown to increase the charge carrier localization, because wrapping the weak van der Waals potential affixing the nanosheets to the surface of the nanowires may be altering the surface potential in favor of increased localization. The Drude-Smith model also allowed us to extract the ambipolar diffusion coefficients  $D^*$  for our CdS-NW films. We could then use the  $D^*$  in our model of charge-carrier lifetimes. Our TRTS of bulk CdS yielded an ambipolar diffusivity of  $D^* \sim 1.3$  cm<sup>2</sup>/s which is in agreement with the reported value of 1.2 cm<sup>2</sup>/s [162]. In the bare CdS nanowires we found  $D^* \sim 0.7$  cm<sup>2</sup>/s, which is significantly larger than the ES-WNWs and IS-WNWs, where  $D^* \sim 0.1 - 0.3$  cm<sup>2</sup>/s.

With the ambipolar diffusion coefficients measured from TRTS, we then constructed a multi-level rate equation to simultaneously describe the photoluminescence and photoconductivity lifetimes. To describe the lifetimes, our model incorporates hot carrier cooling, surface recombination, charge separation, and bimolecular recombination. The model fits the photoluminescence and photoconductivity of all the CdS nanowires, the ex-situ wrapped nanowires, and the in-situ wrapped nanowires. In the CdS nanowires and the ES-WNWs, we find a surface recombination velocity that increases with fluence, and is similar to measurements in bulk CdS ( $S_0 \sim 10^4$  cm/s) [162]. In the IS-WNWs, we find that our model suggests almost no surface recombination is occurring, This may be because the recombination is so fast in those samples that the surface recombination occurs on sub-picosecond timescales. Thus only the bimolecular recombination occurs on the  $>$  ps timescales measured here. The surface recombination velocity was found to increase as the fluence was increased. This is consistent with charge-carrier screening of the surface potential in CdS nanowires. As the density is increased, the charged surface states are screened by the free carriers. This lowers the potential barrier at the nanowire surface and increases access to surface recombination.

Furthermore, our measurements of the charge separation time constant indicate that it takes longer for electrons and holes to separate at high excitation densities. This is also consistent with charge carrier screening of the surface potential because at large densities there are more charge carriers that must recombine before the surface potential is restored.

# Chapter 6

## Atomically Thin WSe<sub>2</sub>

### 6.1 Introduction

In 1972, Philip Anderson wrote a seminal article for *Science* titled *More is Different* [246]. In his article, Anderson argues that the reductionist stance that is used to deduce fundamental principles does not, by itself, imply the existence of a constructivist hypothesis whereby the fundamental principles give rise to immediate and satisfying explanations of the world around us [246]. This gives rise to the concept of emergent properties in physics, and in this chapter we will study transition metal dichalcogenides (TMDs) which have emergent properties that may lead to new technologies.

Transition metal dichalcogenide crystals are a group of semiconductors that form distinct layers that are weakly held together by van der Waals forces. Often denoted as MX<sub>2</sub> (M = Mo, W; X = S, Se, Te) [118, 247], each layer in a TMD crystal consists of a plane of transition metal atoms sandwiched between two planes of chalcogen atoms. In this chapter we will study the TMD WSe<sub>2</sub>. Figure 6.1 shows a schematic of the crystal structure. In Fig. 6.1 (a) we show the top-down orthographic view of a Se-W-Se sandwich, and in (b) we show a perspective side-view of the sandwich. In the literature it is common to discuss the electrical properties along the arm-chair and zig-zag axes of the WSe<sub>2</sub> monolayer, which are shown in Fig. 6.1 (a) for reference.

The emergent properties of TMDs come from the weak bonding of the layers. In bulk, TMDs found little use in the semiconductor industry because of their low electron mobilities

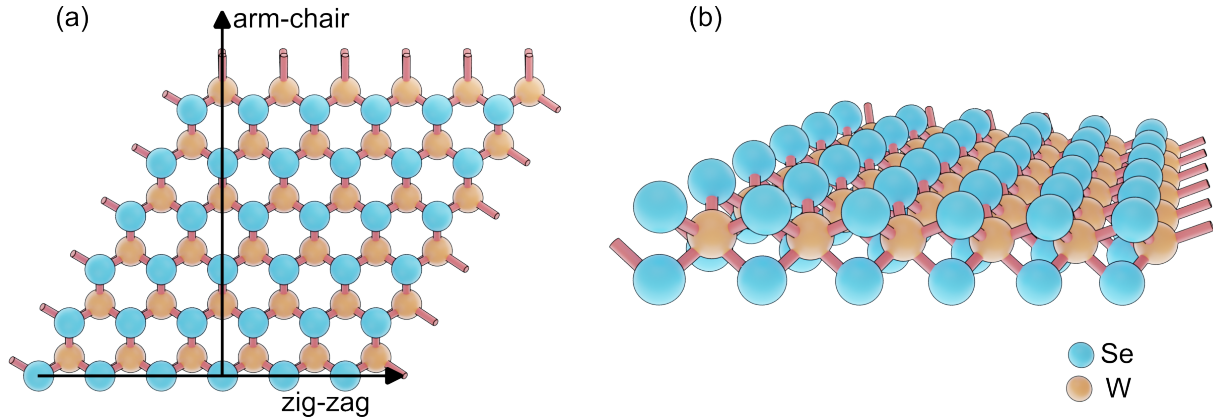


Figure 6.1: Schematic crystal structure of  $\text{WSe}_2$  monolayer. Tungsten atoms are indicated as orange spheres, and selenium are indicated by blue spheres. The bars connecting atoms represent a covalent bond. (a) Top-down structure indicating the arm-chair and zig-zag directions. (b) Perspective side-view of a  $\text{WSe}_2$  monolayer.

of  $\sim 100 \text{ cm}^2/\text{Vs}$ . Bulk TMDs also have an indirect band gap of  $\sim 1 \text{ eV}$  that is not well suited for solar cell applications either. However, as layers are removed from the bulk, the band gap increases and transitions to a direct gap [118, 119, 248]. When reduced to a single monolayer, TMDs have direct band gaps of  $\sim 2 \text{ eV}$  that are better suited for optical absorption. The band structure changes also increase the electron mobility to  $\sim 400 \text{ cm}^2/\text{Vs}$  [249]. The layer-dependent optoelectronic properties of monolayer TMDs thus renewed interest in the subject since it was observed in 2010 [119]. Since 2010 there has since been an explosion of interest in monolayer TMDs.

Recent review articles in this field capture a wide and extensive research effort. On one side is a pursuit of the fundamental quantum properties such as spin, topological superconductivity, and band structure [250–252], and on the other is application-focused research such as optoelectronics, valleytronics, and photonics [253–256]. In between one finds review articles that catalogue measurements of properties for future applications [157, 257–260]. This middle ground between fundamentals and application is where we contribute to the understanding of charge carrier dynamics in atomically thin  $\text{WSe}_2$ .

The unique charge-carrier dynamics in TMDs are also associated with reduced dimensionality. Reducing the dimensions of TMDs to a single monolayer reduces the screening of Coulomb interactions, which yields Exciton binding energies on the order of a few hundred meV [261]. In contrast, exciton binding energies in bulk semiconductors are typically a few

Material	Quasi particle	Binding energy (meV)	Morphology
GaAs	Exciton	4	Bulk[ <a href="#">265</a> , <a href="#">266</a> ]
CdS	Exciton	29.8	Bulk [ <a href="#">267</a> ]
Si	Exciton	15.01	Bulk [ <a href="#">268–270</a> ]
Ge	Exciton	4.18	Bulk [ <a href="#">268</a> , <a href="#">269</a> ]
WSe <sub>2</sub>	Exciton	60	Bulk [ <a href="#">262</a> ]
WSe <sub>2</sub>	Exciton	790	Monolayer [ <a href="#">271</a> ]
WSe <sub>2</sub>	Trion	30	Monolayer [ <a href="#">262</a> ]
WS	Exciton	830	Monolayer [ <a href="#">271</a> ]
MoS <sub>2</sub>	Exciton	230	Monolayer [ <a href="#">272</a> , <a href="#">273</a> ]
MoSe <sub>2</sub>	Exciton	220	Monolayer [ <a href="#">274</a> ]

Table 6.1: Exciton Binding energies in common semiconductors.

meV [[170](#)]. Table 6.1 contains exciton binding energies for a few prototypical semiconductors for reference. Since the Coulomb interactions are heavily screened in monolayer TMDs, more exotic quasi-particles such as trions [[125](#), [262](#)], biexcitons [[263](#)], and negative electron mass excitons [[264](#)] have been discovered.

Ultrafast measurements have played a key role in discovering these quasi particles because excitons form within a few picoseconds after photoexcitation [[275](#), [276](#)]. In 2017, Steinleitner et al. directly measured exciton formation in monolayer WSe<sub>2</sub> using time-resolved mid-infrared spectroscopy [[124](#)]. Time-resolved mid-infrared spectroscopy is a close relative to time-resolved terahertz spectroscopy, but the centre frequency of the probe pulses are on the order of  $\sim 43 \pm 10$  THz ( $\sim 170 \pm 30$  meV). Although though the mid-infrared photons do not have enough energy to ionize an exciton in monolayer WSe<sub>2</sub> (cf. Table. 6.1), they do possess enough energy to induce a  $1s \rightarrow 2p$  transition in the exciton [[124](#)]. Therefore the amount of  $1s \rightarrow 2p$  absorption that is observed serves as a proxy of the exciton population. Interestingly, Steinleitner et al. also note a non-negligible contribution of free charge carriers.

Time-resolved terahertz spectroscopy (TRTS) is better suited for measurements of the free carrier absorption because the centre frequency of the probe pulses are too low to observe exciton resonances ( $1$  THz  $\sim 4$  meV, see Section 2.2.2). TRTS of monolayer WSe<sub>2</sub> was performed by Docherty et al. in 2014 [[125](#)]. Docherty et al. found that the photoconductivity was well described by a Drude-Lorentz model, where the Lorentzian component may have been due to coherent excitation of a Trion [[125](#)]. However, if this is indeed the case, there are

experiments one can do to verify and extend these observations. For example, it is known exciton-phonon interactions can broaden the trion absorption spectrum [277], but this has yet to be observed using TRTS. Furthermore, near-field terahertz microscopy recently showed that excitation density plays a significant role in the exciton recombination kinetics in monolayer WSe<sub>2</sub> because a Mott transition occurs at densities near 10<sup>12</sup> cm<sup>-2</sup> [278]. Motivated by these two avenues, we perform fluence- and temperature-dependent TRTS on monolayer WSe<sub>2</sub>.

## 6.2 Sample Properties

A monolayer of WSe<sub>2</sub> was grown on a 1 cm × 1 cm × 0.3mm c-cut sapphire substrate via chemical vapour deposition (CVD)\*. Atomic force microscopy (AFM) [279] and absorption spectroscopy measurements [280] are established in TMDC literature and serve as appropriate benchmarks of the monolayer nature of our sample. To observe the uniformity of the monolayer film we construct a map of the maximum differential THz transmittance across the surface of the sample. Terahertz time-domain spectroscopy also allows us to measure the equilibrium charge-carrier dynamics.

### 6.2.1 Monolayer Thickness

Microscope images of the WSe<sub>2</sub> monolayer are shown in Fig. 6.2 (a) and (b). We find that the sample contains bilayers of WSe<sub>2</sub> that are non-uniformly dispersed across the surface of the WSe<sub>2</sub> monolayer. Progressing from left to right in Fig. 6.2, we zoom in on one such bilayer. In Fig. 6.2 (c) we use the AFM functionality of our Witec microscope to measure the monolayer thickness and find it to be ~ 0.75 nm, which is consistent with the literature values of ~ 0.7 nm for WSe<sub>2</sub> on sapphire [279].

### 6.2.2 Optical Absorption

According to Beer’s law, the intensity of light transmitted through monolayer WSe<sub>2</sub> on a sapphire substrate ( $I_{samp}$ ) is given by

$$T_{samp}(\lambda) = T_{ref}(\lambda) e^{-\alpha(\lambda) \ell} \quad (6.1)$$

---

\*Samples were ordered from 2D Semiconductors Inc.

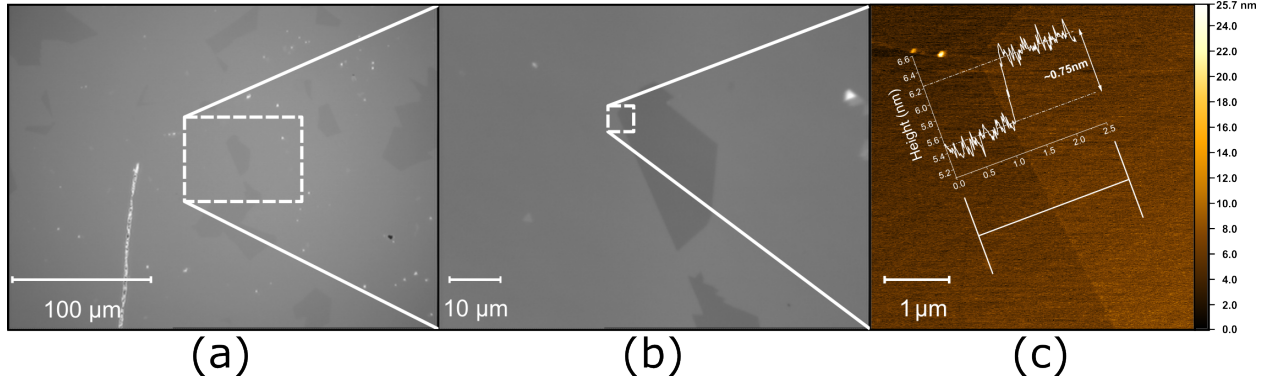


Figure 6.2: Imaging WSe<sub>2</sub> monolayer at progressively smaller scales. (a) Large area image, (b) small area image (c) AFM image of a WSe<sub>2</sub> monolayer. The white bar indicates the region from which the profile was extracted. We find a monolayer thickness of  $\sim 0.75$  nm.

where  $T_{ref}(\lambda)$  is the light transmitted through the sapphire substrate at wavelength  $\lambda$ ,  $\alpha(\lambda)$  is the absorption coefficient, and  $\ell$  is the thickness of the WSe<sub>2</sub> film. By measuring  $T_{ref}$  and  $T_{samp}$ , one can retrieve the absorption by computing the differential transmission (for  $\alpha\ell \ll 1$ )

$$\frac{T_{samp} - T_{ref}}{T_{ref}} = e^{-\alpha\ell} - 1 \approx -\alpha\ell. \quad (6.2)$$

The room-temperature absorption spectrum of our monolayer WSe<sub>2</sub> is shown in Fig. 6.3 (a). The absorption spectrum is measured using the spectrometer outlined in Chapter 4. An Ocean Optics UV-Vis light source is used to excite the sample, and the light transmitted through the sample is collected using a fiber optic cable that directs the light into the spectrometer. A substrate reference is mounted next to the WSe<sub>2</sub> sample in a cryostat so that  $T_{ref}$  and  $T_{samp}$  can be measured by translating the cryostat back and forth.

The absorption spectrum of monolayer WSe<sub>2</sub> was measured in 2016 by Dey et al. [281]. They found that the absorption spectrum is well described by a series of Lorentzian functions, motivating the fit shown in Fig. 6.3 (a), performed on the absorption spectrum at 295 K. The absorption spectrum is modelled with

$$\alpha(E) = \sum_{i=1}^4 \frac{A_i}{\pi} \left[ \frac{\sigma_i}{(E - \mu_i)^2 + \sigma_i^2} \right] \quad (6.3)$$

where  $A_i$  is the amplitude,  $\mu_i$  is the centre energy,  $E$  is the photon energy, and  $\sigma_i$  is the half-width at half-max (ie.  $FWHM = 2\sigma$ ). The individual Lorentzians are shown in Fig.

6.3 (a) as shaded regions under the fit line.  $L_1$  and  $L_2$  correspond to the spin-split direct-gap exciton transitions located at the  $K$  and  $K'$  points of the Brillouin Zone [282, 283]. The large peaks at  $L_3$  and  $L_4$  correspond to regions of the Brillouin zone that exhibit significant nesting of the conduction and valence bands.

Our data agrees well with their model. Fitting the absorption spectrum reveals the temperature dependence of the amplitude, centre energy, and full-width at half-maximum of each Lorentzian. The temperature dependence of these parameters is shown in Fig. 6.3 (b)-(d). Error bars are present but obscured by the marker size. Fig. 6.3 (b) shows how the Lorentzian amplitudes change with temperature. We see little change in the amplitude of the absorption as the sample is cooled. In contrast, Fig. 6.3 (c) reveals that the centre energy has a strong dependence on the sample temperature. As the sample is cooled, every peak blueshifts by  $\sim 0.04$  eV. Finally, in Fig. 6.3 (d) we see that the Lorentzians narrow as the sample is cooled.

The temperature dependence of  $\sigma_1$  and  $\mu_1$  can be used to identify the phonons interacting with free charge carriers [281, 284]. Modelling the temperature dependent  $\mu_1(T)$  and  $\sigma_1(T)$  as energy thresholds proportional to Bose-Einstein statistical factors for phonon emission plus absorption yields the relationships [281, 284]

$$\mu_1(T) = E_0 - E_1 \left[ \frac{2}{\exp(\Theta/k_B T) - 1} + 1 \right] \quad (6.4)$$

and

$$\sigma_1(T) = \sigma_o + \frac{b}{\exp(\Theta/k_B T) - 1} \quad (6.5)$$

where  $T$  is the temperature,  $E_0 - E_1$  is the centre energy at  $T = 0$  K,  $b$  is a phenomenological scaling factor,  $\sigma_o$  is the linewidth at  $T = 0$  K,  $\Theta$  is the dominant phonon interaction energy, and  $k_B$  is the Boltzmann constant.

The simultaneous fit of  $\mu_1(T)$  and  $\sigma_1(T)$  to Eqs. (6.4) and (6.5) are shown in Fig. 6.4. The average phonon interaction energy extracted from these fits is  $\Theta = 14.6 \pm 0.3$  meV, which agrees very well with the 14.2 meV reported in literature [281]. Ab-initio calculations show that the phonons responsible for this temperature dependent absorption are the  $E'$

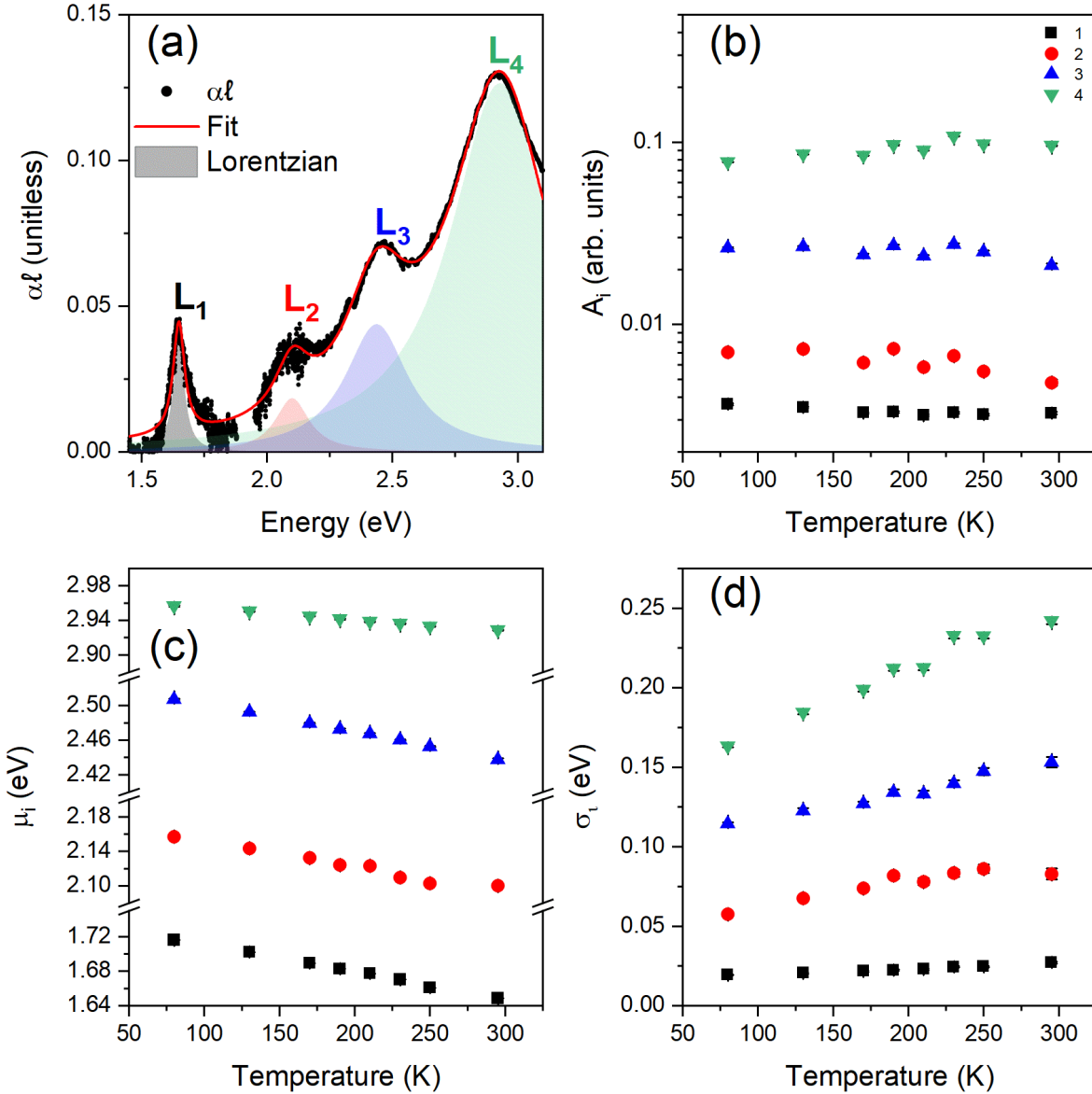


Figure 6.3: UV-Vis absorption in WSe<sub>2</sub> monolayer. (a) UV-Vis absorption spectrum fit to Eq. (6.3) (red line) at 295 K. Individual Lorentzian functions are indicated by the shaded areas underneath the fit line. (b) Temperature dependence of the Lorentzian amplitudes ( $A_i$ ). (c) Temperature dependence of the center energy for each of the Lorentzians ( $\mu_i$ ). (d) Temperature dependent width of the Lorentzians ( $\sigma_i$ ).

$\Theta$	$E_0$	$E_1$	$b$	$\sigma_0$
(meV)	(eV)	(meV)	(meV)	(meV)
$14.6 \pm 0.3$	$1.754 \pm 0.005$	$30 \pm$	$7 \pm 2$	$18.0 \pm 0.7$

Table 6.2: Best-fit electron-phonon coupling parameters from the fits in Fig. 6.4.

(12.6 meV) and  $E''$  phonons (15.8 meV), which have an average energy of 14.2 meV [281]. A complete list of the fit parameters can be found in Table 6.2.

Figures 6.5 and 6.6 show schematics of the  $E'$  and  $E''$  phonon modes, respectively. In these figures, the velocities of the atoms are represented by arrows. The velocities pointing into the plane are denoted by the  $\otimes$  symbol and the out-of-plane velocities are denoted by the  $\odot$  symbol. A top-down view is not sufficient to observe the behaviour of the lower layer of chalcogenide atoms, so a view looking down the arm-chair axis is provided beneath the top down perspectives in Figs. 6.5 and 6.6. It appears that the phonon modes oscillate mostly along the arm-chair axis of the WSe<sub>2</sub> monolayer, which may reduce electron-phonon scattering in the zig-zag direction. Recently, it has been observed that WSe<sub>2</sub> monolayers grown via chemical vapour deposition first assemble triangles, and then the triangles bond together to form a monolayer [285]. Even after the monolayer is assembled, the boundary between the monolayers can be seen with two-photon imaging because the triangles do not form a uniformly oriented sheet of monolayer WSe<sub>2</sub>. Therefore, it is not likely to affect our measurements because the  $\sim 1.5$  mm spot size of the THz pulse averages over all of the smaller domains [286].

### 6.3 Terahertz Time-Domain Spectroscopy

Terahertz time-domain spectroscopy (THz-TDS) was used to identify signatures of equilibrium free charge carriers in the WSe<sub>2</sub> monolayer. The sample was mounted beside a c-cut sapphire reference substrate supplied by 2D-Semiconductors Inc. THz waveforms transmitted through the sapphire substrate and WSe<sub>2</sub> sample are shown in Fig. 6.7 (a). There is a 0.4 ps time delay between the reference and sample waveforms that cannot be accounted for by the WSe<sub>2</sub> monolayer alone. We will return to this shortly. The Fourier amplitudes are shown in Fig. 6.7 (b), and they are nearly identical. This is echoed in the transmission function shown in Fig. 6.7 (c), where we find that the transmission spectrum is flat across the

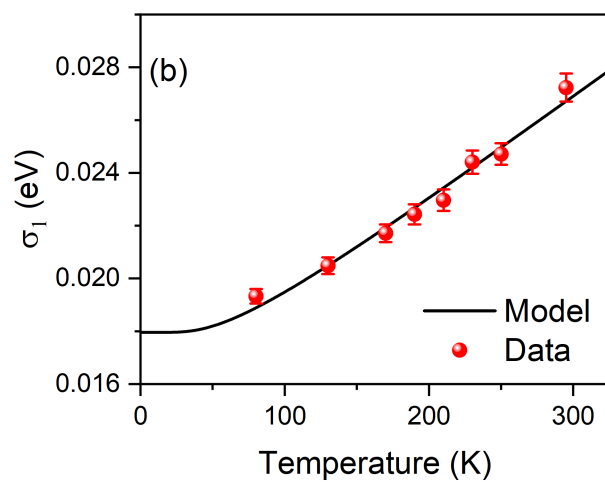
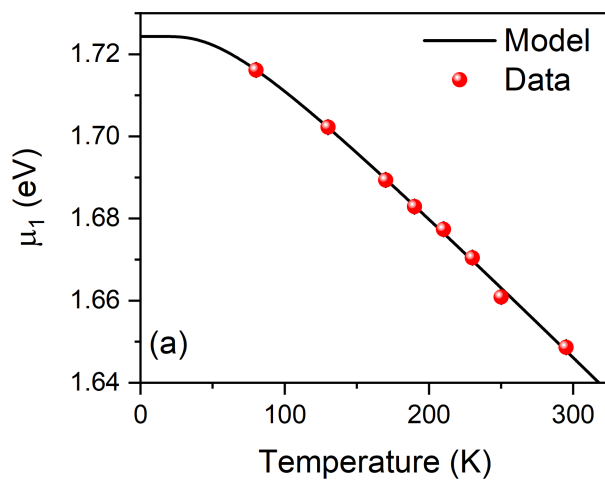


Figure 6.4: Simultaneous fit of the electron-phonon coupling model in monolayer WSe<sub>2</sub>. (a) Temperature dependent center energy ( $\mu_1$ ) and corresponding fit (black line). (b) Temperature dependent width ( $\sigma_1$ ) and corresponding fit (black line).

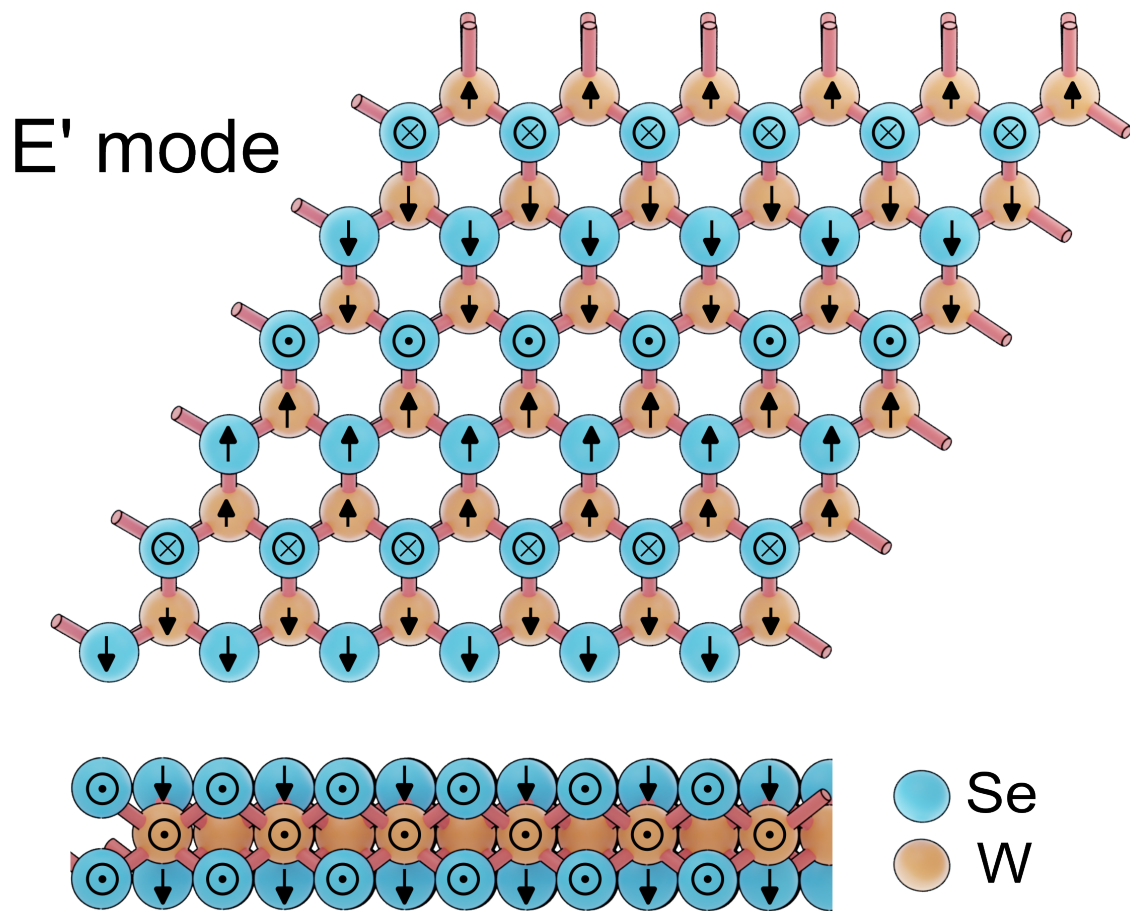


Figure 6.5:  $E'$  phonon mode in monolayer  $WSe_2$ . Top: Top-down view of the  $E'$  phonon mode. Bottom: view looking down the arm-chair axis of the  $WSe_2$  monolayer. Adapted from Ref. [281] and visualization aid from: [https://interactivephonon.materialscloud.io/compute/process\\_example\\_structure/](https://interactivephonon.materialscloud.io/compute/process_example_structure/).

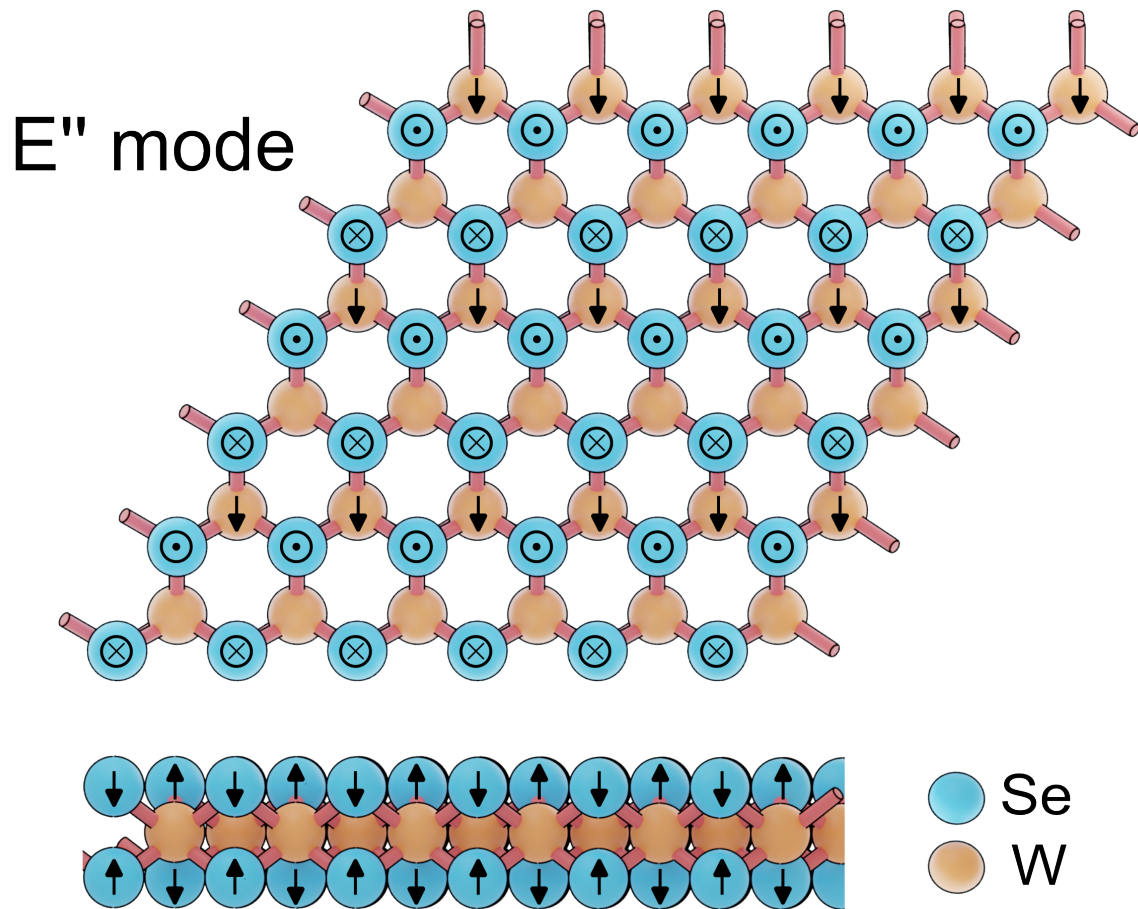


Figure 6.6:  $E''$  phonon mode in monolayer  $\text{WSe}_2$ . Top: Top-down view of the  $E''$  phonon mode. Bottom: View looking down the arm-chair axis of the  $\text{WSe}_2$  monolayer. Adapted from Ref. [281] and visualization aid from: [https://interactivephonon.materialscloud.io/compute/process\\_example\\_structure/](https://interactivephonon.materialscloud.io/compute/process_example_structure/).

THz spectrum. The flatness of the spectrum indicates that there is no significant absorption from free charge carriers in the film. The phase delay seen in Fig. 6.7 is likely from a slight difference in the thicknesses of the two substrates. Using an index of  $n = 3.079$  [172], the difference in optical path length can be estimated by  $\Delta d = c\Delta t/n$ , where  $\Delta d$  is the thickness variation and  $\Delta t$  is the time delay. We find that the thickness difference is  $d \sim 38.7 \mu\text{m}$ . We conclude that we do not see evidence of equilibrium free carrier absorption in the monolayer WSe<sub>2</sub>.

## 6.4 Time-Resolved Terahertz Spectroscopy

### 6.4.1 Experimental Details

The TRTS system outlined in Chapter 4 was used to explore the ultrafast carrier dynamics in monolayer WSe<sub>2</sub>. Since the energy of the 800 nm photons on the excitation path lie below the band gap of monolayer WSe<sub>2</sub>, a BBO ( $\beta - \text{BaB}_2\text{O}_4$ ) crystal was used to frequency double the excitation energy to 3.1 eV. Fluences of  $10 - 190 \mu\text{J}/\text{cm}^2$  were used to photoexcite the sample, similar to other measurements in the literature [125]. The monolayer WSe<sub>2</sub> was mounted on a cryostat under vacuum of  $\sim 10^{-6}$  Torr, and the temperature was varied from 295-80 K using a liquid nitrogen transfer line.

### 6.4.2 Photoconductivity Map

Monolayer uniformity was tested by observing the spatial dependence of maximum differential transmittance  $-\Delta\mathcal{E}/\mathcal{E}_{ref}$  under an excitation fluence of  $150 \mu\text{J}/\text{cm}^2$ . The spotsize of the THz pulse is  $\sim 1.5$  mm, and the 400 nm spot was  $\sim 5$  mm to maintain a uniform excitation across the 1.5 mm THz spot size. To perform this experiment, the sample was mounted on the edge of a sample holder, and the sample was raster scanned across the focus of the THz pulse and optical excitation. A schematic of this procedure is shown in Fig. 6.8. The THz pulse and optical excitation are both incident to the WSe<sub>2</sub> monolayer, and the maximum  $-\Delta\mathcal{E}/\mathcal{E}_{ref}$  was recorded for the starting position in the top-left corner of the sample (cf. Fig. 6.8). The sample was then moved across the focus, and the  $-\Delta\mathcal{E}/\mathcal{E}_{ref}$  was recorded at each step (see Sections 3.3 and 4.2 for details). Individual lifetimes were not recorded in this experiment due to the data acquisition time of such an experiment. The sample was 1

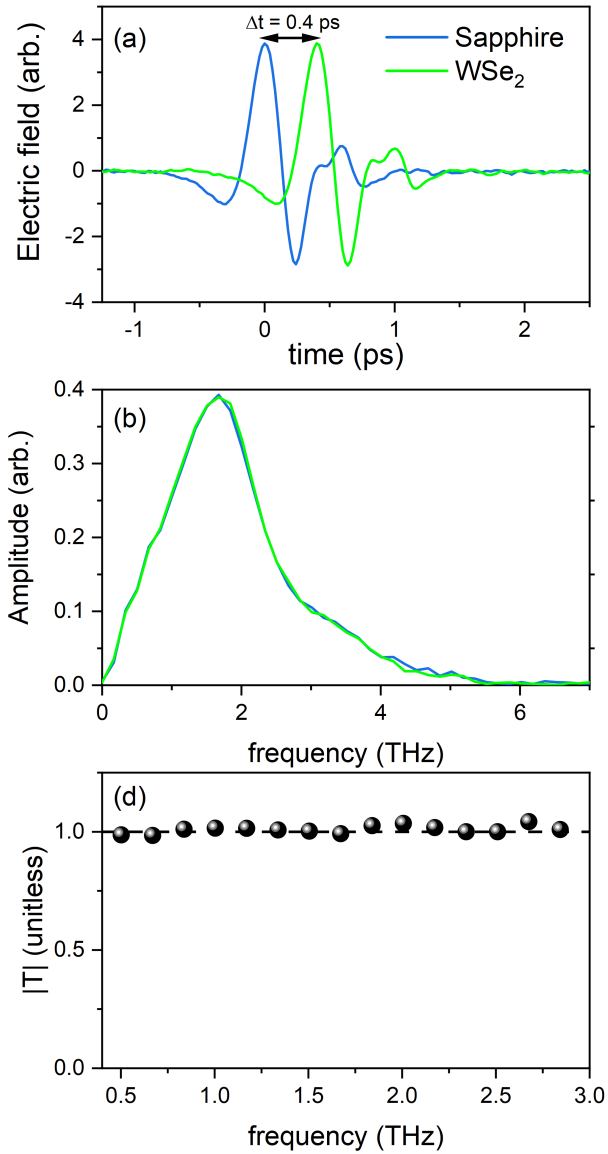


Figure 6.7: THz-TDS of monolayer WSe<sub>2</sub>. (a) Substrate (blue) and sample (green) waveforms. A time delay of  $\Delta t \sim 0.4$  ps exists between the two waveforms. (b) Fourier amplitude spectra of the sample and reference waveforms in (a). (c) Transmission spectrum of the WSe<sub>2</sub> monolayer.

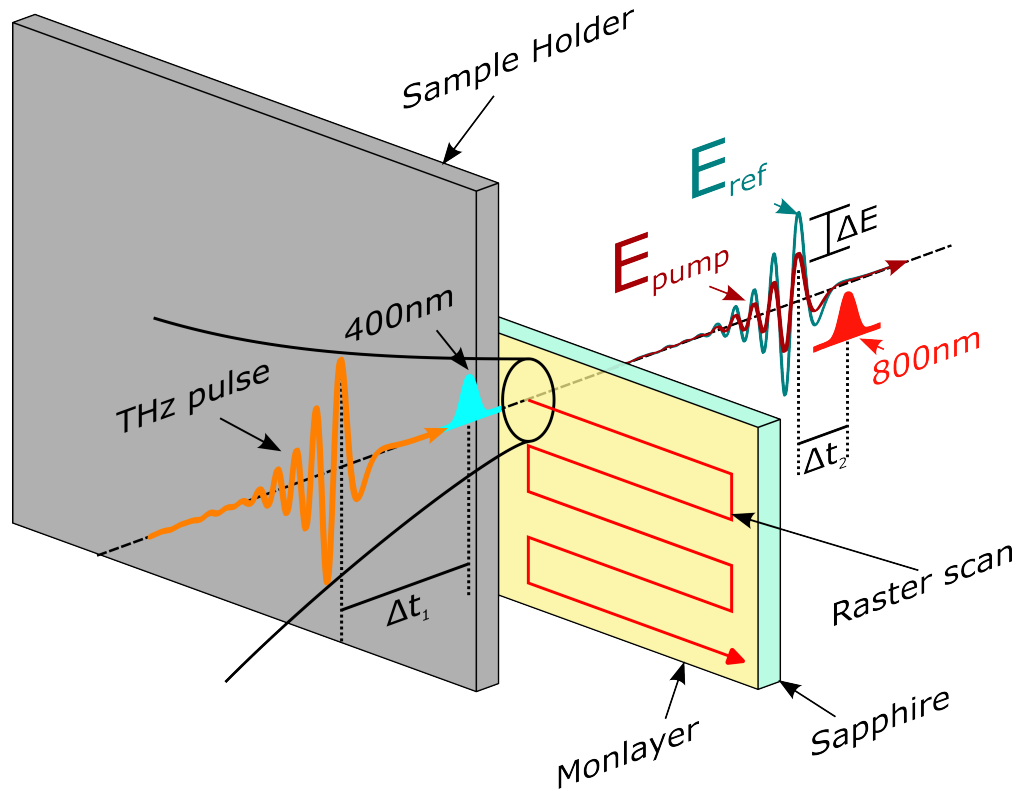


Figure 6.8: Schematic of WSe<sub>2</sub> raster scan. The sample is mounted to the side of the sample holder. The THz pulse and excitation beam are incident to the WSe<sub>2</sub> monolayer, and transmit through the sample.  $-\Delta\mathcal{E}/\mathcal{E}_{ref}$  is recorded at each location of the raster scan. The raster scan path is indicated by the red line covering the sample surface.

cm  $\times$  1 cm, and 1 mm was reserved on either side to limit the influence of the edges of the sample. Since  $-\Delta\mathcal{E}/\mathcal{E}_{ref}$  is proportional to the photoconductivity, this technique effectively makes a map of the sample photoconductivity.

The results of the raster scan are shown shown in Fig. 6.9. We find  $-\Delta\mathcal{E}/\mathcal{E}_{ref} \sim 0.8\%$ , with some areas that are as high as 2%. The areas with larger  $-\Delta\mathcal{E}/\mathcal{E}_{ref}$  appear in areas that are visually darker. This is likely due to the presence of multilayers on the surface, since it is known that the optical absorption is positively correlated with layer thickness [287]. Despite some regions with large  $-\Delta\mathcal{E}/\mathcal{E}_{ref}$ , there is a sufficiently large area with a constant  $-\Delta\mathcal{E}/\mathcal{E}_{ref}$  where THz spectroscopy can be performed. The area used in our experiments is highlighted by the white dashed circle.

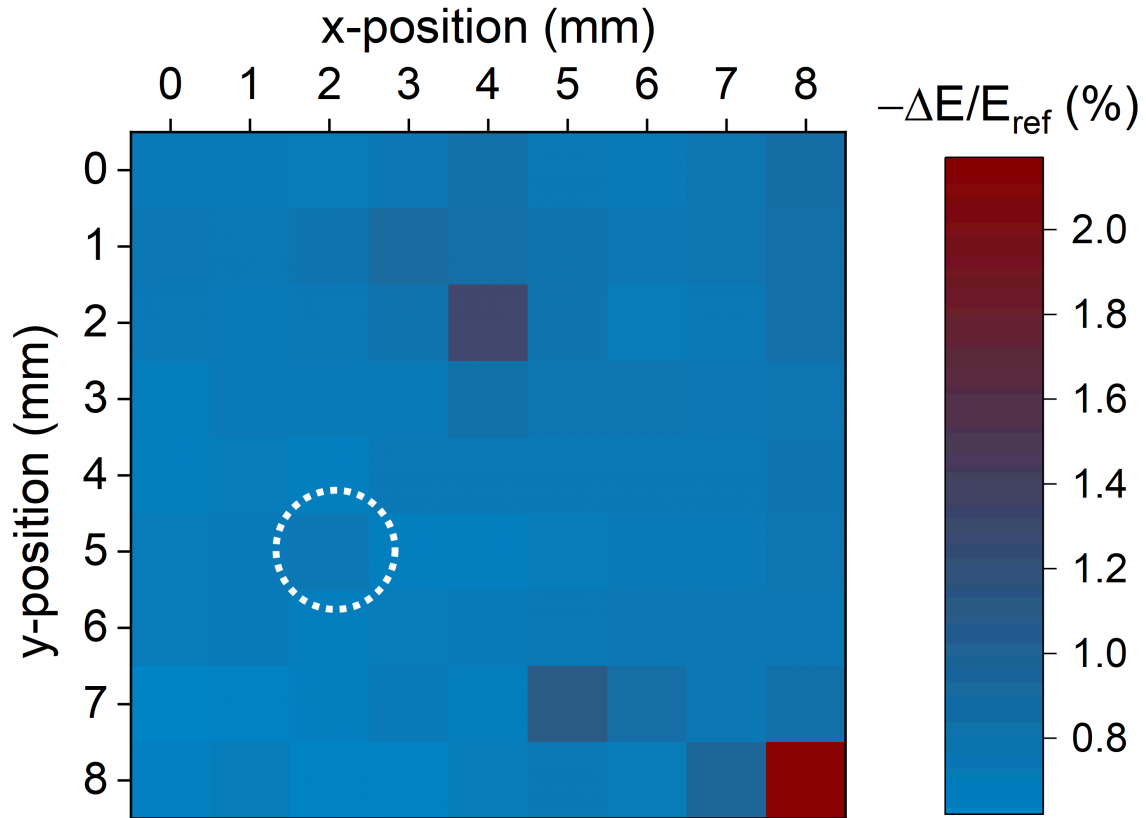


Figure 6.9: Photoconductivity map of monolayer WSe<sub>2</sub> under 400 nm excitation and a fluence of 0.15  $\mu\text{J}/\text{cm}^2$ . Differential terahertz transmission is measured across the surface of the sample. We find  $-\Delta\mathcal{E}/\mathcal{E}_{ref} \sim 0.8\%$ , and regions where  $-\Delta\mathcal{E}/\mathcal{E}_{ref} \sim 2\%$  are likely due to multilayers on the surface. The region where TRTS was performed is highlighted by the dashed white circle.

### 6.4.3 Charge-Carrier Lifetimes

#### Room Temperature

At room temperature, the photoconductivity lifetime and spectroscopy was recorded using a 400 nm excitation beam, at fluences of 49, 195, 294, 391, and 490  $\mu\text{J}/\text{cm}^2$ . The fluence dependent lifetimes are shown in Fig. 6.11. The spacing between lifetimes in Fig. 6.11 is 1% for all of the fluences shown. It is clear that the maximum  $-\Delta\mathcal{E}/\mathcal{E}_{ref}$  is below 1% for all fluences, and lasts for  $\sim 100$  ps. To parameterize the lifetimes, a simple multi-level rate equation is fitted to the lifetimes.

We fit our data to a rate equation that encompasses exciton Auger recombination and exciton dissociation. By directly observing the evolution of the exciton 1-s absorption line  $\sim 40$  THz, it is possible to directly measure the exciton population [124, 126, 288, 289]. It has been found that Exciton Auger recombination best described the lifetime of the exciton population [124]. Exciton Auger recombination is the process where two excitons collide in a bimolecular recombination event. The excitons in WSe<sub>2</sub> also dissociate into free charge carriers, as observed by He et al. [290]. Excitons dissociate into free charge carriers after  $< 1$  ps [290, 291]. Since this is an exciton dissociating into free charge carriers, it is modelled as a monomolecular recombination event. The density of the excitons is thus modelled by the rate equation

$$\frac{dn_x}{dt} = G(t - t_0) - \gamma_{b,x}n_x^2 - \gamma_{a,x}n_x \quad (6.6)$$

where  $G(t - t_0)$  is a 100 fs Gaussian excitation pulse centred at time  $t_0$ ,  $\gamma_{b,x} = 0.06$  cm<sup>2</sup>/s is the bimolecular recombination rate for excitons, and  $\gamma_{a,x}$  is the monomolecular exciton dissociation constant. Since we are limited to a bandwidth of 0.5–2.5 THz, we are not able to directly measure the exciton dynamics. Our bandwidth is better suited for measurements of the free charge-carrier dynamics. Free carriers are generated by the dissociation of excitons, and will undergo bimolecular recombination at the conduction and valence band edges. Letting the free carrier density be  $n_f$ , and the bimolecular free carrier recombination rate

be  $\gamma_{b,f}$ , we model the free carrier lifetime with the following coupled rate equations

$$\begin{aligned}\frac{dn_x}{dt} &= G(t) - \gamma_{b,x}n_x^2 - \gamma_{a,x}n_x \\ \frac{dn_f}{dt} &= \gamma_{a,x}n_x - \gamma_{b,f}n_f^2.\end{aligned}\tag{6.7}$$

The output of this model is then normalized and scaled by a fit parameter  $A$ . An example of this model is given in Fig. 6.10. This example comes from fitting the 490  $\mu\text{J}/\text{cm}^2$  lifetime. In Fig. 6.10,  $\gamma_{b,x} = 0.06 \text{ cm}^2/\text{s}$  is fixed, and  $\gamma_{a,x} = 1.8 \pm 0.1 \text{ ps}^{-1}$ ,  $\gamma_{b,f} = 0.136 \pm 0.004 \text{ cm}^2/\text{s}$ ,  $A = 0.558 \pm 0.005$ , and  $t_0 = 1.71 \pm 0.02 \text{ ps}$ . We see that within  $\sim 5 \text{ ps}$  exciton dissociation has completed and the free carrier population reaches a maximum. Afterwards, bimolecular recombination quickly reduces the population of free electrons and holes. Fitting the data to this model is shown in Fig. 6.11. For all fluences, we find that the fits are good ( $\chi_{red}^2 \sim 10^{-4}$ ) provided there are only four fit parameters.

The best-fit parameters are shown in Fig. 6.12. In Fig. 6.12 (a) we show the bimolecular free-carrier recombination rate. We do not see a clear trend for  $\gamma_{b,f}$  as fluence is increased, but we find that on average  $\gamma_{b,x} \sim 0.41 \text{ cm}^2/\text{s}$ . The monomolecular exciton dissociation constant is shown in Fig. 6.12 (b).  $\gamma_{a,x}$  seems to decrease from  $\sim 2.4 \text{ ps}^{-1}$  to  $\sim 1.8 \text{ ps}^{-1}$  as the fluence is raised. The monomolecular exciton dissociation timescales are given by  $\tau_{m,x} = 1/\gamma_{a,x}$ , which we find to be  $\sim 500 \text{ fs}$ . This is in agreement with previous measurements in literature [290, 291]. In Fig. 6.12 (c) we find that  $A$  (the maximum  $-\Delta\mathcal{E}/\mathcal{E}_{ref}$ ) increases as the fluence is raised, and begins to saturate near the maximum fluence. Unfortunately, we do not have measurements at higher fluences to see if this is indeed saturation. Finally, the fluence dependence of  $t_0$  is shown in Fig. 6.12 (d). We find that it does not vary significantly from 1.7 ps for all fluences.

## Low Temperature

Low temperature measurements were performed using a fluence of 195  $\mu\text{J}/\text{cm}^2$  which was chosen to maximize the signal, while staying within a linear regime of Fig. 6.12 (b). The fits to the lifetimes are given in Fig. 6.13. For all temperatures measured, we find that the lifetimes are well described by the model of Eq. (6.7). For all fits we fix the Exciton bimolecular constant to  $\gamma_{b,x} = 0.06 \text{ cm}^2/\text{s}$  [124]. For the four fit parameters we find  $\chi_{red}^2 \sim$

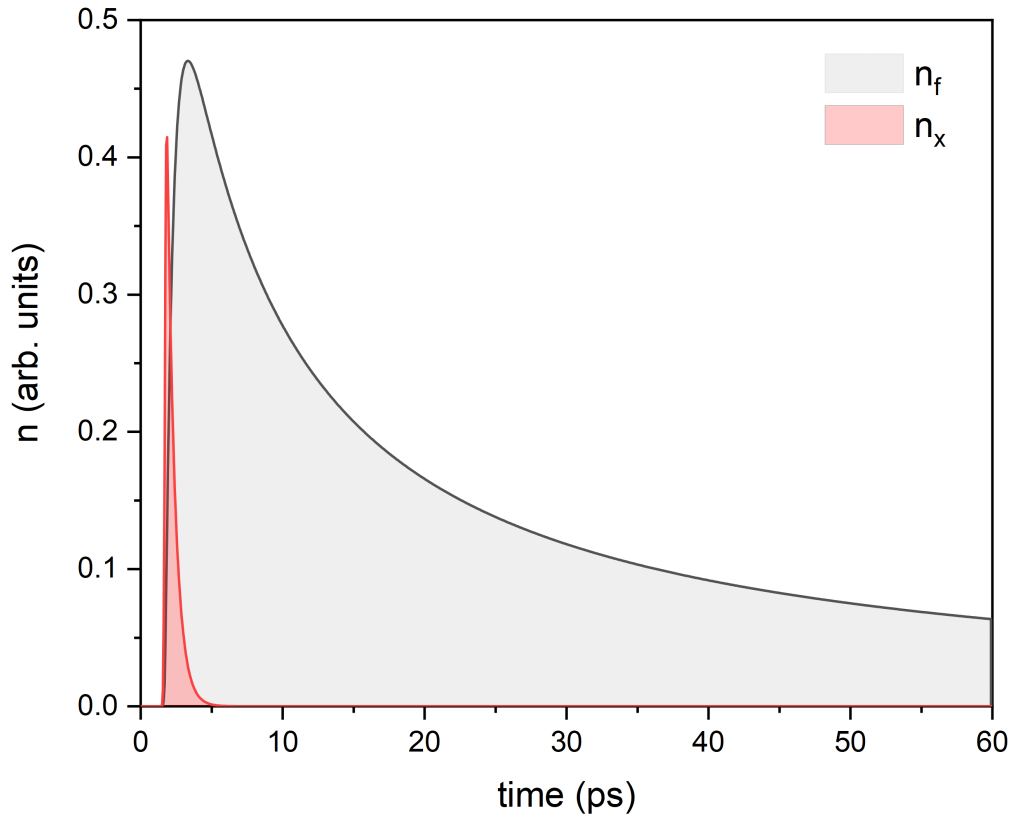


Figure 6.10: Example WSe<sub>2</sub> charge carrier lifetime model. Exciton dissociation is shown in red, and the free carrier lifetime is shown in black. Here,  $\gamma_{b,x} = 0.06 \text{ cm}^2/\text{s}$ ,  $\gamma_{a,x} = 1.8 \pm 0.1 \text{ ps}^{-1}$ ,  $\gamma_{b,f} = 0.136 \pm 0.004 \text{ cm}^2/\text{s}$ ,  $A = 0.558 \pm 0.005$ , and  $t_0 = 1.71 \pm 0.02 \text{ ps}$ .

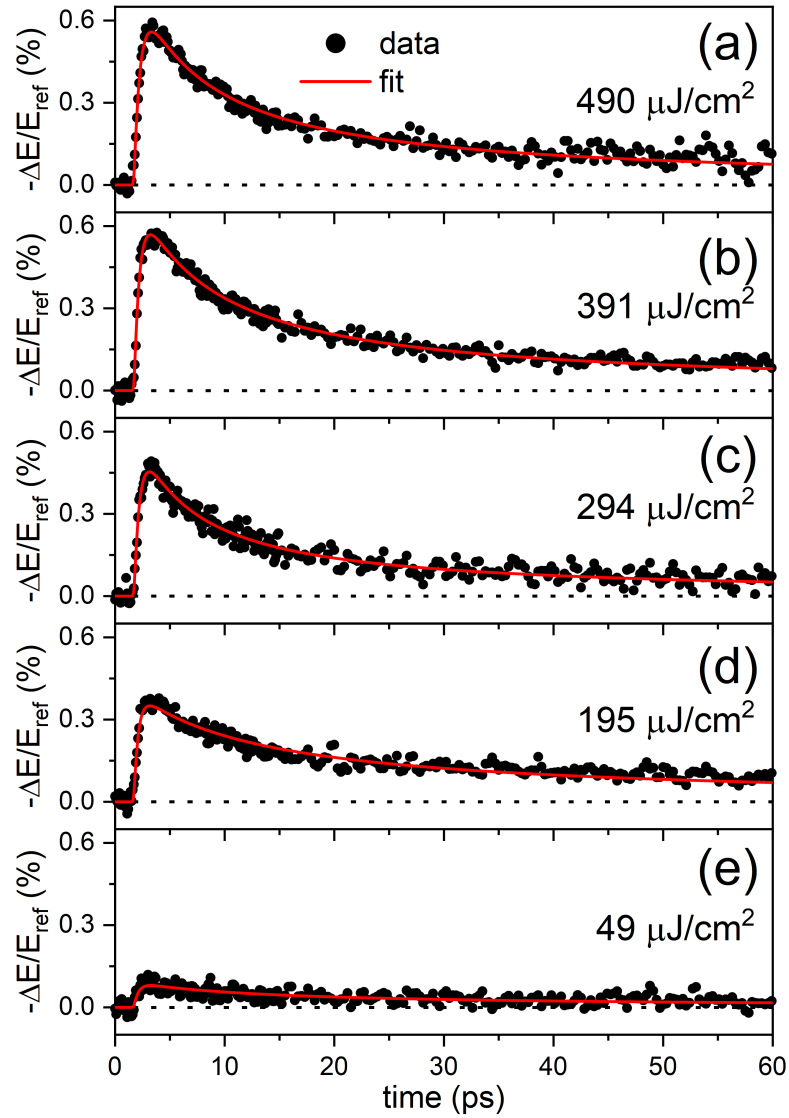


Figure 6.11: Fluence dependent lifetimes in  $\text{WSe}_2$  at 295K. Data are fit to numerical solutions of Eq. (6.7).

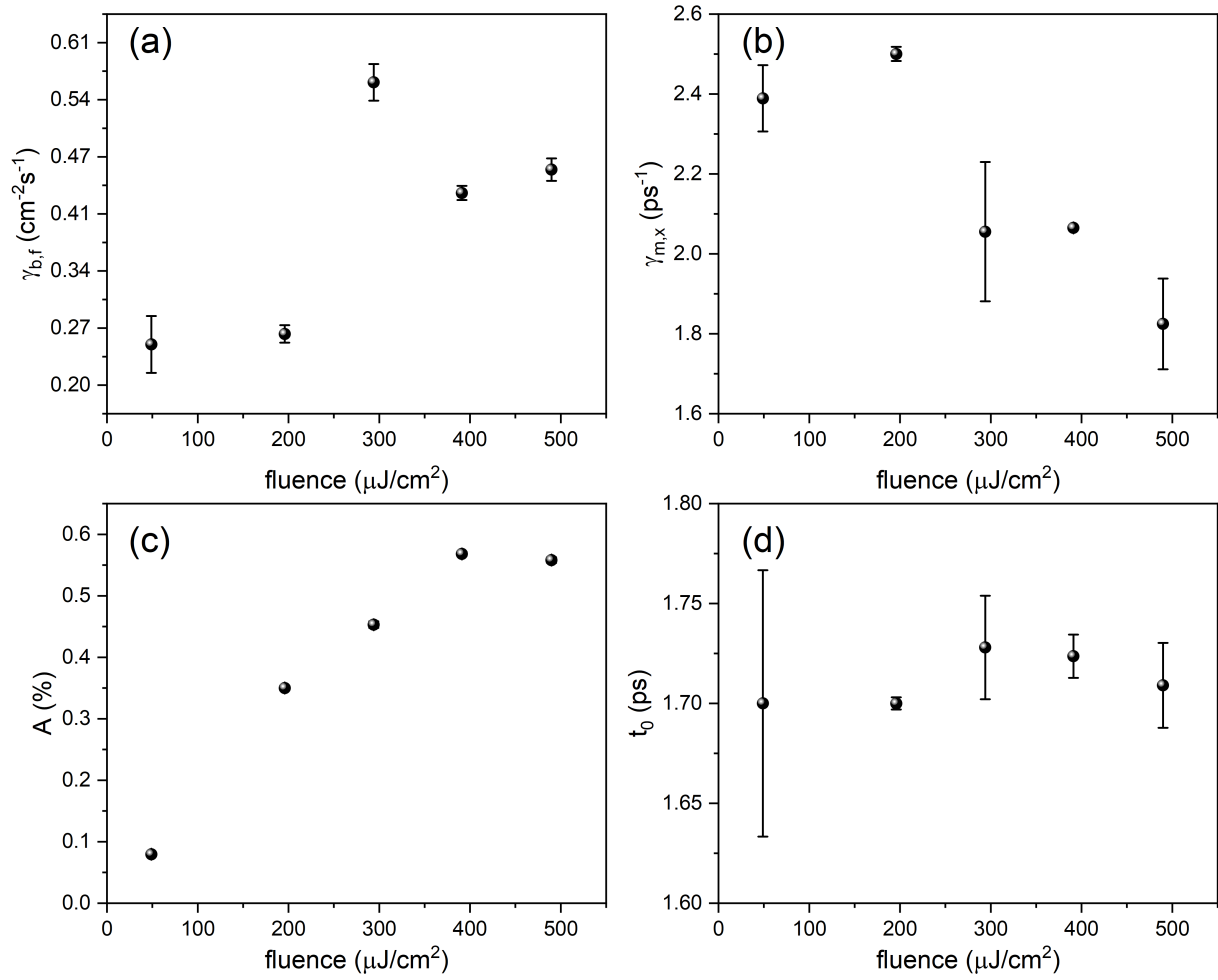


Figure 6.12:  $\text{WSe}_2$  Room temperature lifetime best fit parameters. (a) Bimolecular recombination constant for the free charge carriers. (b) Monomolecular dissociation constant of excitons. (c) Maximum  $-\Delta\mathcal{E}/\mathcal{E}_{ref}$ . Error bars are shown but they are covered by the data point size. (d) Arrival time of the Gaussian excitation.

0.04 which indicates a good fit to our data. The best fit parameters are shown in Fig. 6.14.

Figure 6.14 (a) shows the temperature dependent free carrier bimolecular recombination constant,  $\gamma_{b,f}$ . We find that as temperature is decreased, a minimum occurs around  $\sim 160$  K. The temperature dependence of the monomolecular exciton dissociation is shown in Fig. 6.14 (b). We see that as the temperature is lowered,  $\gamma_{a,x}$  peaks at  $\sim 180$  K and decreases as the temperature is lowered. Figure 6.14 (c) shows that the photoconductivity of the monolayer increases as the sample is cooled. This is in line with the temperature dependent absorption measurements we performed (cf. Fig. 6.3). There, we found that as the sample is cooled, the peak  $L_4$  blue-shifts towards our excitation energy. Because of this blue-shifting, WSe<sub>2</sub> monolayer absorbs more of the excitation, which increases the photoconductivity. As the sample is cooled, we find that  $t_0$  changes. This may be because the sample holder is contracting at lower temperatures. A change of 60  $\mu\text{m}$  would give a pump-probe delay change of 0.2 ps, which agrees with the results shown in Fig. 6.14 (d).

## 6.4.4 Terahertz Electrodynamics

### Room Temperature

Room temperature time-resolved terahertz spectroscopy performed at 1, 3.3, 6.6, and 10 ps after photoexcitation is shown in Fig. 6.15. Conductivity spectra are organized by rows and columns. Columns denote the time elapsed since photoexcitation. Rows are organized by fluence such that Figs. 6.15 (a) - (d) correspond to excitation at 490  $\mu\text{J}/\text{cm}^2$ , Figs. 6.15 (e) - (h) correspond to excitation at 391  $\mu\text{J}/\text{cm}^2$ , Figs. 6.15 (i) - (l) correspond to 293  $\mu\text{J}/\text{cm}^2$ , Figs. 6.15 (m) - (p) correspond to 196  $\mu\text{J}/\text{cm}^2$ , and Fig. 6.15 (q) was taken at 49  $\mu\text{J}/\text{cm}^2$ . At each of these fluences and times we fit photoconductivity to the Drude-Smith model, using an effective mass of  $0.3m_e$  [292–294]. A detailed discussion of the Drude-Smith model can be found in Section 2.2.2. Briefly, the photoconductivity is given by

$$\tilde{\sigma}(\omega) = \frac{ne^2\tau}{m^*} \frac{1}{1 - i\omega\tau} \left( 1 + \frac{c}{1 - i\omega\tau} \right), \quad (6.8)$$

where  $n$  is the charge carrier density,  $\tau$  is the scattering rate,  $m^*$  is the electron effective mass, and  $c$  is the localization constant. The localization constant encompasses carrier

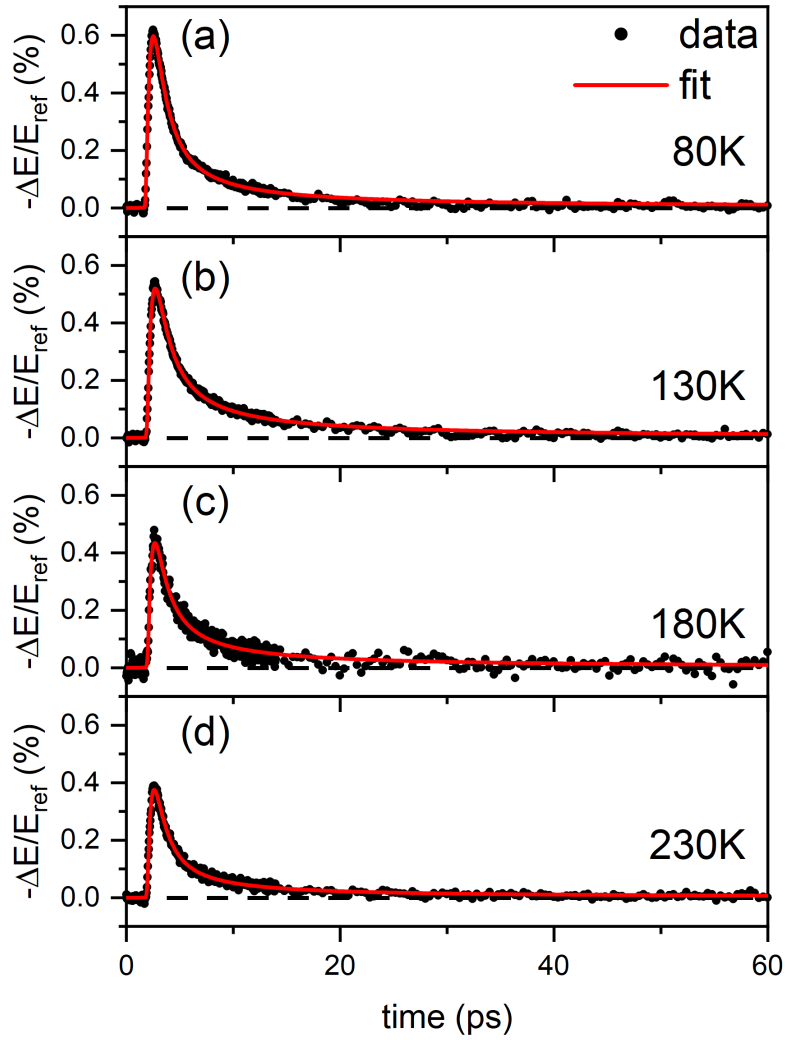


Figure 6.13: Low temperature lifetime fits of WSe<sub>2</sub> monolayer measured at (a) 80 K, (b) 130 K, (c) 180 K, and (d) 230 K. All measurements excited with 410 nm, 100 fs pulses at a fluence of 195  $\mu\text{J}/\text{cm}^2$ .

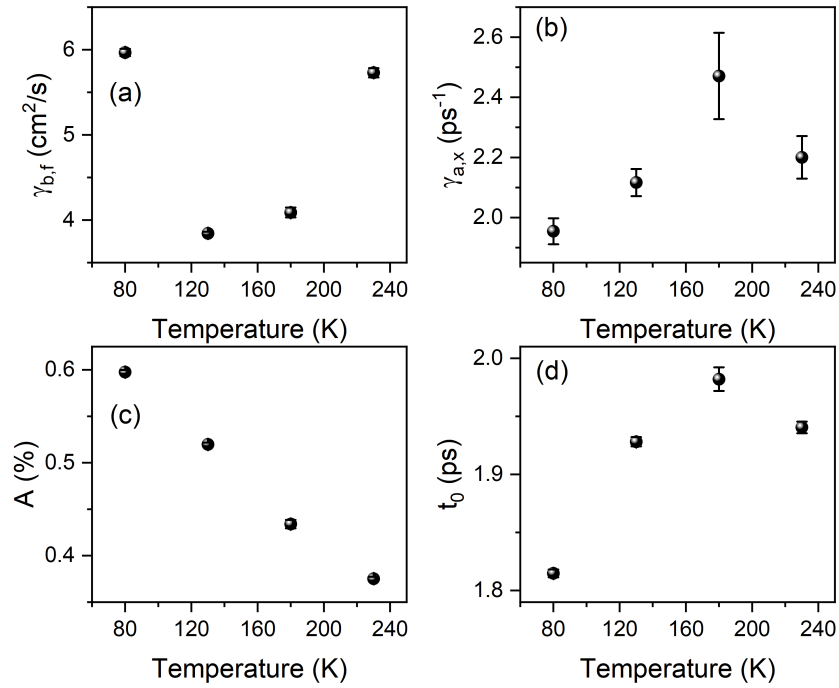


Figure 6.14: Low temperature lifetime best fit parameters of WSe<sub>2</sub> monolayer. (a) Bimolecular recombination constant for the free charge carriers. (b) Monomolecular dissociation constant of excitons. (c) Maximum  $-\Delta\mathcal{E}/\mathcal{E}_{ref}$ . Error bars are shown but they are covered by the data point size. (d) Arrival time of the Gaussian excitation.

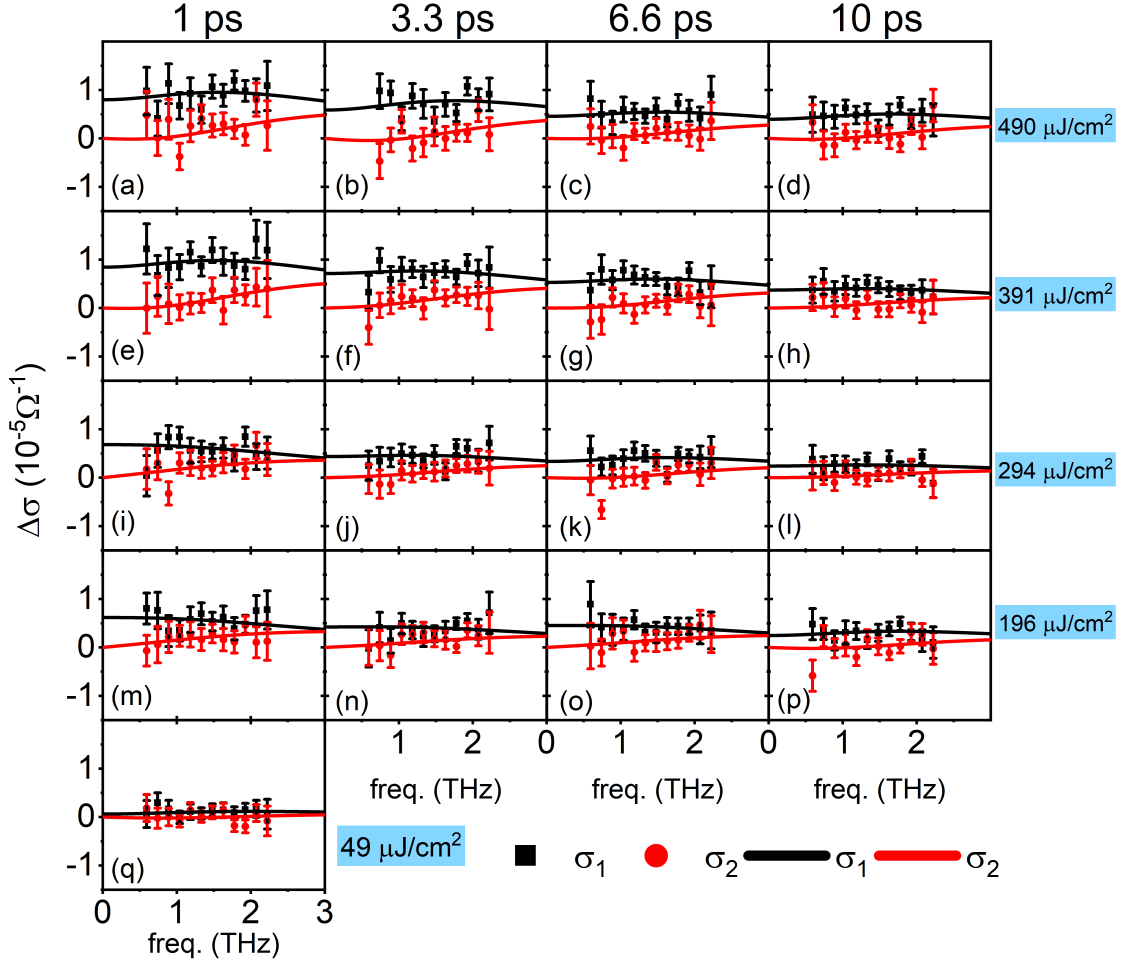


Figure 6.15: WSe<sub>2</sub> Room temperature Drude-Smith fits. (a) - (d) correspond to excitation at 490  $\mu\text{J}/\text{cm}^2$ , (e) - (h) correspond to excitation at 391  $\mu\text{J}/\text{cm}^2$ , (i) - (l) correspond to 293  $\mu\text{J}/\text{cm}^2$ , (m) - (p) correspond to 196  $\mu\text{J}/\text{cm}^2$ , and (q) was taken at 49  $\mu\text{J}/\text{cm}^2$ .

backscattering from an interface, and is on the domain  $[0, -1]$ . The sheet conductivity is given by  $\tilde{\sigma}_{sheet} = \tilde{\sigma}d$ , where  $d = 0.75$  nm is the thickness of the monolayer we measured in Section 6.2.1. Likewise, the sheet carrier density is given by  $n_{sheet} = nd$ . The DC long-range sheet conductivity is given by  $\sigma_{l.r.} = \tilde{\sigma}(\omega = 0) \times d = ne\mu_{s.r.}(1 + c) \times d$ , where  $\mu_{s.r.} = e\tau/m^*$  is the short-range mobility.

The fluence and time dependence of the Drude-Smith parameters are shown in Fig. 6.16. The scattering time  $\tau_{DS}$  did not change with fluence, and so the average value of  $65 \pm 5$  fs was used for all of the fits. This yields a short-range mobility of  $380 \pm 30$   $\text{cm}^2/\text{Vs}$ , which agrees well with measurements of the electron mobility in high-performance monolayer WSe<sub>2</sub>

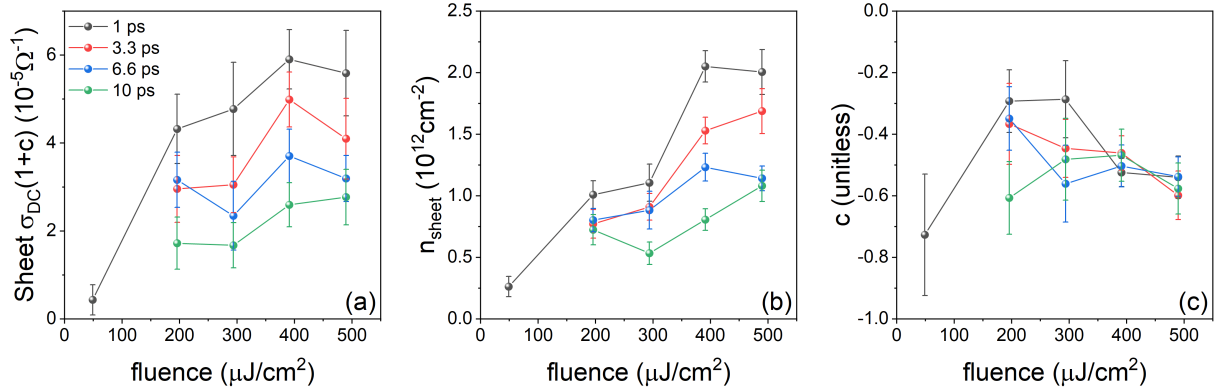


Figure 6.16: WSe<sub>2</sub> room temperature Drude-Smith fit parameters. (a) Long-range DC sheet conductivity, (b) carrier density, and (c) Drude-Smith  $c$  parameter.

field effect transistors [249]. In Fig. 6.16 (a) we show the DC long range sheet conductivity  $\sigma_{sheet}(1+c)$ . The fluence dependence of each pump-probe delay time is shown, with 1 ps (black), 3.3 ps (red), 6.6 ps, (blue), and 10 ps (green) after maximum  $-\Delta\mathcal{E}/\mathcal{E}_{ref}$ . Overall,  $\sigma_{sheet}(1+c)$  increases with fluence, and decreases with time. The behaviour of  $\sigma_{sheet}(1+c)$  is not limited by changes in  $\tau_{DS}$  because it was fixed, which leaves the sheet carrier density  $n_{sheet}$  and the localization parameter,  $c$ , which are shown in Fig. 6.16 (b) and (c), respectively. Generally, as the fluence is increased, the sheet density also increases. Furthermore, as time progresses, the recombination of charge carriers lowers the carrier density. The localization parameter,  $c$ , does not appear to have an overall dependence on fluence, although there may be a maximum around the excitation density of 200  $\mu\text{J}/\text{cm}^2$ , indicating a minimal localization that can be used to optimize device performance.

Since the localization parameter is  $c \sim 0.5$ , we find that the real part of the conductivity plays a dominant role in our observed bandwidth. Because of this, the time-dependence of the short-range sheet conductivity ( $\sigma_{sheet}$ ) closely follows the lifetimes, as shown in Fig. 6.17. It is becoming increasingly common to present this in terms of the carrier density  $n_{sheet}$  [124, 126], and a word of caution is needed. When the charge carrier mobility is large, it is usually the result of a large scattering time  $\tau$ . Furthermore, within the Drude model of conductivity, it is clear that when  $1/\tau$  is below our THz bandwidth ( $1/\tau \lesssim 0.5$  THz), the imaginary part of the conductivity dominates the spectrum. The imaginary part of the Drude-model has, in its numerator, an extra  $\omega\tau$  compared to the real part. In turn this

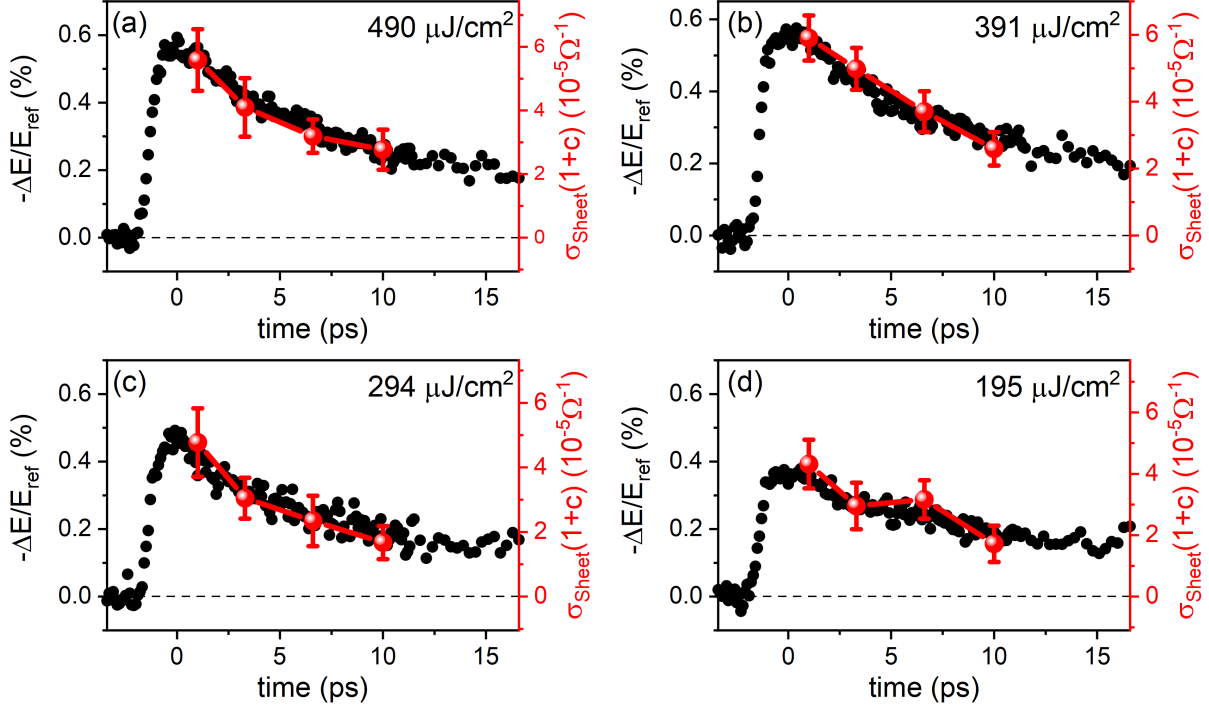


Figure 6.17: WSe<sub>2</sub> 295 K Drude-Smith DC sheet conductivity (red) and differential transmission (black) for all fluences. (a) 490  $\mu\text{J}/\text{cm}^2$ , (b) 391  $\mu\text{J}/\text{cm}^2$ , (c) 294  $\mu\text{J}/\text{cm}^2$ , and (d) 195  $\mu\text{J}/\text{cm}^2$ .

cancels the dependence of  $\tau$ , which makes the lifetimes sensitive to only changes in effective mass and carrier density (i.e. the plasma frequency instead of the DC conductivity). Given the conditions in our experiments, the real part of the conductivity is dominant, and so we indeed find  $-\Delta\mathcal{E}/\mathcal{E}_{ref} \propto \sigma_{sheet}$ .

### Low Temperature

Time-resolved spectroscopy was performed at 80 K, 130 K, 180 K, and 230 K using a fluence of 195  $\mu\text{J}/\text{cm}^2$ . Spectroscopy was also acquired at times of 1 ps, 3.3 ps, 6.6 ps, and 10 ps after peak  $-\Delta\mathcal{E}/\mathcal{E}_{ref}$ . Real and imaginary conductivities acquired at 1 ps after maximum  $-\Delta\mathcal{E}/\mathcal{E}_{ref}$  are shown in Fig. 6.18 with fits to a Drude-Smith model (solid lines). The Drude-Smith model captures the essence of the conductivity spectrum, however there are features that warrant future measurement. First, it seems that the steepness of the real conductivity ( $\sigma_1$ ) is underappreciated by the Drude-Smith model, and becomes significantly different by 80 K. The imaginary part ( $\sigma_2$ ) appears to have oscillations which, to our knowledge, have not

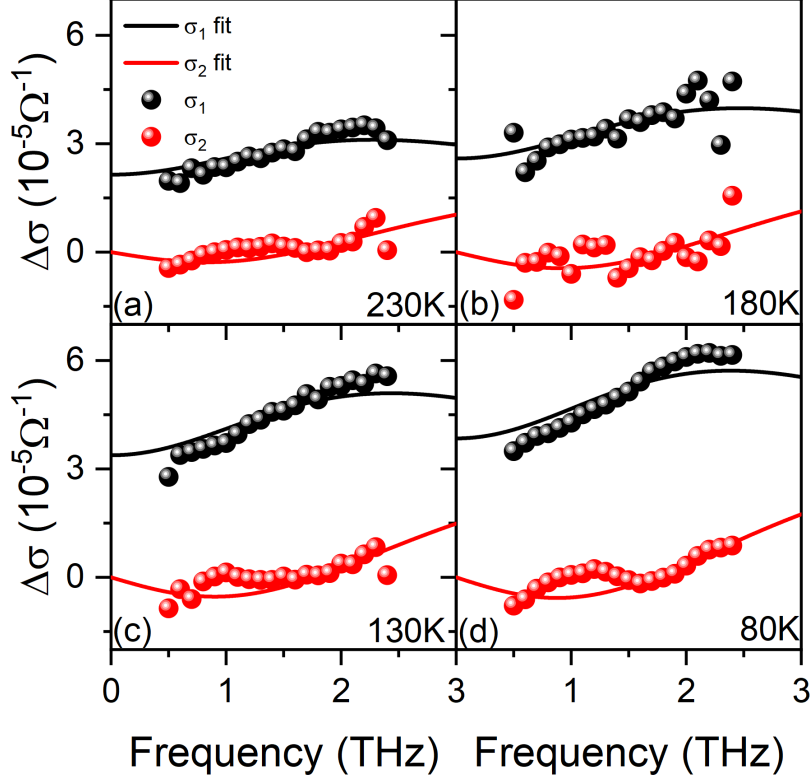


Figure 6.18: Low temperature TRTS of WSe<sub>2</sub> monolayer. Spectra are acquired at (a) 230 K, (b) 180 K, (c) 130 K, and (d) 80 K. All spectra were taken at 1 ps after peak  $-\Delta\mathcal{E}/\mathcal{E}_{ref}$ .

been reported in monolayer WSe<sub>2</sub> before. It is unclear what these features are suggesting, and future work must encompass a bandwidth of at least 5 THz in order to directly observe trion resonances [125].

Drude-Smith fit parameters corresponding to the fits in Fig. 6.18 are given in Fig. 6.19. In Fig. 6.19 (a), we show the Drude-Smith scattering time  $\tau_{DS}$ . Between 295 and 230 K, the scattering rate lowers from  $65 \pm 5$  fs to  $\sim 50$  fs, after which it plateaus and shows no temperature dependence. The most drastic change with temperature is the carrier density  $n_c$  shown in Fig. 6.19 (b). As the sample is cooled, we showed that the peak of the absorption near 3 eV blue shifts. Since we are photoexciting at energies above this peak, the blue-shifting results in an increase in absorption at 410 nm. This is indeed reflected in the carrier densities shown in Fig. 6.19 (b). The long-range mobility is shown in Fig. 6.19 (c). There is an apparent minimum at 180 K, however, given that all of these mobilities agree well with the average value of  $\mu_{l.r.} \sim 90$  cm<sup>2</sup>/Vs (dashed line), it is unclear if this is a significant

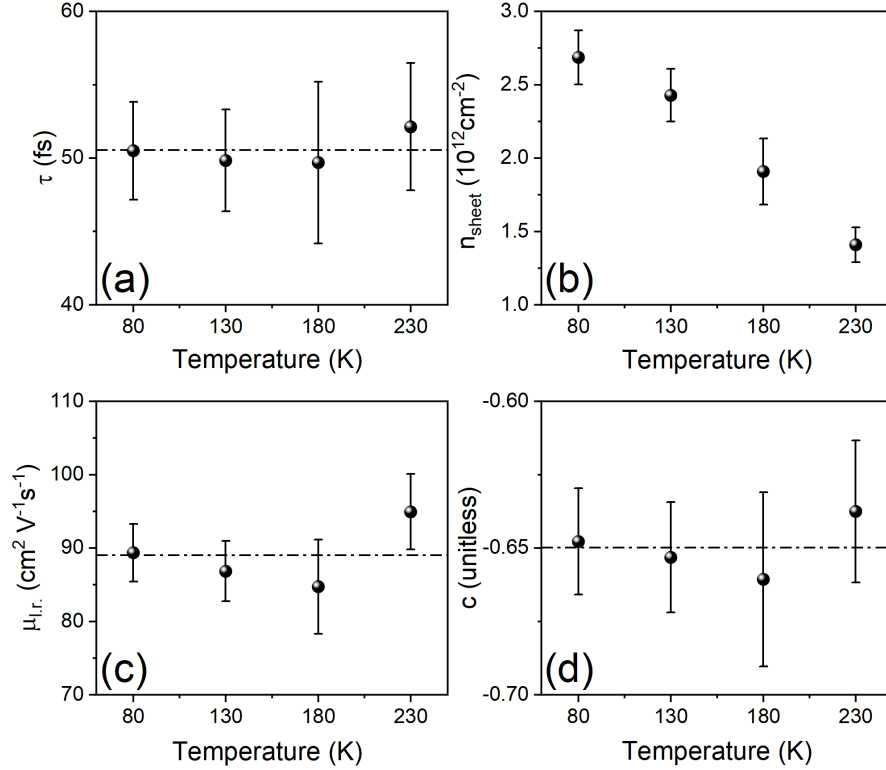


Figure 6.19: Low temperature Drude-Smith results for WSe<sub>2</sub> monolayer. Average values are represented by a dashed line. (a) Scattering time, (b) carrier density, (c) short-range mobility, and (d)  $c$  parameter.

finding. The same goes for the localization parameters in Fig. 6.19 (d), which all seem to agree well with the average value of  $c \sim 0.65$ .

From Fig. 6.19 (d) we find that the localization parameter is near  $c \sim 0.6$ , which results in a negligible  $\sigma_2$  in our spectrum. As a result, the sheet conductivities align well with the differential transmission, as shown in Fig. 6.20.

## 6.5 Summary

In this chapter we investigated the fluence and temperature dependence of the ultrafast photoconductivity in a WSe<sub>2</sub> monolayer within the 0.5-2.5 THz bandwidth.

At room temperature, the photoconductivity lifetimes indicate that exciton formation has a significant impact on the transient carrier density, and early ( $< 1$  ps) exciton dissociation gives rise to a population of free carriers. The free carriers undergo bimolecular recombination. As the fluence is increased from 49 to 490  $\mu\text{J}/\text{cm}^2$ , we observe a slight in-

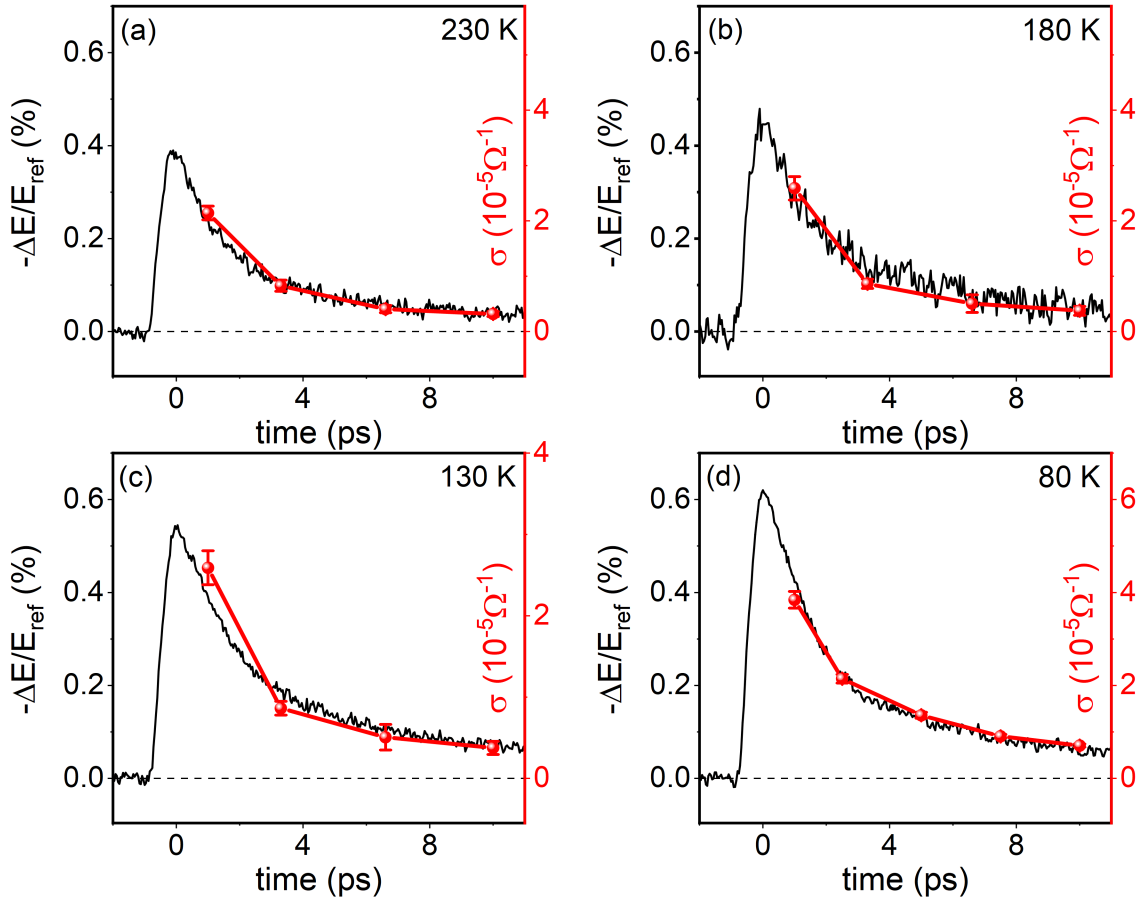


Figure 6.20: Temperature dependence of  $\Delta\mathcal{E}/\mathcal{E}_{ref}$  (black) and  $\sigma_{sheet}(1+c)$  (red). Lifetimes and  $\sigma_{sheet}(1+c)$  at (a) 230 K (b) 180K (c) 130K, and (d) 80K using 410 nm excitation at a fluence of  $195 \mu\text{J}/\text{cm}^2$ .

crease in the free carrier bimolecular recombination constant,  $\gamma_{b,f}$ , from  $\sim 0.25$  to  $\sim 0.44$   $\text{cm}^2/\text{s}$ . The exciton dissociation constant,  $\gamma_{a,x}$ , is found to decrease from  $\sim 2.5$  to  $1.9$   $\text{ps}^{-1}$  as the fluence is raised. This corresponds with an increase of the dissociation time from 400 to 526 fs. The amplitude of the photoconductivity is seen to increase as the fluence is increased, and potential saturation is observed at a fluence of  $490$   $\mu\text{J}/\text{cm}^2$ .

As the sample is cooled, the free carrier bimolecular recombination constant exhibits nontrivial behaviour. Starting at  $1.6$   $\text{cm}^2/\text{s}$  at  $230\text{K}$ ,  $\gamma_{b,f}$  is found to reach a minimum of  $\sim 4$   $\text{cm}^2/\text{s}$  around  $130$  K.  $\gamma_{b,f}$  then increases as the temperature is lowered further. The monomolecular exciton dissociation constant,  $\gamma_{a,x}$ , is found to initially increase as the temperature is lowered and reaches a maximum of  $2.5$  ps at  $180$  K. As the sample is cooled further,  $\gamma_{a,x}$  is found to decrease. The absorption of the sample was found to have a strong temperature dependence. As the sample is cooled, the absorption peak nearest the excitation energy ( $3.1$  eV) is found to blue shift into the excitation energy. This results in an increase of the monolayer absorption, which is reflected in the maximum photoconductivity we observe. As the temperature is lowered, we find that the photoconductivity does indeed increase.

At room temperature we perform time-resolved terahertz spectroscopy. The conductivity spectra are fit to a Drude-Smith model. We find that the sheet conductivity lowers as time progresses after excitation. As the fluence is increased, the conductivity is found to increase as well. The sheet density of carriers is also found to increase with fluence, and the localization parameter does not have a clear dependence on fluence. The  $c$ -parameter is found to be  $\sim -0.5$ .

Cooling the sample does not seem to have a significant effect on the photoconductivity of the  $\text{WSe}_2$  monolayer. The scattering rate is found to be  $\sim 50$  fs for all temperatures. The sheet density of carriers is found to increase as the sample is cooled, which is in line with our observations of the temperature dependent absorption and photoconductivity lifetimes. The long-range mobility and  $c$  parameter are found to be constant,  $\mu_{l,r} \sim 90$   $\text{cm}^2/\text{Vs}$  and  $c \sim 0.65$ , respectively.

# Chapter 7

## Inverse-Opal $\text{Si}_x\text{Ge}_{17-x}$

### Nanostructures

#### 7.1 Introduction

Group 14 elemental semiconductors Si and Ge are important in a broad range of applications such as optoelectronics, sensing, photovoltaic, and battery applications [127–133]. Recently, thin films comprised nanowires, nanoparticles, and periodically porous nanostructures have attracted attention due to their large surface-to-volume ratio. In particular, nanowires [134] and nanoparticles [130, 135–137] have been widely investigated. However, reports on periodically porous nanostructures remain comparably sparse [138], despite the potential to form long-range connectivity within the nanostructure. The primary technique of constructing a periodically porous thin film is through the top-down approach of electrochemically etching a bulk semiconductor [295–298]; however, this approach provides limited control over the final morphology of the porous structure [299]. A bottom-up approach using molecular precursors results in a higher degree of control over the size, shape, and arrangement of the pores.

Metal oxides such as  $\text{TiO}_2$  are suitable candidates for a wide range of periodic porous nanomaterials [300], but there is a lack of suitable precursors for group 14 semiconductors. So far, the existing techniques include cathodic electrodeposition of group 14 halides [301–303], chemical vapour deposition of silanes and germanes [304, 305], and reduction of oxides

with hydrogen [306–308]. Zintl phase group 14 semiconductors were also investigated as a soluble precursor material due to their ability to form nanostructures with tunable composition and electronic properties. The Zintl phase is a product of reacting a group 1, 2 element with a group 13, 14, 15, or 16 element [309]. The Zintl phase is named after Edward Zintl, who provided the rationale behind their structure. Similar to ionic salts (like NaCl), the electropositive group 1,2 element transfers an electron to the more electronegative element in groups 13-16. However, such a bond does not complete the octet of the anion. To minimize the remaining energy, anions bond to one another, resulting in a structure that would normally occur in the material to the right of the group 13-16 element (Owing to the extra electron from the electropositive element)[310]. For example, in  $\text{Na}^+\text{Tl}^-$ , a diamond structure is formed because the free electrons of the  $\text{Tl}^-$  (group 13) minimize energy according to the structure of group 14 elements, among which one finds carbon, silicon and germanium.

Zintl phase compounds are soluble in select solvents [309], and the solubility of the Zintl phase makes it an excellent candidate for a templating process, as demonstrated by Bentlohner et al. [138], where  $\text{K}_4\text{Ge}_9$  was used as a precursor. The unit cell of  $\text{K}_4\text{Ge}_9$  is shown in Fig. 7.1 (a), where the purple spheres represent the K atoms and the grey spheres represent the Ge atoms. In total there are 208 atoms in the unit cell [309]. The solution of  $\text{K}_4\text{Ge}_9$  was deposited onto a scaffold of poly(methyl methacrylate) (PMMA) beads. Oxidation (removal) of the K anion from the Zintl solution occurs by dissolving the Zintl solution in ethylenediamine (en) containing trace amounts of  $\text{H}_2\text{O}$ . The  $\text{H}_2\text{O}$  triggers the oxidation of the Zintl anion (K). The result is a disordered phase of Ge that can be annealed at 600 °C to form a network of amorphous  $\alpha\text{-Ge}^*$  [138]. The PMMA beads underwent pyrolysis at this temperature, and elemental K is also released. After the anneal, a mechanically stable film of Ge is produced, having the nanostructure comprised of the negative space of the PMMA bead scaffold (inverse opal), as shown in Fig. 7.1 (b).

Bentlohner et al. also demonstrated tunability of the Zintl phase [138]. The Zintl phase of  $\text{K}_4\text{Ge}_9$  can be modified by first depositing a  $\text{K}_4\text{Ge}_9$  scaffold, and submitting it to a vapour of  $\text{ECl}_n$  ( $\text{SiCl}_4$ ,  $\text{GeCl}_4$ , or  $\text{PCl}_3$ ). Adding and removing en as above results in a scaffold

---

\* $\alpha\text{-Ge}$  is the hexagonal close-packed phase.

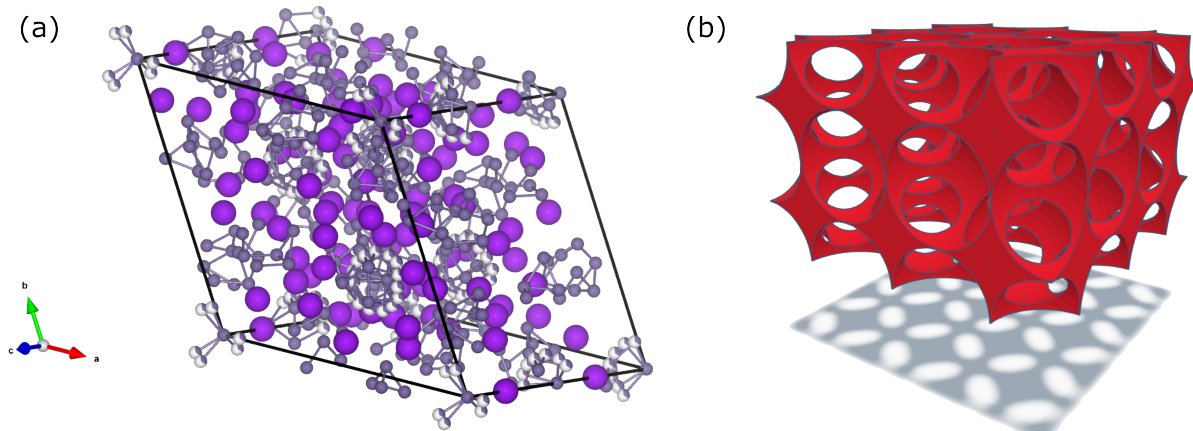


Figure 7.1: (a)  $K_4Ge_9$  Zintl phase unit cell, where purple spheres are K grey spheres are Ge. This image is made using Vesta 3 [189] with crystallographic information is retrieved from the Springer Materials database [311]. (b) Inverse opal structure comprised of a cube with spherical voids resulting from an ABA stacking of spheres.

of amorphous  $Ge_xE_{1-x}$  that can be annealed<sup>†</sup>. Subsequent washing with dimethyl sulfoxide (DMSO) and tetrahydrofuran (THF) removes residual KCl and PMMA that accumulated during the templating process [138].

It is well known that Ge is significantly more expensive than Si, so in this work we leverage the precursor tunability to compare the charge-carrier mobility of the set of  $K_{12}Si_{17-x}Ge_x$  ( $x = 0, 5, 12, 17$ ) precursors for the first time. For future battery and optoelectronics applications, the property of merit is the charge-carrier mobility  $\mu$ , which can be obtained via time-resolved terahertz spectroscopy (TRTS). Further, the non-contact nature of TRTS is ideal for measuring the mobility of inverse-opal thin films because deposition of Ohmic contacts onto the brittle amorphous structure is challenging, if not impossible [32].

## 7.2 Terahertz Spectroscopy Considerations

### 7.2.1 Spectroscopy

The most important physical difference between amorphous and crystalline germanium is the lack of long-range periodicity that occurs in amorphous materials. As discussed in Chapter 2, the long range periodicity of the medium gives rise to Bloch states, which are used to construct the energy bands in reciprocal space. In amorphous mediums there are no Bloch

<sup>†</sup>Here,  $x$  is the germanium fraction. It is unique to each blend, so here we denote it in a more general fashion.

states, and so the focus shifts away from band structure to density of states. Subsequently, depending on the distribution of the mid-gap states, various power laws are derived to describe conduction in a disordered metal [176, 312–315].

In Section 2.2.2 we discussed the conductivity of disordered metals. Photoexcited Ge and Si can be considered metallic because the quasi-Fermi level resides in the conduction band, there is a large number of available charge carriers, and the mobilities of Ge and Si are large (3800 and 1450 cm<sup>2</sup>/Vs, respectively [170]). In the inverse opal nanostructures studied here, we expect to find a disordered structure, and so the photoconductivity falls within the description of a disordered metal.

We will use the Drude-Smith model to fit our photoconductivity spectra. Here we briefly discuss how one can begin with the Drude-Smith model and arrive at an identical description of the photoconductivity to the empirical models of disordered metals we discussed in Section 2.2.2. In the Drude-Smith model, the conductivity spectrum,  $\tilde{\sigma}$ , is given by

$$\tilde{\sigma}(\omega) = \frac{\sigma_{DC}}{1 - i\omega\tau} \left( 1 + \frac{c}{1 - i\omega\tau} \right).$$

where  $\sigma_{DC} = ne^2\tau/m^*$  is the short-range DC conductivity of the film,  $n$  is the charge carrier density,  $m^*$  is the effective mass,  $\tau$  is the scattering time, and  $c$  is the localization parameter that exists on the domain  $[0, -1]$ . In the low-frequency limit  $\tilde{\sigma}(\omega)$  can be expanded in a Taylor series around  $\omega\tau = 0$ . Retaining terms up to  $\mathcal{O}(2)$  gives

$$\tilde{\sigma}(\omega) \approx \sigma_{DC} (1 + c - i\omega\tau(2c + 1) - c\omega^2\tau^2) \quad (7.1)$$

and so

$$\sigma_1(\omega) = \sigma_{DC}(1 + c - c\tau^2\omega^2). \quad (7.2)$$

Keeping in mind that  $c \in [0, -1]$ , it is clear that the Drude-Smith model provides a polynomial dependence on  $\omega$  at low frequency, however we are constrained by  $\alpha = 2$  which is independent of the electron-electron scattering [176] yet also consistent with observations in Si-Ge thin films [316] (cf. Section 2.2.2). Therefore, within the framework of the Drude-

Smith model, the parameters for a disordered metal take the form

$$B = \sigma_{DC}(1 + c) \quad (7.3)$$

and

$$A = -\sigma_{DC}c\tau^2, \quad (7.4)$$

which are both dependent on the localization parameter  $c$ . In Section 2.2.2 we noted that when  $B > 0$  the material is thought to be in a situation of moderate disorder. According to Eq. (7.3), moderate disorder occurs when  $c \in (0, -1)$ . The metal phase happens when  $c = 0$ , and the metal-insulator transition takes place when  $c = -1$ . Therefore, the interpretation of the power-law coefficients is not strictly limited to just electron-electron interactions (through  $\tau$ ), but also on the reflectivity of domain boundaries and the scattering interval through  $c$  and  $\tau$ , respectively [167]. Finally, as  $\omega \rightarrow \infty$ , the leading term of the Drude-Smith model is given by

$$\sigma_1(\omega) \sim \frac{\sigma_{DC}}{1 + \omega^2\tau^2}, \quad (7.5)$$

which clearly satisfies the anticipated  $1/\omega^2$  fall off<sup>‡</sup>. Based on this analysis, we will proceed to fit the photoconductivity spectrum with the Drude-Smith model to parameterize the photoconductivity for comparison against studies of Si-Ge thin films [76–78, 81, 159, 317–323]. Since the Drude-Smith model reduces to the model of disordered transport in metals, we will fit our photoconductivity to the Drude-Smith model.

## 7.2.2 Lifetimes

Extensive work by Nampoothiri et al. documents terahertz photoconductivity dynamics in hydrogenated  $\text{Si}_x\text{Ge}_{1-x}$  thin films [324–327]. Nampoothiri et al. fit their lifetimes to a power law of the form

$$-\Delta\mathcal{E}/\mathcal{E}_{ref} \propto t^{\alpha-1}, \quad (7.6)$$

---

<sup>‡</sup>As does the Drude model.

where the activation energy,  $\alpha$ , is determined through the relation

$$\alpha = \frac{k_B T}{k_B T_0} \quad (7.7)$$

where  $T$  is the sample temperature and  $k_B T_0$  is the activation energy that describes the extent of the localized states [315]. The exponent  $\alpha - 1 \sim -0.5$  has been observed in disordered materials such as radiation damaged silicon and functionalized pentacene [140, 328].

### 7.2.3 Effective Mass

The effective mass of the composite medium is determined by taking the harmonic average of the constituent effective masses [14]. In silicon, the effective mass is found through the average

$$\frac{1}{m_{Si}^*} = \frac{1}{2} \left[ \frac{1}{m_{e,Si}} + \frac{1}{m_{h,Si}} \right], \quad (7.8)$$

where  $m_{Si}^*$  is the effective mass in silicon,  $m_{h,Si} = 0.81m_e$  is the hole mass in silicon, and  $m_{e,Si} = 0.26m_e$  is the electron mass in silicon. Likewise, for germanium, we obtain

$$\frac{1}{m_{Ge}^*} = \frac{1}{2} \left[ \frac{1}{m_{e,Ge}} + \frac{1}{m_{h,Ge}} \right], \quad (7.9)$$

where  $m_{Ge}^*$  is the effective mass in germanium,  $m_{h,Ge} = 0.34m_e$  is the hole mass in germanium, and  $m_{e,Ge} = 0.22m_e$  is the electron mass in germanium [170].

For the composite medium, the effective mass is then

$$\frac{1}{m^*} = \frac{1}{2} \left[ \frac{f_{Ge}}{m_{Ge}^*} + \frac{1 - f_{Ge}}{m_{Si}^*} \right], \quad (7.10)$$

where  $f_{Ge}$  is the germanium fraction of the sample.

## 7.3 Sample Preparation

The substrates used in this experiment were  $\sim 1.0 \text{ cm} \times 1.5 \text{ cm} \times 1.0 \text{ mm}$  fused silica, cleaned in an alkaline solution of Extran, water, and acetone. Substrates were cleaned in an ultrasonic bath for 15 min. each, and subsequently placed in an  $\text{O}_2$  plasma (Femto, Diener, 50% power) for 10 minutes. The cleaned substrates were dip coated in PMMA suspensions,

Sample	Fluence ( $\mu\text{J}/\text{cm}^2$ )	Power law ( $\alpha$ )	Total Power law ( $\alpha - 1$ )	Activation energy (meV)
Si <sub>17</sub>	1296	$0.55 \pm 0.03$	-0.45	46.2
	1610	$0.42 \pm 0.04$	-0.58	60.5

Table 7.1: Table of power law best-fit values for the Si<sub>17</sub> inverse opal film.

comprised of 15% wt. PMMA in water. Coated substrates were dried at 373 K for 4 hours under vacuum. The PMMA scaffold was then infiltrated with a filtered K<sub>12</sub>Si<sub>17-x</sub>Ge<sub>x</sub> (x = 0, 5, 12, 17) precursor solution in en by dropcasting 10  $\mu\text{L}$  onto the substrate. After 1 hour at room temperature, the thin films were treated with GeCl<sub>4</sub> (SiCl<sub>4</sub> for x = 0) overnight. The samples were then dried at 373 K for 1 hour in vacuum before annealing at 773 K for 5 minutes. Residual PMMA and KCl were removed by washing with DMSO and THF for 30 minutes each before drying in vacuum at room temperature.

## 7.4 Results

In the following experiments, 800 nm, 100 fs excitation pulses were used to photoexcite the inverse-opal films. Fluences ranging from 486 - 1610  $\mu\text{J}/\text{cm}^2$  were selected based on the observed photoconductivity response, which significantly varied between samples.

### 7.4.1 Si<sub>17</sub> (0% Ge)

#### Lifetimes

The Si<sub>17</sub> sample exhibited a weak photoconductivity response and so large excitation fluences of 1296 and 1620  $\mu\text{J}/\text{cm}^2$  were needed to photoexcite the Si<sub>17</sub> inverse opal film. The photoconductivity lifetimes at these fluences are shown in Fig. 7.2 (a) and (b). Figure 7.2 (b) shows the data from (a) on a logarithmic y-axis for clarity. The data are fit to the power law of Eq. (7.6). The data are fit for lifetimes greater than 1 ps after maximum  $-\Delta\mathcal{E}/\mathcal{E}_{ref}$  to avoid hot carrier dynamics. The best-fit variables can be found in Table 7.1. From the fits we find that the total power law is  $\sim -0.5$ , which is consistent with previous measurements on radiation-damaged silicon on sapphire and amorphous silicon thin films [318, 324–326]. We also report an activation energy of  $\sim 50$  meV.

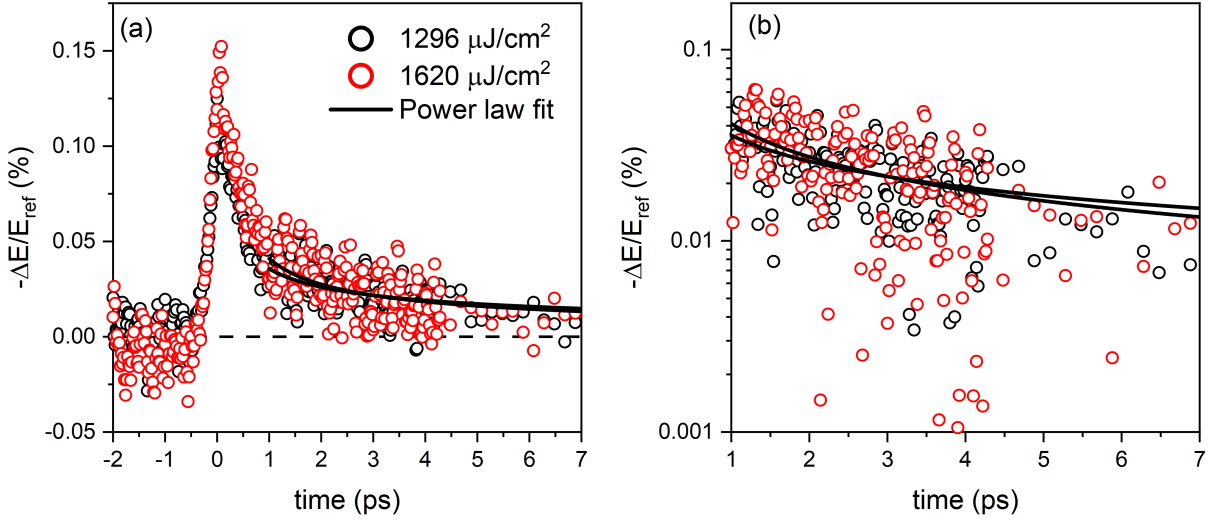


Figure 7.2: Photoconductivity lifetimes for the Si<sub>17</sub> inverse opal film. (a) 1296  $\mu\text{J}/\text{cm}^2$  (black circles) and 1620  $\mu\text{J}/\text{cm}^2$  (red circles). (b) Lifetimes from (a) shown on a logarithmic y-axis for clarity. Black lines are the power law fits, and the dashed black line is the zero photoconductivity baseline.

Fluence ( $\mu\text{J}/\text{cm}^2$ )	$n$ ( $10^{18} \text{ cm}^{-3}$ )	$\tau$ (ps)	$c$ (Unitless)	$\sigma_{l.r.}$ ( $\Omega^{-1}\text{cm}^{-1}$ )	$\mu_{l.r.}$ ( $\text{cm}^2/\text{Vs}$ )
1296	$0.29 \pm 0.02$	0.011	$-0.915 \pm 0.001$	$20 \pm 15$	$4 \pm 3$
1610	$0.23 \pm 0.04$	0.011	$-0.89 \pm 0.04$	$19 \pm 50$	$5 \pm 12$

Table 7.2: Table of Drude-Smith best-fit values for the Si<sub>17</sub> inverse opal film.

## Spectroscopy

Photoconductivity spectra were measured at 1 ps after peak  $-\Delta\mathcal{E}/\mathcal{E}_{ref}$ . Spectra were fit to a Drude-Smith model, and the fit parameters are given in Table 7.2. It is interesting that the carrier density is slightly smaller at larger excitation densities. The two measurements of carrier density,  $n$ , agree within two error intervals, and so this is likely an artifact of the low signal-to-noise ratio. This agrees with the observations of the lifetimes, where we see that they are indistinguishable at 1 ps (cf. Fig. 7.2). The scattering time was fixed because it is known that as  $c \rightarrow -1$ , the fitting algorithm will increase  $\tau$  to be unphysically large [77, 167].

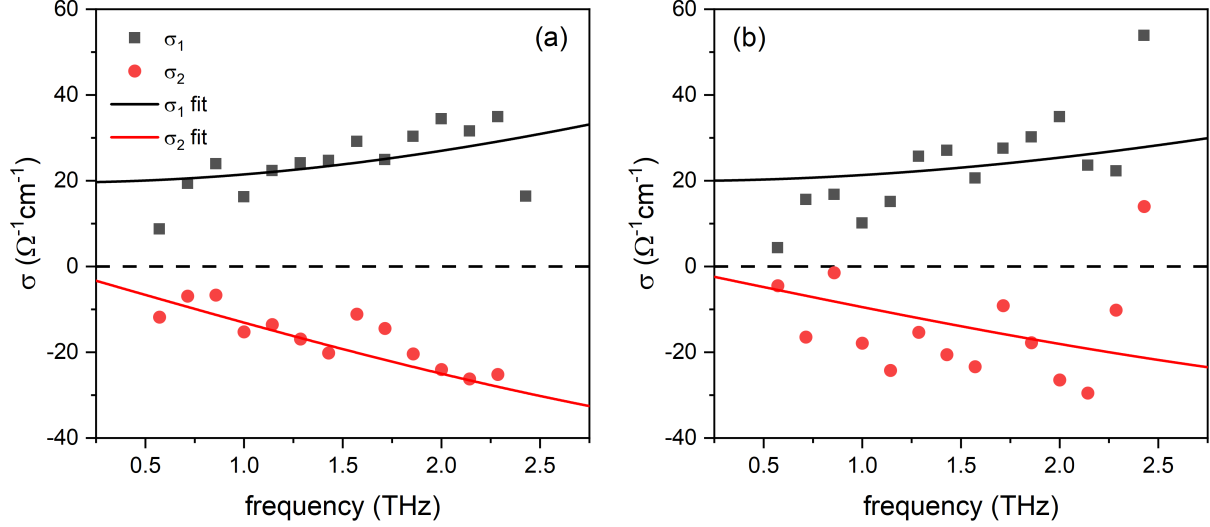


Figure 7.3: Photoconductivity spectra for the Si<sub>17</sub> inverse opal film. (a) Real (black) and imaginary (red) parts of the conductivity spectrum taken at 1296  $\mu\text{J}/\text{cm}^2$ . (b) Real (black) and imaginary (red) parts of the conductivity spectrum taken at 1620  $\mu\text{J}/\text{cm}^2$ . Solid lines are a fit to the Drude-Smith model, and the dashed black line is the zero line. The waveforms used in this analysis were averaged over 16 measurements, and we estimate that the uncertainty in the real and imaginary conductivity is  $\sim 5\Omega^{-1}\text{cm}^{-1}$ .

Sample	Fluence ( $\mu\text{J}/\text{cm}^2$ )	Power law ( $\alpha$ )	Total Power law ( $\alpha - 1$ )	Activation energy (meV)
Si <sub>12</sub> Ge <sub>5</sub>	810	$0.56 \pm 0.02$	-0.44	45.3
	972	$0.46 \pm 0.02$	-0.54	55.2
	1134	$0.45 \pm 0.02$	-0.55	56.4

Table 7.3: Table of power law best-fit values for the Si<sub>12</sub>Ge<sub>5</sub> inverse opal film.

## 7.4.2 Si<sub>12</sub>Ge<sub>5</sub> (30% Ge)

### Lifetimes

Figure 7.4 contains the lifetimes of the Si<sub>12</sub>Ge<sub>5</sub> sample. The sample exhibited stronger photoconductivity than the Si<sub>17</sub>, and so fluences of 810, 972, and 1134  $\mu\text{J}/\text{cm}^2$  were used. The data were fit to the power law of Eq. (7.6), and the best-fit parameters are given in Table 7.3. We find that the total power law is also  $\sim -0.5$ , and that the activation energy for the midgap states is  $\sim 50$  meV.

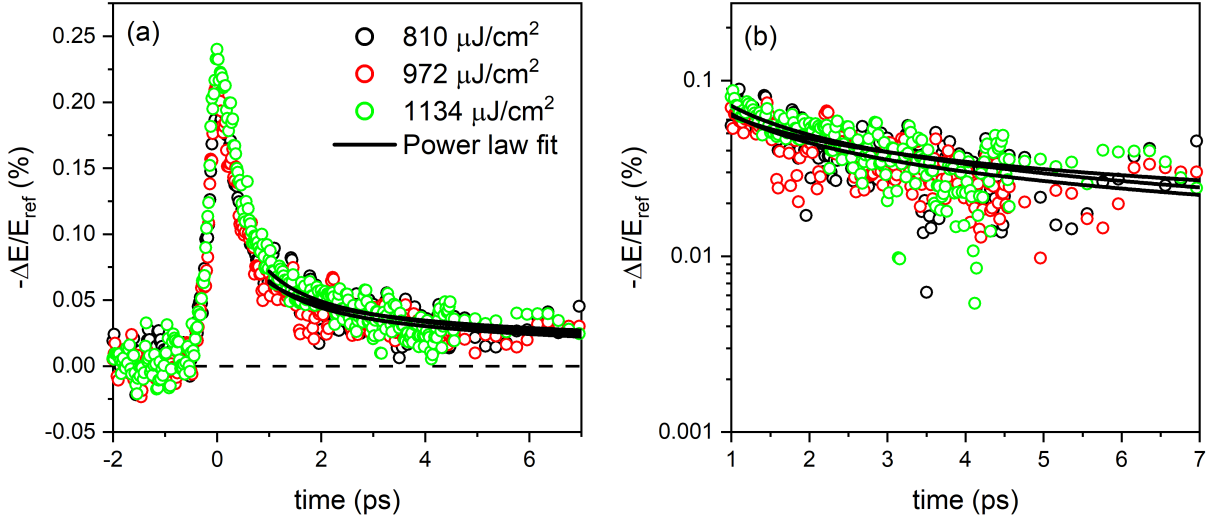


Figure 7.4: Photoconductivity lifetimes for the  $\text{Si}_{12}\text{Ge}_5$  inverse opal film. (a)  $810 \mu\text{J}/\text{cm}^2$  (black circles),  $972 \mu\text{J}/\text{cm}^2$  (red circles) and  $1134 \mu\text{J}/\text{cm}^2$  (green circles). (b) Lifetimes from (a) shown on a logarithmic y-axis for clarity. Black lines are the power law fits, and the dashed black line is the zero photoconductivity baseline.

Fluence ( $\mu\text{J}/\text{cm}^2$ )	$n$ ( $10^{18} \text{ cm}^{-3}$ )	$\tau$ (ps)	$c$ (Unitless)	$\sigma_{l.r.}$ ( $\Omega^{-1}\text{cm}^{-1}$ )	$\mu_{l.r.}$ ( $\text{cm}^2/\text{Vs}$ )
810	$0.51 \pm 0.03$	0.016	$-0.92 \pm 0.01$	$26 \pm 4$	$3.1 \pm 0.4$
972	$0.54 \pm 0.03$	0.016	$-0.91 \pm 0.01$	$31 \pm 4$	$3.6 \pm 0.4$
1134	$0.60 \pm 0.03$	0.016	$-0.91 \pm 0.01$	$36 \pm 4$	$3.8 \pm 0.4$

Table 7.4: Table of Drude-Smith best-fit values for  $\text{Si}_{12}\text{Ge}_5$  inverse opal film.

## Spectroscopy

The photoconductivity spectra of the  $\text{Si}_{12}\text{Ge}_5$  film are given in Fig. 7.5. The data are fit to a Drude-Smith model, and the best-fit values can be found in Table 7.4. Spectra are measured at 1 ps after maximum  $-\Delta\mathcal{E}/\mathcal{E}_{ref}$ . We find that the carrier density increases as the fluence is raised, however, the scattering time still had to be a fixed parameter in these fits. We used the average  $\tau$  from the unconstrained fits to fix  $\tau$ , and found  $\tau \sim 16$  fs.

### 7.4.3 $\text{Si}_5\text{Ge}_{12}$ (70% Ge)

#### Lifetimes

Photoconductivity lifetimes for the  $\text{Si}_5\text{Ge}_{12}$  sample are shown in Fig. 7.7. The  $\text{Si}_5\text{Ge}_{12}$  film demonstrated a significantly larger photoconductivity than the  $\text{Si}_{17}$  or  $\text{Si}_{12}\text{Ge}_5$  films, and so

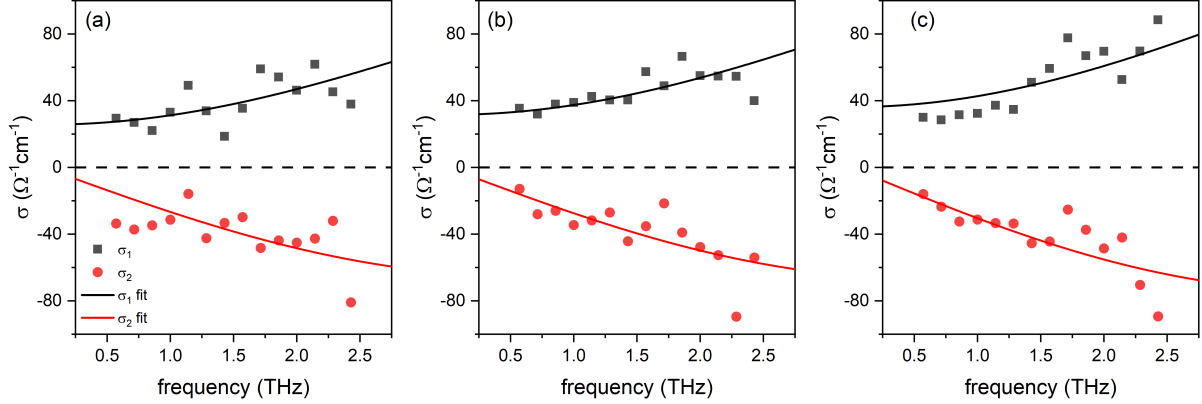


Figure 7.5: Photoconductivity spectra for the  $\text{Si}_{17}$  inverse opal film. (a) Real (black) and imaginary (red) parts of the conductivity spectrum taken at  $810 \mu\text{J}/\text{cm}^2$ . (b) Real (black) and imaginary (red) parts of the conductivity spectrum taken at  $972 \mu\text{J}/\text{cm}^2$ . (c) Real (black) and imaginary (red) parts of the conductivity spectrum taken at  $1134 \mu\text{J}/\text{cm}^2$ . Solid lines are a fit to the Drude-Smith model, and the dashed black line is the zero line. The waveforms used in this analysis were averaged over 32 measurements, and we estimate that the uncertainty in the real and imaginary conductivity is  $\sim 5\Omega^{-1}\text{cm}^{-1}$ .

Sample	Fluence ( $\mu\text{J}/\text{cm}^2$ )	Power law ( $\alpha$ )	Total Power law ( $\alpha - 1$ )	Activation energy (meV)
$\text{Si}_5\text{Ge}_{12}$	486	$0.178 \pm 0.02$	$-0.822$	142.8
	648	$0.32 \pm 0.02$	$-0.68$	79.5
	810	$-0.001 \pm 0.02$	$-1.001$	*
	972	$-0.01 \pm 0.02$	$-1.01$	*

Table 7.5: Table of power law best-fit values for the  $\text{Si}_5\text{Ge}_{12}$  inverse opal film. The \* symbol denotes undetermined values.

a good signal-to-noise could be found at fluences of 486, 648, 810, and 972  $\mu\text{J}/\text{cm}^2$ . The data are fit to a power law for times greater than 1 ps after maximum  $-\Delta\mathcal{E}/\mathcal{E}_{ref}$ . The best-fit parameters are given in Table 7.5 for reference. We find that low fluences have a total power law of  $> -1$ , but higher fluences give a total power  $\sim -1$ . The power  $\alpha$  is found to be zero in the high fluence measurements, so it is not possible to compute an activation energy.

## Spectroscopy

Spectroscopy was performed at 1 ps after maximum  $-\Delta\mathcal{E}/\mathcal{E}_{ref}$ , and the results are shown in Fig. 7.7. The data are fit to a Drude-Smith model and the results are shown in Table 7.6. We find that the carrier density slightly increases as the fluences is raised. The scattering time  $\tau$  was fixed in the same way as both the  $\text{Si}_{17}$  and  $\text{Si}_{12}\text{Ge}_5$  samples. We found an average

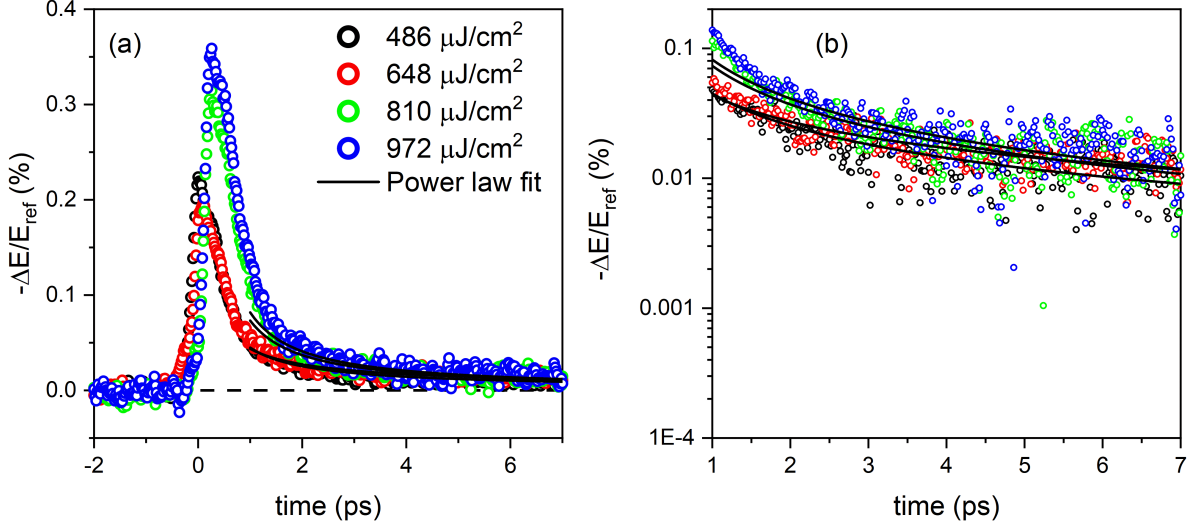


Figure 7.6: Photoconductivity lifetimes for the  $\text{Si}_5\text{Ge}_{12}$  inverse opal film. (a) 486  $\mu\text{J}/\text{cm}^2$  (black circles), 648  $\mu\text{J}/\text{cm}^2$  (red circles), 810  $\mu\text{J}/\text{cm}^2$  (green circles) and 972  $\mu\text{J}/\text{cm}^2$  (blue circles). (b) Lifetimes from (a) shown on a logarithmic y-axis for clarity. Black lines are the power law fits, and the dashed black line is the zero photoconductivity baseline.

Fluence ( $\mu\text{J}/\text{cm}^2$ )	$n$ ( $10^{18} \text{ cm}^{-3}$ )	$\tau$ (ps)	$c$ (Unitless)	$\sigma_{l.r.}$ ( $\Omega^{-1}\text{cm}^{-1}$ )	$\mu_{l.r.}$ ( $\text{cm}^2/\text{Vs}$ )
486	$0.27 \pm 0.2$	0.044	$-0.91 \pm 0.03$	$51 \pm 17$	$12 \pm 4$
648	$0.21 \pm 0.01$	0.044	$-0.86 \pm 0.02$	$62 \pm 10$	$19 \pm 3$
810	$0.30 \pm 0.01$	0.044	$-0.90 \pm 0.02$	$62 \pm 14$	$13 \pm 3$
972	$0.34 \pm 0.02$	0.044	$-0.89 \pm 0.02$	$77 \pm 14$	$14 \pm 3$

Table 7.6: Table of Drude-Smith best-fit values for  $\text{Si}_5\text{Ge}_{12}$  inverse opal nanostructures.

of  $\tau \sim 44$  fs.

## 7.5 Discussion

### 7.5.1 Ultrafast Transient Photoconductivity

Lowering the photoconductivity lifetime is an excellent approach to fabrication of ultrafast photodetectors. To achieve this a crystalline semiconductor can be implanted with ions or damaged with radiation in order to introduce a large number of recombination centers near the surface [318]. In turn, the ultrafast trapping at these recombination centres significantly reduces the lifetime of the photoconducting state. Early work by Sekine et al. on ion-implanted germanium thin-films reveals a charge-carrier lifetime of  $\tau \sim 600$  fs that is tunable

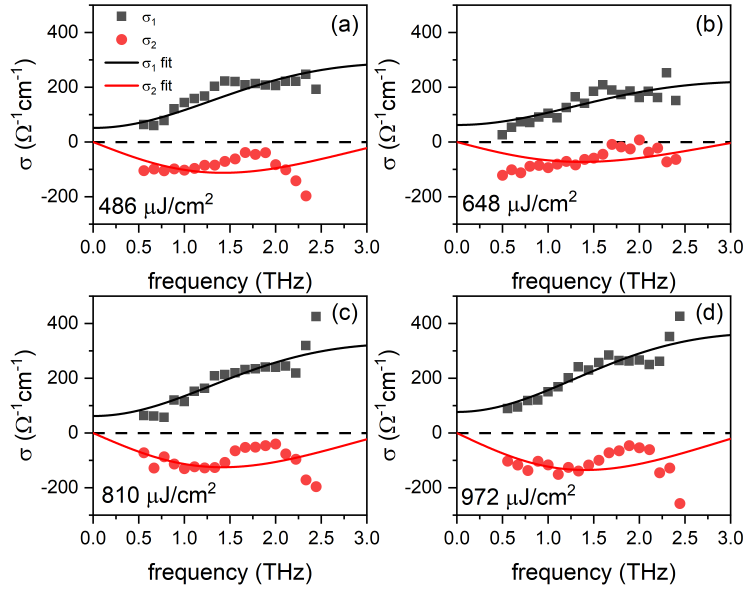


Figure 7.7: Photoconductivity spectra for the  $\text{Si}_5\text{Ge}_{12}$  inverse opal film. (a) Real (black) and imaginary (red) parts of the conductivity spectrum taken at  $486 \mu\text{J}/\text{cm}^2$ . (b) Real (black) and imaginary (red) parts of the conductivity spectrum taken at  $648 \mu\text{J}/\text{cm}^2$ . (c) Real (black) and imaginary (red) parts of the conductivity spectrum taken at  $810 \mu\text{J}/\text{cm}^2$ . (d) Real (black) and imaginary (red) parts of the conductivity spectrum taken at  $972 \mu\text{J}/\text{cm}^2$ . Solid lines are a fit to the Drude-Smith model, and the dashed black line is the zero line. The waveforms used in this analysis were averaged over 4 measurements, and since the signal-to-noise ratio is large, we estimate that the uncertainty in the real and imaginary conductivity is  $\sim 5\Omega^{-1}\text{cm}^{-1}$ .

with the dose of O<sup>+</sup> implantation [329] and, by extension, the amount of disorder. The floor of the relaxation lifetime  $\tau$  occurs at the highest O<sup>+</sup> dosage  $\sim 10^{14}$  cm<sup>-2</sup>, indicating that the recombination dynamics are dominated by saturation of the effective trap density [329]. Mobilities in these thin films reach a maximum of  $\sim 100$  cm<sup>2</sup>/Vs [101]. Later, Lui et al. showed that in radiation damaged silicon-on-sapphire (RD-SOS) the dominant trapping mechanism is a single deep trap level by noting the single exponential relaxation of the photoconductivity [318]. Deep trapping in RD-SOS is thus associated with lifetimes of  $\sim 4$  - 6 ps and traps become saturated with charge carriers near carrier densities of  $\sim 10^{20}$  cm<sup>-3</sup> [318].

Extensive work by Nampoothiri et al. documents terahertz photoconductivity dynamics in hydrogenated Si<sub>x</sub>Ge<sub>1-x</sub> thin films [324–327]. Their finding of few-picosecond lifetimes agrees well with our results in Section 7.4 [316]. Fits of the data recorded at the highest fluences are shown in Fig. 7.8. We find that the lifetimes in our inverse opal structures obey the same  $-\Delta\mathcal{E}/\mathcal{E}_{ref} \propto t^{\alpha-1}$  power law as Nampoothiri et al. indicating an exponential tail of states beneath the conduction band [315, 316]. The power laws found in this work are provided in Table 7.7. We find that the total power  $\alpha - 1 \sim 0.5$  for many of the samples, which has been seen in the photoconductivity of functionalized pentacene crystals<sup>§</sup> and in the lifetimes measured in RD-SOS [318, 328]. From these power laws, the activation energy is determined through the relation

$$\alpha = \frac{k_B T}{k_B T_0} \quad (7.11)$$

where  $T$  is the sample temperature and  $k_B T_0$  is the activation energy [315]. The activation energies are shown together in Table 7.7. We find that generally the activation energies are much larger than what can be explored within the bandwidth of the THz pulse  $\lesssim 10$  meV. Nonetheless, these results are consistent with findings of Nampoothiri et al. and Lui et al, in that they demonstrate that on picosecond time-scales, charge carriers fall into the trap states below the band-edge [316, 318]. Using a THz pulse to probe these charge carriers does not result in re-excitation of the trapped carriers. In contrast, using an 800 nm pulse to probe the trap states reveals a longer lifetime than seen in THz conductivities [316]. This

---

<sup>§</sup>6,13 bis triisopropylsilylethynyl pentacene

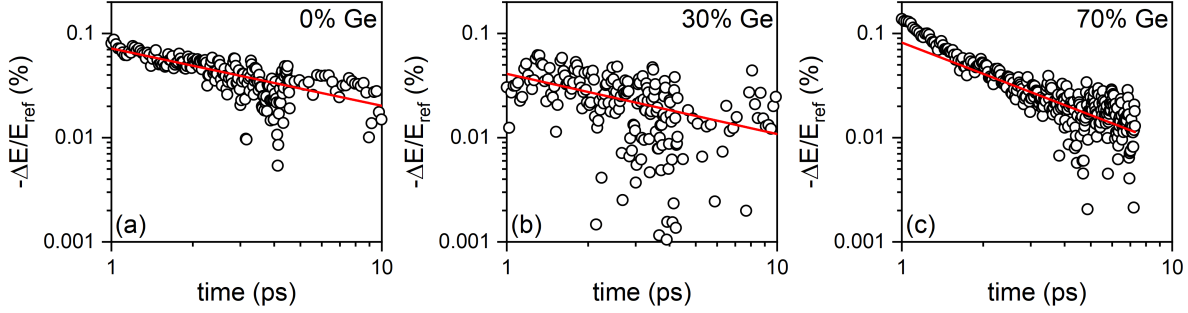


Figure 7.8: Lifetime analysis inverse opal thin films. (a) 0% Ge film at fluence of 1610  $\mu\text{J}/\text{cm}^2$ . (b) 30% film at fluence of 1134  $\mu\text{J}/\text{cm}^2$ . (c) 70% Ge film at fluence of 972  $\mu\text{J}/\text{cm}^2$ .

Sample	Fluence ( $\mu\text{J}/\text{cm}^2$ )	Power law ( $\alpha$ )	Total Power law ( $\alpha - 1$ )	Activation energy (meV)
0% Ge	1296	$0.55 \pm 0.03$	-0.45	46.2
	1610	$0.42 \pm 0.04$	-0.58	60.5
30% Ge	810	$0.56 \pm 0.02$	-0.44	45.3
	972	$0.46 \pm 0.02$	-0.54	55.2
70% Ge	1134	$0.45 \pm 0.02$	-0.55	56.4
	486	$0.178 \pm 0.02$	-0.822	142.8
	648	$0.32 \pm 0.02$	-0.68	79.5
	810	$-0.001 \pm 0.02$	-1.001	*
	972	$-0.01 \pm 0.02$	-1.01	*

Table 7.7: Table of power-law best-fit values for inverse opal nanostructures. The \* symbol denotes undetermined values.

is because the near-infrared pulse possesses an energy beyond the activation energy which results in continued free-carrier screening [316]. There does not appear to be an obvious trend in the activation energies shown in Table 7.7, and future work can elaborate on these results by applying broad-band THz spectroscopy to these samples, as suggested by the results of Cooke et al. on silicon nanocrystal films [76].

## 7.5.2 THz Electrodynamics

From the fits performed in Section 7.4 it is clear that the inverse opal nanostructures loosely follow the Drude-Smith model. In all samples there are oscillations in  $\tilde{\sigma}(\omega)$  that are unaccounted for within the framework of the Drude-Smith model, and here we wish to explore future avenues of research. The Poole-Frenkel effect is a prominent transport mechanism in amorphous semiconductors, including germanium and silicon [313, 330–332]. The Poole-

Frenkel effect describes the electric-field induced lowering of the Coulombic potential surrounding point defects resulting from  $sp^3$  hybridized states of dangling bonds [312, 333]. The field-induced lowering of the barrier results in a conductivity  $\sigma$  that follows the expression [331, 334, 335]

$$\sigma(t) = \sigma_0 \exp\left(\frac{\beta\sqrt{|\mathcal{E}(t)|}}{rk_B T}\right), \quad (7.12)$$

where  $\beta = \sqrt{e^3/\pi\epsilon}$ ,  $\mathcal{E}(t)$  is a transient electric field,  $\epsilon$  is the dielectric constant,  $\sigma_0$  is the initial conductivity,  $T$  is the temperature, and  $r$  is a constant that depends on the position of the Fermi level [335]. Impressively, time-resolved terahertz spectroscopy experiments have shown that an electron trapped  $\sim 90$  meV below the conduction band can be liberated by photons with as little energy as  $\sim 4$  meV [334]. Importantly, after Fourier transformation with a simple Gaussian pulse, one indeed finds oscillations in the real and imaginary parts of the conductivity spectrum that match our own. However, this effect does not explain our results because it has been observed that electric fields of  $\sim 300$  kV/cm [333, 335] are required, which are orders of magnitude larger than the fields used in this experiment ( $\sim 300$  V/cm).

Another model that explains the deviations from the Drude-Smith model is the Bergmann effective medium theory, which we introduced in Section 2.2.2. In our derivation of the plasmon model, it was assumed that the depolarization spectral function was sharply peaked about a single depolarization  $L_0$ , such that  $g(L) \sim g_0\delta(L - L_0)$ . A more detailed calculation of the spectral function may aid in providing a suitable model of the photoconductivity, as suggested by Nĕmec, Kužel and cohorts [31, 174].

Finally, it is becoming increasingly important to consider the dielectric background of the material under study [71, 74, 195, 336]. The absorption from phonon modes in the dielectric background can produce artifacts in the photoconductivity spectrum that require a more rigorous analysis than the thin-film approximation used here. The higher order terms in the transmission coefficient and the multilayer geometry depend on the background dielectric function, which, as was shown in Section 3.2, is measured by THz time-domain spectroscopy. Future work must encompass THz time-domain spectroscopy in order to obviate potential artifacts in the analysis procedure [74].

## 7.6 Summary

In summary, we have performed the first time-resolved terahertz spectroscopy of silicon-germanium inverse-opal nanostructured films. Our results indicate that the primary route of recombination is through ultrafast trapping. There is significant localization of charge as evidenced by our conductivity spectra, and broadband spectroscopy is needed to discern the significance of deep and shallow trapping.

# Chapter 8

## Functionalized Silicon Nanosheets

### 8.1 Introduction

In recent years, there has been considerable interest in two-dimensional materials such as atomically thin transition metal dichalcogenides (TMDCs) [125, 126, 142], high-mobility polymers [143, 337, 338], and semiconductor nanosheets [339–342]. This surge of activity has been motivated by potential applications in, for example, photocatalysis [343–346] and optoelectronics [143, 256, 347–349].

Among these two-dimensional materials is silicene, the silicon analog of graphene that has the potential for enhanced compatibility with current silicon technology. The nonplanar silicon double bonds are too reactive to be isolated, which makes silicene less stable than its planar graphene counterpart. As a result, one of the sublattices in silicene is vertically displaced above the other, creating a buckled honeycomb lattice. Complete hydrogenation is a relatively straightforward approach to reducing the reactivity of the surface [350, 351]; however, Hydride-terminated silicon nanosheets are highly vulnerable to oxidation in ambient environmental conditions and require functionalization for further use.

Functionalization with large organic molecules is a promising avenue to reduce the ambient reactivity of silicene [140, 347, 350, 350]. Narreto et al. showed that dodecene functionalization does not affect the photoluminescence of the nanosheets. The peak photoluminescence occurs near 2.4 eV, with slight variations attributed to the environment of the toluene-suspended nanosheets [140]. Through a temperature dependence of the photolumi-

nescence, Narreto et al. found that the PL efficiency increases as the nanosheets are cooled, owing to increased radiative recombination in the disorder-induced band-tail states. Further evidence is found in the time-resolved photoluminescence, which indicates that recombination of electrons and holes occurs primarily in the band-tail [140].

It is difficult to gather a complete understanding of microscopic charge carrier dynamics from photoluminescence alone. To gain further insight, one can look at the optoelectronic properties, such as the charge carrier mobility. Mobilities in SiNS samples made from SiNS vary from 39 to 100 cm<sup>2</sup>/Vs [352–354] which are significantly smaller than the theoretical limits of  $\sim 2 \times 10^5$  cm<sup>2</sup>/Vs [355]. Mobility measurements of pressed pellets and loose films are made difficult by using contact methods such as the van der Pauw configuration [352–354]. Fortunately, time-resolved terahertz spectroscopy is a non-contact approach to measuring charge carrier mobility, which, to date, has yet to be performed on SiNS.

Time-resolved terahertz spectroscopy provides information complementary to time-resolved photoluminescence (TRPL). The photoconductivity lifetimes provided by TRTS monitor the carrier density, whereas TRPL lifetimes monitor the number of recombination events. Mechanisms directly removing charge carriers from the conduction band suppress lifetime in TRTS, while mechanisms that minimize recombination events suppress PL. Furthermore, modeling the photoconductivity spectrum may provide insight into mechanisms affecting charge carrier mobility in SiNS.

## 8.2 Sample Preparation

Chemical exfoliation of the Zintl salt CaSi<sub>2</sub> yields hydrogenated SiNSs (SiNS-H). Structurally, CaSi<sub>2</sub> consists of alternating layers of Ca and Si, and the addition of concentrated HCl decomposes the Ca<sup>2+</sup> ions into CaCl<sub>2</sub> and monolayers of SiNS-H. In this work, the CaSi<sub>2</sub> was exfoliated in concentrated HCl at -20 °C for seven days, forming SiNS-H [140, 342, 347, 350].

Catalytic hydrosilation (hydrosilylation) adds Si-H bonds to unsaturated bonds (such as double bonds). Hydrosilylation reactions can react with molecular and surface Si-H groups with various unsaturated substrates. Hydrosilylation is the mechanism that is responsible for the formation of SiNS-H. The hydrosilylation process also bonds the Si surface to molecules. Utilizing the unsaturated bond in Si to react surface molecules with SiNS does not occur

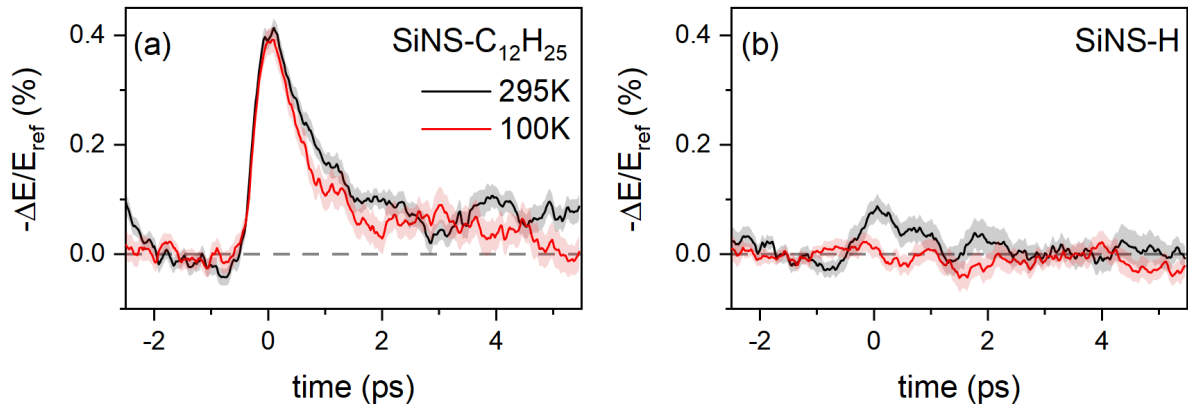


Figure 8.1: Lifetimes of SiNS- $C_{12}H_{25}$  and SiNS-H at 295 K and 100 K. The standard error after 49 measurements is shown as coloured bands. (a) SiNS- $C_{12}H_{25}$  and (b) SiNS-H.

spontaneously and requires initiation. Azobisisobutyronitrile (AIBN) is used to catalyze the hydrosilylation of SiNS with dodecene monomers ( $C_{12}H_{25}$ ) in this work (SiNS-dodecene) [140, 342, 347, 350].

The SiNS-H and SiNS-dodecene was cleaned, suspended in toluene, and stored in a glove box filled with nitrogen. The SiNSs were drop-deposited onto 1 mm-thick fused quartz substrates for time-resolved terahertz spectroscopy. The samples were kept in dry nitrogen until mounted in the TRTS chamber. We minimized the exposure to air by transporting the samples in a dry-nitrogen-filled container. We then quickly mounted the samples and evacuated the TRTS chamber. The vacuum reached a final pressure of  $\sim 10^{-6}$  Torr.

### 8.3 Results and Discussion

Figure 8.1 shows the first-ever TRTS performed on SiNSs. The SiNSs were photoexcited with 400 nm, 100 fs pulses at a fluence of  $218 \mu J/cm^2$ . Figure 8.1 (a) shows the photoconductivity lifetimes of SiNS-dodecene, and Fig. 8.1 (b) shows the lifetimes of SiNS-H. The standard error of 49 averages is the colored bands surrounding the lifetimes. The lifetimes were measured at 295 K (black) and 100 K (red).

The dodecene functionalization has a significantly larger photoconductivity than the SiNS-H, even at low temperatures. Interestingly, there is a very slight photoconductivity in the SiNS-H at 295 K, which barely reaches one standard error above the noise floor at 0 ps. The relatively high conductivity indicates that the dodecene has prevented the oxidizing of

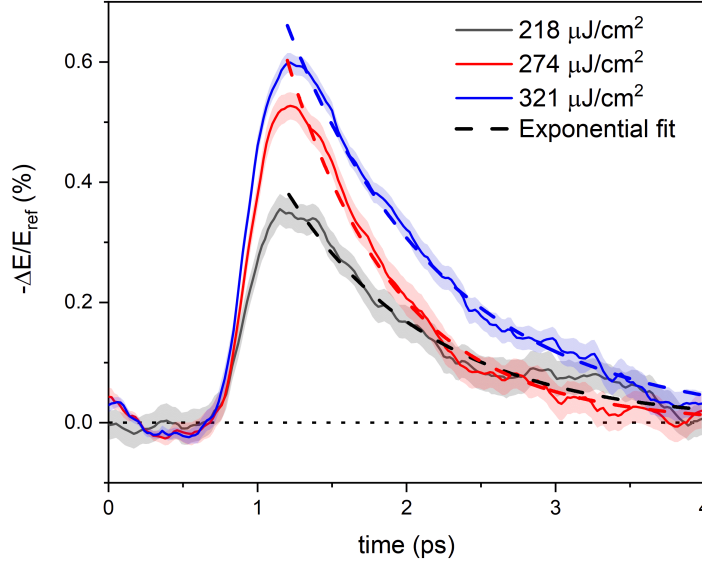


Figure 8.2: Lifetimes of SiNS-C<sub>12</sub>H<sub>25</sub> at 214, 274, and 321  $\mu\text{J}/\text{cm}^2$ . Dashed lines are a fit to an exponential decay model. The horizontal dotted line is the zero line.

the SiNS-H. A lower mobility in oxidized SiNS is expected because in bulk Si, the electron mobility is  $1450 \text{ cm}^2/\text{Vs}$  [170], while the mobility of SiO<sub>2</sub> is  $\sim 30 \text{ cm}^2/\text{Vs}$  [356, 357].

Encouraged by the enhanced conductivity in the SiNS-dodecene sample, we investigated the fluence-dependence of the photoconductivity lifetime in SiNS-dodecene. Figure 8.2 shows the lifetimes as fluences of 218, 274, and 321  $\mu\text{J}/\text{cm}^2$ . Indeed, the photoconductivity increases, indicating that the samples are not degrading from the excitation density. The lifetimes are fit to exponential decays of the form

$$-\frac{\Delta\mathcal{E}}{\mathcal{E}_{ref}} = Ae^{-t/\tau} \quad (8.1)$$

where  $A$  is the amplitude and  $\tau$  is the  $1/e$  time constant (cf. dashed lines in Fig. 8.2). The results of the fits are shown in Table 8.1, and we find that the time constant of the decay is  $\sim 1 \text{ ps}$  for all fluences. This short lifetime is consistent with ultrafast trapping in other nanocrystalline materials and supports the ultrafast trapping model proposed by Narreto et al. [140].

We selected a fluence of  $274 \mu\text{J}/\text{cm}^2$  to balance the number of averages with the possibility

Fluence ( $\mu\text{J}/\text{cm}^2$ )	$A$ (%)	$\tau$ (ps)
218	$1.32 \pm 0.04$	$0.97 \pm 0.02$
274	$3.11 \pm 0.09$	$0.732 \pm 0.009$
321	$2.08 \pm 0.03$	$1.05 \pm 0.01$

Table 8.1: Table of exponential best-fit values for SiNS-dodecene fluence dependence.

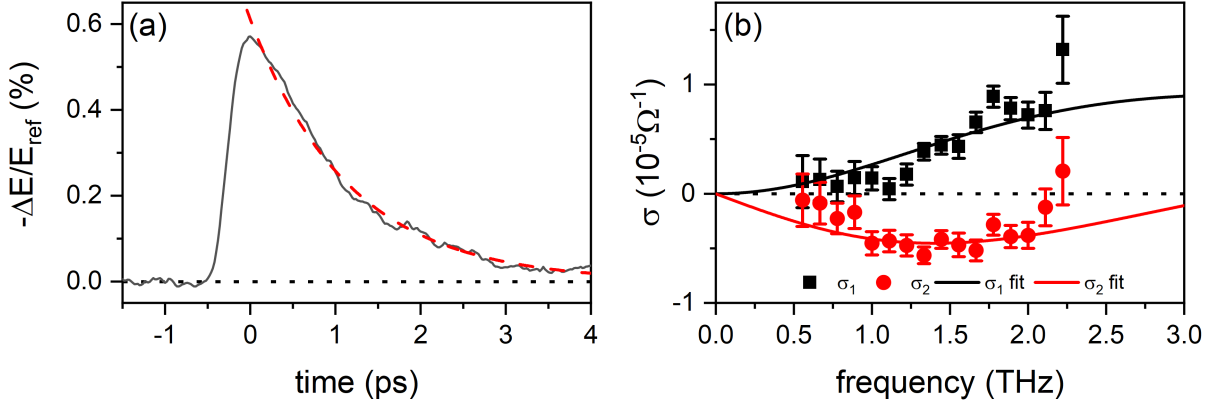


Figure 8.3: SiNS lifetime and photoconductivity. (a) Photoconductivity lifetime. Red dashed line is a fit to an exponential decay model. (b) Photoconductivity spectrum of SiNS- $\text{C}_{12}\text{H}_{25}$  taken at  $274 \mu\text{J}/\text{cm}^2$ . Spectroscopy is performed at 1 ps after maximum  $-\Delta\mathcal{E}/\mathcal{E}_{\text{ref}}$ . Solid lines correspond to a fit to the Drude-Smith model. The horizontal dotted lines are the zero lines.

of sample degradation. Figure 8.3 (a) shows the photoconductivity after 49 averages, fit to an exponential decay. We find a time constant of  $\tau = 1.16 \pm 0.01$  ps. Figure 8.3 (b) shows the complex conductivity with a pump-probe delay time of 1ps. Error bars denote the standard error of the conductivity spectrum after 25 averages.

We find that the Drude-Smith model fits the photoconductivity well. Table 8.2 contains the best-fit Drude-Smith parameters. We find that charge carriers are significantly localized, with a  $c$ -parameter of nearly -1. The extracted carrier density of  $3.29 \times 10^{14} \text{ cm}^{-2}$  is significantly below the areal photon density of  $5.52 \times 10^{14} \text{ cm}^{-2}$ . This discrepancy indicates that a significant degree of charge-carrier trapping occurs during the sub-picosecond onset of photoconductivity which Narreto et al. also observed [140]. The short-range Drude-Smith mobility of  $400 \text{ cm}^2/\text{Vs}$  is in reasonable agreement with the measurements of Tao et al., who recorded mobility of  $\sim 100 \text{ cm}^2/\text{Vs}$  [358] in silicene field-effect transistors. In work by Tao et al., a synthesis-transfer-fabrication process (silicene encapsulated delamination with native

$m^*$ ( $m_e$ )	$n$ ( $10^{11}\text{cm}^{-2}$ )	$\tau$ (ps)	$c$ (unitless)	$\mu_{s.r.}$ ( $\text{cm}^2/\text{Vs}$ )	$\mu_{l.r.}$ ( $\text{cm}^2/\text{Vs}$ )
0.21 [359]	$3.29 \pm 0.9$	$0.047 \pm 0.008$	$-0.99 \pm 0.06$	$400 \pm 60$	$0 \pm 2$

Table 8.2: Table of Drude-Smith best-fit values for SiNS-dodecene at 1 ps post max  $\Delta\mathcal{E}/\mathcal{E}_{ref}$ , at fluence of  $274 \mu\text{J}/\text{cm}^2$ .

electrodes, SEDNE) enabled them to deposit the pristine silicene onto Ag(111) thin film in-situ for STM spectroscopy [358]. This in-situ approach enabled Tao et al. to measure the electrical properties of pristine SiNSs. In the present work, the nanosheets are interrogated directly by the THz radiation, and the dodecene fulfilled the role of preventing oxidation of the SiNS.

It is becoming clear that encapsulation and functionalization are necessary techniques for fully integrating silicene into existing technologies. The mobility of  $400 \text{ cm}^2/\text{Vs}$  is already comparable to those found in transition metal dichalcogenide transistors [142] and  $\text{TiO}_2$  monolayers [340], however, there is much room for improvement if they are to reach their theoretical potential of  $\sim 2 \times 10^5 \text{ cm}^2/\text{Vs}$ . Dodecene functionalization thus provides an excellent avenue for future optoelectronic applications of silicon nanosheets.

## 8.4 Summary

We performed time-resolved terahertz spectroscopy on dodecene-functionalized silicon nanosheets for the first time. Measurements of the photoconductivity lifetime yield a very short charge carrier lifetime of  $\sim 1$  ps. A Drude-Smith model describes the conductivity spectrum well, with a significant degree of carrier localization ( $c \sim -1$ ). The carrier density is significantly smaller than expected from the photon density and is likely the result of ultrafast charge-carrier trapping occurring during the onset of photoconductivity. The dodecene functionalization protects the SiNSs, and contributes to a substantial short-range mobility of  $400 \text{ cm}^2/\text{Vs}$ .

# Chapter 9

## GaN Nanowalls

### 9.1 Introduction

Recently, group III-nitride materials such as GaN have gained considerable attention regarding photocatalytic water splitting. The alignment of the energy bands to many photocatalytic reactions has proven to be favorable, and the ability to remain stable in harsh chemical environments makes them a valuable tool in photocatalysis [144, 145]. Increasing the surface area-to-volume ratio can be achieved by growing GaN nanowires and proves to be an excellent avenue to achieve increased molecular participation in surface chemistry. However, Kraut et al. showed that the nanowire growth exposes the crystallographic *m*-planes to photochemical etching, which erodes the GaN nanowires [146]. Fortunately, the crystallographic *c*-plane is stable [146]. Maximizing the *c*-plane exposure while minimizing *m*-plane exposure can be achieved by moving from a nanowire geometry to a nanowall configuration. By utilizing selective area growth and molecular beam epitaxy, nanowalls with highly tunable height, separation, and length can be grown, opening up many avenues for optimization [144].

Measuring the electronic properties of nanowalls is difficult because the substrate-nanowall connection is highly fragile. To overcome this we use time-resolved terahertz spectroscopy to acquire optoelectronic properties, because TRTS is a non-contact probe of photoconductivity. The electron diffusivity of crystalline GaN is  $D = 4 \text{ cm}^2/\text{s}$  [360]. Therefore, the diffusion length in one oscillation of a THz wave is  $\sim 8 \text{ nm}$ . Since the minimum dimensions of the walls

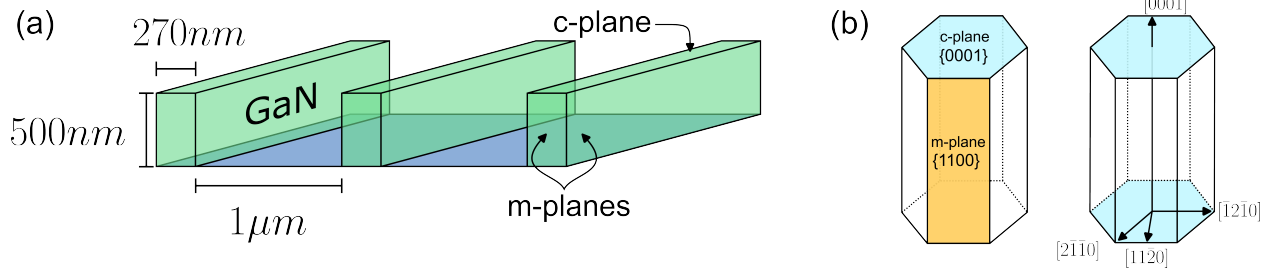


Figure 9.1: (a) Dimensions of GaN nanowalls. The nanowalls are 500 nm tall and 270 nm wide. The c-planes are facing upward, away from the substrate. (b) Conventional unit cell of a hexagonal lattice with the c- and m-planes. The directions shown use the Miller-Bravais notation.

under study are 270 nm, we do not expect charge carriers to undergo a significant degree of localization because THz radiation will probe much smaller length scales.

## 9.2 Sample Properties

Reference [144] contains the details of the nanowall growth. Briefly, the GaN nanowalls were grown by plasma-assisted molecular beam epitaxy directly onto a 1 mm thick, double-side polished, c-plane sapphire wafer in selective area growth mode using a TiN mask. Reference [361] contains a detailed description of the masking process. GaN growth was conducted under a nitrogen-rich environment with a nitrogen flux of 0.363 standard cubic centimeters per minute. Gallium was introduced at a beam-equivalent pressure of  $5 \times 10^{-7}$  mbar and a substrate temperature of  $\sim 850$  °C.

Figure 9.1 (a) shows the dimensions of the nanowalls under study. The nanowalls are 270 nm wide, 500 nm tall, and have a  $1 \mu\text{m}$  pitch. A  $1 \text{ mm} \times 1 \text{ mm}$  patch of nanowalls was grown for this study. The top facet of the nanowalls are c-plane, and the sidewalls are m-planes due to the epitaxial relationship between GaN and sapphire [144]. The c-plane, m-plane, and corresponding directions are shown in Fig. 9.3 (b). Note that the directions are determined using the Miller-Bravais notation\*.

## 9.3 Results and Discussion

The GaN nanowalls were photoexcited with 100 fs, 267 nm photons because the band gap of GaN is 3.4 eV [144, 362]. A fluence of  $2 \mu\text{J}/\text{cm}^2$  was chosen to produce a photoconductivity

---

\*To convert the direction  $[uvw]$  into the Miller-Bravais notation  $[UVTW]$ , use the relations  $U = (2u-v)/3$ ,  $V = (2v-u)/3$ ,  $T = -(U+V)$ , and  $W = w$

$A_1$ (%)	$A_2$ (%)	$A_3$ (%)	$\tau_1$ (ps)	$\tau_2$ (ps)
$3.88 \pm 0.03$	$1.13 \pm 0.02$	$1.44 \pm 0.01$	$5.45 \pm 0.08$	$67 \pm 3$

Table 9.1: Table of biexponential best-fit values for GaN Nanowall photoconductivity lifetime.

well above the noise floor. The charge carrier effective mass is  $m^* = 0.22m_e$  [170], and the penetration depth is  $\delta = 59$  nm [363]. TRTS was performed with the long 1 mm length of the nanowalls parallel to the THz electric field. The incoming THz radiation is vertically polarized.

Figure 9.2 shows the photoconductivity lifetime and spectroscopy at 1, 5, 10, 40, 100 ps after photoexcitation. Figure 9.2 (a) shows the photoconductivity lifetime. Recombination in bulk GaN is dominated by bimolecular recombination, however, in the GaN nanowalls we find that this is not the case. The behaviour is similar to what we observed in the conductivity lifetime of the CdS nanowires in Chapter 5: after a fast initial decay, the photoconductivity levels out. To parameterize this, we fit our data to a biexponential decay of the form

$$-\frac{\Delta\mathcal{E}}{\mathcal{E}_{ref}} = A_1e^{-t/\tau_1} + A_2e^{-t/\tau_2} + A_3, \quad (9.1)$$

where,  $A_1$  and  $A_2$  are the amplitudes of the decay channels with corresponding time constants  $\tau_1$  and  $\tau_2$ , respectively.  $A_3$  is a constant offset that represents the contribution of a recombination pathway with lifetime far larger than the 125 ps window explored here. Future work can elaborate on the mechanisms responsible for this behaviour, and for now we report the best-fit parameters in Table 9.1. We find the short recombination timescale is  $\tau_1 = 5.45 \pm 0.08$  ps, and the longer lifetime is  $\tau_2 = 67 \pm 3$  ps.

Figure 9.2 (b) - (f) shows the spectroscopy acquired at 1, 5, 10, 40, and 100 ps after excitation. Figure 9.3 shows the photoconductivity spectra at 1 ps after excitation. There is no consensus regarding the appropriate model to fit the photoconductivity of GaN, and Figure 9.3 shows the best fit of each model against our data. Figure 9.3 (a) and (b) shows the Generalized Drude model suggested by Tsai's work on GaN thin films [364]. (c) shows the Drude-Lorentz model used by Parkinson et al. on GaN nanowires [67], and (d) contains the Drude model as suggested by the work of many others [67, 365, 366]. Interestingly none

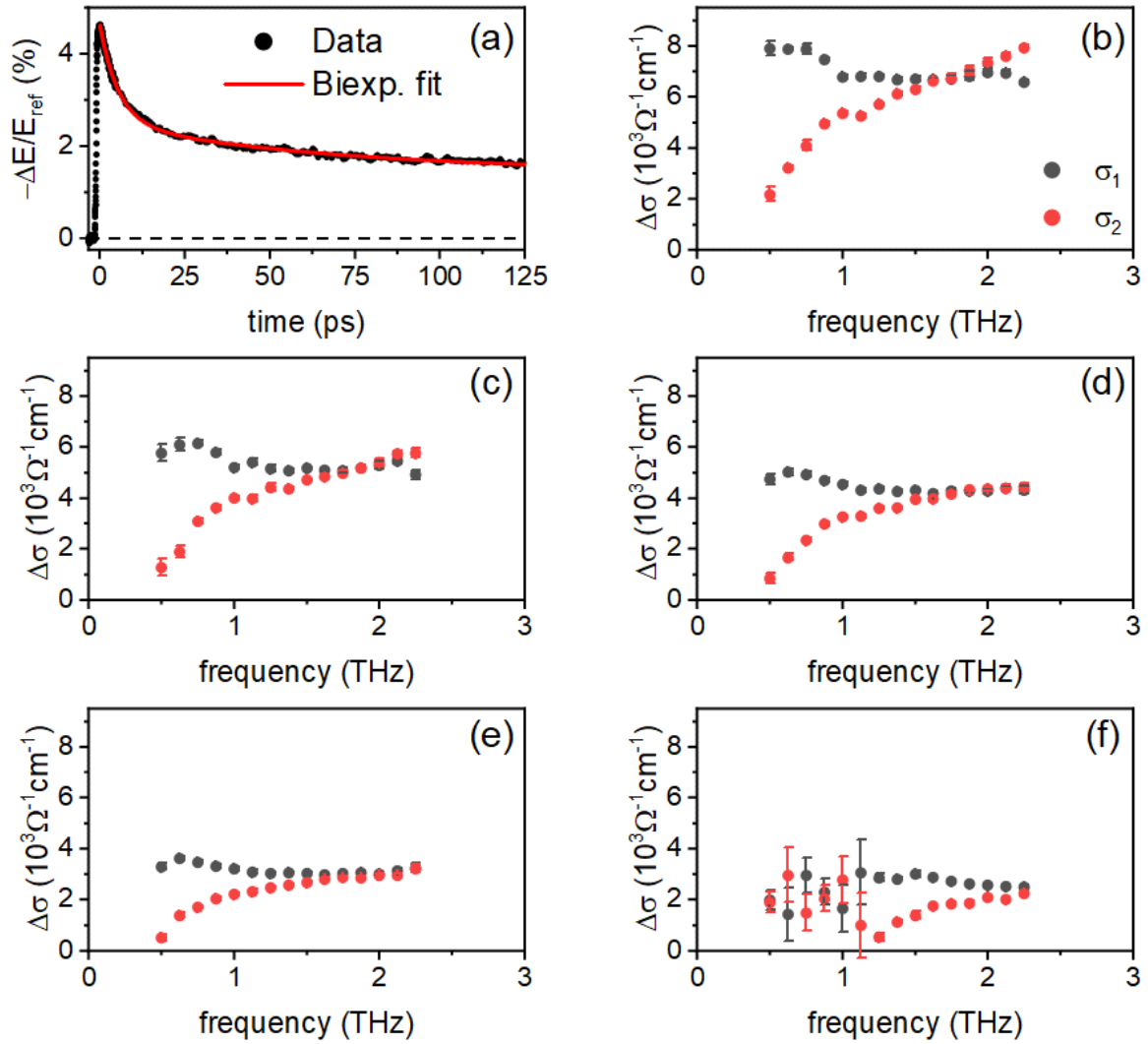


Figure 9.2: Time-resolved terahertz spectroscopy of GaN nanowalls. (a) Photoconductivity lifetime (black line). Red dots indicate the average real conductivity. (b)-(d) Photoconductivity spectra acquired at 1, 5, 10, 40, and 100 ps.

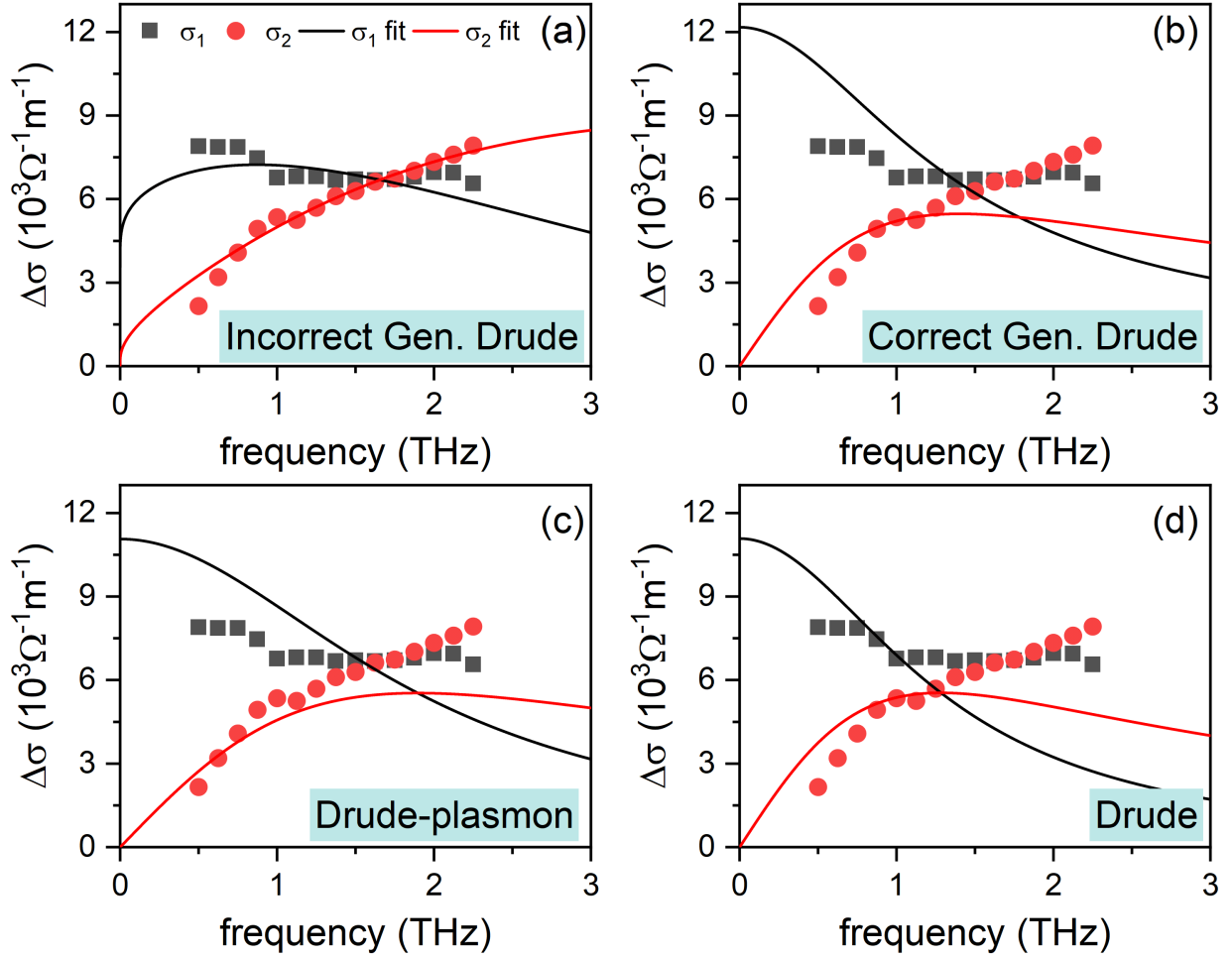


Figure 9.3: Photoconductivity models for GaN nanowalls. (a) The incorrect Generalized Drude model found in literature. (b) The correct Generalized Drude model. (c) Drude-Plasmon model. (d) Drude model.

of these models could simultaneously describe the flatness of the real conductivity and the steepness of the imaginary conductivity.

The first model we investigated was the Generalized Drude model, which extends the Drude model to encompass a distribution of scattering times [197, 364, 367]. The conductivity in the Generalized Drude model is given by

$$\tilde{\sigma}(\omega) = \frac{ne^2\tau}{m^*} \left[ \frac{1}{1 - (i\omega\tau)^{1-\alpha}} \right]^\beta, \quad (9.2)$$

where  $\alpha$  and  $\beta$  are positive empirical fit parameters that determine the width of the spectral

Generalized Drude (incorrect)	$n$ ( $10^{18}\text{cm}^{-3}$ ) $1.0 \pm 0.5$	$\tau$ (ps) $0.04 \pm 0.01$	$\alpha$ (unitless) $0.71 \pm 0.1$	$\beta$ (unitless) $1.0 \pm 0.3$	
Generalized Drude (correct)	$n$ ( $10^{18}\text{cm}^{-3}$ ) $4 \pm 400$	$\tau$ (ps) $0.01 \pm 1$	$\alpha$ (unitless) $0.97 \pm 53$	$\beta$ (unitless) $0.97 \pm 41$	
Drude-plasmon	$n$ ( $10^{18}\text{cm}^{-3}$ ) $1.03 \pm 16$	$\tau$ (ps) $0.08 \pm 0.01$	$\nu$ (unitless) $1 \pm 1$	$\rho$ (unitless) $0.98 \pm 7 \times 10^{13}$	$n_{eq}$ ( $10^{18}\text{cm}^{-3}$ ) $0.033 \pm 2 \times 10^{13}$
Drude	$n$ ( $10^{18}\text{cm}^{-3}$ ) $1.03 \pm 0.08$	$\tau$ (ps) $0.083 \pm 0.008$			

Table 9.2: Best-fit photoconductivity parameters for the GaN nanowalls.

scattering rate distribution [87, 197, 367]. However, upon use, one finds that Eq. (9.2) is unusually sensitive to changes in  $\alpha$ . The complexity of the formula obscures the sensitivity to  $\alpha$  and can be detrimental to the interpretation of results. Calculations of the spectral scattering rates are also volatile with this model (see Appendix C), and it became clear that something was wrong with Eq. (9.2). Comparing work by Iglesias et al. [367] against the formulae found in the terahertz spectroscopy literature [87, 197, 364], there appears to be a mistake that has persisted for many years. To obtain the correct scattering rate distribution, it is important to bring the minus sign of the denominator into the brackets with  $i\omega\tau$  such that

$$\tilde{\sigma}(\omega) = \frac{ne^2\tau}{m^*} \left[ \frac{1}{1 + (-i\omega\tau)^{1-\alpha}} \right]^\beta. \quad (9.3)$$

Initially, we found that Eq. (9.2) fit our data quite well, as shown in Fig. 9.3 (a). However, when we calculated investigated the spectral distribution, large singularities appeared that indicated scattering rates  $\tau > 1 \mu\text{s}$ . Using the correct Generalized Drude model (Eq. (9.3)) yields a smooth distribution of scattering rates that match the work of Iglesias et al. [367]. Unfortunately, after correcting this error, the Generalized Drude model does not describe our data well as seen in Fig. 9.3 (b). The best-fit parameters are reported in Table 9.2.

Parkinson et al. performed optical-pump terahertz-probe spectroscopy on bulk GaN and GaN nanowires with 300 nm diameter [67]. Utilizing three-photon absorption of 800

nm photons, they directly probed the photoconductivity dynamics of GaN. In bulk GaN, Parkinson et al. describe their conductivity with a Drude model and find the mobility is 590 cm<sup>2</sup>/Vs. Interestingly, spectroscopy of their nanowires revealed a Drude-plasmon photoconductivity. The Drude-plasmon model is a model comprised of a Drude component and a Lorentz oscillator. The Drude component of the spectrum is given by

$$\tilde{\sigma}_{Drude}(\omega, N, \Gamma) = i \frac{Ne^2\omega}{m^*(\omega^2 - i\omega\Gamma)}, \quad (9.4)$$

where  $\Gamma$  is the scattering rate,  $N$  is the charge carrier density, and  $m^*$  is the charge carrier effective mass. The plasmon resonance is described by

$$\tilde{\sigma}(\omega, N, \Gamma) = \frac{iNe^2\omega}{m^*(\omega^2 - \omega_{PL}(N)_i^2\omega\Gamma)} \quad (9.5)$$

where  $\omega_{PL} = \sqrt{fNe^2/m^*\epsilon_r}$  is the plasmon frequency,  $f = 1/2$  is a geometrical factor for a cylinder,  $\epsilon_r = 9.4$  is the relative permittivity [67]. In GaN the background conductivity cannot be neglected [131, 365, 366], and has a substantial impact on the differential photoconductivity [115]. Therefore the photoconductivity is given by

$$\begin{aligned} \tilde{\sigma}(\omega) = & \left( \tilde{\sigma}_{Drude}(\omega, \nu\Delta N, \Gamma) + \tilde{\sigma}_{Plasmon}(\omega, (1-\rho)N_{eq} + (1-\nu)\Delta N, \Gamma) \right) \\ & - \tilde{\sigma}_{Plasmon}(\omega, (1-\rho)N_{eq}, \Gamma) \end{aligned} \quad (9.6)$$

where  $N_{eq}$  is the density of carriers in equilibrium,  $\Delta N = N - N_{eq}$  is the difference between the density photoexcited free carriers and equilibrium carriers,  $1 - \nu$  is the fraction of photoexcited carriers in the plasmon mode, and  $1 - \rho$  is the fraction of equilibrium carriers in the plasmon mode. The background combined with a plasma oscillating at the resonant plasma frequency gives rise to a modified Drude-Lorentz model that can describe complicated spectral features with only four fit parameters<sup>†</sup>  $\Delta N$ ,  $\Gamma$ ,  $\nu$ , and  $\rho$  [67, 110, 115]. Figure 9.3 (c) shows the data fit to the Drude-plasmon model, and we find again that the Drude-plasmon model is not a good description of our results.

Finally, the photoconductivity in Fig. 9.3 (d) is fit to a Drude model as suggested by

---

<sup>†</sup>Provided that the equilibrium carrier density is known apriori.

work on bulk GaN [67, 365, 366]. Again we find that the model cannot reproduce the real part's flatness and the imaginary conductivity's steepness.

## 9.4 Summary

In summary, time-resolved terahertz spectroscopy was performed on gallium nitride nanowalls that were grown on sapphire substrates using molecular beam epitaxy. The photoconductivity lifetime is found to be  $> 125$  ps, and we report a short lifetime of  $\tau_1 = 5.45 \pm 0.08$  ps, and a longer lifetime is  $\tau_2 = 67 \pm 3$  ps. There is a significant photoconductivity that persists beyond the 125 ps window measured here.

Modelling the time-resolved spectroscopy proves difficult in this system. By testing the photoconductivity models used in literature, we uncovered a mistake in the reporting of the Generalized Drude model. Correcting this error resulted in poor fits of the photoconductivity. We also found that our results also do not agree with the Drude-plasmon and Drude models.

# Chapter 10

## Conclusions

This thesis contains many studies of ultrafast charge carrier dynamics in various nanomaterials. By leveraging the powerful non-contact nature of time-resolved terahertz spectroscopy, we performed the first TRTS studies on CdS nanowires wrapped in  $C_3N_5$  nanosheets, atomically thin  $WSe_2$  nanosheets, inverse opal germanium-silicon nanostructures, functionalized silicon nanosheets, and gallium nitride nanowalls.

Photocatalysis applications of CdS nanowires wrapped in  $C_3N_5$  nanosheets depend on the ability to optimize charge-carrier participation in surface chemistry. Charge-carrier transport regulates participation in surface chemistry, and in Chapter 5 we measure the ultrafast transport of charge carriers in CdS nanowires. Our terahertz time-domain spectroscopy of bulk CdS and CdS nanowire films showed that our samples possess no significant density of equilibrium charge carriers. We performed TRTS on bulk CdS, and found that surface scattering significantly reduces the mobility in CdS. Our measurements of  $\sim 100 \text{ cm}^2/\text{Vs}$  agree well with estimates of  $\sim 128 \text{ cm}^2/\text{Vs}$  that come from a simple diffuse surface scattering model [219, 220].

We investigated three models of charge carrier dynamics in CdS nanowire films. The plasmon model was shown to not support our results due to inconsistencies in the fluence dependent behaviour of the plasma frequency. The Bruggeman model of conductivity did not fit our data well because it requires a unique combination of charge carrier density and volume fill fraction to match the shape of our photoconductivity spectra. The fill fraction was kept as a global fit parameter, and the unique combination of fill fraction and carrier

density was not always attainable. The Drude-Smith model was found to fit our data well, and provide meaningful insight into the charge carrier localization occurring in the CdS nanowire films. Our results suggest that the short range ( $< 25$  nm) charge-carrier mobilities ( $\sim 400$  cm<sup>2</sup>/Vs) are nearly bulk-like ( $\sim 440$  cm<sup>2</sup>/Vs [203]). Wrapping the nanowires in C<sub>3</sub>N<sub>5</sub> is shown to increase the charge carrier localization, as the weakly bonded C<sub>3</sub>N<sub>5</sub> nanosheets may be modifying the surface potential in favour of further localization. The Drude-Smith model also allowed us to extract the ambipolar diffusion coefficients  $D^*$  for our CdS-NW films. We could then use the  $D^*$  in our model of charge-carrier lifetimes. Our TRTS of bulk CdS yielded an ambipolar diffusivity of  $D^* \sim 1.3$  cm<sup>2</sup>/s which is in agreement with the reported value of 1.2 cm<sup>2</sup>/s [162]. In the bare CdS nanowires we found  $D^* \sim 0.7$  cm<sup>2</sup>/s, which is significantly larger than the ES-WNWs and IS-WNWs, where  $D^* \sim 0.1 - 0.3$  cm<sup>2</sup>/s.

With the ambipolar diffusion coefficients measured from TRTS, we then constructed a multi-level rate equation to simultaneously describe the photoluminescence and photoconductivity lifetimes. To describe the lifetimes, our model incorporates hot carrier cooling, surface recombination, charge separation, and bimolecular recombination. The model fits the photoluminescence and photoconductivity of all the CdS nanowires, the ex-situ wrapped nanowires, and the in-situ wrapped nanowires. In the CdS nanowires and the ES-WNWs, we find a surface recombination velocity that increases with fluence, and is similar to measurements in bulk CdS ( $S_0 \sim 10^4$  cm/s) [162]. In the IS-WNWs, we find that our model suggests almost no surface recombination is occurring, This may be because the recombination is so fast in those samples that the surface recombination occurs on sub-picosecond timescales. Thus only the bimolecular recombination occurs on the  $>$  ps timescales measured here. The surface recombination velocity was found to increase as the fluence was increased. This is consistent with charge-carrier screening of the surface potential in CdS nanowires. As the density is increased, the charged surface states are screened by the free carriers. This lowers the potential barrier at the nanowire surface and increases access to surface recombination. Furthermore, our measurements of the charge separation time constant indicate that it takes longer for electrons and holes to separate at high excitation densities. This is also consistent with charge carrier screening of the surface potential because at large densities there are more charge carriers that must recombine before the surface potential is restored.

In Chapter 6 we investigated the fluence and temperature dependence of the ultrafast photoconductivity in a WSe<sub>2</sub> monolayer within the 0.5-2.5 THz bandwidth. At room temperature, the photoconductivity lifetimes indicate that exciton formation has a significant impact on the transient carrier density, and early ( $< 1$  ps) exciton dissociation gives rise to a population of free carriers. The free carriers undergo bimolecular recombination. As the fluence is increased from 49 to 490  $\mu\text{J}/\text{cm}^2$ , we observe a slight increase in the free carrier bimolecular recombination constant,  $\gamma_{b,f}$ , from  $\sim 0.25$  to  $\sim 0.44$   $\text{cm}^2/\text{s}$ . The exciton dissociation constant,  $\gamma_{a,x}$ , is found to decrease from  $\sim 2.5$  to  $1.9$   $\text{ps}^{-1}$  as the fluence is raised. This corresponds with an increase of the dissociation time from 400 to 526 fs. The amplitude of the photoconductivity is seen to increase as the fluence is increased, and potential saturation is observed at a fluence of 490  $\mu\text{J}/\text{cm}^2$ .

As the sample is cooled, the free carrier bimolecular recombination constant exhibits nontrivial behaviour that warrants further investigation. Starting at 1.6  $\text{cm}^2/\text{s}$  at 230K,  $\gamma_{b,f}$  is found to reach a minimum of  $\sim 4$   $\text{cm}^2/\text{s}$  around 130 K.  $\gamma_{b,f}$  then increases as the temperature is lowered further. The monomolecular exciton dissociation constant,  $\gamma_{a,x}$ , is found to initially increase as the temperature is lowered and reaches a maximum of 2.5 ps at 180 K. As the sample is cooled further,  $\gamma_{a,x}$  is found to decrease. The absorption of the sample was found to have a strong temperature dependence. As the sample is cooled, the absorption peak nearest the excitation energy (3.1 eV) is found to blue shift into the excitation energy. This results in an increase of the monolayer absorption, which is reflected in the maximum photoconductivity we observe. As the temperature is lowered, we find that the photoconductivity does indeed increase.

At room temperature we perform time-resolved terahertz spectroscopy. The conductivity spectra are fit to a Drude-Smith model. We find that the sheet conductivity lowers as time progresses after excitation. As the fluence is increased, the conductivity is found to increase as well. The sheet density of carriers is also found to increase with fluence, and the localization parameter does not have a clear dependence on temperature. The  $c$ -parameter is found to be  $\sim -0.5$ , and future work is needed to unveil the mechanism responsible for the localization we observe.

Cooling the sample does not seem to have a significant effect on the photoconductivity

of the WSe<sub>2</sub> monolayer. The scattering rate is found to be  $\sim 50 fs$  for all temperatures. The sheet density of carriers is found to increase as the sample is cooled, which is in line with our observations of the temperature dependent absorption and photoconductivity lifetimes. The long-range mobility and  $c$  parameter are found to be constant,  $\mu_{l,r} \sim 90 \text{ cm}^2/Vs$  and  $\sim 0.65$ , respectively.

Replacing Ge with Si in inverse-opal nanostructures is important for the industrial-scale application of these structures; however, charge carrier transport in the composite networks is still unknown. In Chapter 7 we performed TRTS on Si-Ge nanostructures containing 0 %, 30 %, and 70 % Ge and found that photoexcited charge carriers exist for  $\sim 2 \text{ ps}$ , and that the Drude-Smith model describes their conductivity. Fitting the lifetimes to a power law allows us to extract activation energies in these systems, and future temperature dependences might prove fruitful in measuring these experimentally. We find energies of  $\sim 50 \text{ meV}$  in the 0 % and 30 % Ge nanostructures and  $\sim 100 \text{ meV}$  in the 70 % nanostructure. We find that the lowest long-range mobility ( $\sim 4 \text{ cm}^2/Vs$ ) occurs in the 30 % Ge sample and is likely due to diffusive back-action at Ge-Si interfaces in the composite nanostructure. In the 0 % and 70 % Ge sample we find mobilities of  $\sim 7.5 \text{ cm}^2/Vs$  and  $\sim 9 \text{ cm}^2/Vs$ , respectively.

The oxidation of silicon nanosheets (SiNSs) is a significant barrier to integrating SiNSs into existing Si-based technologies. We investigate two surface passivations: one comprised of dodecene (SiNS-C<sub>12</sub>H<sub>25</sub>) and another with hydrogen (SiNS-H). We find that the photoconductivity of the SiNS is generally weak; however, encapsulation with dodecene is significantly stronger than SiNS-H. The charge-carrier lifetime of the SiNS-C<sub>12</sub>H<sub>25</sub> film is  $\sim 2 \text{ ps}$ , and we could not measure a lifetime in the SiNS-H film. We find that the conductivity in SiNS-C<sub>12</sub>H<sub>25</sub> is well described by a Drude-Smith model, with a high short-range mobility of  $400 \pm 60 \text{ cm}^2/Vs$ .

Gallium nitride nanowalls are important for future applications in photocatalytic water splitting. However, ultrafast charge carrier dynamics remain unexplored in GaN nanowalls. In Chapter 9 we perform time-resolved terahertz spectroscopy on gallium nitride nanowalls that were grown on sapphire substrates using molecular beam epitaxy. The photoconductivity lifetime is found to be  $> 125 \text{ ps}$ , and we report a short lifetime of  $\tau_1 = 5.45 \pm 0.08 \text{ ps}$ , and a longer lifetime is  $\tau_2 = 67 \pm 3 \text{ ps}$ . There is a significant photoconductivity that per-

sists beyond the 125 ps window measured here. Modelling the time-resolved spectroscopy proves difficult in this system, however, by working through the existing photoconductivity models we did uncover a mistake in the Generalized Drude model shown in terahertz spectroscopy literature. Correcting this error resulted in poor fits of the photoconductivity. Our results also do not agree with existing literature that supports the Drude-plasmon and Drude models.

As devices continue to miniaturize into nanoscale dimensions, it is becoming increasingly important to document the ultrafast charge-carrier dynamics in the nanomaterials that comprise these devices. In this thesis we have investigated a variety of nanomaterials, and the knowledge gained from these experiments will provide future routes for optimizing photocatalytic performance in nanowires, collection efficiencies in battery anodes, and next-generation solar cell performance.

Future directions include terahertz scanning tunnelling microscopy of CdS nanowires in order to visualize the formation of the surface potentials that limit charge carrier transport. Broadband terahertz spectroscopy can be used to access trion resonances in WSe<sub>2</sub>, and excitation of deep trap states in inverse-opal nanostructures. Alternative passivations may continue to increase the mobility of charge carriers in SiNS, and new models may help understand the photoconductivity of GaN nanowalls.

# References

- [1] Ziming Wang, Jie Qiao, Shuqi Zhao, Shilei Wang, Chuan He, Xutang Tao, and Shanpeng Wang. Recent progress in terahertz modulation using photonic structures based on two-dimensional materials. *InfoMat*, 3(10):1110–1133, 2021.
- [2] M Adarsha, S Malathi, Santosh Kumar, and RG Sangeetha. 1 tbps data rate transmission using the super channel in the flexi grid network. *International Journal on Communications Antenna and Propagation*, 13(2), 2023.
- [3] James Lloyd-Hughes, Peter M Oppeneer, T Pereira Dos Santos, Andre Schleife, Sheng Meng, Michael A Sentef, Michael Ruggenthaler, Angel Rubio, Ilie Radu, Margaret Murnane, et al. The 2021 ultrafast spectroscopic probes of condensed matter roadmap. *Journal of Physics: Condensed Matter*, 33(35):353001, 2021.
- [4] J. L. Wood. Far-infrared spectroscopy. *Quarterly Reviews, Chemical Society*, 17(4):362–381, 1963.
- [5] E. D. Palik. A far infrared bibliography. *JOSA*, 50(12):1329–1336, 1960.
- [6] G. R. Wilkinson, S. A. Inglis, and C. Smart. Far infra-red spectroscopy. In *Spectroscopy: Report of the Conference Organized by the Hydrocarbon Research Group of the Institute of Petroleum and Held in London [at the University of London] March 1962*, page 157. Institute of Petroleum, 1962.
- [7] H. M. Randall, D. M. Dennison, Nathan Ginsburg, and Louis R. Weber. The far infrared spectrum of water vapor. *Physical Review*, 52(3):160, 1937.

- [8] Martin Van Exter, Ch Fattinger, and D Grischkowsky. Terahertz time-domain spectroscopy of water vapor. *Optics letters*, 14(20):1128–1130, 1989.
- [9] Peter F. Bernath. The spectroscopy of water vapour: Experiment, theory and applications. *Physical Chemistry Chemical Physics*, 4(9):1501–1509, 2002.
- [10] Alexander I McIntosh, Bin Yang, Stephen M Goldup, Michael Watkinson, and Robert S Donnan. Terahertz spectroscopy: a powerful new tool for the chemical sciences? *Chemical Society Reviews*, 41(6):2072–2082, 2012.
- [11] P Uhd Jepsen, David G Cooke, and Martin Koch. Terahertz spectroscopy and imaging—modern techniques and applications. *Laser & Photonics Reviews*, 5(1):124–166, 2011.
- [12] FA Miller, GL Carlson, FF Bentley, and WH Jones. Infrared spectra of inorganic ions in the cesium bromide region (700-300  $\text{cm}^{-1}$ ). *Spectrochimica Acta (England) Divided into Spectrochim. Acta, Part A and Spectrochim. Acta, Part B*, 16, 1960.
- [13] HY Fan. Infra-red absorption in semiconductors. *Reports on Progress in Physics*, 19(1):107, 1956.
- [14] Neil W Ashcroft and N David Mermin. *Solid state physics*. Cengage Learning, 2022.
- [15] Gwénaél Gouadec and Philippe Colomban. Raman spectroscopy of nanostructures and nanosized materials, 2007.
- [16] Akhilesh K Arora, M Rajalakshmi, TR Ravindran, and V Sivasubramanian. Raman spectroscopy of optical phonon confinement in nanostructured materials. *Journal of Raman Spectroscopy: An International Journal for Original Work in all Aspects of Raman Spectroscopy, Including Higher Order Processes, and also Brillouin and Rayleigh Scattering*, 38(6):604–617, 2007.
- [17] Gert Irmer. Raman scattering of nanoporous semiconductors. *Journal of Raman Spectroscopy: An International Journal for Original Work in all Aspects of Raman Spectroscopy, Including Higher Order Processes, and also Brillouin and Rayleigh Scattering*, 38(6):634–646, 2007.

- [18] M Friedemann, K Pierz, R Stosch, and FJ Ahlers. Graphene on gallium arsenide: Engineering the visibility. *Applied Physics Letters*, 95(10), 2009.
- [19] LZ Liu, XL Wu, ZY Zhang, TH Li, and Paul K Chu. Raman investigation of oxidation mechanism of silicon nanowires. *Applied Physics Letters*, 95(9), 2009.
- [20] Bibo Li, Dapeng Yu, and Shu-Lin Zhang. Raman spectral study of silicon nanowires. *Physical Review B*, 59(3):1645, 1999.
- [21] J Avendano-Lopez, FL Castillo-Alvarado, A Escamilla-Esquivel, G Contreras-Puente, Jaime Ortiz-Lopez, and O Zelaya-Angel. Optical phonons in znxcd1- xse thin films. *Solid state communications*, 100(1):33–36, 1996.
- [22] Erhard W Fischer. Studies of structure and dynamics of solid polymers by elastic and inelastic neutron scattering. In *Macromolecular Chemistry*, pages 1319–1341. Elsevier, 1979.
- [23] AV Belushkin and DP Kozlenko. Structural organization of nanomaterials and nanosystems: neutron scattering insight. *Advances in Natural Sciences: Nanoscience and Nanotechnology*, 1(2):023002, 2010.
- [24] A Debernardi, NM Pyka, A Göbel, T Ruf, R Lauck, S Kramp, and M Cardona. Lattice dynamics of wurtzite cds: Neutron scattering and ab-initio calculations. *Solid state communications*, 103(5):297–301, 1997.
- [25] D Strauch and B Dorner. Phonon eigenvector determination in gaas by inelastic neutron scattering. *Journal of Physics C: Solid State Physics*, 19(16):2853, 1986.
- [26] Kofi W Adu, Humberto R Gutierrez, and Peter C Eklund. Phonons in silicon nanowires. In *Nanosilicon*, pages 258–288. Elsevier, 2008.
- [27] Mei-Jiau Huang, Chieu-Chou Weng, and Tai-Ming Chang. An investigation of the phonon properties of silicon nanowires. *International Journal of Thermal Sciences*, 49(7):1095–1102, 2010.

- [28] Raina J Olsen, Matthew Beckner, Matthew B Stone, Peter Pfeifer, Carlos Wexler, and Haskell Taub. Quantum excitation spectrum of hydrogen adsorbed in nanoporous carbons observed by inelastic neutron scattering. *Carbon*, 58:46–58, 2013.
- [29] Y Fujii, Y Akahama, S Endo, S Narita, Y Yamada, and G Shirane. Inelastic neutron scattering study of acoustic phonons of black phosphorus. *Solid State Communications*, 44(5):579–582, 1982.
- [30] Y Yamada, Y Fujii, Y Akahama, S Endo, S Narita, JD Axe, and DB McWhan. Lattice-dynamical properties of black phosphorus under pressure studied by inelastic neutron scattering. *Physical Review B*, 30(5):2410, 1984.
- [31] Petr Kužel and Hynek Němec. Terahertz spectroscopy of nanomaterials: a close look at charge-carrier transport. *Advanced Optical Materials*, 8(3):1900623, 2020.
- [32] Ronald Ulbricht, Euan Hendry, Jie Shan, Tony F Heinz, and Mischa Bonn. Carrier dynamics in semiconductors studied with time-resolved terahertz spectroscopy. *Reviews of Modern Physics*, 83(2):543, 2011.
- [33] K Mizoguchi, T Furuichi, O Kojima, M Nakayama, S Saito, A Syouji, and K Sakai. Intense terahertz radiation from longitudinal optical phonons in GaAs/AlAs multiple quantum wells. *Applied Physics Letters*, 87(9), 2005.
- [34] Bhabani S Swain, Bibhu P Swain, and Nong M Hwang. Chemical surface passivation of silicon nanowires grown by APCVD. *Current Applied Physics*, 10(3):S439–S442, 2010.
- [35] Junjie Niu, Deren Yang, Jian Sha, Jian Nong Wang, and Ming Li. Infrared spectra of silicon nanowires. *Materials Letters*, 61(3):894–896, 2007.
- [36] Kin Fai Mak, Long Ju, Feng Wang, and Tony F Heinz. Optical spectroscopy of graphene: From the far infrared to the ultraviolet. *Solid State Communications*, 152(15):1341–1349, 2012.
- [37] Muge Acik, Geunsik Lee, Cecilia Mattevi, Adam Pirkle, Robert M Wallace, Manish Chhowalla, Kyeongjae Cho, and Yves Chabal. The role of oxygen during thermal

- reduction of graphene oxide studied by infrared absorption spectroscopy. *The Journal of Physical Chemistry C*, 115(40):19761–19781, 2011.
- [38] CM Randall and RD Rawcliffe. Refractive indices of germanium, silicon, and fused quartz in the far infrared. *Applied Optics*, 6(11):1889–1895, 1967.
- [39] S Lebedkin, B Renker, R Heid, H Schober, and H Rietschel. A spectroscopic study of m@ c82 metallofullerenes: Raman, far-infrared, and neutron scattering results. *Applied Physics A*, 66:273–280, 1998.
- [40] Maddalena D’Amore, Alessandro Piovano, Eleonora Vottero, Andrea Piovano, Svemir Rudic, Alessandro Erba, Elena Groppo, and Bartolomeo Civalleri. Inelastic neutron scattering investigation of mgcl<sub>2</sub> nanoparticle-based ziegler–natta catalysts for olefin polymerization. *ACS Applied Nano Materials*, 3(11):11118–11128, 2020.
- [41] U Pal and J García Serrano. Raman and infrared spectroscopy of ge nanoparticles embedded in zno matrix. *Applied surface science*, 246(1-3):23–29, 2005.
- [42] Donald S Bethune, Gerard Meijer, Wade C Tang, Hal J Rosen, William G Golden, Hajime Seki, Charles A Brown, and Mattanjah S de Vries. Vibrational raman and infrared spectra of chromatographically separated c60 and c70 fullerene clusters. *Chemical Physics Letters*, 179(1-2):181–186, 1991.
- [43] Un Jeong Kim, Clascidia A Furtado, Xiaoming Liu, Gugang Chen, and Peter C Eklund. Raman and ir spectroscopy of chemically processed single-walled carbon nanotubes. *Journal of the American Chemical Society*, 127(44):15437–15445, 2005.
- [44] Yang Lan, Benjamin J Dringoli, David A Valverde-Chávez, Carlito S Ponceca Jr, Mark Sutton, Yihui He, Mercouri G Kanatzidis, and David G Cooke. Ultrafast correlated charge and lattice motion in a hybrid metal halide perovskite. *Science advances*, 5(5):eaaw5558, 2019.
- [45] Yan Wang and Manish Chhowalla. Making clean electrical contacts on 2d transition metal dichalcogenides. *Nature Reviews Physics*, 4(2):101–112, 2022.

- [46] Tae In Kim, Jayoung Kim, Ick-Joon Park, Kyung-Ok Cho, and Sung-Yool Choi. Chemically exfoliated 1t-phase transition metal dichalcogenide nanosheets for transparent antibacterial applications. *2D Materials*, 6(2):025025, 2019.
- [47] Changhai Ru, Yong Zhang, Yu Sun, Yu Zhong, Xueliang Sun, David Hoyle, and Ian Cotton. Automated four-point probe measurement of nanowires inside a scanning electron microscope. *IEEE Transactions on Nanotechnology*, 10(4):674–681, 2010.
- [48] JC Li, Y Wang, and DC Ba. Characterization of semiconductor surface conductivity by using microscopic four-point probe technique. *Physics Procedia*, 32:347–355, 2012.
- [49] Shancheng Yan, Litao Sun, Peng Qu, Ninping Huang, Yinchen Song, and Zhongdang Xiao. Synthesis of uniform cds nanowires in high yield and its single nanowire electrical property. *Journal of Solid State Chemistry*, 182(10):2941–2945, 2009.
- [50] Jeffrey W Elam, Guang Xiong, Catherine Y Han, H Hau Wang, James P Birrell, John N Hryn, Michael J Pellin, John F Poco, and Joe H Satcher. Atomic layer deposition for the conformal coating of nanoporous materials. *MRS Online Proceedings Library*, 876:1–5, 2005.
- [51] Jun-Sik Park and Young-Beom Kim. Synthesis and characterization of nanoporous strontium-doped lanthanum cobaltite thin film using metal organic chemical solution deposition. *Thin Solid Films*, 599:174–178, 2016.
- [52] Yerassyl Yerlanuly, Rakhymzhan Zhumadilov, Renata Nemkayeva, Berik Uzakbaiuly, Almaz R Beisenbayev, Zhumabay Bakenov, Tlekkabul Ramazanov, Maratbek Gabdullin, Annie Ng, Viktor V Brus, et al. Physical properties of carbon nanowalls synthesized by the icp-pecvd method vs. the growth time. *Scientific Reports*, 11(1):19287, 2021.
- [53] JM LaForge, TL Cocker, AL Beaudry, K Cui, RT Tucker, MT Taschuk, FA Hegmann, and MJ Brett. Conductivity control of as-grown branched indium tin oxide nanowire networks. *Nanotechnology*, 25(3):035701, 2013.

- [54] TL Cocker, LV Titova, S Fourmaux, H-C Bandulet, D Brassard, J-C Kieffer, MA El Khakani, and FA Hegmann. Terahertz conductivity of the metal-insulator transition in a nanogranular vo2 film. *Applied physics letters*, 97(22), 2010.
- [55] M Walther, DG Cooke, C Sherstan, M Hajar, MR Freeman, and FA Hegmann. Terahertz conductivity of thin gold films at the metal-insulator percolation transition. *Physical Review B*, 76(12):125408, 2007.
- [56] Soner Balci, William Baughman, David S Wilbert, Gang Shen, Patrick Kung, and Seongsin Margaret Kim. Characteristics of thz carrier dynamics in gan thin film and zno nanowires by temperature dependent terahertz time domain spectroscopy measurement. *Solid-state electronics*, 78:68–74, 2012.
- [57] M Hangyo, M Tani, and T Nagashima. Terahertz time-domain spectroscopy of solids: a review. *International journal of infrared and millimeter waves*, 26:1661–1690, 2005.
- [58] Jens Neu and Charles A Schmuttenmaer. Tutorial: An introduction to terahertz time domain spectroscopy (thz-tds). *Journal of Applied Physics*, 124(23), 2018.
- [59] Tae-In Jeon, D Grischkowsky, AK Mukherjee, and Reghu Menon. Electrical characterization of conducting polypyrrole by thz time-domain spectroscopy. *Applied Physics Letters*, 77(16):2452–2454, 2000.
- [60] Muhammad Bilal, Wen Xu, Chao Wang, Hua Wen, Xinnian Zhao, Dan Song, and Lan Ding. Optoelectronic properties of monolayer hexagonal boron nitride on different substrates measured by terahertz time-domain spectroscopy. *Nanomaterials*, 10(4):762, 2020.
- [61] Yang Yu-Ping, Zhang Zhen-Wei, Shi Yu-Lei, Feng Shuai, and Wang Wen-Zhong. Far-infrared conductivity of cus nanoparticles measured by terahertz time-domain spectroscopy. *Chinese Physics B*, 19(4):043302, 2010.
- [62] Min-Chang Jeong, Sang-Won Lee, Ji-Min Seo, and Jae-Min Myoung. The effect of stacking fault formation on optical properties in vertically aligned zno nanowires. *Nanotechnology*, 18(30):305701, 2007.

- [63] Hannah J Joyce, Jennifer Wong-Leung, Qiang Gao, H Hoe Tan, and Chennupati Jagadish. Phase perfection in zinc blende and wurtzite iii- v nanowires using basic growth parameters. *Nano letters*, 10(3):908–915, 2010.
- [64] Hye Yun Jeong, Si Young Lee, Thuc Hue Ly, Gang Hee Han, Hyun Kim, Honggi Nam, Zhao Jiong, Bong Gyu Shin, Seok Joon Yun, Jaesu Kim, et al. Visualizing point defects in transition-metal dichalcogenides using optical microscopy. *Acs Nano*, 10(1):770–777, 2016.
- [65] Ruei-San Chen, Chih-Che Tang, Wei-Chu Shen, and Ying-Sheng Huang. Thickness-dependent electrical conductivities and ohmic contacts in transition metal dichalcogenides multilayers. *Nanotechnology*, 25(41):415706, 2014.
- [66] Peng Han, Xinke Wang, and Yan Zhang. Time-resolved terahertz spectroscopy studies on 2d van der waals materials. *Advanced Optical Materials*, 8(3):1900533, 2020.
- [67] Patrick Parkinson, Christopher Dodson, Hannah J Joyce, Kris A Bertness, Norman A Sanford, Laura M Herz, and Michael B Johnston. Noncontact measurement of charge carrier lifetime and mobility in gan nanowires. *Nano letters*, 12(9):4600–4604, 2012.
- [68] Patrick Parkinson, Hannah J Joyce, Qiang Gao, Hark Hoe Tan, Xin Zhang, Jin Zou, Chennupati Jagadish, Laura M Herz, and Michael B Johnston. Carrier lifetime and mobility enhancement in nearly defect-free core- shell nanowires measured using time-resolved terahertz spectroscopy. *Nano letters*, 9(9):3349–3353, 2009.
- [69] Kazi M Alam, Charles E Jensen, Pawan Kumar, Riley W Hooper, Guy M Bernard, Aakash Patidar, Ajay P Manuel, Naaman Amer, Anders Palmgren, David N Purschke, et al. Photocatalytic mechanism control and study of carrier dynamics in cds@ c3n5 core-shell nanowires. *ACS Applied Materials & Interfaces*, 13(40):47418–47439, 2021.
- [70] Mohammad M Taheri, Triet M Truong, Siming Li, William N Shafarman, Brian E McCandless, and Jason B Baxter. Distinguishing bulk and surface recombination in cdte thin films and solar cells using time-resolved terahertz and photoluminescence spectroscopies. *Journal of Applied Physics*, 130(16), 2021.

- [71] David N Purschke, Markus RP Pielmeier, Ebru Üzer, Claudia Ott, Charles Jensen, Annabelle Degg, Anna Vogel, Naaman Amer, Tom Nilges, and Frank A Hegmann. Ultrafast photoconductivity and terahertz vibrational dynamics in double-helix snip nanowires. *Advanced Materials*, 33(34):2100978, 2021.
- [72] Wei Zhang, Xulu Zeng, Xiaojun Su, Xianshao Zou, Pierre-Adrien Mante, Magnus T Borgstrom, and Arkady Yartsev. Carrier recombination processes in gallium indium phosphide nanowires. *Nano Letters*, 17(7):4248–4254, 2017.
- [73] S Perera, K Pemasiri, MA Fickenscher, HE Jackson, LM Smith, J Yarrison-Rice, S Paiman, Q Gao, HH Tan, and C Jagadish. Probing valence band structure in wurtzite inp nanowires using excitation spectroscopy. *Applied Physics Letters*, 97(2), 2010.
- [74] Chan La-o Vorakiat, Liang Cheng, Teddy Salim, Rudolph A Marcus, Maria-Elisabeth Michel-Beyerle, Yeng Ming Lam, and Elbert EM Chia. Phonon features in terahertz photoconductivity spectra due to data analysis artifact: A case study on organometallic halide perovskites. *Applied Physics Letters*, 110(12):123901, 2017.
- [75] CE Jensen, KM Alam, A Palmgren, DN Purschke, N Amer, K Shankar, and FA Hegmann. Ultrafast carrier dynamics of cds nanowires wrapped in c 3 n 5 nanosheets. In *2020 45th International Conference on Infrared, Millimeter, and Terahertz Waves (IRMMW-THz)*, pages 1–2. IEEE, 2020.
- [76] DG Cooke, AN MacDonald, A Hryciw, J Wang, Q Li, A Meldrum, and FA Hegmann. Transient terahertz conductivity in photoexcited silicon nanocrystal films. *Physical Review B*, 73(19):193311, 2006.
- [77] Lyubov V Titova, Tyler L Cocker, Sijia Xu, Jean-Marc Baribeau, Xiaohua Wu, David J Lockwood, and Frank A Hegmann. Ultrafast carrier dynamics and the role of grain boundaries in polycrystalline silicon thin films grown by molecular beam epitaxy. *Semiconductor Science and Technology*, 31(10):105017, 2016.

- [78] Lyubov V Titova, Tyler L Cocker, David G Cooke, Xiongyao Wang, Al Meldrum, and Frank A Hegmann. Ultrafast percolative transport dynamics in silicon nanocrystal films. *Physical Review B*, 83(8):085403, 2011.
- [79] Yaping Dan, Kwanyong Seo, Kuniharu Takei, Jhim H Meza, Ali Javey, and Kenneth B Crozier. Dramatic reduction of surface recombination by in situ surface passivation of silicon nanowires. *Nano letters*, 11(6):2527–2532, 2011.
- [80] Hannah J Joyce, Jennifer Wong-Leung, Chaw-Keong Yong, Callum J Docherty, Suriati Paiman, Qiang Gao, H Hoe Tan, Chennupati Jagadish, James Lloyd-Hughes, Laura M Herz, et al. Ultralow surface recombination velocity in inp nanowires probed by terahertz spectroscopy. *Nano letters*, 12(10):5325–5330, 2012.
- [81] Hannah J Joyce, Callum J Docherty, Qiang Gao, H Hoe Tan, Chennupati Jagadish, James Lloyd-Hughes, Laura M Herz, and Michael B Johnston. Electronic properties of gaas, inas and inp nanowires studied by terahertz spectroscopy. *Nanotechnology*, 24(21):214006, 2013.
- [82] Hannah J Joyce, Patrick Parkinson, Nian Jiang, Callum J Docherty, Qiang Gao, H Hoe Tan, Chennupati Jagadish, Laura M Herz, and Michael B Johnston. Electron mobilities approaching bulk limits in “surface-free” gaas nanowires. *Nano letters*, 14(10):5989–5994, 2014.
- [83] Hannah J Joyce, Sarwat A Baig, Patrick Parkinson, Christopher L Davies, Jessica L Boland, H Hoe Tan, Chennupati Jagadish, Laura M Herz, and Michael B Johnston. The influence of surfaces on the transient terahertz conductivity and electron mobility of gaas nanowires. *Journal of Physics D: Applied Physics*, 50(22):224001, 2017.
- [84] Zhiwei Xu, Mingxuan Guo, Jun Bo, Xingtong Chen, Peng Wan, Mengyu Chen, Qinyi Li, Chengzhao Luo, Yu Chen, and Song Chen. Nanocrystal-enabled front-surface bandgap gradient for the reduction of surface recombination in inverted perovskite solar cells. *Solar RRL*, 5(10):2100489, 2021.

- [85] Ilan Shalish, Henryk Temkin, and Venkatesh Narayanamurti. Size-dependent surface luminescence in zno nanowires. *Physical Review B*, 69(24):245401, 2004.
- [86] Martin Van Exter and D Grischkowsky. Carrier dynamics of electrons and holes in moderately doped silicon. *Physical Review B*, 41(17):12140, 1990.
- [87] Matthew C Beard, Gordon M Turner, and Charles A Schmuttenmaer. Transient photoconductivity in gaas as measured by time-resolved terahertz spectroscopy. *Physical Review B*, 62(23):15764, 2000.
- [88] BN Murdin. Far-infrared free-electron lasers and their applications. *Contemporary physics*, 50(2):391–406, 2009.
- [89] M Abo-Bakr, J Feikes, K Holldack, P Kuske, WB Peatman, U Schade, G Wüstefeld, and H-W Hübers. Brilliant, coherent far-infrared (thz) synchrotron radiation. *Physical Review Letters*, 90(9):094801, 2003.
- [90] PM Rentzepis. Ultrafast processes. *Science*, 169(3942):239–247, 1970.
- [91] GR Fleming and GS Beddard. Cw mode-locked dye lasers for ultra fast spectroscopic studies. *Optics & Laser Technology*, 10(5):257–264, 1978.
- [92] AP Schwarzenbach, TS Luk, IA McIntyre, U Johann, A McPherson, K Boyer, and CK Rhodes. Subpicosecond krf\* excimer-laser source. *Optics letters*, 11(8):499–501, 1986.
- [93] P Maine, D Strickland, P Bado, M Pessot, and G Mourou. Generation of ultrahigh peak power pulses by chirped pulse amplification. *IEEE Journal of Quantum electronics*, 24(2):398–403, 1988.
- [94] David H Auston, Kin P Cheung, and Peter R Smith. Picosecond photoconducting hertzian dipoles. *Applied physics letters*, 45(3):284–286, 1984.
- [95] A Rice, Y Jin, XF Ma, X-C Zhang, David Bliss, J Larkin, and M Alexander. Terahertz optical rectification from <110> zinc-blende crystals. *Applied physics letters*, 64(11):1324–1326, 1994.

- [96] F Blanchard, L Razzari, H-C Bandulet, G Sharma, R Morandotti, J-C Kieffer, T Ozaki, M Reid, HF Tiedje, HK Haugen, et al. Generation of 1.5  $\mu\text{j}$  single-cycle terahertz pulses by optical rectification from a large aperture znte crystal. *Optics Express*, 15(20):13212–13220, 2007.
- [97] DJ Cook and RM Hochstrasser. Intense terahertz pulses by four-wave rectification in air. *Optics letters*, 25(16):1210–1212, 2000.
- [98] Donghoon Kuk, YJ Yoo, EW Rosenthal, Nihal Jhajj, HM Milchberg, and Ki-Yong Kim. Generation of scalable terahertz radiation from cylindrically focused two-color laser pulses in air. *Applied Physics Letters*, 108(12):121106, 2016.
- [99] Yun-Shik Lee. *Principles of terahertz science and technology*. Springer Science and Business Media, 2009.
- [100] Michael Schall, Markus Walther, and P Uhd Jepsen. Fundamental and second-order phonon processes in cdte and znte. *Physical Review B*, 64(9):094301, 2001.
- [101] Peter R Smith, David H Auston, and Martin C Nuss. Subpicosecond photoconducting dipole antennas. *IEEE Journal of Quantum Electronics*, 24(2):255–260, 1988.
- [102] Matthew C Beard, Gordon M Turner, and Charles A Schmuttenmaer. Terahertz spectroscopy. *The Journal of Physical Chemistry B*, 106(29):7146–7159, 2002.
- [103] Lin Chen, Deng-gao Liao, Xu-guang Guo, Jia-yu Zhao, Yi-ming Zhu, and Song-lin Zhuang. Terahertz time-domain spectroscopy and micro-cavity components for probing samples: a review. *Frontiers of Information Technology & Electronic Engineering*, 20(5):591–607, 2019.
- [104] Ryan M Smith and Mark A Arnold. Terahertz time-domain spectroscopy of solid samples: principles, applications, and challenges. *Applied Spectroscopy Reviews*, 46(8):636–679, 2011.
- [105] James Lloyd-Hughes and Tae-In Jeon. A review of the terahertz conductivity of bulk and nano-materials. *Journal of Infrared, Millimeter, and Terahertz Waves*, 33:871–925, 2012.

- [106] Martin Koch, Daniel M Mittleman, Jan Ornik, and Enrique Castro-Camus. Terahertz time-domain spectroscopy. *Nature Reviews Methods Primers*, 3(1):48, 2023.
- [107] Hynek Němec, Petr Kužel, and Villy Sundström. Charge transport in nanostructured materials for solar energy conversion studied by time-resolved terahertz spectroscopy. *Journal of Photochemistry and Photobiology A: Chemistry*, 215(2-3):123–139, 2010.
- [108] Krzysztof Iwaszczuk, David G Cooke, Masazumi Fujiwara, Hideki Hashimoto, and Peter Uhd Jepsen. Simultaneous reference and differential waveform acquisition in time-resolved terahertz spectroscopy. *Optics Express*, 17(24):21969–21976, 2009.
- [109] Charles A Schmuttenmaer. Exploring dynamics in the far-infrared with terahertz spectroscopy. *Chemical reviews*, 104(4):1759–1780, 2004.
- [110] Hannah J Joyce, Jessica L Boland, Christopher L Davies, Sarwat A Baig, and Michael B Johnston. A review of the electrical properties of semiconductor nanowires: insights gained from terahertz conductivity spectroscopy. *Semiconductor Science and Technology*, 31(10):103003, 2016.
- [111] Charles A. Schmuttenmaer. Using time-resolved thz spectroscopy to study carrier dynamics and solar energy conversion in nanostructured materials. In *2015 40TH International Conference on Infrared, Millimeter AND Terahertz Waves (IRMMW-THZ)*, 2015.
- [112] Nicholas B. Lawler, Diwei Ho, Cameron W. Evans, Vincent P. Wallace, and K. Swaminathan Iyer. Convergence of terahertz radiation and nanotechnology. *JOURNAL OF MATERIALS CHEMISTRY C*, 8(32):10942–10955, AUG 28 2020.
- [113] Maria G. Burdanova, Alexey P. Tsapenko, Marianna V. Kharlamova, Esko I. Kauppinen, Boris P. Gorshunov, Junichiro Kono, and James Lloyd-Hughes. A review of the terahertz conductivity and photoconductivity of carbon nanotubes and heteronanotubes. *ADVANCED OPTICAL MATERIALS*, 9(24), DEC 2021.
- [114] Meihua Jin, Yingxin Wang, Minqi Chai, Chuanxin Chen, Ziran Zhao, and Tao He.

- Terahertz detectors based on carbon nanomaterials. *ADVANCED FUNCTIONAL MATERIALS*, 32(11, SI), MAR 2022.
- [115] Patrick Parkinson, James Lloyd-Hughes, Qiang Gao, H Hoe Tan, Chennupati Jagadish, Michael B Johnston, and Laura M Herz. Transient terahertz conductivity of gaas nanowires. *Nano Letters*, 7(7):2162–2165, 2007.
- [116] D. G. Cooke, P. Uhd Jepsen, Jun Yan Lek, Yeng Ming Lam, F. Sy, and M. M. Dignam. Picosecond dynamics of internal exciton transitions in cdse nanorods. *Phys. Rev. B*, 88:241307, Dec 2013.
- [117] Lei Cheng, Quanjun Xiang, Yulong Liao, and Huaiwu Zhang. Cds-based photocatalysts. *Energy & Environmental Science*, 11(6):1362–1391, 2018.
- [118] Ashok Kumar and PK Ahluwalia. Electronic structure of transition metal dichalcogenides monolayers 1h-mx<sub>2</sub> (m= mo, w; x= s, se, te) from ab-initio theory: new direct band gap semiconductors. *The European Physical Journal B*, 85(6):1–7, 2012.
- [119] Kin Fai Mak, Changgu Lee, James Hone, Jie Shan, and Tony F Heinz. Atomically thin mos 2: a new direct-gap semiconductor. *Physical review letters*, 105(13):136805, 2010.
- [120] Hiroki Ago, Satoru Fukamachi, Hiroko Endo, Pablo Solís-Fernández, Rozan Mohammad Yunus, Yuki Uchida, Vishal Panchal, Olga Kazakova, and Masaharu Tsuji. Visualization of grain structure and boundaries of polycrystalline graphene and two-dimensional materials by epitaxial growth of transition metal dichalcogenides. *ACS nano*, 10(3):3233–3240, 2016.
- [121] Mike Tebyetekerwa, Jian Zhang, Kun Liang, The Duong, Guru Prakash Neupane, Linglong Zhang, Boqing Liu, Thien N Truong, Rabin Basnet, Xiaojing Qiao, et al. Quantifying quasi-fermi level splitting and mapping its heterogeneity in atomically thin transition metal dichalcogenides. *Advanced Materials*, 31(25):1900522, 2019.
- [122] Marco M Furchi, Armin A Zechmeister, Florian Hoeller, Stefan Wachter, Andreas

- Pospischil, and Thomas Mueller. Photovoltaics in van der waals heterostructures. *IEEE Journal of Selected Topics in Quantum Electronics*, 23(1):106–116, 2016.
- [123] Lujun Huang. *Engineering Optical and Thermal Properties of Two Dimensional Metal Dichalcogenide Monolayer*. North Carolina State University, 2017.
- [124] Philipp Steinleitner, Philipp Merkl, Philipp Nagler, Joshua Mornhinweg, Christian Schüller, Tobias Korn, Alexey Chernikov, and Rupert Huber. Direct observation of ultrafast exciton formation in a monolayer of wse2. *Nano Letters*, 17(3):1455–1460, 2017.
- [125] Callum J Docherty, Patrick Parkinson, Hannah J Joyce, Ming-Hui Chiu, Chang-Hsiao Chen, Ming-Yang Lee, Lain-Jong Li, Laura M Herz, and Michael B Johnston. Ultrafast transient terahertz conductivity of monolayer mos2 and wse2 grown by chemical vapor deposition. *ACS nano*, 8(11):11147–11153, 2014.
- [126] Philipp Merkl, Fabian Mooshammer, Philipp Steinleitner, Anna Girnghuber, K-Q Lin, Philipp Nagler, Johannes Holler, Christian Schüller, John M Lupton, Tobias Korn, S. Ovesen, S. Brem, E. Malic, and R. Huber. Ultrafast transition between exciton phases in van der waals heterostructures. *Nature materials*, 18(7):691–696, 2019.
- [127] Dimitri D Vaughn II and Raymond E Schaak. Synthesis, properties and applications of colloidal germanium and germanium-based nanomaterials. *Chemical Society Reviews*, 42(7):2861–2879, 2013.
- [128] Brian A Korgel. Nanomaterials developments for higher-performance lithium ion batteries, 2014.
- [129] LT Canham, TI Cox, A Loni, and AJ Simons. Progress towards silicon optoelectronics using porous silicon technology. *Applied surface science*, 102:436–441, 1996.
- [130] Mita Dasog, Julian Kehrle, Bernhard Rieger, and Jonathan GC Veinot. Silicon nanocrystals and silicon-polymer hybrids: synthesis, surface engineering, and applications. *Angewandte Chemie International Edition*, 55(7):2322–2339, 2016.

- [131] Mi-Hee Park, Kitae Kim, Jeyoung Kim, and Jaephil Cho. Flexible dimensional control of high-capacity li-ion-battery anodes: From 0d hollow to 3d porous germanium nanoparticle assemblies. *Advanced materials*, 22(3):415–418, 2010.
- [132] Ravi Pillarisetty. Academic and industry research progress in germanium nanodevices. *Nature*, 479(7373):324–328, 2011.
- [133] SA Healy and MA Green. Efficiency enhancements in crystalline silicon solar cells by alloying with germanium. *Solar energy materials and solar cells*, 28(3):273–284, 1992.
- [134] Michele Amato, Maurizia Palummo, Riccardo Rurali, and Stefano Ossicini. Silicon–germanium nanowires: chemistry and physics in play, from basic principles to advanced applications. *Chemical reviews*, 114(2):1371–1412, 2014.
- [135] Joel A Kelly, Eric J Henderson, and Jonathan GC Veinot. Sol–gel precursors for group 14 nanocrystals. *Chemical communications*, 46(46):8704–8718, 2010.
- [136] XD Pi and U Kortshagen. Nonthermal plasma synthesized freestanding silicon–germanium alloy nanocrystals. *Nanotechnology*, 20(29):295602, 2009.
- [137] Brandon Bonham and Grégory Guisbiers. Thermal stability and optical properties of si–ge nanoparticles. *Nanotechnology*, 28(24):245702, 2017.
- [138] Manuel M Bentlohner, Markus Waibel, Patrick Zeller, Kuhu Sarkar, Peter Müller-Buschbaum, Dina Fattakhova-Rohlfing, and Thomas F Fässler. Zintl clusters as wet-chemical precursors for germanium nanomorphologies with tunable composition. *Angewandte Chemie International Edition*, 55(7):2441–2445, 2016.
- [139] Laura Deakin, Robert Lam, Frank Marsiglio, and Arthur Mar. Superconductivity in  $\text{ba}_2\text{sn}_3\text{sb}_6$  and  $\text{srsn}_3\text{sb}_4$ . *Journal of alloys and compounds*, 338(1-2):69–72, 2002.
- [140] Mary Alvean Narreto. *Ultrafast Photoluminescence and Photoconductivity Dynamics of Semiconductors*. PhD thesis, University of ALberta, 2019.

- [141] Hirotaka Okamoto, Yusuke Sugiyama, and Hideyuki Nakano. Synthesis and modification of silicon nanosheets and other silicon nanomaterials. *Chemistry—A European Journal*, 17(36):9864–9887, 2011.
- [142] Branimir Radisavljevic, Aleksandra Radenovic, Jacopo Brivio, Valentina Giacometti, and Andras Kis. Single-layer mos2 transistors. *Nature nanotechnology*, 6(3):147–150, 2011.
- [143] Mingchao Wang, Shuai Fu, Petko Petkov, Yubin Fu, Zhitao Zhang, Yannan Liu, Ji Ma, Guangbo Chen, Sai Manoj Gali, Lei Gao, et al. Exceptionally high charge mobility in phthalocyanine-based poly (benzimidazobenzophenanthroline)-ladder-type two-dimensional conjugated polymers. *Nature Materials*, pages 1–8, 2023.
- [144] Julia Winnerl, Max Kraut, Sabrina Artmeier, and Martin Stutzmann. Selectively grown gan nanowalls and nanogrids for photocatalysis: growth and optical properties. *Nanoscale*, 11(10):4578–4584, 2019.
- [145] K Kishino, T Hoshino, S Ishizawa, and A Kikuchi. Selective-area growth of gan nanocolumns on titanium-mask-patterned silicon (111) substrates by rf-plasma-assisted molecular-beam epitaxy. *Electronics Letters*, 44(13):819–821, 2008.
- [146] Max Kraut, Florian Pantle, Julia Winnerl, Martin Hetzl, Felix Eckmann, Ian D Sharp, and Martin Stutzmann. Photo-induced selective etching of gan nanowires in water. *Nanoscale*, 11(16):7967–7975, 2019.
- [147] Mark Lundstrom. *Fundamentals of carrier transport*. Cambridge University Press, 2000.
- [148] Eugene Hecht. *Optics 4th edition*. Pearson Addison Wesley, 2002.
- [149] GC Reali. Reflection from dielectric materials. *American Journal of Physics*, 50(12):1133–1136, 1982.
- [150] F Bassani, G. Pastori Parravicini, and R. A. Ballinger. *Electronic states and optical transitions in solids*. Pergamon Press, 1975.

- [151] Mark Fox. *Optical properties of solids*. Oxford University Press, 2002.
- [152] Andreas Othonos. Probing ultrafast carrier and phonon dynamics in semiconductors. *Journal of applied physics*, 83(4):1789–1830, 1998.
- [153] FH Su, F Blanchard, G Sharma, L Razzari, A Ayesheshim, TL Cocker, LV Titova, T Ozaki, J-C Kieffer, R Morandotti, et al. Terahertz pulse induced intervalley scattering in photoexcited gaas. *Optics Express*, 17(12):9620–9629, 2009.
- [154] SK Sundaram and Eric Mazur. Inducing and probing non-thermal transitions in semiconductors using femtosecond laser pulses. *Nature materials*, 1(4):217–224, 2002.
- [155] Martin C Nuss, Wolfgang Zinth, and Wolfgang Kaiser. Femtosecond carrier relaxation in semiconductor-doped glasses. *Applied physics letters*, 49(25):1717–1719, 1986.
- [156] Ivan Pelant and Jan Valenta. *Luminescence spectroscopy of semiconductors*. Oxford UNiversity Press, 2012.
- [157] Jens Neu. Optical pump terahertz probe (optp) and time resolved terahertz spectroscopy (trts) of emerging solar materials. *APL Photonics*, 8(7), 2023.
- [158] P Uhd Jepsen, W Schairer, IH Libon, U Lemmer, NE Hecker, M Birkholz, K Lips, and M Schall. Ultrafast carrier trapping in microcrystalline silicon observed in optical pump–terahertz probe measurements. *Applied Physics Letters*, 79(9):1291–1293, 2001.
- [159] Jared H Strait, Paul A George, Mark Levendorf, Martin Blood-Forsythe, Farhan Rana, and Jiwoong Park. Measurements of the carrier dynamics and terahertz response of oriented germanium nanowires using optical-pump terahertz-probe spectroscopy. *Nano letters*, 9(8):2967–2972, 2009.
- [160] DE Aspnes. Recombination at semiconductor surfaces and interfaces. *Surface Science*, 132(1-3):406–421, 1983.
- [161] J. Vaitkus. The nonequilibrium hall effect and related transport phenomena in semiconductors under inhomogeneous excitation by a laser pulse. *physica status solidi (a)*, 34(2):769–775, 1976.

- [162] D Benjamin and D Huppert. Surface recombination velocity measurements of cadmium sulfide single crystals immersed in electrolytes. a picosecond photoluminescence study. *The Journal of Physical Chemistry*, 92(16):4676–4679, 1988.
- [163] MG Calkin and PJ Nicholson. Electrodynamics of a semiclassical free-electron gas. *Reviews of Modern Physics*, 39(2):361, 1967.
- [164] Richard P Feynman, Albert R Hibbs, and Daniel F Styer. *Quantum mechanics and path integrals*. Courier Corporation, 2010.
- [165] Anthony E Siegman. *Lasers*. University science books, 1986.
- [166] J. M. Dickey and A. Paskin. Computer simulation of the lattice dynamics of solids. *Phys. Rev.*, 188:1407–1418, Dec 1969.
- [167] Tyler L Cocker, Devin Baillie, Miles Buruma, Lyubov V Titova, Richard D Sydora, Frank Marsiglio, and Frank A Hegmann. Microscopic origin of the drude-smith model. *Physical Review B*, 96(20):205439, 2017.
- [168] N. V. Smith. Drude theory and the optical properties of liquid mercury. *Physics Letters A*, 26(3):126–127, 1968.
- [169] N. V. Smith. Classical generalization of the drude formula for the optical conductivity. *Physical Review B*, 64(15):155106, 2001.
- [170] Edward D Palik. *Handbook of optical constants of solids*, volume 3. Academic press, 1998.
- [171] A. B. Pippard. Proceedings of the international colloquium. In *Optical Properties and Electronic Structure of Metals and Alloys*, volume 1, page 622, 1966.
- [172] D Grischkowsky, Søren Keiding, Martin Van Exter, and Ch Fattinger. Far-infrared time-domain spectroscopy with terahertz beams of dielectrics and semiconductors. *JOSA B*, 7(10):2006–2015, 1990.

- [173] Hynek Němec, Petr Kužel, and Villy Sundström. Far-infrared response of free charge carriers localized in semiconductor nanoparticles. *Physical Review B*, 79(11):115309, 2009.
- [174] H. Němec, V. Zajac, I. Rychetský, D. Fattakhova-Rohlfing, B. Mandlmeier, T. Bein, Z. Mics, and P. Kužel. Charge transport in titanium dioxide films with complex percolation pathways investigated by time-resolved terahertz spectroscopy. *IEEE Transactions on Terahertz Science and Technology*, 3(3):302–313, 2013.
- [175] D. A. G. Bruggeman. Calculation of different physical constants of heterogenous substances i: dielectric constant and conductivity of media of isotropic substances. *Annalen der Physik*, 421(2):160–178, 1935.
- [176] Martin Dressel and George Grüner. *Electrodynamics of Solids: Optical Properties of Electrons in Matter*. Cambridge University Press, 2002.
- [177] Fatma A Hashim, Reham R Mostafa, Abdelazim G Hussien, Seyedali Mirjalili, and Karam M Sallam. Fick’s law algorithm: A physical law-based algorithm for numerical optimization. *Knowledge-Based Systems*, 260:110146, 2023.
- [178] Marius Grundmann. *Physics of Semiconductors*, volume 11. Springer, 2010.
- [179] Markus Schleuning, Moritz Kölbach, Fatwa F Abdi, Klaus Schwarzburg, Martin Stolterfoht, Rainer Eichberger, Roel van de Krol, Dennis Friedrich, and Hannes Hempel. Generalized method to extract carrier diffusion length from photoconductivity transients: Cases of bivo 4, halide perovskites, and amorphous and crystalline silicon. *PRX Energy*, 1(2):023008, 2022.
- [180] Otfried Madelung. *Semiconductors: data handbook*. Springer Science & Business Media, 2004.
- [181] Masahiko Tani, Shuji Matsuura, Kiyomi Sakai, and Shin-ichi Nakashima. Emission characteristics of photoconductive antennas based on low-temperature-grown gaas and semi-insulating gaas. *Applied optics*, 36(30):7853–7859, 1997.

- [182] Ki-Yong Kim, James H Glowina, Antoinette J Taylor, and George Rodriguez. Terahertz emission from ultrafast ionizing air in symmetry-broken laser fields. *Optics express*, 15(8):4577–4584, 2007.
- [183] HG Roskos, MD Thomson, M Kreß, and T Löffler. Broadband thz emission from gas plasmas induced by femtosecond optical pulses: From fundamentals to applications. *Laser & photonics reviews*, 1(4):349–368, 2007.
- [184] Robert W Boyd. *Nonlinear Optics*. Academic press, 2020.
- [185] Ajay Nahata, Aniruddha S Weling, and Tony F Heinz. A wideband coherent terahertz spectroscopy system using optical rectification and electro-optic sampling. *Applied physics letters*, 69(16):2321–2323, 1996.
- [186] Qi Wu and X-C Zhang. Free-space electro-optic sampling of terahertz beams. *Applied Physics Letters*, 67(24):3523–3525, 1995.
- [187] John R. Rumble. Online handbook of chemistry and physics. <https://hbcpc.chemnetbase.com/faces/contents/ContentsSearch.xhtml>, August 2020.
- [188] R Saravanan, S Israel, and RK Rajaram. Bonding in znte at rt, 200 and 100 k revealed by entropy maximized electron density distribution. *Physica B: Condensed Matter*, 363(1-4):166–177, 2005.
- [189] Koichi Momma and Fujio Izumi. Vesta 3 for three-dimensional visualization of crystal, volumetric and morphology data. *Journal of applied crystallography*, 44(6):1272–1276, 2011.
- [190] Znte crystal structure: Datasheet from “pauling file multinaries edition – 2012” in springermaterials ([https://materials.springer.com/isp/crystallographic/docs/sd\\_1717506](https://materials.springer.com/isp/crystallographic/docs/sd_1717506)). Copyright 2016 Springer-Verlag Berlin Heidelberg & Material Phases Data System (MPDS), Switzerland & National Institute for Materials Science (NIMS), Japan.

- [191] Evans A LaRoche and Hugh M Brown. Rapid stroboscopic study of production looms. *Textile Research Journal*, 19(5):288–291, 1949.
- [192] Q Wu, M Litz, and X-C Zhang. Broadband detection capability of zn te electro-optic field detectors. *Applied Physics Letters*, 68(21):2924–2926, 1996.
- [193] C Winnewisser, P Uhd Jepsen, M Schall, V Schyja, and H Helm. Electro-optic detection of thz radiation in litao 3, linbo 3 and zn te. *Applied Physics Letters*, 70(23):3069–3071, 1997.
- [194] J Petzelt, P Kužel, I Rychetský, A Pashkin, and T Ostapchuk. Dielectric response of soft modes in ferroelectric thin films. *Ferroelectrics*, 288(1):169–185, 2003.
- [195] David N Purschke. *Ultrafast Terahertz Dynamics in Semiconductors and Nanomaterials*. PhD thesis, University of Alberta, 2021.
- [196] RE Glover III and Ms Tinkham. Conductivity of superconducting films for photon energies between 0.3 and 4 0 k t c. *Physical Review*, 108(2):243, 1957.
- [197] Frank A Hegmann, Oksana Ostroverkhova, and David G Cooke. Probing organic semiconductors with terahertz pulses. *Photophysics of Molecular Materials: From Single Molecules to Single Crystals*, pages 367–428, 2005.
- [198] David E Aspnes and AA Studna. Dielectric functions and optical parameters of si, ge, gap, gaas, gasb, inp, inas, and insb from 1.5 to 6.0 ev. *Physical review B*, 27(2):985, 1983.
- [199] PP Debye and Esther M Conwell. Electrical properties of n-type germanium. *Physical Review*, 93(4):693, 1954.
- [200] Charles E Jensen, Naaman Amer, and Frank A. Hegmann. Ultrafast spectroscopy laboratory user’s manual, 2021.
- [201] *Model SR830 DSP Lock-In Amplifier*, 2011.
- [202] Rohit P Prasankumar and Antoinette J Taylor. *Optical techniques for solid-state materials characterization*. CRC press, 2016.

- [203] Xiaocheng Yang, Chunchuan Xu, and NC Giles. Intrinsic electron mobilities in cdse, cds, zno, and zns and their use in analysis of temperature-dependent hall measurements. *Journal of Applied Physics*, 104(7):073727, 2008.
- [204] Mingshan Zhu, Chunyang Zhai, Sooyeon Kim, Mamoru Fujitsuka, and Tetsuro Majima. Monitoring transport behavior of charge carriers in a single cds@ cus nanowire via in situ single-particle photoluminescence spectroscopy. *The Journal of Physical Chemistry Letters*, 10(14):4017–4024, 2019.
- [205] Iris Visoly-Fisher, Sidney R Cohen, Arie Ruzin, and David Cahen. How polycrystalline devices can outperform single-crystal ones: thin film cdte/cds solar cells. *Advanced Materials*, 16(11):879–883, 2004.
- [206] B. Ullrich, D.M. Bagnall, H. Sakai, and Y. Segawa. Photoluminescence and lasing of thin cds films on glass formed by pulsed-laser-deposition. *Journal of Luminescence*, 87-89:1162–1164, 2000.
- [207] H Jerominek, M Pigeon, S Patela, Z Jakubczyk, C Delisle, and R Tremblay. Cds microcrystallites-doped thin-film glass waveguides. *Journal of applied physics*, 63(3):957–959, 1988.
- [208] Tianyou Zhai, Xiaosheng Fang, Liang Li, Yoshio Bando, and Dmitri Golberg. One-dimensional cds nanostructures: synthesis, properties, and applications. *Nanoscale*, 2(2):168–187, 2010.
- [209] Jum Suk Jang, Upendra A Joshi, and Jae Sung Lee. Solvothermal synthesis of cds nanowires for photocatalytic hydrogen and electricity production. *The Journal of Physical Chemistry C*, 111(35):13280–13287, 2007.
- [210] Zhiping Yan, Zijun Sun, Xiang Liu, Hongxing Jia, and Pingwu Du. Cadmium sulfide/graphitic carbon nitride heterostructure nanowire loading with a nickel hydroxide cocatalyst for highly efficient photocatalytic hydrogen production in water under visible light. *Nanoscale*, 8(8):4748–4756, 2016.

- [211] Pawan Kumar, Ehsan Vahidzadeh, Ujwal K. Thakur, Piyush Kar, Kazi M. Alam, Ankur Goswami, Najia Mahdi, Kai Cui, Guy M. Bernard, Vladimir K. Michaelis, and Karthik Shankar. C<sub>3</sub>N<sub>5</sub>: A low bandgap semiconductor containing an azo-linked carbon nitride framework for photocatalytic, photovoltaic and adsorbent applications. *Journal of the American Chemical Society*, 141(13):5415–5436, 2019.
- [212] Lionel Duvillaret, Frederic Garet, and J-L Coutaz. A reliable method for extraction of material parameters in terahertz time-domain spectroscopy. *IEEE Journal of selected topics in quantum electronics*, 2(3):739–746, 1996.
- [213] François Aguet, Dimitri Van De Ville, and Michael Unser. Model-based 2.5-d deconvolution for extended depth of field in brightfield microscopy. *IEEE Transactions on Image Processing*, 17(7):1144–1153, 2008.
- [214] T. L. Cocker, L. V. Titova, S. Fourmaux, G. Holloway, H.-C. Bandulet, D. Brassard, J.-C. Kieffer, M. A. El Khakani, and F. A. Hegmann. Phase diagram of the ultrafast photoinduced insulator-metal transition in vanadium dioxide. *Phys. Rev. B*, 85:155120, Apr 2012.
- [215] Glenda B. De los Reyes, Mita Dasog, MengXing Na, Lyubov V. Titova, Jonathan G. C. Veinot, and Frank A. Hegmann. Charge transfer state emission dynamics in blue-emitting functionalized silicon nanocrystals. *Phys. Chem. Chem. Phys.*, 17:30125–30133, 2015.
- [216] Mingjie Li, Bo Wu, Sandy Adhitia Ekahana, Muhammad Iqbal Bakti Utama, Guichuan Xing, Qihua Xiong, Tze Chien Sum, and Xinhai Zhang. Size and surface effects on transient photoconductivity in cds nanobelts probed by time-resolved terahertz spectroscopy. *Applied Physics Letters*, 101(9):091104, 2012.
- [217] Hongwei Liu, Junpeng Lu, Zongyin Yang, Jinghua Teng, Lin Ke, Xinhai Zhang, Limin Tong, and Chorng Haur Sow. Ultrahigh photoconductivity of bandgap-graded cds x se 1- x nanowires probed by terahertz spectroscopy. *Scientific reports*, 6(1):27387, 2016.

- [218] Z Mics, H Němec, I Rychetský, P Kužel, P Formánek, P Malý, and P Němec. Charge transport and localization in nanocrystalline cds films: A time-resolved terahertz spectroscopy study. *Physical Review B*, 83(15):155326, 2011.
- [219] A. Many, Y. Goldstein, and N. B. Grover. *Semiconductor Surfaces*. North-Holland Publishing Company Amsterdam, 1965.
- [220] LL Kazmerski, WB Berry, and CW Allen. Role of defects in determining the electrical properties of cds thin films. i. grain boundaries and surfaces. *Journal of Applied Physics*, 43(8):3515–3521, 1972.
- [221] LV Titova, Thang Ba Hoang, HE Jackson, LM Smith, JM Yarrison-Rice, JL Lensch, and LJ Lauhon. Low-temperature photoluminescence imaging and time-resolved spectroscopy of single cds nanowires. *Applied physics letters*, 89(5):053119, 2006.
- [222] Xinfeng Liu, Qing Zhang, Jing Ngei Yip, Qihua Xiong, and Tze Chien Sum. Wavelength tunable single nanowire lasers based on surface plasmon polariton enhanced burstein–moss effect. *Nano Letters*, 13(11):5336–5343, 2013. PMID: 24134588.
- [223] Lucas T Kunneman, Marco Zanella, Liberato Manna, Laurens DA Siebbeles, and Juleon M Schins. Mobility and spatial distribution of photoexcited electrons in cdse/cds nanorods. *The Journal of Physical Chemistry C*, 117(6):3146–3151, 2013.
- [224] Ivan Fotev, Leila Balaghi, Johannes Schmidt, Harald Schneider, Manfred Helm, Emmanouil Dimakis, and Alexej Pashkin. Electron dynamics in ingaas shells around gaas nanowires probed by terahertz spectroscopy. *Nanotechnology*, 30(24):244004, mar 2019.
- [225] L. Balaghi, S. Shan, I. Fotev, F. Moebus, R. Rana, T. Venanzi, R. Hubner, T. Mikolajik, H. Schneider, M. Helm, A. Pashkin, and E. Dimakis. High electron mobility in strained gaas nanowires. *Nature Communications*, 30:1–11, 2019.
- [226] WS Baer and RN Dexter. Electron cyclotron resonance in cds. *Physical Review*, 135(5A):A1388, 1964.

- [227] Shigeo Shionoya, Hiroshi Saito, Eiichi Hanamura, and Okikazu Akimoto. Anisotropic excitonic molecules in cds and cdse. *Solid State Communications*, 12(3):223–226, 1973.
- [228] Alexandre Beaudoin, Bassem Salem, Thierry Baron, Pascal Gentile, and Denis Morris. Impact of n-type doping on the carrier dynamics of silicon nanowires studied using optical-pump terahertz-probe spectroscopy. *Physical Review B*, 89(11):115316, 2014.
- [229] Jessica L Boland, Sonia Conesa-Boj, Patrick Parkinson, Gözde Tütüncüoğlu, Federico Matteini, Daniel Ruffer, Alberto Casadei, Francesca Amaduzzi, Fauzia Jabeen, Christopher L Davies, et al. Modulation doping of gaas/algaas core-shell nanowires with effective defect passivation and high electron mobility. *Nano letters*, 15(2):1336–1342, 2015.
- [230] Dick Bedeaux and Jan Vlieger. *Optical properties of surfaces*. Imperial College Press, 2004.
- [231] DAG Bruggeman. Calculation of different physical constants of heterogen substances i dielectric constants and conductibility of mixtures from isotropic substances. *Ann. Phys*, 416(8):665–679, 1935.
- [232] DAG Bruggeman. Calculation of various physical constants of heterogenous substances ii. dielectricity constants and conductivity of non regular multi crystal systems. *Annalen Der Physik*, 25(7):645–672, 1936.
- [233] DAG Bruggeman. Calculation of various physical constants in heterogeneous substances. iii the elastic constants of quasi-isotropic composites from isotropic substances. *Annals of Physics*, 29:160–178, 1937.
- [234] D Huppert, M Evenor, and Y Shapira. *Measurements of surface recombination velocity on CdS surfaces and Au interfaces*. PhD thesis, American Vacuum Society, 1984.
- [235] Y Rosenwaks, L Burstein, Yoram Shapira, and D Huppert. Studies of surface recombination velocity at copper/cadmium sulfide (1120) interfaces. *Journal of physical chemistry*, 94(17):6842–6847, 1990.

- [236] Y Rosenwaks, L Burstein, Y Shapira, and D Huppert. Effects of reactive versus unreactive metals on the surface recombination velocity at cds and cdse (1120) interfaces. *Applied physics letters*, 57(5):458–460, 1990.
- [237] Chaw Keong Yong, Jennifer Wong-Leung, Hannah J Joyce, James Lloyd-Hughes, Qiang Gao, H Hoe Tan, Chennupati Jagadish, Michael B Johnston, and Laura M Herz. Direct observation of charge-carrier heating at wz–zb inp nanowire heterojunctions. *Nano letters*, 13(9):4280–4287, 2013.
- [238] Jung-Hyun Kang, Qiang Gao, Hannah J Joyce, HH Tan, C Jagadish, Y Kim, DY Choi, Y Guo, H Xu, J Zou, et al. Novel growth and properties of gaas nanowires on si substrates. *Nanotechnology*, 21(3):035604, 2009.
- [239] Michele Amato and Riccardo Rurali. Surface physics of semiconducting nanowires. *Progress in Surface Science*, 91(1):1–28, 2016.
- [240] François Léonard, A Alec Talin, BS Swartzentruber, and ST Picraux. Diameter-dependent electronic transport properties of au-catalyst/ge-nanowire schottky diodes. *Physical review letters*, 102(10):106805, 2009.
- [241] Peter A Markowich, Christian A Ringhofer, and Christian Schmeiser. *Semiconductor equations*. Springer Science & Business Media, 2012.
- [242] James Puthussery, Aidong Lan, Thomas H Kosel, and Masaru Kuno. Band-filling of solution-synthesized cds nanowires. *ACS nano*, 2(2):357–367, 2008.
- [243] DW Langer, YS Park, and R No Euwema. Phonon coupling in edge emission and photoconductivity of cdse, cds, and cd (se x s 1- x). *Physical Review*, 152(2):788, 1966.
- [244] Chen Chen, Mitra Dutta, and Michael A Stroschio. Electron scattering via interactions with optical phonons in wurtzite crystals. *Physical Review B*, 70(7):075316, 2004.
- [245] Richard Williams. Surface photovoltage measurements on cadmium sulfide. *Journal of Physics and Chemistry of Solids*, 23(8):1057–1066, 1962.

- [246] Philip W Anderson. More is different: Broken symmetry and the nature of the hierarchical structure of science. *Science*, 177(4047):393–396, 1972.
- [247] JI A Wilson and AD Yoffe. The transition metal dichalcogenides discussion and interpretation of the observed optical, electrical and structural properties. *Advances in Physics*, 18(73):193–335, 1969.
- [248] R Coehoorn, C Haas, J Dijkstra, CJF d Flipse, RA De Groot, and A Wold. Electronic structure of mose 2, mos 2, and wse 2. i. band-structure calculations and photoelectron spectroscopy. *Physical review B*, 35(12):6195, 1987.
- [249] Wei Liu, Jiahao Kang, Deblina Sarkar, Yasin Khatami, Debdeep Jena, and Kaustav Banerjee. Role of metal contacts in designing high-performance monolayer n-type wse2 field effect transistors. *Nano letters*, 13(5):1983–1990, 2013.
- [250] Xiaodong Xu, Wang Yao, Di Xiao, and Tony F Heinz. Spin and pseudospins in layered transition metal dichalcogenides. *Nature Physics*, 10(5):343–350, 2014.
- [251] Yi-Ting Hsu, Abolhassan Vaezi, Mark H Fischer, and Eun-Ah Kim. Topological superconductivity in monolayer transition metal dichalcogenides. *Nature communications*, 8(1):1–6, 2017.
- [252] Sajedah Manzeli, Dmitry Ovchinnikov, Diego Pasquier, Oleg V Yazyev, and Andras Kis. 2d transition metal dichalcogenides. *Nature Reviews Materials*, 2(8):1–15, 2017.
- [253] FHL Koppens, T Mueller, Ph Avouris, AC Ferrari, MS Vitiello, and M Polini. Photodetectors based on graphene, other two-dimensional materials and hybrid systems. *Nature nanotechnology*, 9(10):780–793, 2014.
- [254] Yanping Liu, Yuanji Gao, Siyu Zhang, Jun He, Juan Yu, and Zongwen Liu. Valleytronics in transition metal dichalcogenides materials. *Nano Research*, 12(11):2695–2711, 2019.
- [255] Siwen Zhao, Xiaoxi Li, Baojuan Dong, Huide Wang, Hanwen Wang, Yupeng Zhang, Zheng Han, and Han Zhang. Valley manipulation in monolayer transition metal

- dichalcogenides and their hybrid systems: status and challenges. *Reports on Progress in Physics*, 84(2):026401, 2021.
- [256] Kin Fai Mak and Jie Shan. Photonics and optoelectronics of 2d semiconductor transition metal dichalcogenides. *Nature Photonics*, 10(4):216–226, 2016.
- [257] Yuanzheng Li, Jia Shi, Yang Mi, Xinyu Sui, Haiyang Xu, and Xinfeng Liu. Ultrafast carrier dynamics in two-dimensional transition metal dichalcogenides. *Journal of Materials Chemistry C*, 7(15):4304–4319, 2019.
- [258] Dong Sun, Jia-Wei Lai, Jun-Chao Ma, Qin-Sheng Wang, and Jing Liu. Review of ultrafast spectroscopy studies of valley carrier dynamics in two-dimensional semiconducting transition metal dichalcogenides. *Chinese Physics B*, 26(3):037801, 2017.
- [259] José Ramón Durán Retamal, Dharmaraj Periyanaounder, Jr-Jian Ke, Meng-Lin Tsai, and Jr-Hau He. Charge carrier injection and transport engineering in two-dimensional transition metal dichalcogenides. *Chemical science*, 9(40):7727–7745, 2018.
- [260] Jose H Garcia, Marc Vila, Aron W Cummings, and Stephan Roche. Spin transport in graphene/transition metal dichalcogenide heterostructures. *Chemical Society Reviews*, 47(9):3359–3379, 2018.
- [261] Pavel Leonidovich Pekh, Pavel Vyacheslavovich Ratnikov, and Andrei Pavlovich Silin. Electron-hole liquid in monolayer transition metal dichalcogenide heterostructures. *JETP Letters*, 111:90–95, 2020.
- [262] Ashish Arora, Maciej Koperski, Karol Nogajewski, Jacques Marcus, Clément Faugeras, and Marek Potemski. Excitonic resonances in thin films of wse<sub>2</sub>: from monolayer to bulk material. *Nanoscale*, 7(23):10421–10429, 2015.
- [263] Yumeng You, Xiao-Xiao Zhang, Timothy C Berkelbach, Mark S Hybertsen, David R Reichman, and Tony F Heinz. Observation of biexcitons in monolayer wse<sub>2</sub>. *Nature Physics*, 11(6):477–481, 2015.

- [264] Kai-Qiang Lin, Chin Shen Ong, Sebastian Bange, Paulo E Faria Junior, Bo Peng, Jonas D Ziegler, Jonas Zipfel, Christian Bäuml, Nicola Paradiso, Kenji Watanabe, et al. Narrow-band high-lying excitons with negative-mass electrons in monolayer  $\text{WSe}_2$ . *Nature communications*, 12(1):1–8, 2021.
- [265] AR Goñi, A Cantarero, K Syassen, and M Cardona. High-pressure low-temperature study of the exciton absorption in  $\text{GaAs}$ . *High Pressure Research*, 3(1-6):81–83, 1990.
- [266] SB Nam, DC Reynolds, CW Litton, RJ Almassy, TC Collins, and CM Wolfe. Free-exciton energy spectrum in  $\text{GaAs}$ . *Physical Review B*, 13(2):761, 1976.
- [267] JJ Hopfield and DG Thomas. Fine structure and magneto-optic effects in the exciton spectrum of cadmium sulfide. *Physical Review*, 122(1):35, 1961.
- [268] NO Lipari and M Altarelli. Theory of indirect excitons in semiconductors. *Physical Review B*, 15(10):4883, 1977.
- [269] GG Macfarlane, TP McLean, JE Quarrington, and V Roberts. Exciton and phonon effects in the absorption spectra of germanium and silicon. *Journal of Physics and Chemistry of Solids*, 8:388–392, 1959.
- [270] Martin A Green. Improved value for the silicon free exciton binding energy. *Aip Advances*, 3(11), 2013.
- [271] AT Hanbicki, M Currie, G Kioseoglou, AL Friedman, and BT Jonker. Measurement of high exciton binding energy in the monolayer transition-metal dichalcogenides  $\text{WSe}_2$  and  $\text{WTe}_2$ . *Solid State Communications*, 203:16–20, 2015.
- [272] Chendong Zhang, Amber Johnson, Chang-Lung Hsu, Lain-Jong Li, and Chih-Kang Shih. Direct imaging of band profile in single layer  $\text{MoS}_2$  on graphite: quasiparticle energy gap, metallic edge states, and edge band bending. *Nano letters*, 14(5):2443–2447, 2014.
- [273] Nihit Saigal, Vasam Sugunakar, and Sandip Ghosh. Exciton binding energy in bulk  $\text{MoS}_2$ : A reassessment. *Applied Physics Letters*, 108(13), 2016.

- [274] Gang Wang, Iann C Gerber, Louis Bouet, Delphine Lagarde, Andrea Balocchi, Maël Vidal, Thierry Amand, Xavier Marie, and Bernhard Urbaszek. Exciton states in monolayer mose2: impact on interband transitions. *2D Materials*, 2(4):045005, 2015.
- [275] Chenhao Jin, Eric Yue Ma, Ouri Karni, Emma C Regan, Feng Wang, and Tony F Heinz. Ultrafast dynamics in van der waals heterostructures. *Nature nanotechnology*, 13(11):994–1003, 2018.
- [276] Stefano Dal Conte, Chiara Trovatiello, Christoph Gadermaier, and Giulio Cerullo. Ultrafast photophysics of 2d semiconductors and related heterostructures. *Trends in Chemistry*, 2(1):28–42, 2020.
- [277] Vijila Chellappan, Ai Lin Christina Pang, Soumya Sarkar, Zi En Ooi, and Kuan Eng Johnson Goh. Effect of phonons on valley depolarization in monolayer wse 2. *Electronic Materials Letters*, 14:766–773, 2018.
- [278] Thomas Siday, Fabian Sandner, Samuel Brem, Martin Zizlsperger, Raul Perea-Causin, Felix Schiegl, Svenja Nerreter, Markus Plankl, Philipp Merkl, Fabian Mooshammer, et al. Ultrafast nanoscopy of high-density exciton phases in wse2. *Nano Letters*, 22(6):2561–2568, 2022.
- [279] Thuc Hue Ly, Ming-Hui Chiu, Ming-Yang Li, Jiong Zhao, David J Perello, Magdalena Ola Cichocka, Hye Min Oh, Sang Hoon Chae, Hye Yun Jeong, Fei Yao, et al. Observing grain boundaries in cvd-grown monolayer transition metal dichalcogenides. *ACS nano*, 8(11):11401–11408, 2014.
- [280] Hsiang-Lin Liu, Teng Yang, Jyun-Han Chen, Hsiao-Wen Chen, Huaihong Guo, Riichiro Saito, Ming-Yang Li, and Lain-Jong Li. Temperature-dependent optical constants of monolayer mos 2, mose 2, ws 2, and wse 2: spectroscopic ellipsometry and first-principles calculations. *Scientific reports*, 10(1):15282, 2020.
- [281] Prasenjit Dey, Jagannath Paul, Zefang Wang, CE Stevens, Cunming Liu, AH Romero, Jie Shan, DJ Hilton, and Denis Karaiskaj. Optical coherence in atomic-monolayer

- transition-metal dichalcogenides limited by electron-phonon interactions. *Physical review letters*, 116(12):127402, 2016.
- [282] Tengfei Yan, Siyuan Yang, Dian Li, and Xiaodong Cui. Long valley relaxation time of free carriers in monolayer wse 2. *Physical Review B*, 95(24):241406, 2017.
- [283] Tengfei Yan, Jialiang Ye, Xiaofen Qiao, Pingheng Tan, and Xinhui Zhang. Exciton valley dynamics in monolayer wse 2 probed by the two-color ultrafast kerr rotation. *Physical Chemistry Chemical Physics*, 19(4):3176–3181, 2017.
- [284] L Vina, S Logothetidis, and M Cardona. Temperature dependence of the dielectric function of germanium. *Physical Review B*, 30(4):1979, 1984.
- [285] Siya Zhu and Qian Wang. A simple method for understanding the triangular growth patterns of transition metal dichalcogenide sheets. *AIP Advances*, 5(10), 2015.
- [286] Sabrina N David, Yao Zhai, Arend M Van Der Zande, Kevin O’Brien, Pinshane Y Huang, Daniel A Chenet, James C Hone, Xiang Zhang, and Xiaobo Yin. Rapid, all-optical crystal orientation imaging of two-dimensional transition metal dichalcogenide monolayers. *Applied Physics Letters*, 107(11), 2015.
- [287] Qiannan Cui, Frank Ceballos, Nardeep Kumar, and Hui Zhao. Transient absorption microscopy of monolayer and bulk wse2. *ACS nano*, 8(3):2970–2976, 2014.
- [288] Samuel Brem, Malte Selig, Gunnar Berghaeuser, and Ermin Malic. Exciton relaxation cascade in two-dimensional transition metal dichalcogenides. *Scientific reports*, 8(1):8238, 2018.
- [289] Simon Ovesen, Samuel Brem, Christopher Linderälv, Mikael Kuisma, Tobias Korn, Paul Erhart, Malte Selig, and Ermin Malic. Interlayer exciton dynamics in van der waals heterostructures. *Communications Physics*, 2(1):23, 2019.
- [290] Chuan He, Lipeng Zhu, Qiyi Zhao, Yuanyuan Huang, Zehan Yao, Wanyi Du, Yuhang He, Sujuan Zhang, and Xinlong Xu. Competition between free carriers and excitons

- mediated by defects observed in layered wse2 crystal with time-resolved terahertz spectroscopy. *Advanced Optical Materials*, 6(19):1800290, 2018.
- [291] Mathieu Massicotte, Fabien Violla, Peter Schmidt, Mark B Lundeberg, Simone Latini, Sten Hastrup, Mark Danovich, Diana Davydovskaya, Kenji Watanabe, Takashi Taniguchi, et al. Dissociation of two-dimensional excitons in monolayer wse2. *Nature communications*, 9(1):1633, 2018.
- [292] Jiwon Chang, Leonard F Register, and Sanjay K Banerjee. Ballistic performance comparison of monolayer transition metal dichalcogenide mx2 (m= mo, w; x= s, se, te) metal-oxide-semiconductor field effect transistors. *Journal of Applied Physics*, 115(8):084506, 2014.
- [293] Andor Kormányos, Guido Burkard, Martin Gmitra, Jaroslav Fabian, Viktor Zólyomi, Neil D Drummond, and Vladimir Fal’ko. k·p theory for two-dimensional transition metal dichalcogenide semiconductors. *2D Materials*, 2(2):022001, 2015.
- [294] Nourdine Zibouche, Pier Philipsen, Thomas Heine, and Agnieszka Kuc. Electron transport in mowse monolayers in the presence of an external electric field. *Physical Chemistry Chemical Physics*, 16(23):11251–11255, 2014.
- [295] Hee Cheul Choi and Jillian M Buriak. Preparation and functionalization of hydride terminated porous germanium. electronic supplementary information (esi) available: Ftir thermal stability measurements and sem images. see <http://www.rsc.org/suppdata/c-c/b0/b004011h>. *Chemical Communications*, pages 1669–1670, 2000.
- [296] RS Dubey and DK Gautam. Porous silicon layers prepared by electrochemical etching for application in silicon thin film solar cells. *Superlattices and Microstructures*, 50(3):269–276, 2011.
- [297] Rofle C Anderson, Richard S Muller, and Charles W Tobias. Investigation of porous silicon for vapor sensing. Technical report, Lawrence Livermore National Lab.(LLNL), Livermore, CA (United States), 1989.

- [298] AG Cullis and LT Canham. Visible light emission due to quantum size effects in highly porous crystalline silicon. *Nature*, 353(6342):335–338, 1991.
- [299] Andreas Stein. Germanium takes holey orders. *Nature*, 441(7097):1055–1056, 2006.
- [300] Dina Fattakhova-Rohlfing, Adriana Zaleska, and Thomas Bein. Three-dimensional titanium dioxide nanomaterials. *Chemical reviews*, 114(19):9487–9558, 2014.
- [301] Xiangdong Meng, Rihab Al-Salman, Jiupeng Zhao, Natalia Borissenko, Yao Li, and Frank Endres. Electrodeposition of 3d ordered macroporous germanium from ionic liquids: a feasible method to make photonic crystals with a high dielectric constant. *Angewandte Chemie International Edition*, 48(15):2703–2707, 2009.
- [302] Wuhong Xin, Jiupeng Zhao, Dengteng Ge, Yanbo Ding, Yao Li, and Frank Endres. Two-dimensional si x ge 1- x films with variable composition made via multilayer colloidal template-guided ionic liquid electrodeposition. *Physical Chemistry Chemical Physics*, 15(7):2421–2426, 2013.
- [303] Xin Liu, Jiupeng Zhao, Yiwen Zhang, Xiaokun An, Yanbo Ding, Yi Zhang, Yao Li, and Frank Endres. 3d ordered macroporous ge/al and ge/si bilayer films made by electrodeposition from ionic liquids. *Zeitschrift für Physikalische Chemie*, 227(12):1731–1740, 2013.
- [304] Alexei Esmanski and Geoffrey A Ozin. Silicon inverse-opal-based macroporous materials as negative electrodes for lithium ion batteries. *Advanced Functional Materials*, 19(12):1999–2010, 2009.
- [305] Hernan Miguez, Emmanuel Chomski, Florencio García-Santamaría, Maria Ibisate, Sajeev John, Cefe López, Francisco Meseguer, Jessica P Mondia, Geoffrey A Ozin, Ovidiu Toader, et al. Photonic bandgap engineering in germanium inverse opals by chemical vapor deposition. *Advanced Materials*, 13(21):1634–1637, 2001.
- [306] H Miguez, F Meseguer, C Lopez, M Holgado, G Andreasen, A Mifsud, and V Fornes. Germanium fcc structure from a colloidal crystal template. *Langmuir*, 16(10):4405–4408, 2000.

- [307] Jongkook Hwang, Changshin Jo, Min Gyu Kim, Jinyoung Chun, Eunho Lim, Seongseop Kim, Sanha Jeong, Youngsik Kim, and Jinwoo Lee. Mesoporous ge/geo<sub>2</sub>/carbon lithium-ion battery anodes with high capacity and high reversibility. *ACS nano*, 9(5):5299–5309, 2015.
- [308] Haiping Jia, Richard Kloepsch, Xin He, Juan Pablo Badillo, Pengfei Gao, Olga Fromm, Tobias Placke, and Martin Winter. Reversible storage of lithium in three-dimensional macroporous germanium. *Chemistry of Materials*, 26(19):5683–5688, 2014.
- [309] Slavi C Sevov. Zintl phases. *Intermetallic Compounds-Principles and Practice: Progress*, 3:113–132, 2002.
- [310] E Zintl and A Woltersdorf. Gitterstruktur von lial.(18. mitteilung über metalle und legierungen.). *Zeitschrift für Elektrochemie und angewandte physikalische Chemie*, 41(12):876–879, 1935.
- [311] HG Von Schnering, M Baitinger, U Bolle, W Carrillo-Cabrera, J Curda, Yu Grin, F Heinemann, J Llanos, K Peters, A Schmeding, et al. Binary alkali metal compounds with the zintl anions [ge<sup>9-</sup>]<sup>4-</sup> and [sn<sup>9-</sup>]<sup>4-</sup>. *Zeitschrift für anorganische und allgemeine Chemie*, 623(7):1037–1039, 1997.
- [312] SR Elliott. Electronic transport in amorphous semiconductors. *Defects and Disorder in Crystalline and Amorphous Solids*, pages 261–278, 1994.
- [313] AK Jonscher. Electronic properties of amorphous dielectric films. *Thin solid films*, 1(3):213–234, 1967.
- [314] P Nagels. Electronic transport in amorphous semiconductors. *Amorphous semiconductors*, pages 113–158, 2005.
- [315] Joseph Orenstein and Marc Kastner. Photocurrent transient spectroscopy: measurement of the density of localized states in a-as 2 se 3. *Physical Review Letters*, 46(21):1421, 1981.

- [316] Jie Shan and Susan L Dexheimer. Time-resolved terahertz studies of conductivity processes in novel electronic materials. In *Terahertz Spectroscopy*, pages 191–226. CRC Press, 2017.
- [317] David G Cooke, A Nicole MacDonald, Aaron Hryciw, Al Meldrum, Juan Wang, Q Li, and Frank A Hegmann. Ultrafast terahertz conductivity of photoexcited nanocrystalline silicon. *Journal of Materials Science: Materials in Electronics*, 18:447–452, 2007.
- [318] KPH Lui and FA Hegmann. Ultrafast carrier relaxation in radiation-damaged silicon on sapphire studied by optical pump–terahertz-probe experiments. *Applied Physics Letters*, 78(22):3478–3480, 2001.
- [319] L Fekete, P Kužel, H Němec, F Kadlec, A Dejneka, J Stuchlík, and A Fejfar. Ultrafast carrier dynamics in microcrystalline silicon probed by time-resolved terahertz spectroscopy. *Physical Review B*, 79(11):115306, 2009.
- [320] Paul A George. *Terahertz time-domain spectroscopy: From proteins to nanostructures*. Cornell University, 2009.
- [321] Diego Sabbagh, Johannes Schmidt, Stephan Winnerl, Manfred Helm, Luciana Di Gaspare, Monica De Seta, Michele Virgilio, and Michele Ortolani. Electron dynamics in silicon–germanium terahertz quantum fountain structures. *ACS Photonics*, 3(3):403–414, 2016.
- [322] Wen Xiang Lim, Manukumara Manjappa, Yogesh Kumar Srivastava, Longqing Cong, Abhishek Kumar, Kevin F MacDonald, and Ranjan Singh. Ultrafast all-optical switching of germanium-based flexible metaphotonic devices. *Advanced materials*, 30(9):1705331, 2018.
- [323] L Stolik, MA Eslamisaray, E Nguyen, UR Kortshagen, and J Kakalios. Hopping charge transport in hydrogenated amorphous silicon–germanium alloy thin films. *Journal of Applied Physics*, 131(22):225110, 2022.

- [324] AVV Nampoothiri, BP Nelson, and SL Dexheimer. Femtosecond far-infrared studies of carrier dynamics in hydrogenated amorphous silicon and silicon-germanium alloys. *MRS Online Proceedings Library (OPL)*, 762, 2003.
- [325] AV Vasudevan Nampoothiri and SL Dexheimer. Ultrafast conductivity in amorphous semiconductors by time-resolved thz spectroscopy. In *Conference on Lasers and Electro-Optics, 2004.(CLEO).*, volume 1, pages 2–pp. IEEE, 2004.
- [326] AV Vasudevan Nampoothiri and SL Dexheimer. Ultrafast carrier dynamics in amorphous semiconductors determined by time-resolved thz and nir spectroscopy. In *Quantum Electronics and Laser Science Conference*, page QWC5. Optica Publishing Group, 2005.
- [327] AV Vasudevan Nampoothiri and SL Dexheimer. Ultrafast carrier dynamics in disordered semiconductors determined by time-resolved thz and nir spectroscopy. In *Optical Terahertz Science and Technology*, page TuB4. Optica Publishing Group, 2005.
- [328] Jianbo Gao. Fast photoresponse of functionalized pentacene organic molecular crystals. Master’s thesis, University of Alberta, 2004.
- [329] N Sekine, K Hirakawa, F Sogawa, Y Arakawa, N Usami, Y Shiraki, and T Katoda. Ultrashort lifetime photocarriers in ge thin films. *Applied physics letters*, 68(24):3419–3421, 1996.
- [330] Rf Grigorovici. Amorphous germanium and silicon: Structure and transport phenomena. *Materials Research Bulletin*, 3(1):13–24, 1968.
- [331] JR Yeargan and HL Taylor. The poole-frenkel effect with compensation present. *Journal of Applied Physics*, 39(12):5600–5604, 1968.
- [332] John G Simmons. Poole-frenkel effect and schottky effect in metal-insulator-metal systems. *Physical Review*, 155(3):657, 1967.
- [333] SD Ganichev, E Ziemann, W Prettl, IN Yassievich, AA Istratov, and ER Weber. Distinction between the poole-frenkel and tunneling models of electric-field-stimulated

- carrier emission from deep levels in semiconductors. *Physical Review B*, 61(15):10361, 2000.
- [334] SD Ganichev, J Diener, IN Yassievich, and Wilhelm Prettl. Poole-frenkel effect in terahertz electromagnetic fields. *Europhysics letters*, 29(4):315, 1995.
- [335] Mengkun Liu, Harold Y Hwang, Hu Tao, Andrew C Strikwerda, Kebin Fan, George R Keiser, Aaron J Sternbach, Kevin G West, Salinporn Kittiwatanakul, Jiwei Lu, et al. Terahertz-field-induced insulator-to-metal transition in vanadium dioxide metamaterial. *Nature*, 487(7407):345–348, 2012.
- [336] N. Refvik, D. N. Purschke, W. Pan, C E. Jensen, H. R. J. Simpson, W. Lei, R. Gu, J. Antoszewski, G. A. Umana-Membreno, L. Faraone, and Frank A. Hegmann. Ultrafast photoconductivity dynamics in bulk narrow-gap mercury cadmium telluride films. *in preparation*, 2023.
- [337] Xinliang Feng and A Dieter Schlüter. Towards macroscopic crystalline 2d polymers. *Angewandte Chemie International Edition*, 57(42):13748–13763, 2018.
- [338] Lei Wang, Ying Zhang, Liang Chen, Hangxun Xu, and Yujie Xiong. 2d polymers as emerging materials for photocatalytic overall water splitting. *Advanced materials*, 30(48):1801955, 2018.
- [339] KS Novoselov, SV Morozov, TMG Mohinddin, LA Ponomarenko, Daniel Cunha Elias, Rong Yang, II Barbolina, P Blake, TJ Booth, D Jiang, et al. Electronic properties of graphene. *physica status solidi (b)*, 244(11):4106–4111, 2007.
- [340] Minoru Osada and Takayoshi Sasaki. Exfoliated oxide nanosheets: new solution to nanoelectronics. *Journal of Materials Chemistry*, 19(17):2503–2511, 2009.
- [341] Haoran Mu, Yani Liu, Sudhakara Reddy Bongu, Xiaozhi Bao, Lei Li, Si Xiao, Jincheng Zhuang, Chen Liu, Yamin Huang, Yemin Dong, et al. Germanium nanosheets with dirac characteristics as a saturable absorber for ultrafast pulse generation. *Advanced Materials*, 33(32):2101042, 2021.

- [342] Tobias Helbich, Alina Lyuleeva, Philipp Marx, Lavinia M Scherf, Tapas K Purkait, Thomas F Fässler, Paolo Lugli, Jonathan GC Veinot, and Bernhard Rieger. Lewis acid induced functionalization of photoluminescent 2d silicon nanosheets for the fabrication of functional hybrid films. *Advanced Functional Materials*, 27(21):1606764, 2017.
- [343] Qipeng Lu, Yifu Yu, Qinglang Ma, Bo Chen, and Hua Zhang. 2d transition-metal-dichalcogenide-nanosheet-based composites for photocatalytic and electrocatalytic hydrogen evolution reactions. *Advanced Materials*, 28(10):1917–1933, 2016.
- [344] Gang Guo, Jingzhong Liu, Yajuan Xu, Gencai Guo, and Siyi Tan. Chemical functionalization induced photocatalytic performance for water splitting of silicene: A first-principles investigation. *Colloids and Surfaces A: Physicochemical and Engineering Aspects*, 667:131379, 2023.
- [345] Yuliang Mao, Zihua Yao, Jianmei Yuan, and Xinxin Chang. Two-dimensional germanene-based janus material  $ge_8hnx_8-n$  ( $n=0-8$ ,  $x=f, cl, br, i$ ) for photovoltaic and photocatalytic applications. *Applied Surface Science*, 598:153633, 2022.
- [346] Li-Jun Qiu, Chen-Lan Lin, Chao-Yue Chen, Xin Wang, and Ting-Hai Yang. Synthesis, crystal structure and photocatalytic properties of two 2-d coordination polymer constructed from pyridylmethylphosphonate. *Inorganic Chemistry Communications*, 119:108123, 2020.
- [347] Alina Lyuleeva, Tobias Helbich, Bernhard Rieger, and Paolo Lugli. Polymer-silicon nanosheet composites: bridging the way to optoelectronic applications. *Journal of Physics D: Applied Physics*, 50(13):135106, 2017.
- [348] Bing Huang, Hui-Xiong Deng, Hoonkyung Lee, Mina Yoon, Bobby G Sumpter, Feng Liu, Sean C Smith, and Su-Huai Wei. Exceptional optoelectronic properties of hydrogenated bilayer silicene. *Physical Review X*, 4(2):021029, 2014.
- [349] Sivacarendran Balendhran, Sumeet Walia, Hussein Nili, Sharath Sriram, and Madhu Bhaskaran. Elemental analogues of graphene: silicene, germanene, stanene, and phosphorene. *small*, 11(6):640–652, 2015.

- [350] Tobias Helbich, Alina Lyuleeva, Ignaz MD Hohlein, Philipp Marx, Lavinia M Scherf, Julian Kehrle, Thomas F Fassler, Paolo Lugli, and Bernhard Rieger. Radical-induced hydrosilylation reactions for the functionalization of two-dimensional hydride terminated silicon nanosheets. *Chemistry–A European Journal*, 22(18):6194–6198, 2016.
- [351] Munir H Nayfeh and Lubos Mitas. Silicon nanoparticles: new photonic and electronic material at the transition between solid and molecule. *Nanosilicon*, pages 1–78, 2008.
- [352] Yuliang He, Chenzhong Yin, Guangxu Cheng, Luchun Wang, Xiangna Liu, and GY Hu. The structure and properties of nanosize crystalline silicon films. *Journal of Applied Physics*, 75(2):797–803, 1994.
- [353] Debosmita Karar, Nil Ratan Bandyopadhyay, Ashit Kumar Pramanick, Debanjan Acharyya, Gavin Conibeer, Niladri Banerjee, Olga E Kusmartseva, and Mallar Ray. Quasi-two-dimensional luminescent silicon nanosheets. *The Journal of Physical Chemistry C*, 122(33):18912–18921, 2018.
- [354] Aikebaier Yusufu, Ken Kurosaki, Yoshinobu Miyazaki, Manabu Ishimaru, Atsuko Kosuga, Yuji Ohishi, Hiroaki Muta, and Shinsuke Yamanaka. Bottom-up nanostructured bulk silicon: a practical high-efficiency thermoelectric material. *Nanoscale*, 6(22):13921–13927, 2014.
- [355] Zhi-Gang Shao, Xue-Sheng Ye, Lei Yang, and Cang-Long Wang. First-principles calculation of intrinsic carrier mobility of silicene. *Journal of Applied Physics*, 114(9):093712, 2013.
- [356] Elena Gnani, Susanna Reggiani, and Massimo Rudan. Density of states and group velocity of electrons in sio 2 calculated from a full band structure. *Physical Review B*, 66(19):195205, 2002.
- [357] RC Hughes. Charge-carrier transport phenomena in amorphous si o 2: Direct measurement of the drift mobility and lifetime. *Physical Review Letters*, 30(26):1333, 1973.
- [358] Li Tao, Eugenio Cinquanta, Daniele Chiappe, Carlo Grazianetti, Marco Fanciulli,

- Madan Dubey, Alessandro Molle, and Deji Akinwande. Silicene field-effect transistors operating at room temperature. *Nature nanotechnology*, 10(3):227–231, 2015.
- [359] Koichi Nakamura, Toshiyuki Toriyama, and Susumu Sugiyama. First-principles simulation on piezoresistive properties in doped silicon nanosheets. *IEEJ transactions on electrical and electronic engineering*, 5(2):157–163, 2010.
- [360] ZZ Bandić, PM Bridger, EC Piquette, and TC McGill. Electron diffusion length and lifetime in p-type gan. *Applied physics letters*, 73(22):3276–3278, 1998.
- [361] Fabian Schuster, Martin Hetzl, Saskia Weiszer, Jose A Garrido, Maria De La Mata, Cesar Magen, Jordi Arbiol, and Martin Stutzmann. Position-controlled growth of gan nanowires and nanotubes on diamond by molecular beam epitaxy. *Nano letters*, 15(3):1773–1779, 2015.
- [362] WG Bi and CW Tu. Bowing parameter of the band-gap energy of gan x as 1- x. *Applied Physics Letters*, 70(12):1608–1610, 1997.
- [363] JF Muth, J Dd Brown, MAL Johnson, Zhonghai Yu, RM Kolbas, JW Cook, and JF Schetzina. Absorption coefficient and refractive index of gan, aln and algan alloys. *Materials Research Society Internet Journal of Nitride Semiconductor Research*, 4(S1):502–507, 1999.
- [364] Tsong-Ru Tsai, Shi-Jie Chen, Chih-Fu Chang, Sheng-Hsien Hsu, Tai-Yuan Lin, and Cheng-Chung Chi. Terahertz response of gan thin films. *Optics express*, 14(11):4898–4907, 2006.
- [365] Weili Zhang, Abul K Azad, and D Grischkowsky. Terahertz studies of carrier dynamics and dielectric response of n-type, freestanding epitaxial gan. *Applied Physics Letters*, 82(17):2841–2843, 2003.
- [366] Takeshi Nagashima, Kazue Takata, Shigeki Nashima, Hiroshi Harima, and Masanori Hangyo. Measurement of electrical properties of gan thin films using terahertz-time domain spectroscopy. *Japanese journal of applied physics*, 44(2R):926, 2005.

- [367] TP Iglesias, G Vilao, and João Carlos R Reis. An approach to the interpretation of cole–davidson and cole–cole dielectric functions. *Journal of Applied Physics*, 122(7):074102, 2017.
- [368] Hans Petter Langtangen and Svein Linge. *Finite difference computing with PDEs: a modern software approach*. Springer, 2017.
- [369] PY Han, M Tani, M Usami, S Kono, R Kersting, and X-C Zhang. A direct comparison between terahertz time-domain spectroscopy and far-infrared fourier transform spectroscopy. *Journal of Applied Physics*, 89(4):2357–2359, 2001.
- [370] Elizabeth Berry, Roger D Boyle, Anthony J Fitzgerald, and James W Handley. Time-frequency analysis in terahertz-pulsed imaging. In *Computer Vision Beyond the Visible Spectrum*, pages 271–311. Springer, 2005.
- [371] Yuqiang Deng, Qing Sun, Feng Liu, Changlei Wang, and Qirong Xing. Terahertz time-resolved spectroscopy with wavelet-transform. In *2010 3rd International Congress on Image and Signal Processing*, volume 7, pages 3462–3464. IEEE, 2010.
- [372] Dennis Gabor. Theory of communication. part 1: The analysis of information. *Journal of the Institution of Electrical Engineers-part III: radio and communication engineering*, 93(26):429–441, 1946.
- [373] F. Hlawatsch and François Auger. *Time-frequency analysis : concepts and methods*. Digital signal and image processing series. ISTE, 2008.
- [374] Pauli Virtanen, Ralf Gommers, Travis E Oliphant, Matt Haberland, Tyler Reddy, David Cournapeau, Evgeni Burovski, Pearu Peterson, Warren Weckesser, Jonathan Bright, et al. Scipy 1.0: fundamental algorithms for scientific computing in python. *Nature methods*, 17(3):261–272, 2020.

# Appendices

# Appendix A

## Numerically Solving the Diffusion Equation

### A.1 Introduction

Here we aim to present the numerical method that was used to solve the 1-D diffusion equation in this thesis. The method follows Ref. [368] closely. The diffusion equation reads

$$\frac{\partial n(x, t)}{\partial t} = D \frac{\partial^2 n(x, t)}{\partial x^2} + G(x, t), \quad (\text{A.1})$$

where  $n(x, t)$  is the carrier density distribution (conventionally in units of  $\text{cm}^{-3}$ ),  $x$  is the spatial coordinate,  $t$  is time,  $D$  is the diffusion coefficient (conventionally in units of  $\text{cm}^2/\text{s}$ ), and  $G(x, t)$  is a source term that describes the onset of carriers induced by an ultrafast excitation pulse.  $G(x, t)$  can be simply described by the product of a time-dependent Gaussian function and a spatial exponential decay of the form

$$G(x, t) = A e^{-(t-t_0)^2/w^2} e^{-\alpha x}, \quad (\text{A.2})$$

where  $A$  is the amplitude,  $t_0$  is the moment of excitation,  $w$  characterizes the width of the Gaussian, and  $\alpha$  is the absorption coefficient of the material at the photoexcitation wavelength [162]. The aim, from a THz spectroscopy perspective, is to determine the spatial and temporal evolution of  $n$ , so that the photoconducting film thickness can be estimated.

## A.2 Discretization

The first step in the discretization procedure is to replace the domain  $[0, L] \times [0, T]$  by a set of mesh points. The discretized coordinates will be denoted

$$x_i = i\Delta x, \quad i = 0, 1, 2, \dots, N_x, \quad (\text{A.3})$$

and

$$t_m = m\Delta t, \quad m = 0, 1, 2, \dots, N_t. \quad (\text{A.4})$$

To simplify the notation considerably, we will denote  $n(x_i, t_m) = n_i^m$ . Equation (A.1) is valid for all mesh points, so that

$$\frac{\partial n_i^m}{\partial t} = D \frac{\partial^2 n_i^m}{\partial x^2} + G(x_i, t_m). \quad (\text{A.5})$$

The time-domain is solved by the forward difference approximation, which results in the substitution

$$\frac{\partial n_i^m}{\partial t} \rightarrow \frac{n_i^{m+1} - n_i^m}{\Delta t}. \quad (\text{A.6})$$

A common discretization of the second derivative follows the centre point scheme where [\[368\]](#)

$$\frac{\partial^2 n_i^m}{\partial x^2} \rightarrow \frac{n_i^{m+1} - 2n_i^m + n_i^{m-1}}{(\Delta x)^2}. \quad (\text{A.7})$$

Substituting these identities into Eq. (A.5) gives

$$\frac{n_i^{m+1} - n_i^m}{\Delta t} = D \frac{n_i^{m+1} - 2n_i^m + n_i^{m-1}}{(\Delta x)^2} + G_i^m, \quad (\text{A.8})$$

which, when rearranged for  $n_i^{m+1}$  gives

$$n_i^{m+1} = n_i^m + D \frac{\Delta t}{(\Delta x)^2} (n_{i+1}^m - 2n_i^m + n_{i-1}^m) + \Delta t G_i^m. \quad (\text{A.9})$$

We now have a recursive rule for evolving from  $n_i^m$  to  $n_i^{m+1}$ . The coefficient  $D \frac{\Delta t}{(\Delta x)^2}$  is referred to as the Mesh Fourier Number, and must be kept above 1/2 in order to guarantee meaningful results [\[368\]](#). This update procedure is illustrated in Fig. A.1.

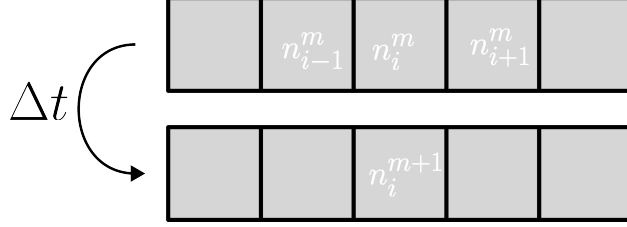


Figure A.1: Schematic of the update equation (Eq. (A.9)) acting on the discretized domain.

### A.2.1 Boundary Conditions

Thus far we have neglected the boundaries in the discretization of the diffusion equation. Since the boundaries present a discontinuity of the discretization, the update equation at the spatial endpoints must be handled in a slightly different way. The Neumann boundary condition stipulates that

$$\left. \frac{\partial n(x, t)}{\partial x} \right|_{x=\text{boundary}} = 0, \quad (\text{A.10})$$

which leads to perfect reflection of the carrier density at the boundaries. In situations where surface recombination plays a significant role in the carrier dynamics, it is common to use the boundary condition

$$\left. \frac{\partial n(x, t)}{\partial x} \right|_{x=\text{boundary}} = -\frac{S_0}{D^*} n(x = \text{boundary}, t). \quad (\text{A.11})$$

The approach we will take is to introduce a so-called ghost point to our discretized domain. On the left hand side ( $x=0$ ), we will add the ghost point  $n_{-1}^m$ , and on the right ( $x = N_x$ ) we will add  $n_{N_x+1}^m$ . In the following sections we will evaluate the Neumann and surface recombination conditions separately.

### A.3 Neumann Boundary Condition

For the Neumann boundary condition we make the approximation

$$\left. \frac{\partial n(x, t)}{\partial x} \right|_{x=\text{boundary}} \approx \frac{n_{\text{boundary}-1}^m - n_{\text{boundary}+1}^m}{2\Delta x} = 0. \quad (\text{A.12})$$

For the left and right boundaries we can solve for the ghost points. On the left hand side ( $x = 0$ ) we get

$$n_{-1}^m = n_1^m \quad (\text{A.13})$$

and on the right hand side ( $x = N_x \Delta x$ ) we find

$$n_{N_x+1}^m = n_{N_x-1}^m. \quad (\text{A.14})$$

Equation (A.9) can then be used to solve for the update equation of the left boundary ( $i = 0$ ). Starting with the definition

$$n_0^{m+1} = n_0^m + D \frac{\Delta t}{(\Delta x)^2} (n_{+1}^m - 2n_0^m + n_{-1}^m) + \Delta t G_0^m, \quad (\text{A.15})$$

we can substitute  $n_{-1}^m$  with Eq. (A.13), giving us the left boundary update equation

$$n_0^{m+1} = n_0^m + 2 \frac{D \Delta t}{(\Delta x)^2} [n_1^m - n_0^m] + \Delta t G_0^m. \quad (\text{A.16})$$

Following the same logic as above, one can easily show that the right hand boundary has the form

$$n_{N_x}^{m+1} = n_{N_x}^m + 2 \frac{D \Delta t}{(\Delta x)^2} [n_{N_x-1}^m - n_{N_x}^m] + \Delta t G_{N_x}^m. \quad (\text{A.17})$$

A full python implementation of this is given below in Listing A.1, where  $n$  is initialized as a unit height spike at  $x = 0$ .

```

import numpy as np
import matplotlib.pyplot as plt
# Initializing the arrays
x = np.linspace(0,1,100)
times = np.linspace(0,10,100)
dt = np.abs(times[1]-times[0])
dx = np.abs(x[1]-x[0])
ninit = np.zeros(len(x))
ninit[0] = 1
ninit[-1] = 1
D = 0.0001
# Defining the update function
def time_update(x,times,n,D):
    dt = np.abs(times[1]-times[0])
    dx = np.abs(x[1]-x[0])
    newn = np.zeros(len(n))
    print('Mesh Fourier Number: %0.3f' %(D*dt/dx/dx))
    for m,tm in enumerate(times):
        if tm == times[0]: #work with initial n array
            for i, xi in enumerate(x):
                if xi == x[0]: # Left Boundary
                    newn[i] = n[0] + 2*D*dt*(n[1] - n[0])/dx/dx
                elif xi == x[-1]: # Right Boundary
                    newn[i] = n[i] + 2*D*dt*(n[i-1] - n[i])/dx/dx
                else: # Every other point
                    newn[i] = n[i] + 2*D*dt*(n[i+1] - 2*n[i] + n[i-1])/dx/dx
            else: # work with n array
                for i,xi in enumerate(x):
                    if xi == x[0]: # Left Boundary
                        newn[i] = newn[0] + 2*D*dt*(newn[1] - newn[0])/dx/dx
                    elif xi == x[-1]: # Right Boundary
                        newn[i] = newn[i] + 2*D*dt*(newn[i-1] - newn[i])/dx/dx
                    else: # Every other point
                        newn[i] = newn[i] + 2*D*dt*(newn[i+1]-2*newn[i] + newn[i-1])/dx/dx
        return newn
# Plotting the results
newn = time_update(x,times,ninit,D)
plt.figure()
plt.scatter(x,ninit)
plt.plot(x,newn,'r-')
plt.show()

```

Listing A.1: Python 3.9 solution of the diffusion equation with Neumann boundary conditions.

## A.4 Surface Recombination Boundary Condition

The boundary condition for surface recombination can be found by a similar approach as above. To begin, we note that

$$\left. \frac{\partial n(x, t)}{\partial x} \right|_{x=\text{boundary}} \approx \frac{n_{\text{boundary}-1}^m - n_{\text{boundary}+1}^m}{2\Delta x} = -\frac{S_0}{D^*} n_{\text{boundary}}^m. \quad (\text{A.18})$$

And following the same logic as above, it is easy to show that the left side ghost point is given by

$$n_{-1}^m = n_1^m - 2\frac{S_0\Delta x}{D} n_0^m. \quad (\text{A.19})$$

The ghost point on the right hand side is subtly different because surface recombination reduces carriers at the interface. This makes the gradient of the carrier distribution point downwards, changing the sign of the boundary condition. This gives the relation

$$n_{N_x+1}^m = n_{N_x-1}^m - 2\frac{S_0\Delta x}{D} n_{N_x}^m. \quad (\text{A.20})$$

From Eqs. (A.19) and (A.20), the new update equations can be found. The right hand side update equation is given by

$$n_0^{m+1} = \left[ 1 - \frac{2S_0}{\Delta x} \right] n_0^m + \frac{2D\Delta t}{(\Delta x)^2} [n_1^m - n_0^m] + \Delta t G_0^m, \quad (\text{A.21})$$

and the left hand side is given by

$$n_{N_x}^{m+1} = \left[ 1 - \frac{2S_0}{\Delta x} \right] n_{N_x}^m + \frac{2D\Delta t}{(\Delta x)^2} [n_{N_x-1}^m - n_{N_x}^m] + \Delta t G_{N_x}^m. \quad (\text{A.22})$$

A working Python 3.9 example of this for is provided in Listing A.2.

```

import numpy as np
import matplotlib.pyplot as plt
# Initializing the arrays
x = np.linspace(0,1,100)
times = np.linspace(0,10,100)
dt = np.abs(times[1]-times[0])
dx = np.abs(x[1]-x[0])
ninit = np.zeros(len(x))
ninit[0] = 1
ninit[-1] = 1
D = 0.0001
S0 = 0.0002
# Defining the update function
def time_update(x,times,n,D,S0):
    dt = np.abs(times[1]-times[0])
    dx = np.abs(x[1]-x[0])
    newn = np.zeros(len(n))
    print('Mesh Fourier Number: %0.3f' %(D*dt/dx/dx))
    for m,tm in enumerate(times):
        if tm == times[0]: #work with initial n array
            for i, xi in enumerate(x):
                if xi == x[0]: # Left Boundary
                    newn[i] = n[0]*(1 - 2*S0/dx) + 2*D*dt*(n[1] - n[0])/dx/dx
                elif xi == x[-1]: # Right Boundary
                    newn[i] = n[i]*(1 - 2*S0/dx) + 2*D*dt*(n[i-1] - n[i])/dx/dx
                else: # Every other point
                    newn[i] = n[i] + 2*D*dt*(n[i+1] - 2*n[i] + n[i-1])/dx/dx
            else: # work with n array
                for i,xi in enumerate(x):
                    if xi == x[0]: # Left Boundary
                        newn[i] = newn[0]*(1 - 2*S0/dx) + 2*D*dt*(newn[1]-newn[0])/dx/dx
                    elif xi == x[-1]: # Right Boundary
                        newn[i] = newn[i]*(1 - 2*S0/dx) + 2*D*dt*(newn[i-1] - newn[i])/dx/dx
                    else: # Every other point
                        newn[i] = newn[i] + 2*D*dt*(newn[i+1]-2*newn[i]+newn[i-1])/dx/dx
    return newn
# Plotting the results
newn = time_update(x,times,ninit,D,S0)
plt.figure()
plt.scatter(x,ninit)
plt.plot(x,newn,'r-')
plt.show()

```

Listing A.2: Python 3.9 solution of diffusion equation with surface recombination boundary conditions.

# Appendix B

## Lock-In Detection and the 2-Chop Technique

### B.1 Introduction

Lock-In amplifiers are a vital electronic measurement tool found in virtually all physics laboratories throughout the world. Their strength comes from allowing measurements of extremely small voltages, and they do so by using phase-sensitive detection. Time-Resolved Terahertz Spectroscopy (TRTS) is a spectroscopy technique that allows researchers to measure frequency dependent conductivity in a large variety of materials, and requires the measurement of very small voltage differences.

Here, we will introduce the reader to the basics of phase-sensitive detection and how it is used to measure the amplitude of a simple sine-wave input. From this we construct a procedure that allows us to explore the phase sensitive detection of a general input signal. With this generalization we then calculate the calibration factors for a Dirac comb input signal, which is often employed in TRTS measurements \*

Afterwards, we demonstrate that a calibration factor must be considered when attempting to compare a differential voltage measurement ( $V_1 - V_2$ ) to a sum voltage measurement ( $V_1 + V_2$ ). This factor is indeed dependent on the Fourier coefficients of the Dirac comb

---

\*We choose to work with Dirac combs, because a transient current observed by a photodiode lasts on the order of microseconds. Since a Lock-In amplifier samples the input signal with nearly the same resolution, the input signal effectively appears as a Dirac comb to good approximation.

function, but we show (for the first time) that the relative phase between an input and reference signal provides a significant contribution to this calibration factor that has thus far been neglected.

Finally, we demonstrate that there is no reason to use two Lock-In amplifiers when performing a differential transmission measurement. A single Lock-In amplifier can be used to simultaneously measure a sum and difference measurement by correctly phasing the x component of a Lock-In amplifier. We show that if the x-component is phased correctly to read a sum voltage measurement, then the y-component will naturally measure a difference voltage.

## B.2 Lock-In amplifier theory

### B.2.1 Simple Example

Phase-sensitive detection (PSD) allows experimentalists to distinguish small voltages signal from noise. It does so by multiplying a known reference signal (usually a sine or cosine wave) and the signal of interest. In the examples that follow, the work flow of a Lock-In amplifier will be approximated by a three-step process:

Input  $\rightarrow$  Multiply  $\rightarrow$  Filter.

To begin, let us consider a reference signal  $V_{ref}(t)$  and an input signal  $V_{in}(t)$ . For simplicity they will both be sine-waves defined as

$$V_{in}(t) = V_{in} \sin(\omega_{in}t + \theta_{in}) \tag{B.1}$$

and

$$V_{ref}(t) = V_{ref} \sin(\omega_{ref}t + \theta_{ref}). \tag{B.2}$$

where,  $\theta_{ref}$  and  $\theta_{in}$  are phases of the reference signal and input signal respectively. Multiplying Eq.(B.1) by Eq.(B.2), and using elementary trigonometric identities we arrive at the

signal  $V_m$ ,

$$V_m(t) = \frac{V_{in}V_{ref}}{2} \left[ \cos \left( \theta_{in} - \theta_{ref} + (\omega_{in} - \omega_{ref})t \right) - \cos \left( \theta_{in} + \theta_{ref} + (\omega_{in} + \omega_{ref})t \right) \right]. \quad (\text{B.3})$$

Equation (B.3) is a function with a term containing a sum of frequencies  $(\omega_{in} + \omega_{ref})$ , and another term containing a difference of frequencies  $(\omega_{in} - \omega_{ref})$ . Thus, when the input frequency is matched to the reference frequency, we attain

$$V_m(t) = \frac{V_{in}V_{ref}}{2} \left[ \cos \left( \theta_{in} - \theta_{ref} \right) - \cos \left( \theta_{in} + \theta_{ref} + 2\omega_{ref}t \right) \right]. \quad (\text{B.4})$$

In Eq.(B.4), there is a term that oscillates at twice the reference frequency, and one that does not oscillate at all (often referred to as the DC term). Therefore, by applying a low-pass filter, one can extinguish the frequency doubled term, and measure a constant voltage that is proportional to the input voltage ( $V_{psd}$ )

$$V_{psd} = \frac{V_{ref}V_{in}}{2} \cos \left( \theta_{in} - \theta_{ref} \right). \quad (\text{B.5})$$

Let us now draw our attention to the relative phase  $\theta_{in} - \theta_{ref}$ . A Lock-In amplifier has the ability to adjust the relative phase between the input signal and the reference signal. In the example so far, the user would ideally like to shift the reference phase to match the input phase ( $\theta_{in} = \theta_{ref}$ ), so as to maximize  $V_{psd}$ , and yield a true reading of  $V_{in}$ . Normally, the factor of  $V_{ref}/2$  is removed within the Lock-In amplifier, and so the output voltage  $V_{out}$  will be given by

$$V_{out} = V_{in}. \quad (\text{B.6})$$

From this elementary example we have shown that a Lock-In amplifier transforms the amplitude of an AC signal into a DC voltage. In the next section, we consider a general signal, so that this method can be applied to any input signal a user may want.

## B.2.2 General Input Signal

According to Fourier's theorem, a signal can be decomposed into an infinite sum of sine-waves, each term having their own amplitude  $a_n$  and phase  $\theta_n$ . Therefore, an arbitrary input signal can be written in the form

$$V_{in}(t) = V_{in} \sum_{n=0}^{\infty} a_n \sin \left( (2n+1)\omega_{in}t + \theta_n \right). \quad (\text{B.7})$$

Now  $V_{in}(t)$  can be multiplied by the reference signal, which yields

$$V_m(t) = V_{in}V_{ref} \sum_{n=0}^{\infty} a_n \sin \left( (2n+1)\omega_{in}t + \theta_n \right) \times \sin \left( \omega_{ref}t + \theta_{ref} \right). \quad (\text{B.8})$$

Using the identity

$$\sin u \sin v = \frac{1}{2} \left[ \cos(u-v) - \cos(u+v) \right] \quad (\text{B.9})$$

on each of the terms in the above series, Eq.(B.8) can be written as

$$V_m = \frac{V_{in}V_{ref}}{2} \sum_{n=0}^{\infty} a_n \left[ \cos \left( (2n+1)\omega_{in}t + \theta_n - \omega_{ref}t - \theta_{ref} \right) - \cos \left( (2n+1)\omega_{in}t + \theta_n + \omega_{ref}t + \theta_{ref} \right) \right]. \quad (\text{B.10})$$

Let us now assume, as in Section B.2, that the relative phase is matched so that  $\theta_{ref} = \theta_n$ . We further assume that the reference sine wave is generated such that  $\omega_{ref} = \omega_{in}$ , so that we may rewrite Eq.(B.10) as

$$V_m = \frac{V_{in}V_{ref}}{2} \sum_{n=0}^{\infty} a_n \left[ \cos \left( 2n\omega_{ref}t \right) - \cos \left( (2n+2)\omega_{ref}t + 2\theta_{ref} \right) \right]. \quad (\text{B.11})$$

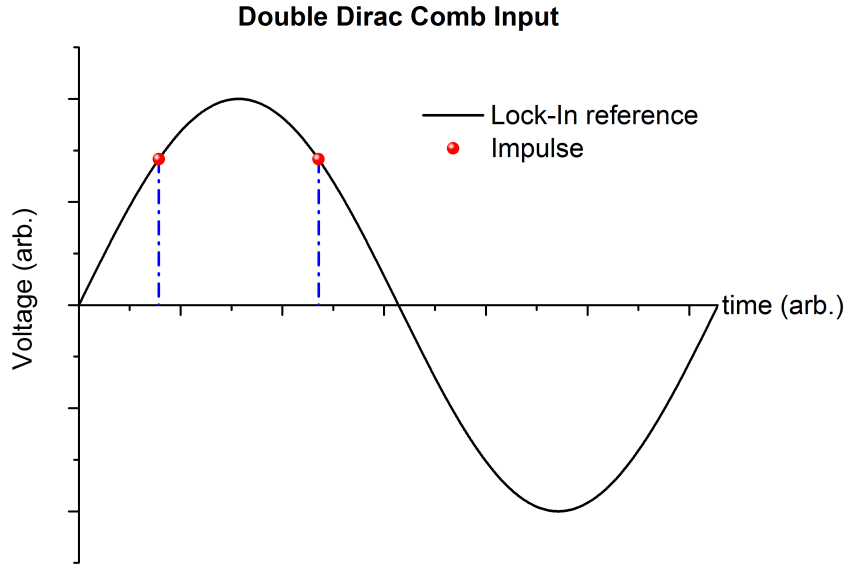


Figure B.1: The reference and Dirac Comb input given by Eq.(B.17) are shown.

Passing  $V_m$  through the low pass filter eliminates all terms of higher order than  $n = 0$ , and so the phase-sensitive output voltage is

$$V_{psd} = \frac{V_{in} V_{ref}}{2} a_0. \quad (\text{B.12})$$

Since the factor  $V_{ref}/2$  is solely due to the multiplication of the internal reference and the input signal, this factor is normally removed within the Lock-In amplifier. Consult the operation manual of your Lock-In amplifier. Thus, for a general input signal, with matched reference phases, the output of a Lock-In amplifier will read

$$V_{out} = V_{in} a_0. \quad (\text{B.13})$$

In the following sections, we will be using  $a_0$  from the Fourier series of various Dirac combs, and we will see that other coefficients emerge when various phases are considered.

### B.2.3 Measuring $V_1 + V_2$

In this section, we will discuss the situation where the input signal is comprised of two Dirac combs. These combs are separated from each other by a phase of  $\pi/2$  and they repeat with a period equal to the period of the reference frequency ( $\omega_{ref} = 2\pi f_{ref}$ ). See Fig. B.1 for a visual representation. The Fourier series of a Dirac comb is

$$III(t) = \frac{1}{T} \sum_{n=-\infty}^{n=\infty} e^{i\frac{2\pi n}{T}t}, \quad (\text{B.14})$$

where  $T = 1/f_{ref}$  is the time between Dirac deltas. For convenience, let us write Eq.(B.14) as a completely real function. We begin by noting that  $e^{ix} = \cos(x) + i\sin(x)$ . Since  $\sin(-x) = -\sin(x)$ , the imaginary parts cancel term-by-term under the sum. Furthermore, since  $\cos(-x) = \cos(x)$ , the Fourier series acquires a factor of 2, and thus we get

$$III(t) = \frac{2}{T} \sum_{n=0}^{n=\infty} \cos\left(\frac{2\pi n}{T}t\right). \quad (\text{B.15})$$

We may now use this to write down the Fourier series of the signal in Fig. B.1 as

$$\begin{aligned} V_{in}(t) = \frac{2}{T} \sum_{n=0}^{\infty} V_1 \cos(n\omega_{in}t + \theta_n) \\ + V_2 \cos(n\omega_{in}t + \theta_n - \pi/2) \end{aligned} \quad (\text{B.16})$$

where,  $\omega_{in} = 2\pi/T$ ,  $\theta_n$  is the phase shift between time  $t = 0$  and the first Dirac comb, and  $V_1$  and  $V_2$  are the amplitudes of the respective Dirac combs. Considering that  $\cos(x - \pi/2) = \sin(x)$ , we arrive at the final form of the Fourier series for an input of a double Dirac comb

$$V_{in}(t) = 2\frac{1}{T} \sum_{n=0}^{\infty} V_1 \cos(n\omega_{in}t + \theta_n) + V_2 \sin(n\omega_{in}t + \theta_n). \quad (\text{B.17})$$

Multiplying by the internal reference signal

$$V_{ref}(t) = V_{ref} \sin\left(\omega_{ref}t + \theta_{ref}\right), \quad (\text{B.18})$$

we now get

$$V_m = 2 \frac{V_{ref}}{T} \sum_{n=0}^{\infty} V_1 \left( \cos(n\omega_{in}t + \theta_n) + V_2 \sin(n\omega_{in}t + \theta_n) \right) \times \sin(\omega_{ref}t + \theta_{ref}), \quad (\text{B.19})$$

which can be rewritten as

$$V_m = 2 \frac{V_{ref}}{2T} \sum_{n=0}^{\infty} V_1 \left[ \sin \left( (n+1)\omega_{in}t + \theta_n + \theta_{ref} \right) - \sin \left( (n-1)\omega_{in}t + \theta_n - \theta_{ref} \right) \right] + V_2 \left[ \cos \left( (n-1)\omega_{in}t + \theta_n - \theta_{ref} \right) - \cos \left( (n+1)\omega_{in}t + \theta_n + \theta_{ref} \right) \right]. \quad (\text{B.20})$$

Differentiating Eq.(B.20) respect to the relative phase ( $\theta = \theta_n - \theta_{ref}$ ), it is easy to show that the phase which yields the maximum  $V_m$  is given by

$$\theta_n - \theta_{ref} = -\pi/4 + n\pi. \quad (\text{B.21})$$

Therefore, when one adjusts the relative phase to achieve a maximum signal with this input, Eq.(B.20) becomes

$$V_m = \frac{2V_1}{T} \frac{V_{ref}}{2} \left[ -\sin(-\pi/4) + \sin(\omega_{in}t - \pi/4) - \dots \right] + \frac{2V_2}{T} \frac{V_{ref}}{2} \left[ \cos(-\pi/4) + \cos(-\omega_{in}t - \pi/4) - \dots \right]. \quad (\text{B.22})$$

Filtering out all but the DC component, we arrive at the output of the phase sensitive detector:

$$V_{psd} = \frac{2}{\sqrt{2}T} \left( V_1 + V_2 \right) \frac{V_{ref}}{2}. \quad (\text{B.23})$$

Since the Lock-in amplifier internally handles the  $V_{ref}/2$  term, we arrive at the output voltage

$$V_{out} = \frac{2}{T} (V_1 + V_2) \frac{1}{\sqrt{2}} \quad (\text{B.24})$$

The leftmost  $2/T$  is the Fourier coefficient of the Dirac comb, and is the same for all harmonics. The Fourier coefficient of the Dirac comb is very important for this signal input, because it is dependent on the period of the comb. Since optical choppers can alter the period between Dirac comb elements, these Fourier coefficients are crucial to consider when calculating quantities from measured data. Up until now, the rightmost factor of  $1/\sqrt{2}$  has been referred to as a calibration factor, and is usually measured directly. This factor originates from the relative phase of the Dirac comb input, and not from the amplitude of the Fourier coefficient. The results of this section will show up again in later sections, but for now let's explore how a Lock-In amplifier can be used to measure a difference of voltages.

### B.2.4 Measuring $V_1 - V_2$

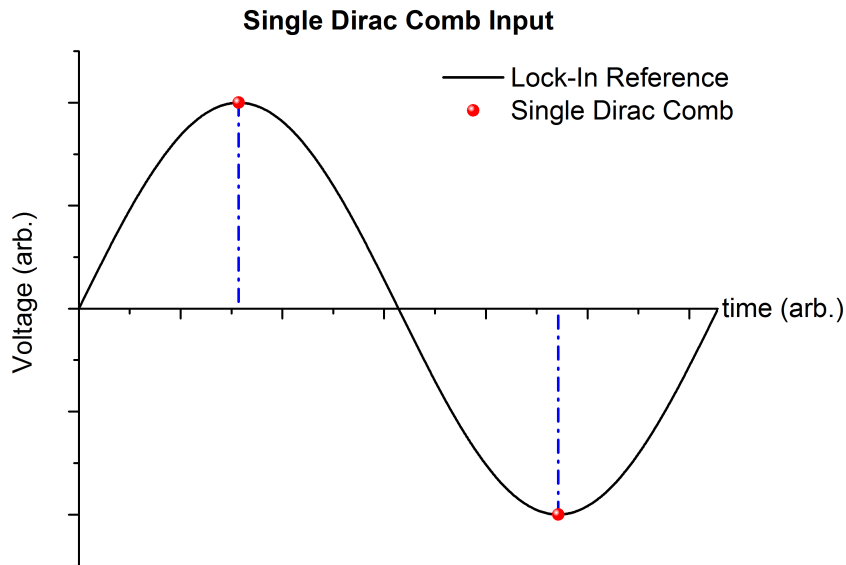


Figure B.2: Dirac comb input in  $V_1 - V_2$  mode.

We now shift our attention to a different situation involving two Dirac comb functions.

This time the combs are separated by a phase of  $\pi$ , and they repeat with a period equal to the period of the reference frequency, as shown in Fig. B.2. Under these considerations, the Fourier series of the input signal is simply

$$V_{in}(t) = \frac{2}{T} \sum_{n=0}^{\infty} V_1 \cos(n\omega_{int}t + \theta_n) + V_2 \cos(n\omega_{int}t + \theta_n - \pi). \quad (\text{B.25})$$

Since  $\cos(x - \pi) = -\cos(x)$ , we may write the input signal as

$$V_{in}(t) = \frac{2}{T} \sum_{n=0}^{\infty} V_1 \cos(n\omega_{int}t + \theta_n) - V_2 \cos(n\omega_{int}t + \theta_n). \quad (\text{B.26})$$

Again, multiplying by the reference signal given in Eq.(B.18), and using the identity

$$\cos(u) \sin(v) = \frac{1}{2} [\sin(u + v) - \sin(u - v)] \quad (\text{B.27})$$

we get

$$\begin{aligned} V_m = 2 \frac{V_{ref}}{2T} \sum_{n=0}^{\infty} V_1 & \left[ \sin\left((n+1)\omega_{int}t + \theta_n + \theta_{ref}\right) \right. \\ & \left. - \sin\left((n-1)\omega_{int}t + \theta_n - \theta_{ref}\right) \right] \\ & - V_2 \left[ \sin\left((n+1)\omega_{int}t + \theta_n + \theta_{ref}\right) \right. \\ & \left. - \sin\left((n-1)\omega_{int}t + \theta_n - \theta_{ref}\right) \right]. \end{aligned} \quad (\text{B.28})$$

From this, it is clear that when  $V_1 = V_2$ , the output voltage of the Lock-In amplifier is 0. Differentiating with respect to the relative phase, it is easy to show that the maximum signal occurs at  $\theta_n - \theta_{ref} = -\pi/2 + n\pi$ . Isolating the DC term with a low pass filter, and using  $\theta_n - \theta_{ref} = -\pi/2$  yields the output of the phase sensitive detector

$$V_{psd} = \frac{2}{T} (V_1 - V_2) \frac{V_{ref}}{2}. \quad (\text{B.29})$$

Within a Lock-In amplifier, the coefficient of  $V_{ref}/2$  is accounted for, and the output voltage

from a Lock-In amplifier is thus

$$V_{out} = \frac{2}{T} (V_1 - V_2). \quad (\text{B.30})$$

With the above result, and the result from Section B.2.3, we will now demonstrate how to implement this information with a sample calculation. Afterward, we will demonstrate the correctness of this calculation by checking the results experimentally.

## B.2.5 Using Values from Two Different Lock-In Amplifiers

It is common to measure the photoconductivity ( $\sigma(t)$ ) through the relation

$$\sigma(t) \propto -\frac{\mathcal{E}_{ref} - \mathcal{E}_{pump}}{\mathcal{E}_{ref}}, \quad (\text{B.31})$$

where  $\mathcal{E}_{ref}$  is the amplitude of the THz pulse transmitted through a sample in equilibrium, and  $\mathcal{E}_{pump}$  is the amplitude of the THz pulse transmitted through the photoexcited sample. Using the results from Section B.2.4, we can measure voltage differences. The fact that these voltages are proportional to a THz electric field is explained in Section 4.2, and here we simply note that the output of a Lock-In amplifier will read

$$V_{diff} = \frac{2}{T_{diff}} (\mathcal{E}_{ref} - \mathcal{E}_{pump}), \quad (\text{B.32})$$

where,  $T_{diff} = 1/f_{diff}$  is the period between successive Dirac combs in the difference Lock-In amplifier.

It is common to block the photoexcitation line, and measure the reference signal using the method in Section B.2.3 as

$$V_{sum} = \frac{2}{T_{sum}} (\mathcal{E}_{ref} + \mathcal{E}_{ref}) \frac{1}{\sqrt{2}}, \quad (\text{B.33})$$

where,  $T_{sum}$  is the period between successive Dirac combs in the summing Lock-In amplifier. At this point, it is very important to note that the period of the summing and difference measurements are not likely to be the same. Therefore, if one rearranges Eq. (B.32) and

Eq. (B.33), one can rewrite Eq. (B.31) as

$$\frac{\mathcal{E}_{ref} - \mathcal{E}_{pump}}{\mathcal{E}_{ref}} = \sqrt{2} \frac{T_{diff}}{T_{sum}} \frac{V_{Diff}}{V_{sum}}. \quad (\text{B.34})$$

In our lab, the difference period is exactly half of the sum period, and so Eq. (B.31) can be simplified as

$$\frac{\mathcal{E}_{ref} - \mathcal{E}_{pump}}{\mathcal{E}_{ref}} = \frac{1}{\sqrt{2}} \frac{V_{Diff}}{V_{sum}}. \quad (\text{B.35})$$

In this calculation, have accounted for all of the pre-factors that come from Fourier coefficients and the phase of the incoming signals.

# Appendix C

## Generalized Drude Model

The Generalized Drude model is an extension of the Drude model that accommodates a non-uniform distribution of scattering rates. The conductivity is given by

$$\tilde{\sigma}(\omega) = \frac{ne^2\tau}{m^*} \left[ \frac{1}{1 + (-i\omega)^{1-\alpha}} \right]^\beta, \quad (\text{C.1})$$

where  $\alpha$  and  $\beta$  are phenomenological fit parameters that describe the distribution of scattering rates. To make the distribution of scattering rates more clear, consider the conductivity given by the Drude model (Eq. (2.47)). One may write the relationship between the real and imaginary parts as

$$\sigma_2(\omega) = \omega\tau\sigma_1(\omega). \quad (\text{C.2})$$

Therefore, on a graph of  $\sigma_2/\omega$  vs.  $\sigma_1$ , the slope of the line is the scattering rate  $\tau$ . We now have a justification for the relation

$$\tau(\omega) = \frac{d\sigma_2(\omega)/\omega}{d\sigma_1(\omega)} = \left[ \frac{d}{d\omega} \left( \frac{\sigma_2(\omega)}{\omega} \right) \right] \left[ \frac{d}{d\omega} \sigma_1(\omega) \right]^{-1} \quad (\text{C.3})$$

which provides instructions on how to compute the scattering rate distribution for any complex conductivity [367].

# Appendix D

## A New Approach to Time-Resolved Spectroscopy

### D.1 Introduction

The foundations of TRTS were laid by Beard and cohorts, where they explored the photoconductivity dynamics of the prototypical semiconductor GaAs [87]. In this work they lay out the procedure of extracting photoexcited carrier dynamics, and raise an interesting subtlety about how pump-probe spectroscopy cannot be interpreted in the same way as time-domain spectroscopy. The issue is that photoexcitation rapidly transitions a semiconductor into a metallic state.

When a material is transitioning from a semiconductor to a metal, it can occur on subpicosecond timescales. Therefore, when a THz pulse is incident at just the right time, half the THz pulse will experience a semiconductor, and the other half will be attenuated by a metal. It is known that THz pulses are up-chirped by the normal dispersion of ZnTe, and so the low-frequencies generally exit the source before the high frequencies. Therefore, if the THz pulse is chirped, and it is “clipped” by the excitation, the higher frequencies are disproportionately attenuated by the excitation. Ultimately this brings the validity of Fourier transformation into question, and led to the wide-spread adoption of a projected pump-probe time domain  $t-t''$  [87]. Experimentally it has been verified that there is nothing intrinsically wrong with working in the projected domain, however, to-date, no one has mentioned how

time-frequency analysis can be used to bypass this issue altogether.

## D.2 Time-Frequency Analysis Fundamentals

Time-frequency analysis is an approach to understanding signals that is beginning to see attention in THz time-domain spectroscopy and imaging communities [369–371], yet to the best of our knowledge, no work has been done to connect this to optical-pump terahertz-probe spectroscopy. Time-frequency analysis began in 1946 when Dennis Gabor published a 3-part landmark work titled “Theory of Communication” which used the mathematics of Quantum mechanics to rigorously explore the concept of a transient frequency. The key outcome of Gabor’s analysis is the Gabor transform [372]. The Gabor transform is similar to a Fourier transform, in that it provides access to the frequencies that compose a signal. However, a well-known problem of the Fourier transform is that one loses all sense of causality, since it requires each sine/cosine wave to exist for all time (both before and after the physics being described). To this end, the Gabor transform retains the causal nature of a signal by decomposing the time-domain into orthogonal time and frequency domains.

As with many things in life, there is no free lunch. The cost of gaining frequency resolution, is a necessary sacrifice of time resolution. This trade-off between time and frequency resolution is encapsulated by an uncertainty principle  $\Delta t \Delta f \geq 1/2$ , which is a direct result of using the mathematics of quantum mechanics to describe an arbitrary signal. Fig. D.1 demonstrates this principle, where the time axis is divided into regions of  $\Delta t$ , and the frequency domain is divided into regions of  $\Delta f$ . Each rectangle in Fig. D.1 is referred to as a time-frequency atom\*, having an area that satisfies  $\Delta f \Delta t \geq 1/2$ . Orthogonal to the time-frequency plane is the amplitude of each atom. To understand what this surface is, Gabor used the analogy of a bank of reeds. As a sound wave flows over the bank of reeds, they individually resonate at their resonance frequency for a short period of time. The amplitude of the reed oscillation is then the amplitude we show in Fig. D.1.

The decomposition of a real function  $x(t)$  into its constituent atoms can generally be

---

\*Gabor referred to them as logons, intending to describe the quantum of information.

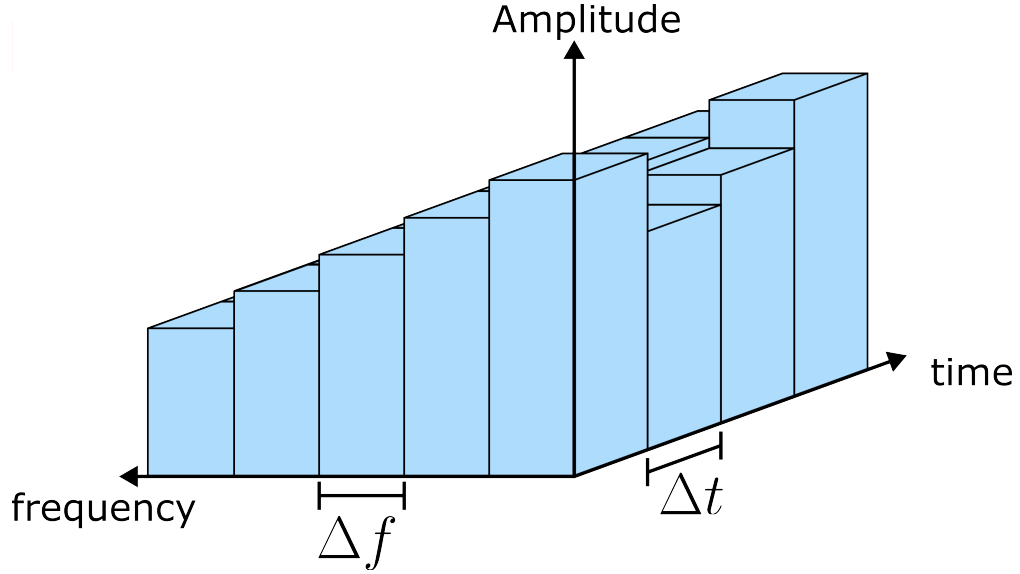


Figure D.1: Time-frequency space corresponding to the bank-of-reeds analogy.

expressed by the integral transform [373]

$$G_x(t, f) = \int_{-\infty}^{\infty} x(t')g(t - t')e^{i2\pi ft'} dt' \quad (\text{D.1})$$

where  $g(t)$  is referred to as the window function. This integral can be thought of as a convolution of  $x(t)$  with the sliding window  $g^*(t' - t)$  at a frequency defined by  $e^{i2\pi ft'}$ . Gabor showed that the window function that achieves atoms of exactly  $\Delta f \Delta t = 1/2$  is given by [372]

$$g(t - t') = e^{-\pi(t-t')^2} \quad (\text{D.2})$$

so that Eq. (D.1) becomes

$$G_x(t, f) = \int_{-\infty}^{\infty} x(t')e^{-\pi(t-t')^2} e^{i2\pi ft'} dt'. \quad (\text{D.3})$$

The Gabor transform is invertible [372], and we will use this invertibility later. The Gabor transform bears significant resemblance to the Fourier transform

$$\mathcal{F}_x(f) = \int_{-\infty}^{\infty} x(t)e^{i2\pi ft} dt, \quad (\text{D.4})$$

which leads me to believe that the Gabor transform can be used for time-resolved terahertz spectroscopy.

### D.3 Optical Constants

The Tinkham formula connects the complex, frequency-dependent transmission function to the optical conductivity spectrum at pump-probe delay time  $\Delta t_1$  and frequency  $\omega$ . We have found that it possesses the functional form

$$\tilde{t} = \frac{\tilde{\mathcal{E}}_{pump}(\omega, \Delta t_1)}{\tilde{\mathcal{E}}_{ref}(\omega, \Delta t_1)} = \frac{n_2 + 1}{n_2 + 1 + Z_o \tilde{\sigma}(\omega, \Delta t_1) d}. \quad (\text{D.5})$$

Inspired by this form, we suggest, for the first time, the following time-frequency formulation of the Tinkham equation

$$\tilde{t}(\omega, \tau) = \frac{\tilde{\mathcal{E}}_{pump}(\omega, \tau)}{\tilde{\mathcal{E}}_{ref}(\omega, \tau)} = \frac{n_2 + 1}{n_2 + 1 + Z_o \tilde{\sigma}(\omega, \tau) d}. \quad (\text{D.6})$$

The transmission function has always served as a connection between the reference signal and the signal acquired after photoexcitation (i.e.  $\tilde{\mathcal{E}}_{pump}$ ), and it is explicitly tied to the optical properties encompassed by  $\sigma$ . This forms the basis of the recipe we use in terahertz spectroscopy. First measure  $\tilde{\mathcal{E}}_{ref}$ , then  $\tilde{\mathcal{E}}_{pump}$ , and proceed to compute  $\sigma$ . Equation (D.6) provides the same recipe. First record  $\tilde{\mathcal{E}}_{ref}$ , then measure  $\tilde{\mathcal{E}}_{pump}$ , and proceed to compute  $\sigma$ .

Indeed, it is important to remember that Eq. (D.6) relates two-dimensional surfaces. At each pump-probe delay time, there is a corresponding set of frequencies upon which one can perform spectroscopy. An important consequence of this is that it does not matter if the rise dynamics occur within the THz probe pulse because the asymmetric attenuation will be handled by the early frequency bandwidth.

### D.4 Simulating $\mathcal{E}_{pump}$ with Time-Frequency Analysis

We now show that the Gabor transform can be used to accurately model a pump-probe experiment, and so we will assume some behaviours of the photoexcited medium. First, we will suppose that the recombination dynamics are sufficiently longer than the scattering

dynamics so that we may decouple the conductivity according to the following Drude model

$$\tilde{\sigma} = n(\tau) \frac{e^2 \tau_{drude}}{m^*} \frac{1}{1 - i\omega \tau_{drude}}, \quad (\text{D.7})$$

where we will assume  $m^*$  and  $e$  are 1 for simplicity. We will further assume that  $\tau_{drude} = 1/2\pi$  ps so that the Drude crossover frequency is 1 THz. Finally, assume that  $n(\tau)$  has the form

$$n(\tau) = n_{max}(1 - e^{-\tau/\tau_1})e^{-\tau/\tau_2}, \quad (\text{D.8})$$

where,  $\tau_1$  is the rise time of the charge-carrier population,  $\tau_2$  is the recombination lifetime, and  $n_{max}$  is the maximum number of carriers.

Suppose that the semiconductor was photoexcited 1.5 ps before the THz pulse arrives, and forms  $n(t)$  such that  $\tau_1 = 0.05$  ps,  $\tau_2 = 50$  ps, and  $n_{max} = 2$  arbitrary units as illustrated by the blue line in Fig. D.2. In the reference frame of the THz pulse (black line), there is a finite change in the carrier density that will alter the waveform according to Eq. (D.6). The THz reference frame is equivalent to the electro-optic sampling (EOS) time  $\tau$ .

The transient conductivity produces a 2D surface in  $\omega$  and  $\tau$ . This surface is illustrated in Fig. D.3. The real part is shown in Fig. D.3 (a) and the imaginary part is shown in Fig. D.3 (b). The real and imaginary parts evolve in the time domain following  $n(\tau)$ , and the frequency dependence is the result of the Drude spectrum.

We can now compute the time-frequency Tinkham transmission function with some further simplifying assumptions. Assuming  $n_2 = 1$ ,  $Z_0 = 1$ , and  $d = 1$ , Eq. (D.6) takes the form

$$\tilde{t}(\omega, \tau) = \frac{\tilde{\mathcal{E}}_{pump}(\omega, \tau)}{\tilde{\mathcal{E}}_{ref}(\omega, \tau)} = \frac{2}{2 + \tilde{\sigma}(\omega, \tau)}. \quad (\text{D.9})$$

The amplitude of the transmission function ( $|\tilde{t}(\omega, \tau)|$ ) is shown in Fig. D.4. The transmission function strongly decreases after photoexcitation at  $\tau = -1.5$  ps, just as one would expect from free carrier absorption. Furthermore, low-frequencies are attenuated strongest as one would expect from a Drude conductivity.

It is now possible to compute the transmitted THz electric field  $\tilde{\mathcal{E}}_{pump}$ . First, we compute  $\tilde{\mathcal{E}}_{ref}(\omega, \tau)$  using a numerical implementation of the Gabor transform [374]. This gives the

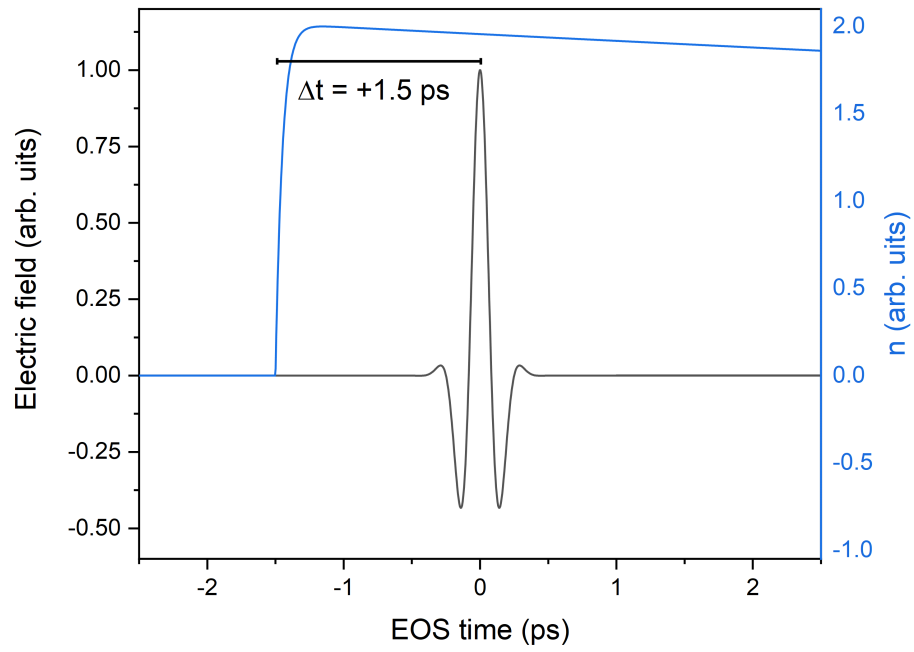


Figure D.2:  $\mathcal{E}_{ref}-n(\tau)$  relationship.

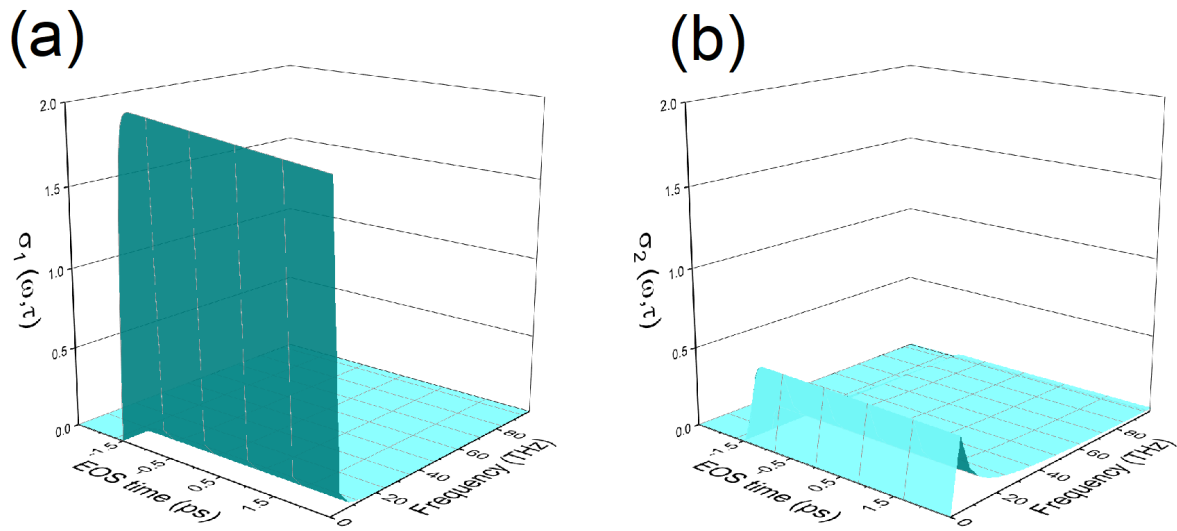


Figure D.3: Photoconductivity surface in time-frequency space. (a) Real and (b) imaginary parts of the conductivity.

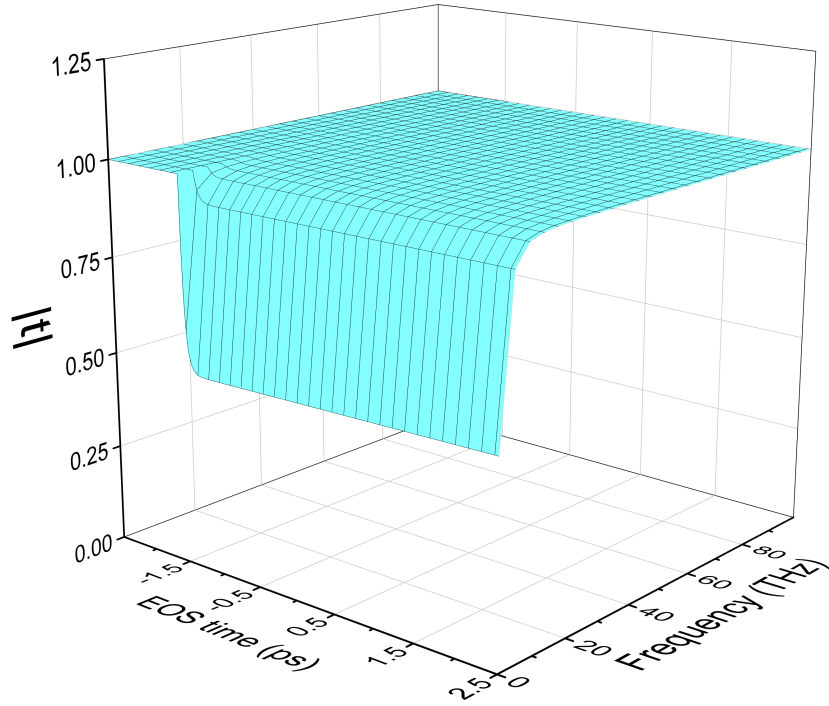


Figure D.4: Transmission function.

complex surfaces shown in Fig. D.5. Figure D.5 (a) shows the real part and Fig. D.5 (b) contains the imaginary part.

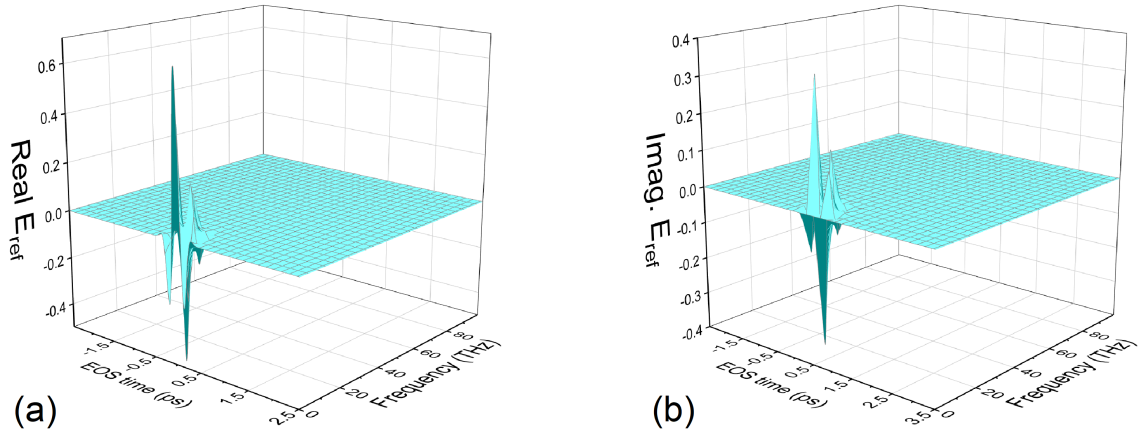


Figure D.5: Time-frequency  $\mathcal{E}_{ref}$ . (a) Real part and (b) imaginary part.

Now, multiplying  $\mathcal{E}_{ref}(\omega, \tau)$  by  $\tilde{t}(\omega, \tau)$ , we find  $\tilde{\mathcal{E}}_{pump}(\omega, \tau)$ , as shown in Fig. D.6. Figure D.6 (a) shows the real part and Fig. D.6 (b) contains the imaginary part.

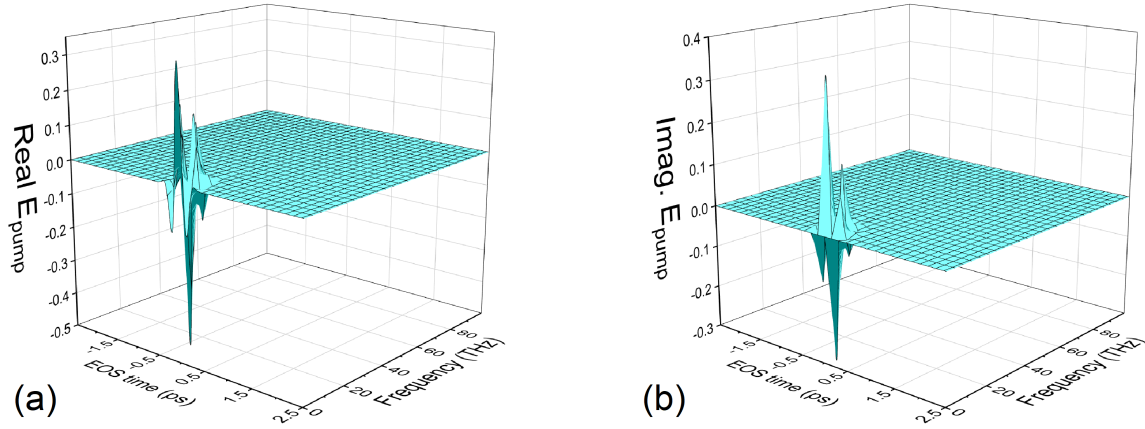


Figure D.6: Time-frequency  $\mathcal{E}_{pump}$ . (a) Real part and (b) imaginary part.

Performing the inverse Gabor transform on  $\tilde{\mathcal{E}}_{pump}(\omega, \tau)$  yields the transmitted  $\mathcal{E}_{pump}(\tau)$  shown in Fig. D.7 (red).  $\mathcal{E}_{pump}$  is shown along side the reference waveform (black) and carrier density (blue).

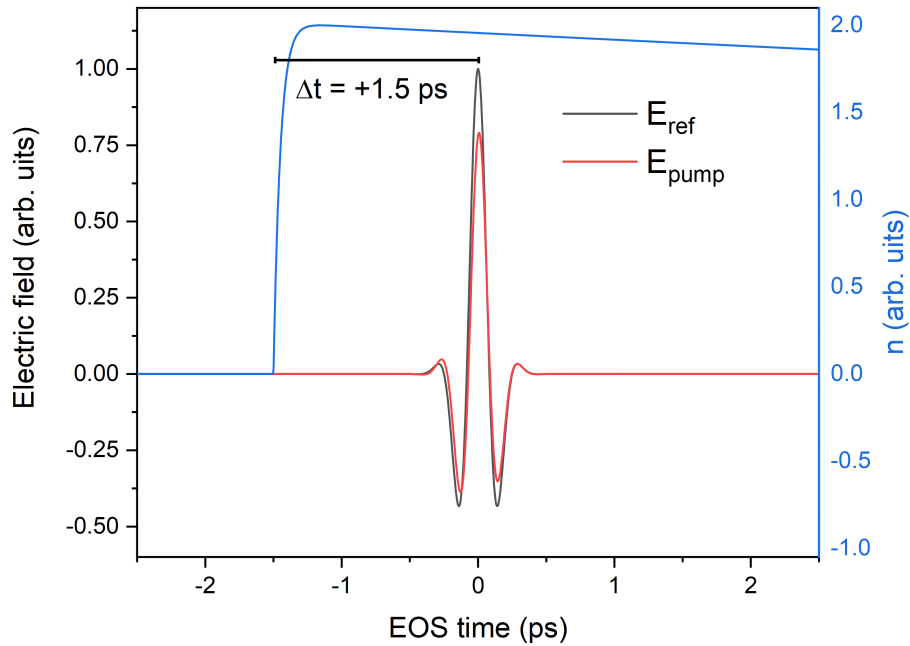


Figure D.7:  $\mathcal{E}_{pump}$  simulated with time-frequency analysis.

## D.5 Discussion

Working in the reference frame of the THz pulse allows us to compare our simulations to the foundations of Beard et al. [87]. At early pump-probe delay times the visible excitation arrives at the sample *as* the THz pulse is propagating through it. In these early times the excitation only attenuates the trailing parts of the THz pulse, leading to a different set of optical properties that were not experienced by the leading parts of the THz pulse [87]. This is observed best by plotting  $\Delta\mathcal{E} = \mathcal{E}_{ref} - \mathcal{E}_{pump}$  for each pump-probe delay. This is shown in the contour plot of Fig. D.8 (a). This simulation uses the same values as the previous simulation, and varies the pump-probe delay from -1.5 to 2.5 ps. The prior simulation occurs at the pump-probe delay of 1.5 ps. The black line represents the projection axis of Beard et al. [87].

At a fixed pump-probe delay we can calculate  $\Delta\mathcal{E}$ , as shown in Fig. D.8 (b) where the pump-probe delay is 0 ps. The dashed-line in Fig. D.8 (b) corresponds to the reference field, and by comparison it is clear that  $\Delta\mathcal{E}$  varies across the waveform. This is the feature noted by Beard et al, where there is a finite  $\Delta\mathcal{E}$  for one half of the THz field, and no  $\Delta\mathcal{E}$  for the other half.

Fixing the electro-optic sampling time at 0 ps, and varying the pump-probe delay time gives rise to a measurement of  $\Delta\mathcal{E}$  that is proportional to the charge carrier lifetime. This is shown in Fig. D.8 (c), where the black solid line corresponds to  $\Delta\mathcal{E}$ , and the red dotted line is  $0.119 \times n(t)$ . Indeed we find beyond-excellent agreement between the two.

## D.6 Summary

We have shown that by assuming a time-frequency perspective, we are able to model a time-resolved terahertz spectroscopy experiment while working in the unprojected time domain suggested by Beard et al. Future work is needed to formulate a more rigorous foundation for this technique, as it may be promising for direct observation of hot-carrier cooling dynamics that occur during the rise-time of a pump-probe experiment.

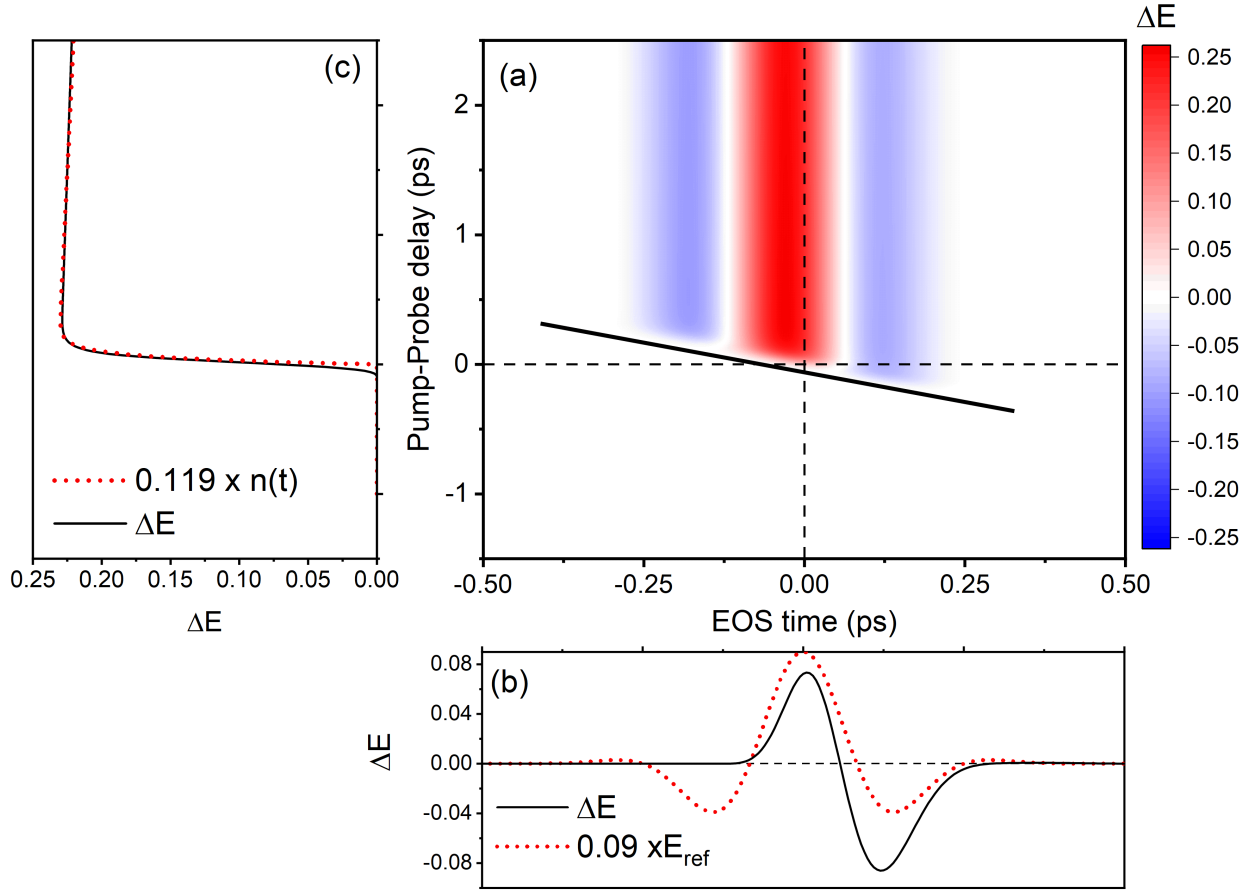


Figure D.8:  $\Delta\mathcal{E}$  contour plot. (a) Contour plot of  $\Delta\mathcal{E} = \mathcal{E}_{ref} - \mathcal{E}_{pump}$ . The x-axis is the reference frame of the THz pulse (electro-optic sampling time), and the y-axis is the pump-probe delay time. (b) Finite  $\Delta\mathcal{E}$  for positive EOS time, and near zero for negative EOS times indicating the this model captures the asymmetric attenuation noted by Beard et al. [87]. (c) Fixing the EOS time to 0 ps and scanning the relative pump-probe delay results in  $\Delta\mathcal{E}$  (black line) that closely mirrors the carrier density  $n$  (red dotted line). The black line in (a) is a  $45^\circ$  line that corresponds to the axis upon which Beard et al. project their data [87].

# Appendix E

## Negative $\sigma_1$ Impulse Response

### E.1 Introduction

Initial measurements of HgCdTe revealed an interesting feature of the photoconductivity spectrum. When applying the Tinkham formula, it was found that the real part of the photoconductivity transitioned from positive to negative around 1 THz [336]. This prompted many follow up measurements and analyses, and the work presented here was part of that effort. Nonetheless, this work is (as far as I am aware) entirely new to the THz community, and warrants documentation.

Recall that the conductivity spectrum is given by the Fourier transform of the impulse response

$$\tilde{\sigma}(\omega) \approx \int_{-\infty}^{\infty} K(t) \exp(i\omega t) dt.$$

Exploring various forms of the impulse response  $K(t)$ , a natural question emerges: “What would the impulse response look like if the interrogating pulse did not have the form of a delta function?”. A simple solution may have the form

$$K(t) = \left(1 - \exp(-t/\tau_1)\right) \exp(-t/\tau_2) \Theta(t) \tag{E.1}$$

where  $\tau_1$  parameterizes a slow onset of the current density (perhaps from hot carrier cooling), and  $\tau_2$  represents the relaxation timescale, and  $\Theta(t)$  is the Heaviside step function.

Expanding Eq. (E.1), we find

$$K(t) = \frac{ne^2}{m^*} \left( \exp(-t/\tau_2) - \exp(-t/\tau_{eff}) \right) \Theta(t) \quad (\text{E.2})$$

where the effective time constant is defined as  $1/\tau_{eff} = 1/\tau_1 + 1/\tau_2$ . An example of this is given in Fig. E.1 (a) for  $\tau_1 = 1.65$  ps and  $\tau_2 = 0.54$  ps\*. The blue line represents the momentum relaxation, governed by  $\tau_2$ . The red line is for the rise dynamics, governed by  $\tau_1$ . The black line is the full response, as given by Eq. (E.1).

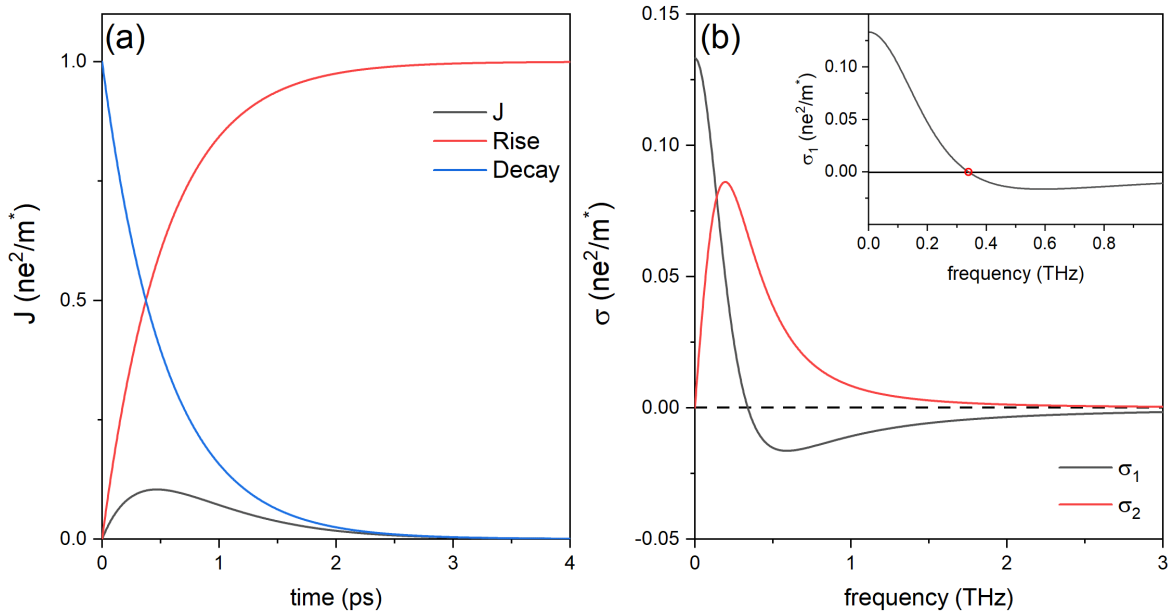


Figure E.1: Impulse-response function with negative real conductivity. (a) Impulse response and (b) complex conductivity.

Since the Fourier transform is a linear operator, we may transform each component of  $K(t)$  individually, giving similar results to what was found Chapter 2. The conductivity is thus given by

$$\tilde{\sigma}(\omega) = \frac{ne^2}{m^*} \left[ \frac{\tau_2}{1 - i\omega\tau_2} - \frac{\tau_{eff}}{1 - i\omega\tau_{eff}} \right]. \quad (\text{E.3})$$

The crossover from positive to negative of the real part can be found in a straightforward

---

\*Numbers chosen randomly by my officemates.

calculation by setting the real part  $\Re[\tilde{\sigma}] = 0$ . The crossover frequency  $f_0$  is given by

$$f_0 = \frac{1}{2\pi} \sqrt{\frac{1}{\tau_2 \tau_{eff}}}. \quad (\text{E.4})$$

Figure E.1 (b) shows an example of the conductivity spectrum using the same values as Fig. E.1 (a). The inset of Fig. E.1 (b) shows a close up of  $\sigma_1$  where we can see that it turns negative at  $f_0 = 0.33955\dots$  THz, as predicted from Eq. (E.4).

## E.2 Application to $\text{Hg}_{0.8}\text{Cd}_{0.2}\text{Te}$ Thin Film

As promised, this model was applied to TRTS performed on a  $\text{Hg}_{0.8}\text{Cd}_{0.2}\text{Te}$  thin film. The  $\text{Hg}_{0.8}\text{Cd}_{0.2}\text{Te}$  film was 4  $\mu\text{m}$  thick, grown on a lattice-matched 0.8 mm substrate made of  $\text{Cd}_{0.96}\text{Zn}_{0.04}\text{Te}$ . The  $\text{Hg}_{0.8}\text{Cd}_{0.2}\text{Te}$  film was illuminated with 800 nm pulses at a fluence of 12  $\text{nJ}/\text{cm}^2$ . The photoconductivity was measured 250 ps after photoexcitation, and the temperature was increased from 20 K to 295 K. Figure E.2 shows the results of fitting the  $\text{Hg}_{0.8}\text{Cd}_{0.2}\text{Te}$  photoconductivity spectrum to Eq. (E.3).

In Fig. E.2 (a) and (b), the real and imaginary parts are shown, respectively, for two temperatures of 20 K and 295 K. There is a significant difference in both  $\sigma_1$  and  $\sigma_2$ . At 20 K,  $\sigma_1$  the crossover frequency appears near  $\sim 1$  THz. At 295 K,  $\sigma_1$  is much lower due to the weaker absorption, and exhibits no negative photoconductivity. Recall that once  $\tau_1$  and  $\tau_2$  are found, we can reconstruct the current density through Eq. (E.1). Over a variety of temperatures from 20 K to 295 K, the photoconductivity is fit to Eq. (E.2), and the corresponding  $K(t)$ , as shown in Fig. E.2 (c). We can see a general trend in the impulse response, where the rise time appears to become more significant at lower temperatures, which explains the observed negative  $\sigma_1$ . Quite simply, it takes longer for carriers to cool at lower temperature because the scattering mechanisms are frozen out. Finally, at 295 K  $\tau_1$  had to be fixed to 0 ps, which corresponds to a simple Drude model.

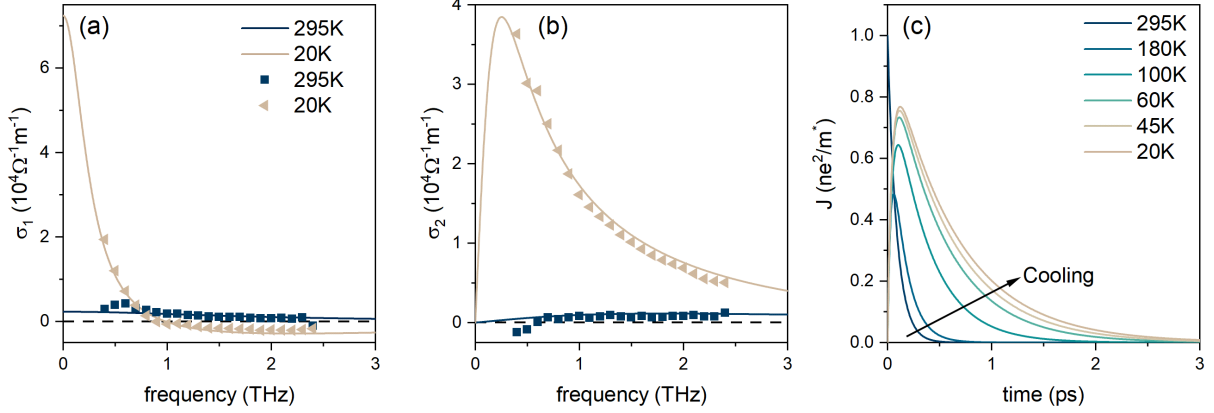


Figure E.2: Fitting the  $\text{Hg}_{0.8}\text{Cd}_{0.2}\text{Te}$  TRTS with the custom impulse response. (a) 20 K fit. (b) 295 K fit. (c) Temperature dependence of the response function.

The temperature dependence of the fit parameters are provided in Fig. E.3. Our observations regarding  $\tau_1$  and  $\tau_2$  can be seen in Fig. E.3 (a) and (b).  $\tau_1$  appears to increase as the sample is cooled, quickly saturating around a value of  $\sim 0.045$  ps. On the other hand,  $\tau_2$  appears to increase significantly as the sample is cooled, starting at  $\sim 0.1$  ps and increasing to a substantial fraction of a picosecond  $\sim 0.625$  ps. In Fig. E.3 (c) we find that the carrier density increases as the temperature is lowered, reaching a maximum near  $\sim 100$  K after which  $n$  decreases. To quantify the mobility, we set  $\omega = 0$  in Eq. (E.2), from which it is found that

$$\sigma_{DC} = \frac{ne^2}{m^*} (\tau_2 - \tau_{eff}) \equiv ne\mu. \quad (\text{E.5})$$

The mobility is hence given by

$$\mu = \frac{e}{m^*} (\tau_2 - \tau_{eff}). \quad (\text{E.6})$$

The mobility is shown in Fig. E.3 (d). Owing to the large increase in  $\tau_2$ , the mobility reaches values of  $\sim 2 \times 10^5$   $\text{cm}^2/\text{Vs}$ , roughly 20 times higher than the high mobility semiconductor GaAs.

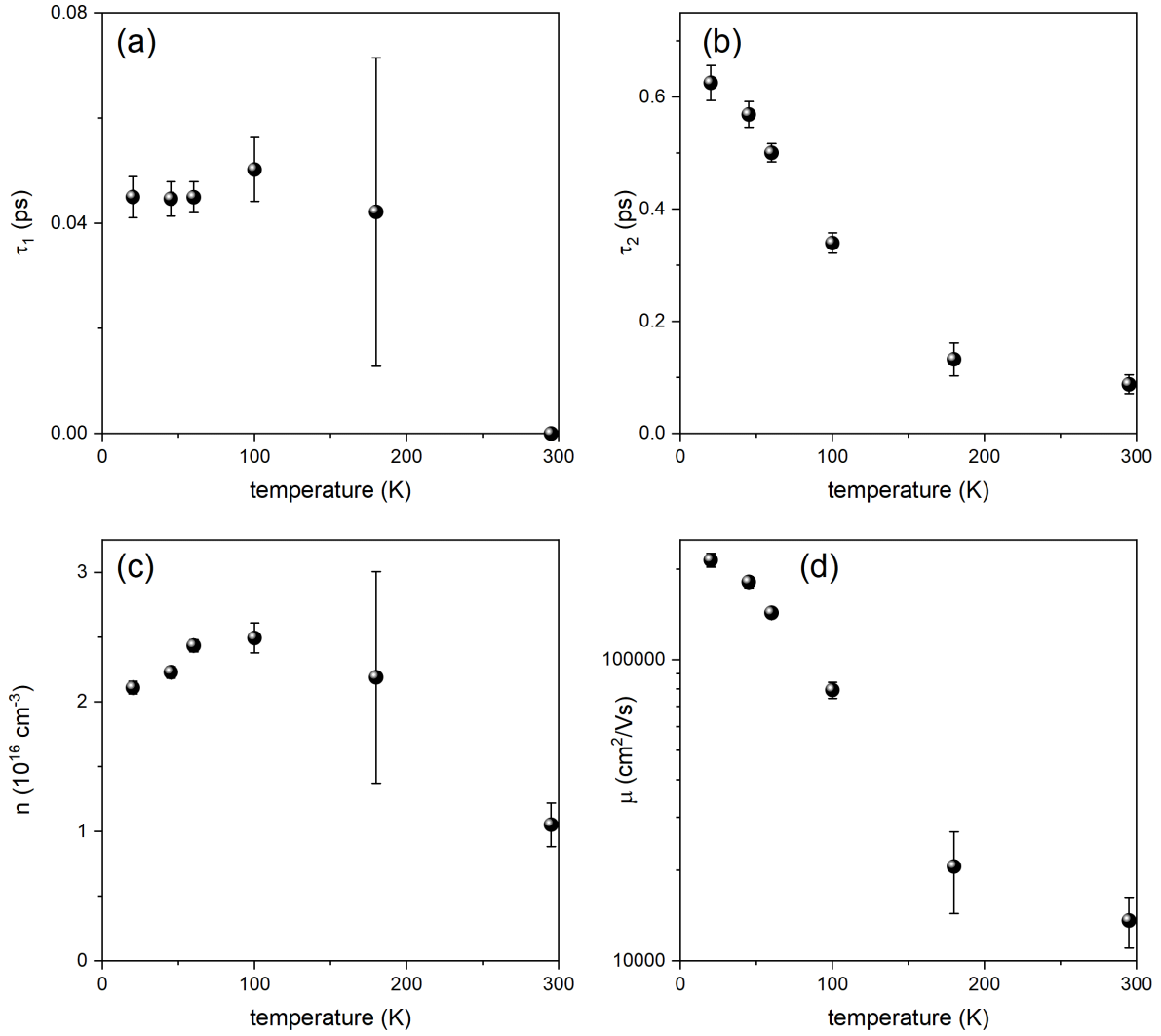


Figure E.3: Temperature dependent fit parameters of Hg<sub>0.8</sub>Cd<sub>0.2</sub>Te thin film. (a)  $\tau_1$ , (b)  $\tau_2$ , (c)  $n$ , and (d)  $\mu$ .